INVERSE DESIGN OF HEAT TREATMENT PROCESSES IN RADIANT FURNACES

A Dissertation

by

Ersin Yıldız

Submitted to the
Graduate School of Sciences and Engineering
in Partial Fulfillment of the Requirements for
the Degree of

Doctor of Philosophy

in the
Department of Mechanical Engineering

Özyeğin University
August 2024

Copyright © 2024 by Ersin Yıldız

INVERSE DESIGN OF HEAT TREATMENT PROCESSES IN RADIANT FURNACES

Approved by:

Asst. Prof. Altuğ M. Başol
Department of Mechanical Engineering
Özyeğin University

Prof. Hakan Ertürk
Department of Mechanical Engineering
Boğaziçi University

Prof. M. Pınar Mengüç
Department of Mechanical Engineering
Özyeğin University

Prof. Mehmet Şahin
Department of Astronautical Engineering
Istanbul Technical University

Date Approved: August 12, 2024

Assoc. Prof. Özgür Ertunç
Department of Mechanical Engineering
Özyeğin University

To my wife, my parents, my sister, and my nieces, with all my love

ABSTRACT

This dissertation focuses on optimizing heat treatment processes, crucial for manufacturing industries, with the aim of ensuring desired treatment of workpieces while addressing energy costs. Traditional optimization approaches have primarily concentrated on uniform treatment over the workpiece surface, often neglecting internal conduction, leading to significant modeling errors when internal thermal gradients are critical in industrial scenarios. Our model employs a design point approach within the workpieces to define design conditions, overcoming the limitations of traditional methods that ignore internal conduction of workpieces.

The study investigates the heat treatment of workpieces within batch furnaces, where the radiation heat transfer within the enclosure is dominant while incorporating internal conduction inside workpieces. A novel gradient-based optimization methodology has been developed, incorporating a direct differentiation approach for calculating sensitivity coefficients. Regularization techniques are employed to address the ill-posed nature of inverse radiant boundary design problems.

Calculating sensitivity coefficients through direct differentiation typically requires explicit formulations of the variables, which are often unavailable due to radiation-conduction coupling in our target problems. To overcome this, floating random walk methods were utilized to derive explicit formulations for workpiece surface and internal design point temperatures, a novel application for inverse radiant boundary design problems.

The research involves comprehensive analyses to verify and apply the developed methodology. The methodology is verified by reconstructing known heater temperatures for heating two glass panes. Analysis of design point configurations reveals

that increased number of design point enhances the accuracy of the inverse solution by providing more precise sensitivity information. The study also examines the impact of noisy input data and regularizer weights, demonstrating the robustness and stability of the developed methodology.

Comparative analysis of furnace operation using temperature-based and power-based approaches showed that both methods achieved uniform heating of six glass panes, with the Power-based Approach being more practical by avoiding negative power inputs. Analysis of different heating curves showed, smoother heating-to-soaking transition reduced power demands, providing insights into optimal heating curves.

For a six-hour heating treatment of a cubic stainless-steel workpiece, the inverse solution determined required transient heater powers, with central heaters driving heating and edge heaters ensuring uniformity in soaking phase. Analysis of heater layout configurations showed that increasing the number of heater elements enhances temperature uniformity, providing more precise thermal management. The cooling phase analysis compared two approaches; determination of heater powers together alongside a predefined constant cooling and simultaneous determination of heater and chamber powers. The latter achieved high cooling uniformity but required higher energy, highlighting trade-offs between uniformity and energy demands.

These analyses demonstrate the robustness and practical applicability of the developed methodologies, providing valuable insights for optimizing furnace design and operation. The study's findings are particularly relevant for industries such as glass, semiconductor, automotive and aerospace, where precise heat treatment processes are essential for producing high-quality components. By adopting these optimized practices, furnace designers and operators can gain significant understanding into optimizing furnace operating parameters, leading to improved process effectiveness, energy savings, and high-quality outcomes.

ÖZETÇE

Bu tez, imalat sanayileri için kritik olan ısıl işlem uygulamalarını optimize etmeye odaklanmakta ve iş parçalarının istenilen şekilde ısıl işlem görmesini sağlarken enerji gerekliliklerini incelemeyi amaçlamaktadır. Geleneksel optimizasyon yaklaşımları iş parçası yüzeyinde üniform işlem sağlamaya odaklanmış, sıklıkla iç ısıl iletimi ihmal etmiş ve endüstriyel senaryolarda iç termal gradyanlar kritik olduğunda önemli modelleme hatalarına yol açmıştır. Modelimiz, tasarım koşullarını tanımlamak için iş parça için tasarım noktası yaklaşımı kullanmaktadır ve iç ısıl iletimi göz ardı eden geleneksel yöntemlerin sınırlamalarını aşmaktadır.

Çalışma, iş parçalarının iç ısıl iletimini dahil ederken radyasyon ısı transferi baskın yığımlı fırınlarında ısıl işlem uygulamalarını araştırmaktadır. Duyarlılık katsayılarını hesaplamak için doğrudan türev alma yaklaşımını içeren yenilikçi bir gradyan tabanlı optimizasyon metodolojisi geliştirilmiştir. Ters ışınım sınır tasarım problemlerinin kötü koşullanmış doğasını ele almak için düzenleme teknikleri kullanılmaktadır.

Duyarlılık katsayılarını doğrudan türev alma yoluyla hesaplamak, hedef problemlerimizde radyasyon-iletim bağlantısı nedeniyle genellikle mevcut olmayan değişkenlerin açık formülasyonlarını gerektirir. Bunu aşmak için, iş parçası yüzeyi ve iç tasarım noktası sıcaklıkları için açık formülasyonlar türetmek amacıyla değişken rastgele yürüyüş yöntemleri kullanılmıştır. Bu yaklaşım, ters ışınım sınır tasarım problemleri için yenilikçi bir uygulamadır.

Bu araştırma, geliştirilen metodolojiyi doğrulamak ve uygulamak için kapsamlı analizleri içermektedir. Metodoloji, iki cam levhayı ısıtmak için bilinen ısıtıcı sıcaklıklarını yeniden oluşturarak doğrulanmıştır. Tasarım noktası konfigürasyonlarının analizi, daha yoğun bir yerleşimin, daha hassas duyarlılık bilgileri sağlayarak ters çözümün

doğruluğunu artırdığını ortaya koymaktadır. Çalışma ayrıca gürültülü veri ve düzenleyici katsayılarının etkisini inceleyerek geliştirilen metodolojinin sağlamlığını ve kararlılığını göstermektedir.

Sıcaklık tabanlı ve güç tabanlı yaklaşımlar kullanılarak yapılan fırın operasyonu analizleri, her iki yöntemin de altı cam levhanın eşit ısıtılmasını sağladığını, güç tabanlı yaklaşımın negatif güç gereksiniminden kaçınarak daha pratik olduğunu göstermiştir. Farklı ısıtma stratejilerinin analizi, ısıtma ve bekletme aşamaları arasındaki daha yumuşak geçişlerin güç taleplerini azalttığını ve optimal ısıtma eğrileri hakkında bilgiler sağladığını göstermiştir.

Altı saatlik kübik paslanmaz çelik bir iş parçasının ısıl işlemi için ters çözüm, merkezi ısıtıcıların ısıtmayı sağladığı ve kenar ısıtıcıların bekletme aşamasında üniformite sağladığı zamana bağlı ısıtıcı güçlerini belirlemiştir. Isıtıcı yerleşim konfigürasyonlarının analizi, daha yoğun ısıtıcı eleman yerleşiminin daha hassas termal yönetim sayesinde daha iyi bir sıcaklık üniformitesi sağladığını göstermiştir. Soğutma aşaması analizinde iki yaklaşımı karşılaştırmıştır; önceden tanımlanmış sabit soğutmaya ek ısıtma güçlerinin ayarlanması, ve ısıtma ve soğutma güçlerinin eşzamanlı olarak ayarlanması. İkincisi, daha yüksek soğutma üniformitesi sağlamış ancak daha fazla enerji gerektirmiş, üniformite ve enerji talepleri arasındaki ödünleşimleri vurgulamıştır.

Bu analizler, geliştirilen yöntemlerin istikrarlılığını ve pratik uygulanabilirliğini göstererek, fırın tasarımı ve işletimini optimize etmek için değerli bilgiler sağlamaktadır. Çalışmanın bulguları, cam, yarı iletken, otomotiv ve havacılık gibi yüksek kaliteli bileşenler üretmek için hassas ısıl işlem süreçlerinin gerekli olduğu endüstriler için özellikle önemlidir. Bu optimize edilmiş uygulamaları benimseyerek, fırın tasarımcıları ve operatörleri, fırın işletme parametrelerini optimize etme konusunda önemli anlayış kazanabilir, ve bu da ısıl işlem uygulamalarının etkinliğini artırır, enerji tasarrufu sağlar ve yüksek kaliteli sonuçlar elde etmeyi mümkün kılar.

ACKNOWLEDGEMENTS

I would like to express my deepest gratitude to a number of people without whom this thesis would not have been possible.

First and foremost, I am eternally grateful to my wife, Fatmanur Tiryaki Yıldız, for her immense love, unwavering support, and cheerful presence throughout both my PhD journey and life. Fatmanur understands my experiences and challenges better than anyone else, making her not just my partner but also my greatest confidant. We listen to and genuinely value each other's perspectives, understanding our lives and enriching our shared experiences and growth together. Her encouragement during the times of doubt and her joy during the moments of success have been my guiding light. Her belief in my abilities has been a constant source of motivation, driving me to strive for excellence. I deeply thank her for being an integral part of my life and for all the moments we share.

I am profoundly grateful to my mother, Fatma Yıldız, and my father, Halil Yıldız, who have been embodiments of grace and dedication. Their boundless, unconditional love and selfless actions have always been aimed at making life easier for their children. They have raised us with thoughtfulness and care, consistently putting our needs and well-being first. I am forever thankful for having them as my parents and appreciate everything they have done. Their support and sacrifices have been fundamental to my achievements, and I owe them more than words can express.

I owe immense gratitude to my sister, Esra Kırmızı, who has always been the best sister one could ever hope for. She has been a constant source of support and understanding, always striving to empathize and assist in whatever way she can. Beyond just family, she has also been a treasured friend with whom I can share anything

without hesitation. Her unwavering friendship and sisterly love have been a cornerstone of my personal and academic life. She is also the mother of my two wonderful nieces, Nil Kırmızı and Ezgi Kırmızı. The feeling of being an uncle to such great kids is incredibly valuable and fills me with pride. Additionally, I am grateful to my brother-in-law, Nevzat Kırmızı, for his warmth and companionship. His welcoming nature and supportive attitude have greatly enhanced our family gatherings.

I am profoundly grateful to my PhD supervisor, Altuğ M. Başol, not only for his guidance but also for his kindness and support. His approach has significantly enriched my doctoral experience. His unwavering encouragement and insightful feedback have been invaluable throughout my research journey. I also extend my sincere thanks to my thesis monitoring committee members, M. Pınar Mengüç and Hakan Ertürk. Working with such experienced and esteemed academics has been a truly fortunate experience. Specifically, I want to express my deepest appreciation to M. Pınar Mengüç. It has been a privilege to study under his tutelage, benefiting from his helpful, supportive nature and vast academic knowledge. A special thanks goes to him for the Radiative Heat Transfer course he delivered, which expanded both my knowledge and understanding.

I would like to extend my thanks to my colleagues at Özyeğin University, specifically M. Kürşat Uzuner, Berkay Halvaşi, Tolga Altınoluk, A. Enes Öksüz and Gönenç Can Altun. Our environment was not only fun but also enthusiastic, making our time together both enjoyable and intellectually rewarding. Unfortunately, our opportunity to spend more time together was curtailed by the COVID-19 pandemic. I deeply wish we could have continued our collaborations and daily interactions for much longer. I am grateful for their companionship and collaboration during those times and hope for nothing but the best for each of them in their future endeavors.

I must also extend my heartfelt gratitude to my friends, Bahadır Pamuk, Emre Saydam, A. Ozan Kaygısız, Cansu Büyükbalcı, Ozan Ege Erdal, Özge Duman, Umut

Batman (from Gotham city), Can Turgut, Erdem Başkök and Ali Berk Kahraman for being companions throughout my journey. Their companionship has brought countless moments of joy and relaxation throughout the rigorous demands of today's life. We have shared many enjoyable moments and have always stood by each other, providing mutual support and laughter when it was needed most. I am thankful for both the fun times and the strength we have drawn from each other, and I cherish the enduring friendships we have built together.

Finally, I am grateful to Özyeğin University, including the faculty members and officers of the Mechanical Engineering Department, Especially, I would like to thank the administrative supervisor, Gizem Bakır, for her invaluable assistance. She was always helpful and promptly answered all my questions regarding everything about my PhD at Özyeğin University.

This thesis stands as a milestone in my life, and I am proud to share this achievement with all of you.

TABLE OF CONTENTS

DEDICATION . . . . . **iii**

ABSTRACT . . . . . **iv**

ÖZETÇE . . . . . **vi**

ACKNOWLEDGEMENTS . . . . . **viii**

LIST OF TABLES . . . . . **xix**

LIST OF FIGURES . . . . . **xx**

I INTRODUCTION **1**

1.1 Motivation from a Historical Perspective 1

1.2 Heat Treatment Processes 2

1.2.1 Principles and Significance of Heat Treatment 2

1.2.2 Heat Treatment Techniques and Furnaces 3

1.2.3 Mechanisms of Heat Transfer 4

1.2.4 Challenges in Heat Treatment Furnace Operation 5

1.2.5 Heat Treatment Process Focused in This Study 7

1.3 Introduction to Inverse Problems 8

1.3.1 Overview of Forward and Inverse Problems 8

1.3.2 Types of Inverse Heat Transfer Problems 9

1.3.3 Ill-posed Characteristics of Inverse Problems 9

1.3.4 Pioneering Studies in Inverse Radiation Heat Transfer Problems 10

1.4 Mathematical Properties of Inverse Problems 11

1.4.1 Linear Inverse Problems 11

1.4.2 Nonlinear Inverse Problems 12

1.5 Solution Methods for Inverse Problems 14

1.5.1 Linear Regularization Techniques 14

1.5.2 Gradient-Based Optimization Methods 16

1.5.3 Calculating Sensitivity Coefficients in Gradient-Based Optimization Methods . . . 18
1.5.4 Other Inverse Solution Methods . . . 21
1.5.5 Selecting a Suitable Inverse Solution Method . . . 22
1.5.6 Inverse Solution Method Employed in This Study . . . 24
1.6 Radiant Enclosure Design Problems . . . 25
1.6.1 Heat Transfer Mechanisms Involved . . . 25
1.6.2 Design Condition Definition . . . 26
1.6.3 Design Variable Definition . . . 27
1.6.4 Heat Transfer Modeling Approaches Used in Inverse Radiant Boundary Design Problems . . . 28
1.6.5 Experimental Validations of Inverse Solutions . . . 31
1.6.6 Applications of Inverse Solution in Radiant Enclosure Problems 32
1.7 Random Walk-Based Methods in Heat Transfer Analyses . . . 33
1.8 Research Objectives . . . 34
1.9 Limitations . . . 37
1.10 Organization of the Dissertation . . . 38
II INVERSE PROBLEM DESCRIPTION . . . 39
2.1 Model Problem Overview . . . 39
2.2 Material Properties . . . 42
2.3 Heat Transfer Modeling . . . 42
2.3.1 Conduction within the Workpieces . . . 42
2.3.2 Lumped Capacitance Approach for Furnace Surface Temperature . . . 43
2.3.3 Radiation Heat Transfer . . . 43
2.3.4 Heat Loss at the Furnace Surfaces . . . 44
2.4 Assumptions in the Model . . . 45
2.4.1 Material and Surface Property Assumptions . . . 45
2.4.2 Assumptions for Radiant Furnace Enclosure . . . 45
2.4.3 Assumptions Arising from Discretizations . . . 46

2.4.4 Assumptions in Thermal Modeling of Furnace Surface Elements 46
2.5 Design Condition: Desired Design Point Temperature 46
2.6 Design Variable: Furnace Operating Parameters 47
2.6.1 Furnace Operating Surfaces 48
2.6.2 Furnace Operating Variables 48
2.6.3 Furnace Operating Variable Function 49
2.6.4 Furnace Operating Parameters 50
2.7 Inverse Problem Formulation 51
III NUMERICAL METHODOLOGY FOR FORWARD SOLUTION 53
3.1 Forward Solution 53
3.1.1 Conduction within Workpiece 53
3.1.2 Conduction-Radiation Coupling at Workpiece Boundaries . . 54
3.1.3 Radiative Heat Fluxes at Workpiece and Furnace Surfaces . . 55
3.1.4 Exchange Factors in Radiation Heat Transfer Model 55
3.1.5 Calculations for Furnace Thermal Modeling 55
3.1.6 Solver Architecture 56
3.1.7 Forward Solution Overview 57
3.1.8 Use of Forward Solution in Thesis Context 57
3.2 Monte Carlo Ray Tracing for Calculation of Exchange Factors . . . 58
3.2.1 Location of Emission 59
3.2.2 Direction of Emission 59
3.2.3 Absorption or Reflection by a Surface 59
3.2.4 Exchange Factors by Monte Carlo Ray Tracing 60
3.2.5 Backward Monte Carlo Ray Tracing 61
3.2.6 Verification of Monte Carlo Ray Tracing Code 61
3.2.6.1 Verification of View Factor Calculation 62
3.2.6.2 Verification of Exchange Factor Calculation 63

3.2.7 Remarks on Monte Carlo Ray Tracing for Exchange Factor Calculation . . . 64
3.3 Computational Framework Developed for Forward Solution . . . 66
3.3.1 OpenFOAM . . . 66
3.3.2 OptiX Ray Tracing Engine . . . 66
IV NUMERICAL METHODOLOGY FOR INVERSE SOLUTION . . . 68
4.1 Inverse Solution . . . 68
4.1.1 Gradient-Based optimization . . . 68
4.1.2 Gauss-Newton Algorithm . . . 69
4.1.3 Sensitivity Coefficients . . . 70
4.1.4 Regularization Applied to Inverse Problem . . . 71
4.1.4.1 Proximal Point Regularizer with L2-norm . . . 73
4.1.4.2 Custom Regularizer with L1-norm . . . 73
4.1.5 Convergence Criteria . . . 74
4.1.6 Inverse Solution Flowchart . . . 75
4.2 Sensitivity Coefficient Calculation . . . 75
4.2.1 Derivatives of the Furnace Operating Variable Function . . . 78
4.2.2 Derivatives of the Furnace Surface Element Temperature . . . 78
4.2.3 Derivatives of the Heat Loss at the Furnace Surfaces . . . 78
4.2.4 Derivatives of the Radiative Heat Fluxes . . . 79
4.2.5 Derivatives of the Workpiece Surface Temperature . . . 79
4.2.6 Derivatives of the Design Point Temperature . . . 80
4.2.7 Final Form of the Sensitivity Coefficients . . . 80
4.3 Subdomain Optimization with Overlap . . . 82
4.4 Computational Framework Developed for Inverse Solution . . . 85
4.4.1 PetSc/TAO . . . 85
4.4.2 GPU Computing with CUDA C++ . . . 85
4.5 Computational Hardware Specifications . . . 86

V FLOATING RANDOM WALK METHOD 87

5.1 Classical Floating Random Walk Method 87

5.1.1 Fundamentals of Particle's Random Walk 88

5.1.2 Application in Complex-Shaped Domains 89

5.1.3 Updating Particles' Position and Time 89

5.1.4 Sampling from Cumulative Distribution Functions 90

5.1.5 Implementation in Boundary Strip 91

5.1.6 Implementation at Boundary 92

5.1.7 Particle Termination 93

5.1.8 Overview of the Floating Random Walk Procedure 93

5.2 Verification of Floating Random Walk Solution for Conduction 94

5.2.1 Semi-infinite Three-dimensional Steady-state Heat Conduction 95

5.2.2 One-dimensional Transient Heat Conduction 96

5.3 Formulation of Design Point Temperature by Classical FRW method 97

5.4 Formulation of Workpiece Surface Temperature by Modified FRW method 99

5.5 Remarks on Floating Random Walk Method 101

VI DETERMINATION OF STEADY HEATER TEMPERATURES FOR TRANSIENT HEATING OF TWO GLASS PANES . . . 104

6.1 Problem Definition: Heating of Two Glass Panes 104

6.2 Numerical Settings and Parameters 108

6.3 Sensitivity Coefficients 108

6.4 Results 108

6.4.1 Numerical Analyses 110

6.4.1.1 Time Step Size Analysis 111

6.4.1.2 Statistical Analyses 112

6.4.1.3 Sensitivity Coefficient Verification 113

6.4.2 Test Case 1: Reconstruction of Known Solution 114

6.4.2.1 Impact of Design Point Layout 116
6.4.2.2 Impact of Design Point Depth 116
6.4.2.3 Impact of Design Point Plane 118
6.4.2.4 Impact of Noise in Desired Design Point Temperature Data 118
6.4.3 Test Case 2: Determination of Heater Temperature for Uniform Heating 121
6.4.3.1 Impact of Design Point Layout 121
6.4.3.2 Impact of Design Point Depth 123
6.4.3.3 Heating Uniformity 125
6.4.3.4 Regularizer Weight Analysis 126
6.4.3.5 Initial Guess Analysis 129
6.4.4 Comparison Between Steady and Transient Heater Temperature Solutions 131
6.4.5 Computational Time Costs 133
6.5 Concluding Remarks 135

VII COMPARISON OF FURNACE OPERATION APPROACHES AND HEATING STRATEGIES FOR HEAT TREATMENT OF SIX GLASS PANES 138

7.1 Problem Definition: Heating and Soaking of Six Glass Panes 139
7.1.1 Design Conditions for Three Cases 141
7.1.2 Design Variable and Heater Arrangement 142
7.2 Numerical Settings and Parameters 143
7.3 Numerical Analyses 144
7.3.1 Time Step Size Analysis 144
7.3.2 Statistical Analyses 145
7.3.3 Sensitivity Coefficient Verification 146
7.4 Results 148
7.4.1 Case 1: Linear Heating with Sharp Transition to Soaking . . 148
7.4.2 Case 2: Heating with Smooth Transition to Soaking 151

7.4.3 Case 3: Prolonged Heating with Smooth Transition to Soaking 153
7.4.4 Determined Heater Temperature Distributions 153
7.4.5 Determined Total Heater Powers 156
7.4.6 Computational Time Costs 159
7.5 Concluding Remarks 159

VIII EVALUATING FURNACE DESIGN CONFIGURATION FOR DESIRED HEATING OF STAINLESS-STEEL CUBIC WORKPIECE 162

8.1 Problem Definition: Heating Phase of a Cubic Workpiece in a Radiant Furnace 163
8.1.1 Thermal Model 163
8.1.2 Design Condition 165
8.1.3 Design Variable and Heater Element Grouping 166
8.2 Numerical Settings and Parameters 167
8.3 Numerical Analyses 168
8.4 Results 170
8.4.1 Determining Necessary Heater Powers for Uniform Heating . 170
8.4.2 Impact of Overall Heat Transfer Coefficient $\bar{U}$ 177
8.4.3 Impact of Chamber Reflectivity 179
8.4.4 Impact of Heater Layout 181
8.4.5 Impact of Heater Material 184
8.5 Computational Time Costs 186
8.6 Concluding Remarks 186

IX EVALUATING FURNACE OPERATION PRACTICES FOR ACHIEVING DESIRED COOLING OF STAINLESS-STEEL CUBIC WORKPIECE 189

9.1 Problem Definition: Cooling Phase of a Cubic Workpiece in a Radiant Furnace 190
9.2 Design Variable and Furnace Operating Surface Grouping 190
9.2.1 Operating Group Set 1 191

9.2.2 Operating Group Set 2 . . . 191
9.3 Numerical Settings and Parameters . . . 193
9.4 Results . . . 193
9.4.1 Forward Solution with Predefined Cooling Source . . . 194
9.4.2 Case 1: Comparison of Operating Group Sets . . . 199
9.4.2.1 Design Condition . . . 200
9.4.2.2 Resulting Design Point Temperatures and Temperature Uniformity . . . 201
9.4.2.3 Determined Heater and Chamber Powers . . . 202
9.4.2.4 Resulting Heater and Chamber Temperatures . . . 205
9.4.3 Case 2: Ensuring a Custom Cooling Curve Uniformly . . . 208
9.4.3.1 Design Condition . . . 208
9.4.3.2 Resulting Design Point Temperature and Determined Heater and Chamber Powers . . . 208
9.4.3.3 Resulting Total Heater and Chamber Powers . . . 209
9.4.3.4 Resulting Heater and Chamber Temperatures . . . 211
9.5 Computational Time Costs . . . 214
9.6 Concluding Remarks . . . 214
X CONCLUSIONS . . . 217
10.1 Outcomes of The Study . . . 217
10.2 Contributions to Literature . . . 220
10.3 Recommendations for Future Work . . . 221
10.4 Final Thoughts . . . 222
REFERENCES . . . 223
VITA . . . 234

LIST OF TABLES

1 Material properties for the furnace components and workpieces 42

2 Verification of exchange factor calculation: Calculated mean exchange factors (Γ) with their relative standard deviations RSD_{Γ}, and the net radiative heat transfer rates (Q_r). The table also compares the calculated net radiative heat transfer rates with reference values $Q_{r,\mathrm{REF}}$, showcasing the relative errors (RE_{Q_r}) to emphasize the accuracy of the calculations. 64

3 Verification of the floating random walk solution for semi-infinite three-dimensional steady-state heat conduction problem: Comparison of analytical solution ($T_{\mathrm{analytical}}$) with floating random walk solution (T_{FRW}). Standard deviation (SD) is also provided. 95

4 Computational time comparison between CPU and GPU implementations for floating random walk simulations in semi-infinite three-dimensional steady-state heat conduction problem 96

5 Energy requirements for three distinct heating strategies 158

6 Impact of the overall heat transfer coefficient on energy considerations with estimated equivalent insulation thicknesses 179

7 Impact of the chamber surface reflectivity on energy considerations . 181

LIST OF FIGURES

1 A typical heat treatment process showing the heating, soaking, and cooling stages 3

2 Heat treatment furnaces 4

3 Schematic representation of a radiant furnace with two workpieces inside, showing the chamber and heater surfaces, and the design points 40

4 Overview of the forward solution procedure 57

5 Configuration of the case used to verify the developed Monte Carlo ray tracing code, adapted from *thermalradiation.net*, featuring two coaxial, parallel square plates 62

6 Verification of view factor calculation: Comparison of mean view factors against the reference value and their corresponding relative standard deviations for varying numbers of rays used in Monte Carlo ray tracing simulations. 63

7 Flowchart depicting the computational steps of the inverse solution algorithm 76

8 Variables in the inverse problem for both approaches. The direction of dependency among the variables is indicated by arrows. For example; T_D depends on T_S. 77

9 Overview of the sensitivity coefficient calculation procedure 81

10 Illustration of optimization over the entire time domain alongside examples of subdomain optimization with varying extents of overlap . . 84

11 Illustration of a random walk within a complex-shaped domain, showing consecutive steps taken from the initial point (x_0, y_0, z_0) with variable step lengths r_i terminating at the boundary. $r_{\min}$ denotes the boundary strip thickness. 90

12 The boundary strip when a particle arrives within. The temperature at particle's position is denoted by T_i. 91

13 Temperature estimates with associated standard deviations at design point 1 obtained from the FRW solution, depicted for a range of particle sizes (N_p). Each circle represents the mean temperature estimate, and the error bars indicate the standard deviation, demonstrating the impact of particle count on solution precision. 96

14 Comparison of design point temperatures from FRW simulations T_{FRW} and analytical solutions T_{an} for one-dimensional transient heat conduction problem. Relative error percentages are demonstrated on the right y-axis. 98

15 The problem of transient heating of two workpieces (glass panes) inside a radiant furnace. (a) Geometry of the problem. (b) Heater surface elements located at the furnace upper wall. (c) Workpiece geometry. . 105

16 Design point configurations in each workpiece where the design points are marked as red dots. The design points are overlapped with the finite volume cell centers. Grid lines represent finite volume cell edges. (a) Configurations with the design point layouts on $x - z$ plane with depth of 0.5 mm. (b) Configurations with the design point planes $x-y$ and $y - z$. 107

17 Overview of the two test cases. (a) Flow charts of the two test cases. (b) Assumed heater temperature imposed in Test Case 1. (c) Desired uniform heating history imposed as design condition in Test Case 2 for the specified design point depths. 110

18 Time step size analysis: Temperature differences at a specific design point at $t = 10$ s for various time step sizes. 111

19 Selected design points and heater elements for sensitivity verification analysis 114

20 Sensitivity verification analysis. (a) Sensitivity coefficients evaluated for all design points temperatures at $t = 50$ s with respect to the temperature of heater element 1. (b) Sensitivity coefficients evaluated for the temperature of design point 46 at $t = 50$ s with respect to heater temperatures, where unknown index represents heater index. (c) Sensitivity coefficients evaluated for the temperature of design point 46 with respect to the temperature of heater element 9 over time. . . 115

21 Impact of the design point layout on (a) average relative percentage error history and (b) determined heater temperature in Test Case 1 . 117

22 Impact of depth and plane of design points on average relative percentage error history (a_1 and a_2), and determined heater temperature (b_1 and b_2) in Test Case 1 119

23 Impact of the noise in design point temperature data on (a) average relative percentage error history and (b) determined heater temperature in Test Case 1 120

24 Impact of design point layout on (a) average relative percentage error history and (b) determined heater temperature in Test Case 2 122

25 Impact of design point depth on (a) average relative percentage error history and (b) determined heater temperature in Test Case 2 124

26 Heating uniformity at the design points and within workpieces: (a) Maximum absolute and relative error in design point temperatures over time. (b) Temperature distribution across the two workpieces at the 50-second mark, shown at the cross-section y = 4.5 mm where design points are situated. The color code reflects a ±2 K range around the desired design point temperature. 125

27 Regularizer weight analysis: Impact of various regularizer weights on (a) average relative percentage error history and (b) determined heater temperature in Test Case 2. 128

28 Initial guess analysis: Impact of various initial guesses on (a) average relative percentage error history and (b) determined heater temperature in Test Case 2. 130

29 Comparative analysis of steady vs. transient heater temperature solutions. (a) Average relative percentage error histories. (b) Maximum absolute error in design point temperatures over time. (c) Heater temperatures at specific times in the transient model. 132

30 Computational time cost of (a) routines in inverse solution, (b) FRW simulations for design point layouts 133

31 The problem of transient heating of six workpieces (glass panes) inside a radiant furnace. (a) Geometry of the problem. (b) Chamber surfaces divided into square elements. (c) Heater surface elements located at the furnace upper wall. (d) Geometry of the workpieces. (e) Design points within the workpieces, represented by red dots. 140

32 Design conditions: (a) Desired uniform heating profiles used as design conditions across three distinct cases. (b) Heating rates of the desired heating profiles. 141

33 Arrangement of heater element groups exploiting geometric symmetry. The six indexed heater element groups are designated as monitoring groups where temperatures and powers are plotted. 142

34 Time step size analysis: Error in design point temperatures for various time step sizes. 145

35 Sensitivity verification analysis. (a) Sensitivity coefficients calculated by present methodology and finite difference approximation. (b) Workpiece ordering and selected heater elements used in sensitivity coefficient verification. 147

36 Inverse solution results for the design condition in Case 1. (a_1) and (a_2): Resulting design point temperature and resulting temperature uniformity. (b_1) and (b_2): Temperatures of the selected heater groups over time. (c_1) and (c_2): Powers of the selected heater groups per heater element over time. The selected heater group indices are demonstrated in Fig. 33. 'HG' denotes heater group index. 149

37 Inverse solution results for the design condition in Case 2. (a_1) and (a_2): Resulting design point temperature and resulting temperature uniformity. (b_1) and (b_2): Temperatures of the selected heater groups over time. (c_1) and (c_2): Powers of the selected heater groups per heater element over time. The selected heater group indices are demonstrated in Fig. 33. 'HG' denotes heater group index. 152

38 Inverse solution results for the design condition in Case 3. (a_1) and (a_2): Resulting design point temperature and resulting temperature uniformity. (b_1) and (b_2): Temperatures of the selected heater groups over time. (c_1) and (c_2): Powers of the selected heater groups per heater element over time. The selected heater group indices are demonstrated in Fig. 33. 'HG' denotes heater group index. 154

39 Heater temperature distributions determined from the Temperature-based approach for three cases 155

40 Total heater powers determined by the Power-based approach for three cases 157

41 Geometry of the heat treatment problem, including (a) the overall setup, comprising (b) the chamber, (c) heater elements, and (d) a single workpiece. Additionally, (e) illustrates the design points within the workpiece. 164

42 Demonstration of thermal modeling for heat loss from chamber surface elements. Overall heat transfer coefficient represents the effect of insulation layer and heat transferred to environment from the exterior shell surface. 165

43 Design Condition: Desired design point temperatures T_D^* to be uniformly maintained across all design points. The right y-axis shows the equivalent heating rate. 166

44 Arrangement of heater element groups exploiting geometric symmetry, where the numbers represent the six distinct heater group indices. The 6×6 layout on the left is replicated on each face of the cubic heater configuration to the right. 167

45 Sensitivity coefficient verification analysis. (a) Sensitivity coefficients related to the temperature at the first design point at $t = 10$ minutes. (b) Time evolution of sensitivity coefficient related to the temperature at the first design point with respect to power of the first heater group. 171

46 Findings of the inverse solution for uniform heating: (a) Determined powers for six heater groups per element. 'HG' denotes heater group index. (b) Total heater power needed for the treatment. (c) Resulting design point temperatures. 172

47 Resulting heater temperatures for uniform heating: (a) A line plot representing the temperatures of six heater groups over time. 'HG' denotes heater group index. (b) Visualization of temperatures at specific time points on the geometric layout. The color code illustrates the local temperatures at these times. ΔT denotes the maximum temperature differences between heater elements. 174

48 Resulting workpiece surface temperatures at specific times. ΔT denotes the maximum temperature difference at specified times. 175

49 Resulting temperature field inside the workpiece (representing one-eighth of the entire workpiece) at specific times. ΔT denotes the maximum temperature difference at specified times. 176

50 Resulting incoming radiative heat flux on workpiece surface elements at specific times 177

51 Impact of the overall heat transfer coefficient on (a) total heater powers and (b) temperature uniformity at the design points 178

52 Impact of the chamber surface reflectivity on (a) temperature uniformity at the design points and (b) resulting mean chamber temperatures 180

53 Arrangement of heater element groups in 4×4 layout exploiting geometric symmetry, where the numbers represent the three distinct heater groups. The 4×4 layout on the left is replicated on each face of the cubic heater configuration to the right. 182

54 (a) The determined powers of heater groups per element in 4×4 heater layout. 'HG' denotes heater group index. (b) Impact of the heater layout on temperature uniformity at the design points 183

55 Comparison of the impact of heater material on (a) resulting design point temperature variations, (b) total heater powers, and (c) heater temperatures. 'HG' denotes heater group index. 185

56 (a) Arrangement of heater element groups with the indices for six heater element groups. (b) Arrangement of chamber surface groups with the indices for four chamber surface groups. The arrangements on the left are replicated on each face of the cubic heater configuration to the right. (c) The operating surfaces employed in two distinct Operating Group Sets. 192

57 Results of the forward solution with the predefined cooling $\bar{U}_{\text{cooling}}$ at chamber surfaces: (a) Resulting design point temperatures. (b) Resulting chamber power per surface element for each chamber group, where 'CG' denotes the chamber group index. (c) Total chamber power required for the cooling treatment. 195

58 Resulting chamber temperatures: (a) Time-dependent profiles of the maximum, mean, and minimum chamber temperatures, demonstrating changes over a 60-minute period. (b) Spatial distribution of temperatures across the chamber surfaces at $t = 60$ minutes. 197

59 Resulting heater temperatures: (a) Heater element temperatures over a 60-minute, where each line corresponds to a different heater group, denoted as 'HG'. (b) Spatial distribution of temperatures across the heater elements at $t = 60$ minutes. 198

60 Temperature distributions of the workpiece on the surface showing a high-temperature center with cooler edges and corners (left), and within the internal domain (right, representing one-eighth of the entire workpiece), illustrating the slower cooling rates of the core compared to the surface. 199

61 Design condition in Case 1: Desired cooling curve at design points. . 200

62 Resulting design point temperatures (a) for Operating Group Set 1 and (b) for Operating Group Set 2 201

63 Determined heater powers per element (left) for Operating Group Set 1 and (right) for Operating Group Set 2, where each line corresponds to the heater group denoted by 'HG' 202

64 Chamber powers per surface element (left) resulting from predefined cooling for Operating Group Set 1 and (right) determined by inverse solution for Operating Group Set 2. Each line corresponds to the chamber group denoted by 'CG'. 203

65 Resulting total heater and chamber powers over time for Operating Group Set 1 and 2 204

66 Resulting heater temperatures for Operating Group Set 1 and 2 in Case 1: (a) Resulting heater temperatures, where each line corresponds to the heater group denoted by 'HG'. (b) Spatial distribution of temperatures across the heater elements at t = 10 minutes. 206

67 Resulting chamber temperatures for Operating Group Set 1 and 2 in Case 1: (a) Resulting chamber temperatures, where each line corresponds to the chamber group denoted by 'CG'. (b) Spatial distribution of temperatures across the chamber surfaces at t = 10 minutes. . . . 207

68 Design condition in Case 2: Desired cooling curve at design points. . 208

69 Results of the inverse solution in Case 2: (a) Resulting design point temperatures. (b) Determined heater powers per element for each heater group, where 'HG' denotes the heater group index. (b) Determined chamber power per surface element for each chamber group, where 'CG' denotes the chamber group index. 210

70 Resulting total heater and chamber powers over time for Case 2 with Operating Group Set 2 211

71 Resulting heater temperatures in Case 2: (a) Time-dependent profiles of the heater temperatures, where each line corresponds to a different heater group, denoted as 'HG'. (b) Spatial distribution of temperatures across the heater elements at certain times. 212

72 Resulting chamber temperatures in Case 2: (a) Time-dependent profiles of the chamber temperatures, where each line corresponds to a different chamber group, denoted as 'CG'. (b) Spatial distribution of temperatures across the chamber surfaces at certain times. 213

CHAPTER I

INTRODUCTION

1.1 Motivation from a Historical Perspective

The journey of human innovation has been a long and remarkable one, beginning with the crafting of the first stone tools and advancing through the development of steam engines to today's high-tech solutions. This journey has consistently been driven by a combination of necessity, curiosity, and the desire to improve various aspects of daily living, with each new invention bringing about significant advancements. The industrial revolution stands as a pivotal moment in this journey, introducing innovations that fundamentally altered societies and economies, significantly improving human life by revolutionizing manufacturing, transportation, and numerous other fields.

However, the broader implications of these advancements were not immediately evident. It took over a century for the true costs of industrialization to become apparent, revealing significant negative consequences on the planet's climate, ecosystems, and the overall environment. The manufacturing industry, born out of the industrial revolution, has played a crucial role in shaping the modern world with its energy-intensive processes. Yet, it is now under examination for its environmental impacts, including pollution and its contribution to the climate crisis.

As we face urgent environmental challenges, there is a growing recognition of the need to shift towards sustainable practices in every sector, including manufacturing. This shift requires a reevaluation and redesign of industrial processes to reduce their environmental impact while maintaining, or even enhancing, efficiency. Engineers and researchers are at the forefront of this transformation, dedicated to innovating and improving industrial processes.

In light of these challenges and the urgent call for sustainable development, this study focuses on optimizing heat treatment processes—a fundamental aspect of manufacturing that significantly impacts energy consumption and production effectiveness. The primary aim is to ascertain optimal operating conditions that meet the technical requirements of manufactured products and enhance the efficiency and effectiveness of industrial heat treatment processes. By focusing on optimizing these processes, this research not only aims to improve production outcomes but also contributes to the broader goal of reducing environmental impact. This research represents a crucial step towards more efficient manufacturing practices, thereby aligning human innovation with the health of our planet.

1.2 Heat Treatment Processes

1.2.1 Principles and Significance of Heat Treatment

Heat treatment processes involve series of controlled heating, soaking, and cooling operations applied to a variety of materials, including metals, glasses, ceramics, and polymers, to alter their physical and mechanical properties without changing the workpieces' shape. These processes are crucial for enhancing attributes such as strength, hardness, toughness, and resistance to wear, thus tailoring materials to meet the rigorous demands of various industrial or end-use applications.

A typical heat treatment process is illustrated in Fig. 1, highlighting the stages of heating, soaking, and cooling. During the heating phase, the workpiece is gradually elevated to a specific temperature. Once the desired temperature is reached, the workpiece enters the soaking phase, represented by the plateau in the figure, where it is maintained at a constant temperature for a designated period. This soaking phase allows the heat to uniformly penetrate the material, ensuring consistent property development. Following soaking, the workpiece undergoes controlled cooling. The cooling stage, which may include multiple steps with intermediate soaking

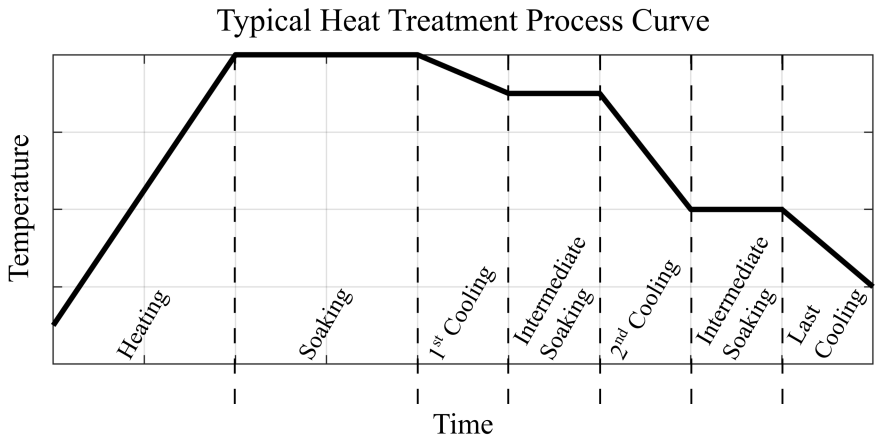


Figure 1: A typical heat treatment process showing the heating, soaking, and cooling stages

periods, gradually reduces the temperature to achieve specific material properties. Careful management of the cooling rate is crucial to ensure the desired mechanical characteristics are attained.

Heat treatment processes are employed across diverse sectors, including glass, automotive, aerospace, and tool manufacturing. They are essential for producing end-use products and components with precise mechanical properties necessary to endure operational conditions and stresses. For example, the automotive industry uses heat-treated steel to create gears and shafts with enhanced wear resistance and strength, which are critical for vehicle durability and safety.

The importance of heat treatment processes in manufacturing cannot be overstated. They not only enable the production of components that meet specific engineering requirements but also play a significant role in improving the efficiency of manufacturing operations. By enhancing material properties, heat treatment extends the life of components, reducing waste and the need for frequent replacements.

1.2.2 Heat Treatment Techniques and Furnaces

Among the various types of heat treatment processes, annealing, tempering, hardening, and quenching are the most common, each serving different purposes and

a) Batch Furnace



b) Continuous Furnace



Figure 2: Heat treatment furnaces

applications. Annealing, specifically, involves heating a material to a specific temperature, maintaining that temperature for a period, and then cooling it at a controlled rate. This process is essential for eliminating internal stresses within the workpiece. For example, in the production of soft steel for deep drawing, annealing is crucial to ensure the metal can be shaped without tearing.

Choosing the right furnace for heat treatment (whether continuous or batch) depends on the specific needs of the process. Batch furnaces, as demonstrated in Fig. 2(a), offer the flexibility needed for precise control over temperature, atmosphere, and cooling rates, making them suitable for materials that demand high-precision treatments. The ability to customize the furnace atmosphere, using techniques such as vacuum or protective gas, underscores the preference for batch furnaces in high-value or sensitive applications. On the other hand, continuous furnaces, as shown in Fig. 2(b), are designed for large-scale, uninterrupted material processing by enabling a steady flow of workpieces through various temperature zones for consistent treatment. Ideal for operations demanding high throughput, but these furnaces offer less flexibility in terms of customizing individual batch parameters.

1.2.3 Mechanisms of Heat Transfer

Heat treatment processes often encompass all three modes of heat transfer: conduction, convection, and radiation, operating simultaneously. Conduction primarily

occurs within solid domains, such as workpieces and furnace components, facilitating the transfer through direct contact. Meanwhile, convection is responsible for the transfer of heat from the furnace atmosphere to the workpiece, often enhanced by forced convection mechanisms such as fans or the effects of burners, ensuring efficient and even heat distribution.

Radiation becomes particularly dominant at high temperatures [1–7], influencing heat transfer through the emission of energy from hot surfaces, gases, or as a result of chemical reactions within the furnace environment. This mode is crucial for its ability to transfer heat to the workpiece, regardless of direct contact. Particularly in situations where other forms of heat transfer are relatively minimal, such as in vacuum conditions or instances involving natural convection, radiation from the furnace to the workpieces becomes the dominant mode of heat transfer.

1.2.4 Challenges in Heat Treatment Furnace Operation

The selection of the heat treatment process is determined by the specific requirements of the end product. Some treatments, such as tempering, intentionally create nonuniform temperature distributions to enhance hardness through rapid cooling. In contrast, processes like annealing require uniform temperatures and slower cooling rates to achieve desired material characteristics.

Ensuring a uniform temperature distribution within workpieces during the heat treatment process is a significant challenge. This issue is particularly pronounced in vacuum furnaces, where heating is predominantly affected by radiation. Hao et al. [8] highlight that during the heating process, the furnace heats up quickly while the workpieces lag behind. This phenomenon, known as thermal hysteresis, occurs because the temperature of the workpieces rises much slower than that of the furnace due to their different thermal capacities. According to Mochida et al. [9], maintaining a uniform temperature within ± 5 °C in vacuum batch furnaces is crucial for effective

treatment.

While most studies have focused on uniform heating [4,6–8,10–17], achieving uniform cooling is equally important. Ben et al. [18] state that uniform cooling in vacuum furnaces is crucial for preventing internal stresses and ensuring the dimensional stability of components.

Maintaining a spatially uniform temperature distribution involves managing furnace design, optimizing furnace operating parameters, and careful workpiece placement. Even minor variances in thermal treatment can compromise the integrity of workpieces, leading to failures in operational use or as end-products for customers. Therefore, research on optimizing heat treatment for temperature uniformity (or deliberate nonuniformity) is crucial to achieve reliable desired outcomes.

In addition to temperature uniformity, other challenges include the shadowing effect in radiation, which can occur due to the positioning layout of workpieces. Complex-shaped workpieces exacerbate nonuniform heating, and may lead to inconsistencies in the final product. These nonuniformities can critically compromise the integrity of workpieces or components.

Energy costs are another significant consideration in heat treatment processes, especially since these processes often operate 24 hours a day. Optimizing heat treatment processes is crucial for minimizing energy consumption and ensuring product quality. This involves both the design of the furnace and its operational parameters. Key aspects include selecting the correct furnace geometry, choosing appropriate materials, determining the optimal workpiece loading strategy, setting the right operating parameters, and establishing an effective treatment schedule. Together, these elements form a comprehensive approach to refining heat treatment processes for enhanced performance.

For instance, Li et al. [19] demonstrated that optimizing the design of a high-temperature vacuum furnace with a data-based thermal analysis approach led to

a 31.9% reduction in total heat consumption. This was achieved by adjusting the thickness of the insulator, the intervals between the heater and the insulator, and optimizing the number and placement of heaters.

1.2.5 Heat Treatment Process Focused in This Study

This study focuses on heat treatment processes that necessitate desired temperature maintenance throughout heating, soaking, and cooling stages, with a particular emphasis on surface-to-surface radiation as the primary mode of heat transfer between the furnace and the workpiece. Given these aspects, cooling is considered relatively slow, aligning with processes that do not employ forced convection for rapid cooling. This criterion points to annealing as the most suitable process for our investigation. Particularly, our investigation privileges the use of batch furnaces—especially vacuum batch furnaces—that offer distinguished control over the treatment environment, enhancing the uniformity of temperature within a prescribed margin across the workpiece. Within these contexts, surface-to-surface radiation is the only mechanism for transferring heat between the furnace and the workpiece.

Our research is centered on optimizing the furnace operating parameters for maintaining the desired temperature profiles within workpieces. Delving into the optimization of these parameters, our focus is on finding well-optimized furnace operating conditions while ensuring precise temperature management essential for annealing processes within vacuum batch furnaces. Emphasizing the role of radiation in heat transfer, our study seeks to provide a thorough comprehension of these treatments and their optimization. Ultimately, our focus is on improving process effectiveness and efficiency while attaining desired temperature maintenance through meticulous adjustment of furnace operating parameters.

1.3 Introduction to Inverse Problems

1.3.1 Overview of Forward and Inverse Problems

Engineering problems are typically tackled by predicting the response of a system based on prescribed causes. These causes, which include the geometry of the system, the properties of the materials used, and the boundary conditions, constitute a well-defined system for analysis, leading to an unambiguous solution [20]. This type of problems is categorized as a *forward problem*, where the causes are specified, and the resulting effects are determined through analysis.

On the other hand, a wide spectrum of engineering challenges requires inferring unknown causes from known or desired effects. This type of problem, known as an *inverse problem*, diverges from a forward problem by working backward, starting from the effects to uncover the underlying causes.

A functional representation of engineering problem-solving framework can be expressed as

$$\text{System}(\text{Causes}) = \text{Effects} \tag{1}$$

where the system represents the governing physics that relates the causes to the resulting effects or responses. In *forward analysis*, the causes are specified and their features are blended by the system based on the governing physics, resulting in subsequent effects. This direction, from left to right of Eq. (1), reflects the *forward solution* process. An instance of this is how specified furnace heater input powers lead to resulting temperature fields in workpieces.

Conversely, in *inverse analysis*, the outcomes or effects are known, and the task is to infer or estimate the causes that led to these effects. This involves working from the right to the left of Eq. (1), effectively reversing the direction of the forward solution. This process is known as the *inverse solution*. For instance, one might need to determine the input powers of furnace heaters necessary to achieve specific, desired, or measured temperature profiles in workpieces through the inverse solution.

1.3.2 Types of Inverse Heat Transfer Problems

Inverse heat transfer problems can be classified into two main categories. *Inverse design problems* [2,3,7,10–17,21–68] aim to determine the design configurations that yield specific ideal or desired outcomes. For example, achieving prescribed radiative heat flux on workpiece surfaces by optimizing the temperature or power input of heater elements. On the other hand, *parameter estimation problems* [38,56,69–76] involve inferring unknown parameter or property distributions from measurement data. An instance of this is the reconstruction of thermal conductivity from boundary heat flux measurements.

Inverse design problems, based on the type of design parameter involved, can be divided into three main branches; boundary design (or boundary condition design), geometry design, and heat source design. *Boundary design* [2,3,7,10,11,14–17,21–25,27–34,36–46,48–52,56–68] deals with identifying necessary boundary conditions to achieve desired outcomes. *Geometry design* [12,13,26,52–55] focuses on the optimal shaping or dimensions of an existing structure or component to meet predefined criteria. *Heat source design* [35,47] involves the strategic placement and intensity adjustment of heat sources within the system.

In this study, our focus lies on boundary design problems, aiming to determine furnace operating conditions that serve as boundary conditions for the heat treatment of workpieces.

1.3.3 Ill-posed Characteristics of Inverse Problems

As discussed previously, forward problems are inherently well-defined because they include sufficient information for addressing the task at hand. This abundance of information ensures that a unique solution can be determined, making forward problems *well-posed*.

The concept of well-posedness was identified by Hadamard [77] in the early 1900s.

According to Hadamard, for a problem to be considered well-posed, it must satisfy three criteria; the existence of a solution, the uniqueness of that solution, and the solution's stability with respect to small changes in the problem definition.

Inverse problems are inherently *ill-posed* [2,3,56], as they fail to meet Hadamard's criteria for well-posedness due to the absence of sufficient information required to specify a unique and stable solution. This information insufficiency can lead to multiple distinct solutions that all nearly produce the observed or desired effects [50], thus complicating the task of identifying the true or most practical solution. Additionally, the desired or ideal effects sought may sometimes be unattainable, leaving the inverse problem with no exact solution. For instance, the aim of achieving a uniform temperature distribution in a workpiece can be satisfied by multiple furnace configurations, each varying slightly in heater power levels. Moreover, achieving a perfectly uniform temperature distribution in workpieces during transient treatment is often not precisely attainable, resulting in the inverse problem lacking an exact solution.

Initially regarded as artificial and of theoretical interest rather than practical significance, ill-posed problems have been recognized as extending beyond theoretical curiosities to widespread real-world applications, significantly shifting problem-solving strategies [20]. This shift underscores the importance of employing sophisticated techniques to address the complexities inherent in inverse problems.

1.3.4 Pioneering Studies in Inverse Radiation Heat Transfer Problems

A conventional approach to inverse design problems typically relies on experience and a trial-and-error procedure [59], wherein an assumed set of designs is tested to evaluate their responses. If the outcomes are deemed satisfactory, the design set is accepted; otherwise, it is modified for further testing. However, this traditional

trial-and-error method is costly, requiring extensive experimental work or many computational simulations of forward solutions. This approach often leads to sub-optimal solutions. Consequently, there is a clear need for specialized solution techniques that can streamline the process, reduce costs, and improve accuracy in finding the best solutions for inverse design problems.

The exploration of specialized techniques for solving inverse heat transfer problems began earnestly in the 1960s, focusing primarily on conduction heat transfer. These pioneering works [78, 79] laid the foundation for subsequent research in the field, which later expanded with significant contributions from [49, 56]. By the 1990s, the application of inverse solutions had expanded to include radiation heat transfer within participating media [80–82]. In the late 1990s, applications of inverse solutions began extending to surface radiation [15,83], broadening the scope across various heat transfer challenges.

These foundational studies, along with succeeding research and current advancements, continue to inspire new directions and technological developments, underscoring their enduring relevance to modern engineering challenges.

1.4 Mathematical Properties of Inverse Problems

Understanding the mathematical properties of inverse problems is crucial for effectively addressing the challenges they present. Inverse problems can be broadly categorized into linear and nonlinear types.

1.4.1 Linear Inverse Problems

In solution of heat transfer problems, the governing differential or integral equations are generally converted into a discrete set of equations. This results in a system of equations typically represented as

$$\boldsymbol{A}u = b \tag{2}$$

when the problem is linear.

The solvability of the system $\boldsymbol{A}u = b$ is influenced by the characteristics of the matrix $\boldsymbol{A}$. If $\boldsymbol{A}$ is rank-deficient, there may be no solution or infinitely many solutions. For a consistent system where the rank of $\boldsymbol{A}$ is equal to the rank of the augmented matrix $[A|b]$, multiple solutions can exist. If the ranks are not equal, there is no solution. Even if solutions exist for systems with a rank-deficient $\boldsymbol{A}$, they may not necessarily correspond to physically meaningful solutions.

For forward problems, determining the unknown vector u is relatively straightforward, given that the matrix $\boldsymbol{A}$ is usually *well-conditioned* enough to ensure a stable and unique solution. A well-conditioned matrix has a low condition number, which indicates that small changes in the right hand side b will result in small changes in the solution u. An example of such a problem can be observed in the analysis of radiative enclosures, where each boundary is assigned a specific boundary condition, and at least one boundary has a defined temperature.

In contrast, inverse problems often involve matrices $\boldsymbol{A}$ that are *ill-conditioned*, meaning they have a high or infinite condition number. This high condition number makes solving the system for determining u difficult or even impossible. This complexity is inherent to inverse problems, such as those encountered in inverse boundary design, where certain boundaries may lack predefined conditions (information deficit).

1.4.2 Nonlinear Inverse Problems

Most heat transfer problems are nonlinear, involving a nonlinear relationship between causes and effects, making them more complex to analyze and solve. The general form of a nonlinear inverse problem can be expressed as

$$\mathcal{F}(u) = b \tag{3}$$

where $\mathcal{F}$ denotes a nonlinear operator. Examples of nonlinear inverse heat transfer problems include boundary design challenges involving conjugate heat transfer, radiative heat transfer, wavelength-dependence, and temperature-dependence. The

inverse problem we focus on, in particular, is nonlinear due to the involvement of radiative heat transfer.

Since nonlinear systems are not directly invertible, solving these problems typically requires iterative methods. These problems are often framed as minimization tasks, where an objective function quantifies the quality of the estimated solution. The iterative minimization approach involves repeatedly updating the estimate. After each estimate update, its effectiveness is assessed by solving the forward problem, ensuring that the solution aligns with the desired outcomes.

If the objective function of the nonlinear inverse problem is convex, leveraging local curvature information can be highly effective, efficiently guiding the search towards the global minimum. However, nonlinear inverse heat transfer problems are frequently nonconvex, mostly within the neighborhood of the desirable solution, which means they can have multiple local minima. In such cases, the global minimum may not correspond to a zero-valued objective function, reflecting the inherent challenges and complexities in achieving an optimal solution. This nonconvexity may require more sophisticated techniques to avoid getting trapped in local minima and to approximate the global solution effectively.

When tackling an inverse problem using gradient-based approaches, estimate updates are performed by forming and solving a search direction equation. This search direction equation, in the form of Eq. (2), is often ill-conditioned. To address this, regularization terms can be added to the objective function, effectively treating the ill-conditioning to the required extent. Additionally, regularization mitigates the ill-posedness of the inverse problem by introducing constraints or prior information, promoting desired solution characteristics and enhancing the practicality of the solutions for real-world scenarios.

Our aim in this section was to provide a concise overview of the mathematical

characteristics of inverse problems. For a more comprehensive exploration, we recommend consulting Chapter 18 of the excellent book by Howell et al. [20].

1.5 Solution Methods for Inverse Problems

Daun et al. [84] categorized inverse problem solution approaches into three main branches: trial-and-error techniques, direct inversion techniques, and optimization techniques. As mentioned previously, the trial-and-error techniques rely heavily on the designer's experience and involves investigating multiple trials to find a satisfactory solution. On the other hand, for linear problems, the inverse problem can be formulated as a linear equation system $Au = b$, referred to as *direct formulation*. Direct inversion techniques (linear regularization techniques) [2, 3, 16, 17, 24, 31, 41, 42, 46, 50, 51, 57–60] aim to obtain a useful solution by addressing the ill-posedness of the problem through regularization of the linear system. Optimization techniques [7, 10–15, 17, 23–28, 30, 32, 34–39, 43–45, 47, 48, 50, 52–56, 61–65, 67, 69–76], applicable to both linear and nonlinear inverse problems, involve an iterative process to find an optimized solution. This approach of solving inverse problems is referred to as *indirect formulation*. The method used to update the estimate during this iterative process determines the specific type of optimization technique employed.

This section covers linear regularization techniques, gradient-based optimization methods, and other methodologies for solving inverse heat transfer problems, emphasizing their advantages and practical applications.

1.5.1 Linear Regularization Techniques

In inverse radiant boundary design problems, the initial approaches were mostly based on linear regularization techniques, such as truncated singular value decomposition (TSVD) [3, 17, 24, 31, 42, 46, 51], Tikhonov regularization [17, 41, 50, 51], and conjugate gradient regularization (CGR) [2, 3, 16, 17, 50, 51, 57–60]. These techniques aim to numerically stabilize the solution of linear systems of equations by reducing the effects

of high-frequency solution modes, thereby finding a useful solution that satisfies the inverse problem within the desired accuracy. The selection of the parameters in these methods typically involves a trial-and-error approach, supported by tools like the L-curve [85], which helps avoid overly diminishing the residual norm and ensures more practical solutions.

Highlighted below are some of the significant studies that have employed linear regularization techniques. Howell et al. [51] conducted one of the pioneering works in this area, comparing three different regularization methods for both two-dimensional and three-dimensional surface-to-surface radiation enclosure problems. Ertürk et al. [57] investigated irregularly shaped geometries with shading and blockage effects, including conditions of participating media in two-dimensional problems, utilizing CGR. França et al. [46] focused on multi-mode heat transfer mechanisms, incorporating fluid flow solutions for convection in steady-state two-dimensional problems, applying TSVD. Ertürk et al. [3] addressed three-dimensional radiation enclosure problems that included an absorbing-emitting and anisotropically scattering medium. The study provided a detailed comparison of various regularization methods, evaluating their convergence and effectiveness in obtaining solutions. Ertürk et al. [16] tackled rapid thermal processing problems by comparing the obtained results with experimental data while determing the necessary heater powers. Ertürk et al. [59] investigated a two-dimensional transient problem where heater powers were determined. The thermal model included surface-to-surface radiation and one-dimensional conduction within the workpiece. França et al. [86] studied various problems using multiple regularization methods. They concluded that inverse solutions can lead to multiple potential designs for thermal treatment that satisfy the desired outcomes, offering practical designs that might not be discovered through conventional trial-and-error approaches. Ertürk et al. [60] addressed a three-dimensional problem with a moving load. The study included lumped conduction and convection as boundary conditions

for the loads, and transient heater powers were determined using CGR. França et al. [42] investigated a transient problem where heat loss from enclosure walls was considered. The study focused on the TSVD regularization parameter, concluding that the optimal value for this parameter varies across different applications. A uniform thermal treatment was achieved by determining the necessary heat flux distribution on the heater elements. Hoffmann et al. [31] employed the TSVD method to address a three-dimensional steady-state problem involving surface-to-surface spectral radiation. The study determined the necessary heater powers and investigated heater configurations, including both transversal and longitudinal heaters. Mosavati et al. [41] applied an additional regularization term to obtain smooth conditions across successive heaters. The study determined the required heater temperatures to ensure a uniform heat flux over the design surface under steady-state conditions, utilizing Tikhonov regularization.

However, a significant drawback of regularization with direct formulation is its incapacity to address nonlinear problems and accommodate specific constraints, such as ensuring positive emissive power across a heater's surface, which is often essential for obtaining practical solutions suitable for real-world applications.

1.5.2 Gradient-Based Optimization Methods

In optimization approaches for solving inverse problems, the objective function is iteratively minimized by following a search direction, which is determined by the specific type of optimization method employed. Among the various optimization approaches, gradient-based optimization [13–15, 17, 23, 25–27, 30, 32, 34, 35, 38, 45, 47, 50, 52–56, 61–65, 67, 70, 73, 75, 76] leverages the local curvature of the objective function to determine the search direction.

The search direction equation is derived using the sensitivity information of the

objective function. These sensitivity coefficients are obtained from the partial derivatives of the objective function with respect to the unknown variables. The distinction between different gradient-based optimization methods lies in how they utilize these sensitivity coefficients to form the search direction equation.

Methods such as steepest descent [52–55] and conjugate gradient [23, 25–27, 30, 32, 35, 47, 56, 62–65, 73] use the gradient of the objective function, which involves first-order derivatives. On the other hand, Newton's method [50, 55] employ the Hessian of the objective function, incorporating second-order derivatives to form the search direction. Due to the computational expense of calculating second-order derivatives, the Hessian matrix is often approximated through various methods, resulting in quasi-Newton (Newton-like) methods [14, 17, 50, 55].

When the objective function is defined as a nonlinear least squares problem, the Jacobian of the residuals can be used to determine the search direction, leading to the Gauss-Newton method. In this approach, the Hessian matrix is approximated using Jacobian products that consist only of first-order derivatives. The Levenberg-Marquardt method [15, 45, 61, 67, 70, 75, 76] utilizes a damping term, which adjusts the influence of the diagonal terms in the search direction equation. Initially, with a large damping term, the method produces a steepest-descent direction. As the iterations proceed and the damping term is reduced in each minimizing step, the search direction gradually approaches that of the Gauss-Newton method.

Gradient-based optimization methods have been employed in inverse radiation heat transfer problems with participating media [38, 70, 75, 76, 80–82] since around 1990, and their use continues to this day. Additionally, these methods have also been extensively utilized in the geometry design of radiative enclosure problems. Notably, Daun et al. [53–55] applied gradient-based optimization techniques to these problems, and studies on these problems have been continued and expanded by subsequent researchers [13, 26, 52].

Gradient-based optimization methods have been widely applied to inverse radiant boundary design problems, demonstrating their effectiveness across various studies. Fedorov et al. [15] conducted the first study using an optimization method for inverse boundary design problems in radiative enclosures. This study addressed a transient quasi-three-dimensional inverse enclosure problem with a moving load, employing the Levenberg-Marquardt method. They determined the optimum temperatures for the furnace heaters located on the upper wall of the furnace, which produced uniform heating on the moving load. Daun et al. [14] determined the transient heat flux on heater surfaces modeled as cubic polynomial functions in a two-dimensional surface-to-surface radiation problem with convection as a boundary condition at the furnace walls. In another study, Daun and Howell [50] compared linear regularization techniques and gradient-based optimization methods in a steady-state two-dimensional surface-to-surface radiation problem. They highlighted that optimization solvers have the significant advantage of imposing design constraints, enabling the achievement of more practical solutions. Kowsary et al. [34] employed a variable metric method, which utilizes gradient information, to determine the heat flux at heater surfaces in a steady-state inverse radiant boundary design problem including participating media. They imposed a regularization parameter to reduce fluctuations in neighboring heat fluxes and studied the impact of this parameter. Bayat et al. [32] determined heater powers in a surface-to-surface radiation model with diffuse-nongray surfaces using conjugate gradient optimization. Further studies employing gradient-based optimization methods for radiant boundary design problems can be found in [26, 27, 45, 63–65, 67].

1.5.3 Calculating Sensitivity Coefficients in Gradient-Based Optimization Methods

In the field of radiation heat transfer, solving inverse boundary design problems using gradient-based optimization methods presents a considerable challenge, particularly

when it comes to the efficient calculation of sensitivity coefficients. *Sensitivity coefficients* represent the partial derivatives of the objective function with respect to the unknown variables, indicating how changes in these variables impact the objective function's value. They are crucial in gradient-based optimization as they guide the search direction and update steps, helping to minimize the objective function effectively. However, determining these coefficients is often computationally expensive and can be complex.

Several approaches have been employed in prior studies to calculate sensitivity coefficients, each with its advantages and drawbacks. The simplest method is finite difference approximation [27, 52, 54, 76], also known as numerical differentiation. This technique requires a high number of forward problem solutions, making it time-consuming. Additionally, determining the appropriate perturbation size can be challenging and critical for determining solutions.

The Broyden combined update method [45] begins by calculating sensitivities using finite difference approximation. It then updates these sensitivities based on the differences in the objective function and the unknown parameters between successive iterations, thus approximating the changes in the sensitivity matrix more efficiently.

The adjoint method [26, 33, 56, 73], offers a more efficient alternative by solving the adjoint problem only once per iteration; however, it is limited to calculating the gradient of the objective function and cannot compute the Jacobian or Hessian. Although its formulation is complex, it is advantageous when the number of unknowns is high because the entire gradient vector can be calculated by solving the adjoint system.

Another method is complex variable differentiation (CVD) method [23, 76], which uses complex arithmetic to calculate derivatives by adding a small imaginary perturbation to real-valued variables. This approach provides high accuracy and computational efficiency, making it valuable for sensitivity analysis. However, it requires

functions to be evaluated with complex numbers and assumes the function is analytic, which may not be suitable for all functions or numerical libraries.

In many studies [25, 30, 32, 34, 35, 47, 52, 54, 61–65, 67], sensitivity coefficients are obtained by solving multiple forward problems. Each forward problem is formed by differentiating the original problem with respect to each unknown variable, which requires a high number of forward problem solutions in total and is computationally intensive.

Direct differentiation [53] applies the chain rule to compute sensitivity coefficients, providing exact derivatives without intermediate approximations. While it ensures high accuracy, direct differentiation requires explicit formulations for the variables involved and can be computationally expensive for large systems. This method is precise but challenging to implement for problems involving complex physics.

Moreover, in most optimization iterations, sensitivity coefficients must be updated repeatedly, further increasing the computational burden. As a result, the computational cost of calculating sensitivity coefficients can become prohibitively high, especially when dealing with large systems and a large number of unknown variables.

Therefore, finding more computationally efficient methods for computing sufficiently accurate sensitivity coefficients is of great importance. Advancing research in this area not only reduces the overall computational cost of solving inverse heat transfer problems but also significantly enhances the reliability of the sensitivity coefficients calculated, ultimately contributing to more effective and practical applications in the field.

In this study, we adopt the direct differentiation approach for calculating sensitivity coefficients. For problems involving surface-to-surface radiation within a radiant enclosure, aiming to achieve desired heat flux over workpiece surfaces, the formulation using radiative heat flux with exchange factors provides explicit formulations for the variables involved. Thus, sensitivity coefficients can be directly calculated using the

direct differentiation approach without additional complexity.

However, when conduction heat transfer within the workpiece's internal domain is involved, the calculation procedure for sensitivity coefficients becomes more complex. This is because internal and surface temperatures of the workpiece are not directly specified and must be related to other intermediate variables. Our study distinguishes itself by utilizing the Floating Random Walk (FRW) method and its modified variant to derive explicit formulations for the temperatures at internal locations and surfaces of the workpiece. This approach enables us to formulate explicit relations for all variables in the problem, thereby making it possible to employ the direct differentiation approach in sensitivity coefficient calculation. Our approach yields sufficiently accurate sensitivity coefficients within a robust framework, ensuring manageable computational effort compared to traditional methods.

1.5.4 Other Inverse Solution Methods

Metaheuristic optimization methods [7, 10–12, 17, 24, 28, 29, 36, 37, 39, 43, 44, 48, 64, 69–72, 74] have emerged as powerful tools for solving inverse problems. These are algorithms inspired by natural processes that search for optimal solutions by exploring and exploiting the solution space without requiring gradient information. Methods such as Simulated Annealing [7, 17], Genetic Algorithms [10, 11, 11, 28, 29, 37, 39, 43, 44, 48, 70, 71, 74], Particle Swarm Optimization [37, 64, 72], the Generalized Extreme Optimization Algorithm [12, 24], and Teaching-Learning-Based Optimization [36, 69] have been widely used in the field of inverse radiation heat transfer problems including boundary design, heat source design, and parameter estimation.

Radfar et al. [37] tackled the inverse radiative boundary design problem in an absorbing, emitting, and participating medium. Their study aimed to compare different metaheuristic optimization methods to find the optimum power of heaters from a discrete set of powers, ensuring the desired temperature and heat flux profile over

the design surface. They concluded that Genetic Algorithms outperformed other techniques for designing radiative furnaces with discrete power levels.

Metaheuristics offer several advantages: They are effective for solving "on-off" problems where gradient information does not exists [11], do not require sensitivity calculations, can easily accommodate different types of design variables simultaneously, and often perform better on nonconvex problems. However, these methods also have disadvantages, primarily the need for a large number of forward problem solutions (objective function evaluations), which can be problematic for large or complex problems due to the high computational cost.

Beyond optimization techniques, several other methods have been employed to solve inverse heat transfer problems. Filtering approaches, such as particle filtering [40] and Kalman filters [68], have proven effective in these applications. Additionally, Bayesian methods [21, 66, 70] and artificial neural networks [22, 70] are increasingly utilized. For a comprehensive overview of these methods applied to inverse radiation heat transfer problems, readers are encouraged to consult the review paper by Ertürk et al. [87].

On the other hand, hybrid approaches combine different classes of techniques to solve inverse problems. In some cases, researchers use one method to address a specific type of design variable and another method for a different type of design variable [24,38]. Alternatively, a hybrid approach might involve using one method to generate a good initial guess, which is then refined by another method, as demonstrated in the study by Sepahvand et al. [39].

1.5.5 Selecting a Suitable Inverse Solution Method

Choosing the appropriate inverse solution method depends on several factors, including the type of inverse problem, the mathematical properties of the problem (such as being linear, nonlinear, convex, or nonconvex), the desired outcomes, available

computational resources, prior information, and the types and number of unknowns involved.

Optimization methods are advantageous because they allow for the application of regularization techniques and the imposition of bound constraints. Even for linear problems, optimization methods can be beneficial due to these capabilities. For nonlinear convex problems, gradient-based optimization methods often outperform metaheuristic methods by effectively exploiting local curvature information.

However, when calculating sensitivity coefficients for gradient-based methods is impractical or computationally expensive, metaheuristic methods can be employed, even for convex problems, provided that the forward problem (objective function evaluation) is not too costly. Methods such as artificial neural networks (ANN), metaheuristics, and Bayesian inference require repeated evaluations of the forward solution, making them suitable when the forward problem solution is relatively inexpensive.

Alternatively, surrogate models can be used to represent the original physical model with reduced fidelity and lower computational costs. For instance, ANN-based surrogate models combined with metaheuristic optimization methods have been utilized in previous studies [7, 39] applied to inverse radiation heat transfer problems.

Several studies have conducted comparative analyses of solution methods for inverse radiation heat transfer problems. Daun et al. [55] compared gradient-based methods in the geometry design of a diffuse-walled radiant enclosure and found that Newton and quasi-Newton methods required less CPU time than the steepest-descent method due to their fewer iterations for convergence. In another study, Daun et al. [50] compared linear regularization methods, such as TSVD, Tikhonov, and conjugate gradient methods, with Newton's method in a two-dimensional steady-state problem to determine heat flux at heater surfaces. They concluded that Newton's method provided more practical solutions. Additionally, Daun et al. [17] explored

solutions using Tikhonov regularization, truncated singular value decomposition, conjugate gradient regularization, quasi-Newton minimization, and simulated annealing for a three-dimensional transient problem. Their goal was to determine the required heater power to achieve uniform heat flux on the design surface. They found that regularization methods provided smoother heater input distributions compared to optimization techniques, which resulted in more uneven distributions but allowed for a reduction in the number of active heaters.

1.5.6 Inverse Solution Method Employed in This Study

In this study, we employ a gradient-based optimization method for solving the inverse radiant boundary design problem. Specifically, we utilize the Gauss-Newton algorithm due to its efficiency in handling nonlinear least squares problems. This choice is motivated by the fact that the thermal modeling of our target problems can be computationally intensive. Thus, metaheuristic methods are not feasible due to the high computational costs associated with the forward solutions required to be performed numerous times. Gradient-based optimization with the Gauss-Newton algorithm, on the other hand, offers a more computationally efficient approach, making it well-suited for our needs.

We calculate sensitivity coefficients using the direct differentiation approach, which involves deriving explicit formulations for the temperatures at internal locations and surfaces of the workpiece. This method is enhanced by employing the Floating Random Walk method and its modified variant to ensure accurate and efficient computation of sensitivity coefficients. To enhance the robustness and to promote certain desired solution characteristics, we utilized regularization terms into the objective function.

This methodology allows for the precise estimation of the unknown furnace operating parameters, such as heater temperatures or powers, to achieve the desired

temperature histories at certain locations within the workpiece. By combining the strengths of the Gauss-Newton algorithm, direct differentiation for sensitivity coefficients, and regularization techniques, our approach provides a robust and efficient solution to the inverse heat transfer problem.

1.6 Radiant Enclosure Design Problems

The design and optimization of radiant enclosure systems pose significant challenges due to the complex interactions between various heat transfer mechanisms. Understanding and effectively solving inverse design problems in this context require a comprehensive analysis of heat transfer models, design conditions, and variables, as well as a thorough consideration of the spatial and temporal dependencies of the heat treatment processes. This section delves into the key aspects of radiant enclosure design problems, reviewing the mechanisms involved, defining the design conditions and variables, addressing the importance of fidelity in computational models, and highlighting the investigations conducted in the literature.

1.6.1 Heat Transfer Mechanisms Involved

Research in the field of inverse radiation heat transfer addresses problems involving various heat transfer models. These models include surface-to-surface radiation [2, 14–17, 24, 28–32, 42–44, 48, 50–55, 58–60], radiation within participating media [3, 7, 10–13, 25, 26, 33, 34, 36, 37, 39, 47, 57, 61, 63–65, 67, 70], and radiation combined with gas conduction within participating media [35, 38, 40, 62, 62, 68, 69, 71, 72]. Additionally, some studies focus on radiation combined with convection [27, 45, 46]. Furthermore, spectral radiation has been considered in several studies [15, 63–65].

Radiation combined with solid conduction encompasses various scenarios. These include one-dimensional or lumped conduction on workpiece surfaces (design surfaces) [58–60], two-dimensional steady-state conduction inside workpieces [30], two-dimensional transient conduction on workpiece surfaces [15], and conduction within

furnace elements [14]. Typically, heat transfer within the internal domains of workpieces is often simplified, either considered as lumped systems or modeled in one dimension on design surfaces, rather than accounting for internal heat transfer dynamics.

In this study, we address the internal heat transfer within workpieces using a transient heat treatment model. Our methodology includes lumped conduction within furnace components, surface-to-surface radiation within the radiant enclosure between furnace and workpiece surfaces, and conduction within the workpiece domain. By moving beyond simplified models, our approach aims to meticulously capture the detailed internal thermal behavior of workpieces during heat treatment. This inclusion of internal heat transfer dynamics within a transient, three-dimensional framework ensures a more accurate representation of the physical processes involved, offering enhanced fidelity when internal temperature gradients inside the workpieces are of importance.

1.6.2 Design Condition Definition

The design condition is the desired outcome that is aimed to be achieved through solving inverse problems. In inverse heat transfer problems, the design condition is typically defined by the desired temperature or desired incident heat flux. From the earliest studies in the late 1990s to the present day, the design condition is predominantly specified on the surface of the workpiece, also known as the *design surface* [2, 3, 7, 10–12, 14–17, 24, 26–29, 31–48, 50, 51, 53–55, 57–65, 67, 69, 70].

In defining design conditions on the design surface of workpieces, traditional approaches often neglect the complexities of heat transfer within the internal domain of the workpieces. However, to achieve more specific and controlled thermal conditions within the workpieces, it is crucial to define the design condition at internal locations within the workpiece itself. Such internal locations are referred to as *design points*.

This approach is of significant importance as it allows for a more precise management of thermal conditions, leading to improved material properties. By focusing on design points within the workpiece, it is possible to address and mitigate internal thermal gradients and stresses more effectively, ensuring desired heat treatment process.

There are only a limited number of studies in inverse heat transfer problems where the design condition is defined within the workpiece domain itself. A example of this can be seen in the work by Dehgani et al. [30], who addressed a two-dimensional, steady-state problem and determined heater temperatures of radiant enclosure using Newton's method. Additionally, other studies [49,56] have employed the design point approach for defining design conditions, but these are generally focused on inverse conduction problems without radiation boundary condition or radiant enclosure.

In this study, we adopt the design point approach to define the design conditions within the workpiece domain, extending its application to inverse radiant boundary design problems. This approach presents additional challenges, as the temperatures of the workpiece surfaces are not directly prescribed and must be treated as intermediate variables in the inverse problem formulation. This complexity also increases the effort required for sensitivity coefficient calculation, as it becomes more difficult to relate the design condition to the furnace operating parameters.

1.6.3 Design Variable Definition

Design variables are the unknown variables in the inverse problem that need to be determined to achieve the desired outcome from the heat treatment process. In the literature, design variables have been considered as heater temperature [3, 15, 27, 30, 39, 41, 43, 44], heat flux at heater surfaces [7, 14, 24, 25, 27, 33, 34, 36, 38, 40, 42, 46, 50, 62–64, 67], heater power [10, 11, 16, 17, 28, 29, 31, 32, 37, 45, 48, 58–61, 65], and positions of the heaters [12, 13, 24, 26, 43].

Most studies have concentrated on the heating phase of heat treatment, aiming

for uniform heating. As a result, the design variables typically pertain to the heater elements of the furnace, ensuring effective management of the heating process.

In a typical heat treatment furnace, heating and cooling components are distinct because heater elements cannot be used directly as a cooling source during the cooling phase. Therefore, the investigation of the cooling phase requires operating the cooling surfaces of the furnace geometry, often the furnace chamber surfaces, for example, with a cooling fluid circulated through a cooling jacket.

In this study, we consider both heating and cooling phases. During the heating phase, the process is managed by the heater elements. In the cooling phase, the design variable is the heat extraction from the cooling surfaces on furnace chamber. Additionally, we include balancing heat inputs for uniform cooling from the heater elements as design variables. This comprehensive approach, which is further explored in Chapter 9, distinguishes our study from previous ones.

1.6.4 Heat Transfer Modeling Approaches Used in Inverse Radiant Boundary Design Problems

Our literature review on inverse radiant boundary design problems reveals that most studies focus on two-dimensional problems [2, 7, 11, 14, 25–27, 30, 32–37, 41, 45–47, 50, 53–55, 57–59, 62–65, 67]. These studies encompass a variety of inverse solution methods and address scenarios involving participating media with nonhomogeneous nonisothermal properties, nongray surfaces, and radiation combined with gas conduction.

Additionally, we found that many one-dimensional problems [38,40,68–72] are also being extensively studied. These studies often focus on near real-time estimation with moving boundaries using artificial neural network [22], online monitoring of transient boundary heat flux in graded index media using particle filter algorithms [40], and simultaneous reconstruction of time-dependent heat flux and physical properties [38]. In another example, the boundary time-dependent heat flux and internal temperature field in participating media are often retrieved in near real-time from temperature

measurements on the surface using Kalman smoothing technique [68].

The remaining references consider three-dimensional problems [3, 10, 12, 17, 24, 28, 29,31,39,41–44,48,51,60,61]. These studies employed various types of inverse solution methods discussed earlier, demonstrating the adaptability of these methods to more complex, higher-dimensional scenarios.

Even when a furnace operates steadily for its specific operation (for example, continuous annealing furnaces), the heat treatment system is in a transient condition during the treatment because the workpiece is heated, soaked, and cooled depending on the treatment phase and sometimes also moves with a conveyor belt. Therefore, transient problems typically offer greater fidelity in modeling these processes.

However, when we investigate the time dependence of the problems that previous studies addressed, we observe that the majority addressed steady-state inverse radiant boundary design problems [3, 7, 10–12, 16, 24–37, 39, 41, 43–48, 50–55, 57, 61–65, 67, 70]. In contrast, relatively small number of studies have addressed transient problems [2, 14, 17, 38, 40, 42, 58–60, 68, 69, 71, 72] in inverse radiant boundary design.

Fidelity in computational heat transfer and heat treatment process analyses refers to the degree to which the model accurately represents the real-world scenario. High fidelity models incorporate detailed physics, fine spatial and temporal resolutions, and comprehensive treatment of boundary conditions, which are essential for precise predictions of temperature distributions during heat treatment processes. Achieving high fidelity involves complex mathematical modeling, advanced computational techniques, and extensive validation against experimental data to ensure the reliability of simulation results.

The highest fidelity in modeling heat treatment systems is typically achieved through detailed computational heat transfer and fluid dynamics analyses in a forward solution manner. Studies such as [4, 6] have tackled three-dimensional transient

heat treatment problems in vacuum furnaces, emphasizing the importance of capturing both temporal and spatial dependencies accurately. Liu et al. [6] specifically noted the significant computational effort required for these (relatively) high-fidelity simulations, with some models taking over 30 hours to complete, underscoring the intensive computational demands of achieving such precise results.

In the field of inverse design in radiant enclosure problems, the fidelity of solutions has been progressively enhanced by including more detailed modeling. Studies, for example, have made efforts to incorporate both conduction and convection at furnace walls [14], gas conduction effects [35, 69], the impact of nongray surfaces [31, 32], irregularly shaped design objects [28], and nongray media [39].

Some studies have introduced surrogate models to substitute high-fidelity forward models, offering reduced fidelity but significantly faster computational solutions. For example, artificial neural network-based surrogate models have been integrated into metaheuristic optimization methods [10, 44, 88]. Yadav et al. [10] specifically highlighted that the computational expense of metaheuristic optimization in heat treatment processes stems from solving the forward problem, motivating the development of a surrogate method to alleviate these costs.

Methodologies developed for control purposes in heat treatment processes often suffer from reduced fidelity due to the need for real-time estimation and control with feedback loops. Studies have implemented real-time control using PID controllers [8,89]. Real-time heat flux estimation using Kalman filters has been explored, although this approach is generally restricted to one-dimensional problems [68]. Artificial neural networks have been employed for control purposes [58], while model-based control systems have been developed for continuous annealing furnaces and thermal rapid processes of silicon wafers [90,91]. Recent advancements in real-time estimations using ANN and Kalman filtering approaches remain largely confined to conduction problems with limited dimensional scope [22, 40].

Optimizing heat treatment processes with high fidelity remains a significant challenge due to the complex interplay of various factors that must be accurately modeled and computationally managed. Depending on the specific requirements of the application, an appropriate approach should be selected to balance computational efficiency and model accuracy. The solution of inverse design problems continues to be an area ripe for further development, particularly in achieving transient and three-dimensional representations of the problems while adequately considering the relevant heat transfer mechanisms.

Notably, our study distinguishes itself by including heat transfer inside the workpiece within a radiant furnace, an aspect often overlooked in prior research. This approach ensures a more accurate representation of the physical processes involved, leading to more reliable and precise outcomes in heat treatment applications.

1.6.5 Experimental Validations of Inverse Solutions

In the field of inverse design and optimization for heat treatment processes, most of the studies have been limited to numerical and theoretical cases, with only a few incorporating experimental validation. Notable works in this area include studies by Howell et al. [92] and Ertürk et al. [16], who conducted experimental validations on silicon wafer heating. Su et al. [73] and Daouas et al. [75] used experimental data for parameter estimation to validate their inverse solutions. Additionally, some studies [8, 93] focused on experimental investigations of heat treatment processes without directly addressing inverse problems.

In this study, no experimental processes are included. While incorporating experimental validation would enhance the robustness and reliability of the inverse design solutions, it was not feasible within the scope of this research. Future studies could benefit from building on the theoretical and computational models presented in this study by incorporating experimental validations.

1.6.6 Applications of Inverse Solution in Radiant Enclosure Problems

Several studies have contributed valuable insights to the field of inverse radiation heat transfer problems, advancing our understanding of the impact of several key design considerations in designing and optimizing thermal systems.

Heater configuration has been studied, with notable investigations [10–13, 24, 31] examining aspects such as on-off patterns, the optimal number and location of heaters, and the shape of heating filaments.

The location of the workpiece within the enclosure, including its number and placement, has been studied in several studies [30, 43, 44, 48]. Additionally, Dehghani et al. [30] have examined the number and location of design points within workpieces for defining design conditions.

Surface emissivity, a material property directly affecting radiation heat transfer, has been investigated in several studies. Emissivity of the heater surfaces has been examined [37], as well as the workpiece surface emissivity [7, 37, 51].

Inverse design problems typically do not account for noise in the input data, as the input represents a desired outcome rather than a measured quantity, thus no noise or error is expected in these desired outcomes. However, to demonstrate the stability of the methodology, noise in the input data is often considered in solving inverse problems, including inverse design problems. In the context of inverse radiant enclosure problems, several studies [30,38,69,72] have investigated the impact of noise in the input data to ensure robustness of the solutions.

Several studies have focused on different aspects of solving radiant enclosure design problems. The impact of regularization applied to the objective function has also been a significant area of investigation [34, 42]. Research has addressed the function types of the unknown parameters, including polynomial and exponential forms [38]. Additionally, studies have explored various operational parameters such as heating rate and preheating temperature [6], conveyor belt speed or residence time [15], and

geometry aspect ratio [17]. The conditions of the participating medium have been another critical focus, providing insights into the complex interactions within the system [7, 57].

In our study, we have investigated a wide range of design considerations for heat treatment processes. These include the configuration of design points (their number and location), the impact of noise in the desired temperature data, the definition of design variables (whether heater temperature or power), various temperature profiles for heating, furnace heater configuration (including heater layout, material, and surface emissivity), heat loss from the furnace chamber to its surroundings, and the configuration of furnace operating surfaces during the cooling phase. These comprehensive investigations aim to optimize the heat treatment process, ensuring improved overall effectiveness.

1.7 Random Walk-Based Methods in Heat Transfer Analyses

Random walks are statistical methods involving the release of a large number of particles, tracing their random walks, and utilizing their histories to calculate certain unknowns. The first studies on the solution of differential equations by statistical methods date back to the 1950s. One such early study by Todd [94] involved solving two-dimensional differential equations by discretizing them using finite differences, releasing particles that move to one of the neighboring points, with the probability of moving to any neighboring point being predetermined.

Floating random walk (FRW) is a variant of random walks where the walks are driven in continuous space and time. The first application of the FRW method to heat transfer problems was conducted by Haji-Sheikh and Sparrow [95] for heat conduction problems. Subsequently, many studies have utilized variants of the random walk method to solve various heat conduction problems in a forward solution manner, including those by [96–101].

Random walk methods for heat conduction provide explicit formulations of the temperatures at specific locations within a conducting solid object based on the specified boundary conditions, which can be considered as sensitivity relations. Chantasiriwan [102] demonstrated that the sensitivity coefficients of a linear heat conduction problem could be calculated using random walk methods. Although these sensitivity relations are crucial for solving inverse problems, such as those utilizing direct differentiation, the application of random walk methods in inverse heat transfer problems has been relatively limited. These studies are generally restricted to linear heat conduction applications in geometrically simple domains, mostly focusing on transient one-dimensional or steady-state two-dimensional conduction problems [103–107].

To our knowledge, no study has utilized random walks to solve inverse heat transfer problems that include both conduction and radiation heat transfer mechanisms, which makes the problem particularly challenging. In this study, we have employed the direct differentiation approach for sensitivity coefficient calculation, utilizing both the classical Floating Random Walk method and its modified variant to derive explicit formulations for the variables defined within workpieces. This novel approach aims to address the complexities of combined conduction and radiation heat transfer, providing a new avenue for calculating the sensitivity coefficients in gradient-based optimization methods to solve inverse boundary design problems with radiant enclosure.

1.8 Research Objectives

Previous research in inverse radiant boundary design problems has mainly focused on achieving desired temperatures or heat flux on the surfaces of workpieces within furnace enclosures. However, targeting specific locations within the workpieces, referred to as design points, which can be located anywhere inside or on the surface of the workpiece, provides a more accurate representation of real-world applications.

Ensuring desired temperatures at these internal design points is promising for achieving precise thermal conditions within the workpieces. This approach allows for the consideration of internal conduction heat transfer within workpieces using a transient heat treatment model, which captures the detailed internal thermal behavior of workpieces during the heat treatment process. Despite its importance, this method is rarely employed; the study by Dehghani et al. [30] is one of the few examples, but it was limited to steady-state and two-dimensional scenarios, which lack the fidelity required for real-world applications.

Our study addresses this gap by extending heat transfer modeling to include internal heat transfer within workpieces in a three-dimensional domain and transient analysis, and by defining design conditions at specific design points within the workpieces. This approach enhances applicability of the results, offering a significant contribution to the literature on inverse radiant boundary design problems.

Another novel aspect of this research is the methodology used to calculate sensitivity coefficients in gradient-based optimization algorithms. Existing methods often suffer from high computational costs or approximation errors. In this study, we employed a direct differentiation approach, involving explicit formulations for the variables, which distinguishes this research.

Additionally, the use of the Floating Random Walk method for formulating design point temperatures in sensitivity coefficient calculation is a significant innovation applied to inverse radiant boundary design problems. While previous studies utilizing FRW for inverse heat transfer problems were limited to pure heat conduction in simple geometries, primarily estimating wall temperatures or heat flux, this research extends the utilization of FRW method to more complex scenarios. With our methodology, calculations for sensitivity coefficients were conducted with manageable computational costs and sufficient accuracy.

Previous studies have investigated various aspects of heat treatment processes,

such as heater configurations, surface emissivities, and the impact of regularization, typically focusing on the heating phase. Our study, however, examines the complete treatment process, including heating, soaking, and cooling phases. We explore the effects of heater material and layout, heat loss conditions, and surface reflectivities, while comparing temperature and power-based approaches for determining furnace operating parameters. Additionally, we investigate the impacts of different heating curves, design points, and multiple workpieces. These comprehensive studies aim to enhance our understanding of how these variables influence furnace operation, treatment requirements, energy consumption, and power requirements.

The broad objective of this research is to develop a numerical methodology for optimizing heat treatment processes in radiant furnaces, with a comprehensive modeling approaches and optimization strategies. The specific objectives of this study include:

- Develop a novel approach for defining design conditions at specific points within workpieces (design points) to achieve precise thermal conditions, moving beyond the traditional surface-based approaches.

- Extend heat transfer modeling to include internal conduction heat transfer within workpieces in a three-dimensional domain and transient analysis, enhancing the fidelity and applicability of the results for real-world applications.

- Employ direct differentiation for sensitivity coefficient calculation in gradient-based optimization algorithms, with a manageable computational costs and sufficient accuracy.

- Innovate by utilizing the floating random walk methods for explicit formulation of design point temperatures used in sensitivity coefficient calculations, applying it to inverse radiant boundary design problems.

- Examine the complete heat treatment process, including heating, soaking, and cooling phases, to develop a comprehensive understanding of how various factors influence furnace operation and treatment outcomes.

- Investigate the effects of heater material, layout, heat loss conditions, surface reflectivities, and compare temperature and power-based approaches for determining furnace operating parameters.

- Assess the impact of different heating curves and design point configurations on treatment uniformity, obtained furnace operating solutions, energy consumption, and overall process effectiveness.

By addressing these objectives and gaps, this dissertation significantly advances heat treatment optimization, offering practical solutions and a strong foundation for industrial applications and future research.

1.9 Limitations

The study has several limitations. The models developed assume constant material properties and employ a diffuse-gray radiation model, which simplifies the actual radiative heat transfer process and may not fully capture the complexities of real-world materials. Additionally, potential errors due to spatial discretization for both the workpiece and furnace surfaces, as well as from the thermal modeling of the furnace elements, can affect the accuracy and precision of the simulations.

Despite these assumptions, this study demonstrates improved fidelity for targeted problems in representing real-world conditions compared to previous research. The numerical solutions obtained are highly efficient, with computations completed in a couple of minutes to hours rather than days, even on a personal computer. This balance between model simplicity and computational efficiency ensures that the research offers practical and rapid solutions for industrial applications.

1.10 Organization of the Dissertation

This dissertation is organized into ten chapters. The model problem, heat transfer modeling, and inverse problem formulation are described in Chapter 2, with an outline of the assumptions and material properties. Chapter 3 details the numerical methods for solving the forward heat transfer problem, including conduction and radiation mechanisms. The focus of Chapter 4 is on the inverse solution methodology, covering gradient-based optimization, sensitivity calculations, and regularization techniques. In Chapter 5, the Floating Random Walk method is described, which is used to formulate the temperatures of design points and workpiece surfaces utilized in sensitivity coefficient calculation, and its verification is provided. The inverse solution is applied in Chapter 6 to estimate steady heater temperatures in a radiant furnace heating two glass panes, examining the impact of design point configuration on convergence and the resulting solution. In Chapter 7, optimization approach is extended to the heating and soaking of six glass panes, with an exploration of various heating strategies and their effects on the obtained solutions and energy requirements. Chapter 8 delves into the influence of furnace configuration and material properties on the performance of heating and soaking a stainless steel cubic workpiece. Chapter 9 addresses the challenge of achieving uniform cooling in a cubic workpiece during the cooling phase, investigating different furnace operating strategies. Finally, Chapter 10 summarizes the findings, contributions, and potential future work.

CHAPTER II

INVERSE PROBLEM DESCRIPTION

In this chapter, we describe the inverse problem that focuses on optimizing heat treatment processes in radiant furnaces. We begin by providing an overview of the model problem, focusing on the furnace and workpiece structures, then discussing their respective material properties. The heat transfer modeling is detailed where we delve into the mathematical foundations of heat transfer mechanisms, which include energy balance, conduction, radiation, and heat loss considerations. Then, the assumptions employed to translate the complex thermal environment into a manageable model are outlined. We define the design condition of the inverse problem through the desired temperature histories at critical locations within the workpiece. Following that, we comprehensively detail our modeling on the furnace operating conditions, encompassing the operating surfaces, variables, their functional representation and parameters, leading to the unknown variable of the inverse problem. Lastly, we present the formulation of our inverse problem, with the objective function and bound constraints defined. Collectively, these sections lay a comprehensive groundwork for understanding the inverse problem addressed in this study.

2.1 Model Problem Overview

A simple demonstration of a three-dimensional radiant furnace and two workpieces placed inside is presented in Fig. 3.

The computational model of the furnace is constructed from discrete surface elements, primarily comprising the chamber and heater surfaces. The chamber constitutes the boundary of the furnace, while the heater elements are either embedded within certain boundary sections, such as the upper wall, or positioned internally,

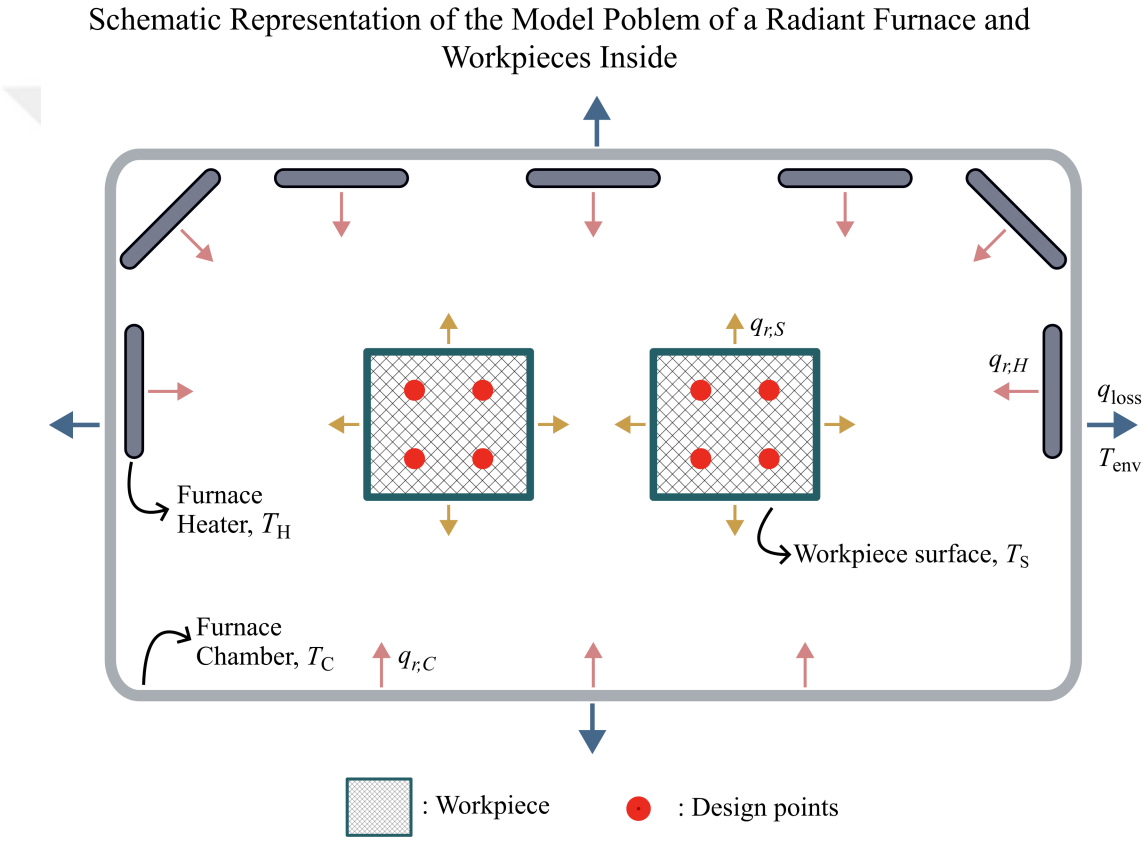


Figure 3: Schematic representation of a radiant furnace with two workpieces inside, showing the chamber and heater surfaces, and the design points

as in Fig. 3. The furnace surfaces are divided into N_f surface elements. This is the summation of N_c chamber surface elements and N_h heater surface elements, such that $N_f = N_c + N_h$. For indexing, f refers to the general furnace surface elements, c to chamber elements, and h to heater elements. Even though the furnace geometry is depicted by surface elements lacking thickness, in heat transfer modeling, the furnace surface elements are assigned a thickness of L to accommodate the lumped capacitance thermal modeling.

Temperature across the furnace surface elements is denoted by T_F, encapsulating both the chamber temperature T_C and the heater temperature T_H, such that $T_F = [T_C, T_H]$. Each furnace surface element is defined by its density ρ, specific heat capacity c_p, and surface area A. For heat transfer analyses, each furnace element is assigned a volume V calculated as $V = A \times L$.

Radiative heat transfer within the furnace enclosure is considered, with heat fluxes labeled as $q_{r,C}$, $q_{r,H}$, and $q_{r,S}$ for chamber, heater, and workpiece surfaces, respectively. The furnace's radiative heat flux, $q_{r,F}$, encompasses both chamber and heater surfaces, such that $q_{r,S} = [q_{r,C}, q_{r,H}]$. Additionally, the loss from chamber surfaces to the environment is considered, denoted by the corresponding heat flux q_{loss} with the environmental temperature T_{env}.

The workpiece is modeled as a three-dimensional solid, discretized into finite volumes. This discretization yields N_i discrete surface elements, each denoted by the index i, whose temperature is is denoted by T_S.

Within the workpieces, critical locations where the temperature monitoring can be significant in heat treatment processes are identified as *design points*, as demonstrated in Fig. 3. Importantly, these design points are not locations where any measuring instruments must be physically installed within the workpiece. Instead, these points serve as reference markers where the desired temperature histories, crucial to the heat treatment's efficacy, are established and evaluated. Further elaboration on design

points and their significance in the inverse solution can be found in Section 2.5.

2.2 Material Properties

In the following table, we present the material properties concerning both the furnace elements and the workpiece. These material properties are assumed to remain independent of space and temperature. This assumption is further discussed in Section 2.4.1 in detail. The specific materials employed in different scenarios are indicated within the problem descriptions found in the dedicated chapters.

Table 1: Material properties for the furnace components and workpieces

Component	Material	Thermal conductivity (W/mK)	Density (kg/m^3)	Specific heat (J/kgK)	Surface emissivity
Workpiece / Chamber	AISI 420 stainless steel	24.9	7800	460	0.4
Workpiece	Glass	1.3	2500	955	0.8
Heater	Graphite	24	2250	700	0.9
Heater	Tungsten	175	19250	134	0.4
Chamber	Inconel 601	18	8100	460	0.3

2.3 Heat Transfer Modeling

The heat transfer modeling for the heat treatment of workpieces inside a radiant furnace encompasses; the conduction within workpieces, the application of lumped capacitance for furnace surface temperatures, the radiative heat transfer between the surfaces, and the heat loss from the furnace surfaces.

2.3.1 Conduction within the Workpieces

Conduction heat transfer within the workpieces is governed by the three-dimensional transient heat conduction equation. In the absence of internal heat generation and

assuming constant material properties, this equation is expressed as

$$\alpha \nabla^2 T = \frac{\partial T}{\partial t} \tag{4}$$

where ∇^2 is the Laplacian operator and α represents the thermal diffusivity. At the workpiece boundaries, the radiative heat flux $q_{r,S}$ is applied, accounting for heat exchange between the workpiece surfaces and the furnace enclosure surfaces. It is formulated as

$$q_{r,S} = -\lambda \frac{\partial T_S}{\partial s} \tag{5}$$

where λ denotes the thermal conductivity of the workpiece and s is the outward surface normal.

2.3.2 Lumped Capacitance Approach for Furnace Surface Temperature

Utilizing the lumped capacitance method, the change in the temperature of furnace surface element f at time t can be expressed as the following.

$$\frac{dT_F(t,f)}{dt} = \frac{1}{\rho_f V_f c_{p,f}} \left(\dot{E}_F(t,f) - A_f \left(q_{r,F}(t,f) + q_{\text{loss}}(t,f) \right) \right) \tag{6}$$

The equation above is derived from an energy balance for a furnace surface element, taking into account the internal energy generation term $\dot{E}_F(t,f)$, the outgoing radiative heat flux $q_{r,F}(t,f)$, and the heat loss term $q_{\text{loss}}(t,f)$.

The internal energy generation term is specifically incorporated only for the scenarios where the furnace power serves as the operating variable of the heat treatment process, as detailed in Section 2.6.

2.3.3 Radiation Heat Transfer

In this study, radiative heat transfer within the furnace enclosure is modeled as surface-to-surface radiative exchange between diffuse-gray surfaces. Our radiative heat transfer formulation utilizes exchange factors, which quantify the thermal radiation interactions between different surface elements in an enclosure, taking into

account reflections and absorptions. Following [20], the net radiative heat fluxes at any time t on the workpiece surface element i and the furnace surface element f are given by the following equations, respectively.

$$q_{r,S}(t,i) = \epsilon_i \sigma \left(T_S(t,i)^4 - \sum_{f=1}^{N_f} \Gamma_{S,i\to f} T_F(t,f)^4 - \sum_{i^*=1}^{N_i} \Gamma_{S,i\to(N_f+i^*)} T_S(t,i^*)^4 \right) \tag{7}$$

$$q_{r,F}(t,f) = \epsilon_f \sigma \left(T_F(t,f)^4 - \sum_{f^*=1}^{N_f} \Gamma_{F,f\to f^*} T_F(t,f^*)^4 - \sum_{i=1}^{N_i} \Gamma_{F,f\to(N_f+i)} T_S(t,i)^4 \right) \tag{8}$$

In the equations above, ϵ stands for the surface emissivity and σ is the Stefan-Boltzmann constant. $\Gamma_{j\to j^*}$ represents the exchange factor indicating the fraction of thermal radiation emitted from surface element j that reaches and is absorbed by any surface element j^*. The subscripts S and F in the exchange factors designate the origin of the emitted radiation, corresponding to the workpiece and furnace surface elements respectively.

2.3.4 Heat Loss at the Furnace Surfaces

Incorporating heat loss into our furnace model's thermal calculations, we employ Newton's law of cooling to quantify the heat flux due to heat loss. For each furnace surface element f at any time t, the heat flux associated with heat loss is calculated as

$$q_{\text{loss}}(t,f) = \bar{U}(f) \left(T_F(t,f) - T_{\text{env}} \right) \tag{9}$$

where $\bar{U}$ denotes the overall heat transfer coefficient, which represents the insulation layer of the furnace and the heat transfer from the furnace's external shell to the environment through convection and radiation. Throughout this thesis, the surrounding environment temperature, T_{env}, is consistently set to 300 K.

2.4 Assumptions in the Model

In this study, several assumptions have been made to structure the modeling process, ensuring a balance between accurate heat treatment analysis and the efficient utilization of computational resources. The subsequent sections detail the assumptions made in each specific category.

2.4.1 Material and Surface Property Assumptions

In our targeted heat treatment processes, significant temperature changes are observed. The incorporation of temperature-dependent material properties can notably enhance the accuracy of our models, making them more representative of real-world scenarios. However, the integration of such properties would considerably escalate both the computational costs and the complexity of the mathematical model. Hence, for practicality, it is assumed that the material properties of both the furnace elements and the workpiece remain constant throughout the entire process.

Additionally, the model assumes that the surface elements are opaque with properties characteristic of diffuse-gray surfaces. These assumptions facilitate the implementation of radiative heat transfer by neglecting complex aspects, such as spectral properties, directional dependence and transmissions across the interfaces, thus simplifying the overall modeling.

2.4.2 Assumptions for Radiant Furnace Enclosure

We concentrate on radiant furnaces in this study, where radiation is the primary mode of heat transfer, dominating the effects of convection. Consequently, a vacuum condition is presumed within the furnace enclosure. This leads to the assumption that convective heat transfer within the furnace chamber is negligible. Moreover, the medium inside the furnace is treated as nonparticipating in the radiation heat transfer model, meaning it neither emits nor absorbs radiation. While these assumptions simplify the model, they are fitting for scenarios where convection is minimal, and

the medium inside the enclosure is largely transparent to radiation.

2.4.3 Assumptions Arising from Discretizations

Computational models typically transform governing equations, originally defined in continuous space and time, into discrete representations. In our model, the furnace's geometry is constructed using surface elements, and the workpiece's domain is discretized by finite volume methodology. Within this discretization framework, we assume that all surface elements in the model are isothermal. This implies that temperature gradients within these surfaces are considered negligible in the calculations.

2.4.4 Assumptions in Thermal Modeling of Furnace Surface Elements

In our approach, the changes in temperature of the furnace surface elements over time are represented using the lumped capacitance method. This technique relies on an energy balance for each isothermal surface element. Additionally, we model the heat loss from the furnace to its surroundings using Newton's law of cooling. This law establishes a linear correlation between the rate of heat loss and the temperature differential between the furnace surface elements and the surrounding environment. We also assume that the overall heat transfer coefficient, which characterizes the insulation properties between the furnace and its surroundings, remains constant throughout the treatment process.

2.5 Design Condition: Desired Design Point Temperature

In the inverse problem, the design condition is characterized by the desired temperature at specific locations within the workpiece, known as design points. These points are critical locations where temperature monitoring plays a significant role in the success of the desired outcome from heat treatment processes. The design condition, therefore, is defined by the desired temperature histories at these points. A representative illustration of the design points within the workpieces can be seen in Fig.

3.

It is essential to note that the solution of the inverse boundary design problem does not require placing any temperature measuring instruments at these design points. Specifically, these points serve as reference markers for establishing desired temperature profiles and for evaluating the resulting temperatures.

Within our computational model, total number of N_d design points are defined, where their temperatures are stored in a vector denoted by T_D. The *desired design point temperature* denoted by T_D^*, being the design condition, serves as the known variable in our inverse problem formulation.

The time resolution of desired temperature histories at design points is defined by a constant time step size Δt_{INV}. Considering the entire time domain of $t_{\max}$, the total number of time steps in the inverse solution, represented as $N_{l,\text{INV}}$, is determined by $N_{l,\text{INV}} = t_{\max}/\Delta t_{\text{INV}}$. As a result, the desired temperature histories for the inverse solution are provided at specific time instances $t = l\Delta t_{\text{INV}}$ for the time step index $l = 1, 2, \ldots, N_{l,\text{INV}}$. Accordingly, the sizes of the vectors T_D^* and T_D are established as $M = N_{l,\text{INV}} \times N_d$.

If one were to include experimental measurements to gather data for the design condition, which is beyond the scope of this thesis, temperature measurement at these design points would be required using appropriate devices. These measurements are typically conducted on the workpiece surfaces, which aligns well with the developed inverse framework, as the design points can be defined on the workpiece surfaces.

2.6 Design Variable: Furnace Operating Parameters

Operating a heat treatment furnace is the primary focus of this study, and it is characterized by the concept of *furnace operating conditions*. The modeling of furnace operating conditions in this study is detailed as follows.

2.6.1 Furnace Operating Surfaces

The effective thermal source in furnace operation is determined by specific surface elements, selected based on the phase of the heat treatment being considered. For instance, during the heating phase, the heater surfaces act as the primary heat sources. On the other hand, the cooling phase typically involves controlled heat removal from the chamber surfaces, with potential heating inputs from the heater surfaces as necessary to stick to the desired cooling profile.

This concept is referred to as the *operating surface*, which identifies the specific furnace surfaces whose thermal conditions are adjusted by the inverse solution. In other words, these are the furnace surfaces where the unknown variables of the inverse problem have their impact. When focusing specifically on the operating surfaces, we adopt a different set of indices. Thus, $\bar{f}$, $\bar{c}$, and $\bar{h}$ are used to distinctly represent the operating furnace surfaces, chamber surfaces, and heater surfaces, respectively. The respective counts of these surfaces are represented by $N_{\bar{f}}$, $N_{\bar{c}}$, and $N_{\bar{h}}$. This differentiation in indexing is essential to distinguish between the overall furnace surfaces and those surfaces actively adjusted by the inverse solution,

2.6.2 Furnace Operating Variables

The thermal modeling aspect of furnace operating conditions lies in the *operating variable*, for which we investigate the following two approaches.

- In **Temperature-based Approach**, the furnace is operated by the time-varying furnace temperatures, denoted by $T_{\bar{F}}$, directly. Therefore, the lumped capacitance model in Eq. (6) is not utilized for the operating furnace surface elements. An inherent drawback of the Temperature-based Approach is the potential for generating unrealistic thermal scenarios. For instance, adhering to the determined furnace temperature profile may necessitate either extracting heat from the operating heater surfaces or injecting heat into the operating

chamber surfaces. Such situations can result in furnace behaviors that do not accurately represent real-world conditions. To prevent these unrealistic conditions, specifically designed constraints can be integrated into implementation, which is not included in this study. Despite this drawback, the Temperature-based Approach offers a simpler method for thermal modeling of the furnace, eliminating the need for an additional energy balance equation for furnace surface elements.

- In **Power-based Approach**, the furnace is operated by the time-varying furnace powers, represented by $\dot{E}_{\bar{F}}$. This approach utilizes the lumped capacitance model detailed in Eq. (6), incorporating the energy generation term $\dot{E}_F(t, f)$. Unlike the Temperature-based Approach, this method does not lead to unrealistic furnace behavior. It achieves this by directly adjusting the energy input or extraction, making it better suited for practical implementations.

The subscript $\bar{F}$ signifies that these operating variables are specific to operating surfaces, rather than all furnace surface elements. Since each approach eventually sets a boundary condition for the transient heat treatment of the workpiece, they both represent instances of an inverse boundary design problem.

2.6.3 Furnace Operating Variable Function

The operating variable is articulated through an *operating variable function*, Ψ. This function establishes the temporal evolution of the operating variables, which are either $T_{\bar{F}}$ for temperature or $\dot{E}_{\bar{F}}$ for power, based on the selected approach. The temperature or power of a specific furnace operating surface element $\bar{f}$ at any given time t is defined

by the operating variable function Ψ, as illustrated below.

$$\Psi(u_{\bar{f}}, t) = \begin{cases} u_{\bar{f},1} + (u_{\bar{f},2} - u_{\bar{f},1})\frac{t}{t_1} & 0 \leq t < t_1 \\ u_{\bar{f},2} + (u_{\bar{f},3} - u_{\bar{f},2})\frac{t-t_1}{t_2-t_1} & t_1 \leq t < t_2 \\ \vdots & \vdots \\ u_{\bar{f},\eta} + (u_{\bar{f},\eta} - u_{\bar{f},\eta+1})\frac{t-t_{\eta-1}}{t_\eta - t_{\eta-1}} & t_{\eta-1} \leq t < t_\eta \\ \vdots & \vdots \\ u_{\bar{f},N_\eta} + (u_{\bar{f},N_\eta} - u_{\bar{f},N_\eta+1})\frac{t-t_{N_\eta-1}}{t_{\max}-t_{N_\eta-1}} & t_{N_\eta-1} \leq t \leq t_{\max} \end{cases} \tag{10}$$

This function models the operating variable using piecewise linear functions over time, where each segment corresponds to an *operating time segment* indexed by η. Consequently, this piecewise formulation divides the time domain into N_η distinct time segments. It is designed such that the transitions between these time segments are continuous. The choice of this function type is deliberate, as each parameter $u_{\bar{f},\eta}$ within it influences a maximum of two time segments. This approach avoids overlapping temporal effects of the parameters in the inverse problem, thereby enhancing the effectiveness of the optimization process. Note that, a steady operating variable function can be set by only a single parameter $u_{\bar{f},1}$ for each $\bar{f}$.

2.6.4 Furnace Operating Parameters

Each operating surface $\bar{f}$ requires a set of $N_\eta + 1$ *operating parameters*, contained within $u_{\bar{f}}$, for the function Ψ. The initial temperature or power is set by the first component $u_{\bar{f},1}$, with subsequent values determined by consecutive components.

With each operating surface associated with its unique set of parameters in $u_{\bar{f}}$, the *furnace operating parameters* encompass all operating surfaces and represented by the vector u. Specifically, this vector u includes the operating parameters for all operating surfaces, indexed as $u_{\bar{f},\eta}$ for $\bar{f} = 1, 2, \ldots, N_{\bar{f}}$, and $\eta = 1, 2, \ldots, N_\eta + 1$.

The combination of operating surfaces, variables and their functional representation leads to the furnace operating parameters, which becomes the *design variable* in the inverse problem. The vector u, encompassing these parameters, serves as the *unknown variable* in the inverse problem. Its size, denoted by N, is calculated as $N = N_{\bar{f}} \times (N_\eta + 1)$, representing the total number of operating parameters across all operating furnace surfaces and time segments.

In the inverse problem, the unit of the unknown variable is arranged as the following. When the Temperature-based Approach is used, the unit for the unknown variable is set as Kelvin (K). Conversely, in the Power-based Approach, the unit is defined as mega-Watts-per-cubic-meter ($\mathrm{MW/m^3}$).

This choice is strategic: using $\mathrm{MW/m^3}$ normalizes the power relative to the heater's geometric configuration (such as area or volume), making it independent of these factors. Furthermore, this power unit is scaled down by dividing by 10^6 to prevent excessively large magnitudes which can complicate the computational process.

2.7 Inverse Problem Formulation

The inverse boundary design problem for heat treating workpieces in a radiant furnace focuses on identifying the necessary operating parameters, encapsulated in the unknown u, to ensure the desired outcome of the heat treatment process, as defined by the design condition. For this purpose, we formulate the inverse problem as a nonlinear least square minimization problem, expressed as

$$\min_{u \in \mathbb{R}^N} \Phi(u) \qquad \text{subject to} \quad B_{\min,n} \leq u_n \leq B_{\max,n} \quad \text{for} \;\; n = 1, 2, \ldots, N \tag{11}$$

where, the objective function $\Phi : \mathbb{R}^N \to \mathbb{R}$ is formulated as:

$$\Phi(u) = \frac{1}{2} \sum_{m=1}^{M} r_m(u)^2 \tag{12}$$

The objective function above is expressed as a summation of squared residual components, where the residual vector $r : \mathbb{R}^N \to \mathbb{R}^M$ is defined as:

$$r(u) = T_D(u) - T_D^* \tag{13}$$

The residual vector serves as an measure of how well the estimated solution u satisfies the design condition. Specifically, it represents the difference between the desired design point temperatures T_D^* and the temperatures at design points T_D resulting from the current estimate u. Each component of the residual vector in Eq. (12), denoted as r_m, corresponds to the temperature at a specific design point d at a specific time step l. This indexing can be arranged as $m = (l-1)N_d + d$ for $l = 1, 2, \ldots, N_{l,\text{INV}}$ and $d = 1, 2, \ldots, N_d$.

The bound constraints, denoted as $B_{\min,n}$ and $B_{\max,n}$, define the feasible solution space for each component of the unknown vector u, ensuring that the estimated parameters remain within realistic and practical ranges. In the Temperature-based Approach, these constraints are particularly useful in maintaining the furnace temperatures within designated design limits, reflecting the operational boundaries of a real-world furnace. Conversely, in the Power-based Approach, the constraints aid in preventing unrealistic heat extraction from operating heater surfaces or any energy insertion to operating chamber surfaces. This careful management of operational parameters ensures that the model aligns closely with real-world furnace behaviors. The specific values assigned to these bound constraints in different scenarios are detailed in the respective results sections of the thesis.

CHAPTER III

NUMERICAL METHODOLOGY FOR FORWARD SOLUTION

This chapter presents the numerical methodology employed for the forward solution in the computational framework developed in this study. The forward solution simulates the thermal behavior of the heat treatment processes under consideration, evaluating the response of the thermal system based on the prescribed causes. Firstly, the general framework of the forward solution is explained, including discrete form of the governing equations, conduction-radiation coupling at workpiece boundary and solution strategy for the resulting set of equations. Then, the Monte Carlo ray tracing method is introduced, which is utilized to calculate exchange factors in the radiative heat transfer model.

3.1 Forward Solution

For a given furnace operating parameter u, whether the operating variable being temperature or power as detailed in Section 2.6.2, the forward solution calculates the temperatures for workpiece and furnace surface elements. The forward solution considers the thermal modeling detailed in Chapter 2, including conduction within the workpiece, radiation heat transfer inside the furnace enclosure, thermal modeling of furnace surface elements by lumped capacitance method with a heat loss from chamber to environment.

3.1.1 Conduction within Workpiece

For conduction heat transfer within the workpiece, the three-dimensional transient heat equation shown in Eq. (4) is discretized using the finite volume method in

Cartesian coordinates. This discretization employs a second-order central scheme for spatial derivatives and utilizes a first-order implicit scheme for time derivatives. Forward solution utilizes the time step size denoted by Δt_{FS} with the number of time steps denoted by $N_{l,\mathrm{FS}}$. At the workpiece boundaries, the boundary condition is defined by a specified gradient, representing temperature gradients arising from the net radiation heat flux, which is updated at each time step. The resulting set of equations is solved using a conjugate gradient linear solver, with a diagonal-based incomplete Cholesky preconditioner and an absolute tolerance of 10^{-9}.

3.1.2 Conduction-Radiation Coupling at Workpiece Boundaries

Computing the temperature field within the workpiece at time t necessitates the evaluation of boundary gradients at time t due to the implicit time scheme. As radiative heat transfer is applied on the workpiece boundaries, the fourth-power term of the workpiece surface temperature T_S at time t introduces nonlinearity into the equation set.

In our implementation, we compute the gradients on workpiece boundaries using radiative heat fluxes at time $t - \Delta t_{\mathrm{FS}}$ instead of t. This approach essentially utilizes an explicit time scheme for evaluating the gradients on workpiece boundaries given in Eq.(5), as demonstrated below.

$$\left.\frac{\partial T_S(t^*, i)}{\partial s}\right|_{t^*=t} = \left.\frac{-1}{\lambda} q_{r,S}(t^*, i)\right|_{t^*=t-\Delta t_{\mathrm{FS}}} \tag{14}$$

This modified scheme retains first-order accuracy in time while simplifying the solution process by eliminating nonlinearity in the equation set. In this thesis, a comprehensive time step analysis has been performed for each problem addressed, and the findings are documented in the corresponding results chapters.

3.1.3 Radiative Heat Fluxes at Workpiece and Furnace Surfaces

The net radiative heat fluxes at workpiece and furnace surfaces are given by Eq. (7) and (8) at any time t.

3.1.4 Exchange Factors in Radiation Heat Transfer Model

The exchange factors in radiation heat transfer model, as expressed in Eq. (7) and (8), are calculated utilizing the backward Monte Carlo ray tracing (MCRT) method [108], elaborated in Section 3.2. Given the absence of moving components in the considered problem and the diffuse-gray radiation model (no temperature dependence), a one-time calculation of the exchange factor is feasible. However, this approach disregards the statistical inherence of the Monte Carlo procedure, causing its stochastic nature to vanish. The statistical errors in the one-time calculated exchange factors can be minimized by employing a large number of rays, thereby ensuring an accurate representation of the true exchange factors. Consequently, we precomputed the exchange factors in advance before performing the forward solution process, storing them for subsequent use. Statistical analyses of the calculated exchange factors for each problem are conducted and discussed later on in this thesis.

3.1.5 Calculations for Furnace Thermal Modeling

In our approach to thermal modeling of the furnace, an explicit time scheme is utilized for the lumped capacitance method described in Eq. (6), as expressed by the following.

$$\frac{T_F(t,f) - T_F(t-\Delta t_{\mathrm{FS}},f)}{\Delta t_{\mathrm{FS}}} = \frac{1}{\rho_f V_f c_{p,f}} \Bigg(\dot{E}_F(t-\Delta t_{\mathrm{FS}}/2,f) - A_f \Big(q_{r,F}(t-\Delta t_{\mathrm{FS}},f) + q_{\mathrm{loss}}(t-\Delta t_{\mathrm{FS}},f) \Big) \Bigg) \tag{15}$$

In the Power-based Approach, when computing T_F at time t, we evaluate the power term $\dot{E}_F$ at the midpoint of the time step, namely at time $t - \Delta t_{FS}/2$. This

ensures that the furnace power is accurately incorporated into the thermal modeling process, as the piecewise linear furnace operating variable function described in Eq. (10) would be conservatively integrated.

3.1.6 Solver Architecture

The developed solver primarily focuses on simulating conduction heat transfer within the workpiece, with the workpiece domain loaded into memory. Radiative heat fluxes are applied at the boundaries of the workpiece to simulate heat treatment processes, while the geometry of the furnace itself is not directly incorporated into the solver implementation. Instead, the effects of the furnace are captured through the radiative heat fluxes computed using precomputed exchange factors.

The forward solution solver is constructed by expanding upon the foundation provided by the existing solver *laplacianFoam* within the OpenFOAM framework. For the workpiece boundaries, the temperature boundary condition is established as *fixedGradient*. In order to integrate the radiative heat flux as a boundary condition for the workpiece, the gradient values are manipulated accordingly at each time step for each boundary element within the developed solver code.

The forward solution solver is optimized for parallel computation executed on central processing units (CPUs), leveraging the Message Passing Interface (MPI). The workpiece domain is partitioned into subdomains, with each processor responsible for a specific portion of the workpiece domain. Similarly, the exchange factor matrix for the workpiece is distributed among processors to ensure that each processor only contains the exchange factors relevant to its assigned boundaries.

Calculations related to the furnace thermal model, such as computing radiative heat fluxes at furnace surfaces, applying the lumped capacitance method, and accounting for heat loss from chamber elements, are executed by the main processor.

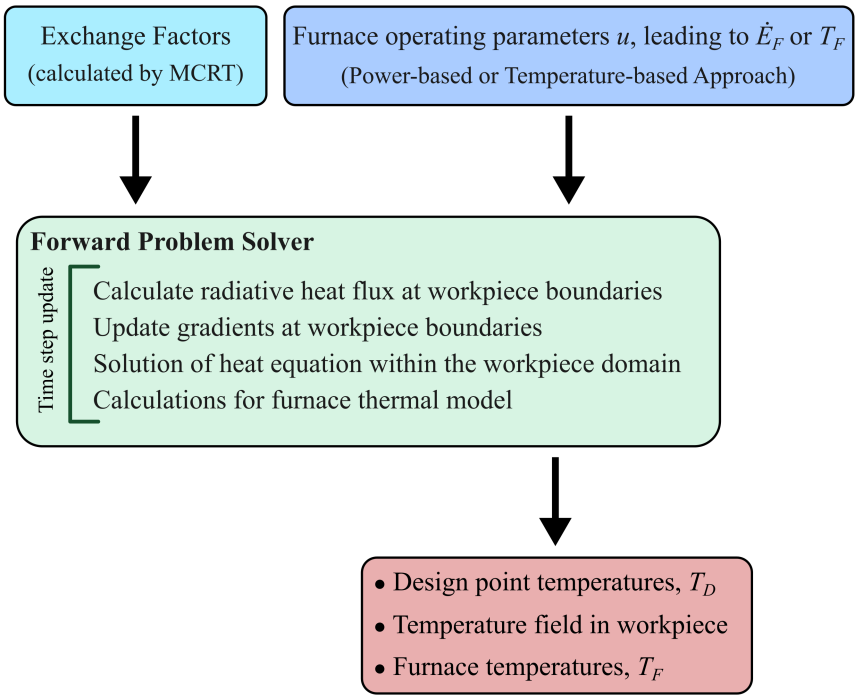


Figure 4: Overview of the forward solution procedure

Consequently, the exchange factor matrix for the furnace is stored on the main processor.

3.1.7 Forward Solution Overview

The forward solution procedure explained in this chapter is summarized in Fig. 4. With precalculated exchange factors and given furnace operating parameters, the forward solution calculates temperatures for both workpiece and furnace components. This includes determining the temperature of the design points within the workpieces.

3.1.8 Use of Forward Solution in Thesis Context

Given the primary focus of this thesis on the inverse solution of heat treatment processes, utilization of the forward solution may initially appear confusing to readers. However, it serves an essential role in the evaluation process of the inverse solution. Specifically, the inverse solution necessitates the solution of the forward problem to assess the efficacy of estimated furnace operating parameters in meeting the design

condition, which involves evaluating the objective function in Eq. (12). This involves performing a forward solution for given furnace operating parameters stored in the vector u to calculate the residual in Eq. (13).

Furthermore, the forward solution serves an additional purpose in generating specific design conditions using simplified furnace operating parameters. This facilitates the derivation of physically meaningful design point temperatures, which can be subsequently employed to design a desired temperature profile. After certain manipulations, this profile can serve as a design condition for inverse solution to find well-optimized furnace operating parameters. This becomes particularly relevant when the aim of the inverse solution is to reconstruct the furnace operating parameters, where the resulting design point temperature from a specific forward solution directly corresponds to the design condition of the inverse solution.

3.2 Monte Carlo Ray Tracing for Calculation of Exchange Factors

In radiative heat transfer analysis, the Monte Carlo method has been a fundamental tool, offering a robust statistical approach to model complex systems. Monte Carlo ray tracing method involves simulating the behavior of photons or photon bundles and accurately represents physical events such as emission, absorption, reflection, and scattering. We employed backward Monte Carlo ray tracing method in this study, to calculate exchange factors in the radiative heat flux formulations given in Eq. (7) and (8).

In line with the assumptions detailed in Section 2.4, this study applies the Monte Carlo ray tracing method to surface elements, with no dependence on wavelength and temperature. The determination of emission location and direction also holds to these assumptions. Implementations covering temperature and wavelength dependence can be found in [109, 110].

3.2.1 Location of Emission

Determination of emission location varies depending on the geometrical representations of the real-world problem. For our geometrical representations that consist of triangular surfaces, Barycentric coordinates are employed to determine the point of emission. Consider a triangle with vertices at coordinates v_1, v_2, and v_3. The emission point p_e is then calculated using the following equation.

$$p_\mathrm{e} = (1 - \sqrt{R_1})v_1 + \sqrt{R_1}(1 - R_2)v_2 + \sqrt{R_1}R_2v_3 \tag{16}$$

Here, R_1 and R_2 are uniformly distributed random numbers, ensuring a uniform emission across the triangle's surface.

3.2.2 Direction of Emission

The direction of emission is represented by the zenith angle θ and the azimuthal angle ϕ. Using uniformly distributed random numbers R_θ and R_ϕ, these angles are determined by the following equations for diffuse emitters.

$$\begin{aligned} \theta &= \sin^{-1}\sqrt{R_\theta} \\ \phi &= 2\pi R_\phi \end{aligned} \tag{17}$$

3.2.3 Absorption or Reflection by a Surface

Upon emitting a ray, defined by its specific emission location and direction, it is traced until it either intersects with another surface or exits the computational domain. The interaction of a ray with a surface, specifically whether it is absorbed or reflected at the point of intersection, is determined by a randomly generated number R_α. Considering the hemispherical absorptivity α and reflectivity ρ of the intersected surface, where $\alpha + \rho = 1$ signifies no transmission, the ray is absorbed if $R_\alpha < \alpha$. In contrast, it is reflected if $R_\alpha > \alpha$.

Rays that are absorbed terminate at their point of intersection. On the other hand, reflected rays are immediately re-emitted from their impact point on the reflective

surface. This process enables the ray to continue its trajectory, potentially interacting further with the surrounding environment. The direction of the newly reflected ray is determined following the same principles outlined in Eq. (17).

3.2.4 Exchange Factors by Monte Carlo Ray Tracing

In Monte Carlo ray tracing for radiation heat transfer, a common method involves estimating exchange factors between the surface elements of a system. These exchange factors are then integrated into the radiative heat flux equations as formulated in Eq. (7) and (8).

In this exchange factor approach, the rays are emitted from each surface element and their paths are tracked until absorption occurs. The tracking of these rays is managed through *ray tracing* algorithms, which utilize random numbers and cumulative distributions to determine the course of events from emission to absorption.

During the ray tracing process, a counter is utilized to record the emission and absorption events of the rays. Consider a ray is emitted from surface element i and absorbed by surface element j after all means of intermediate reflections. This event is recorded by incrementing two counters; $N_e(i)$ for emission and $N_a(i,j)$ for absorption. After completing the tracing of all rays emitted from every surface element, these records are used to calculate the exchange factors as below.

$$\Gamma_{i-j} = \frac{N_a(i,j)}{N_e(i)} \tag{18}$$

Specifically, the exchange factor Γ_{i-j} represents the fraction of emission from surface element i that reaches surface element j and is absorbed by all means including intermediate reflections. The net outward rate of thermal radiation heat transfer at surface element i is expressed as follows.

$$Q_{r,i} = \epsilon_i \sigma T_i^4 A_i - \sum_{j=1}^{N_i} \epsilon_j A_j \sigma T_j^4 \Gamma_{j-i} \tag{19}$$

In the equation above, N_i represents the number of surface elements in the enclosure. The first term on the right-hand side quantifies the rate of energy emission from surface element i. Conversely, the second term accounts for the total rate of energy absorbed at surface element i

3.2.5 Backward Monte Carlo Ray Tracing

The Monte Carlo ray tracing method explained above involves tracing photon bundles from their point of emission to absorption, known as *forward Monte Carlo ray tracing*. This approach computes the exchange factors for all surface elements within the system. However, this method can be inefficient when the focus is on a smaller, specific portion of the system.

To address this, the backward Monte Carlo method [108] reverses the photon bundle tracing process. It begins at the points of absorption in the area of interest and traces back to the emission origins. This backward approach leverages the reciprocity relation between diffuse-gray surface elements i and j, as shown below.

$$\epsilon_i A_i \Gamma_{i-j} = \epsilon_j A_j \Gamma_{j-i} \tag{20}$$

With the exchange factors Γ_{i-j} for surface elements within the area of interest calculated, the net rate of heat transfer at surface element i can be expressed as follows.

$$\begin{aligned} Q_{r,i} &= \epsilon_i \sigma T_i^4 A_i - \epsilon_i A_i \sum_{j=1}^{N_i} \sigma T_j^4 \Gamma_{i-j} \\ &= \epsilon_i \sigma A_i \left(T_i^4 - \sum_{j=1}^{N_i} T_j^4 \Gamma_{i-j} \right) \end{aligned} \tag{21}$$

3.2.6 Verification of Monte Carlo Ray Tracing Code

To validate the Monte Carlo ray tracing (MCRT) code developed, a verification case was adopted from the Catalog of Radiation Heat Transfer Configuration Factor's Section C-12 in *thermalradiation.net* [111]. As depicted in Fig. 5, this particular

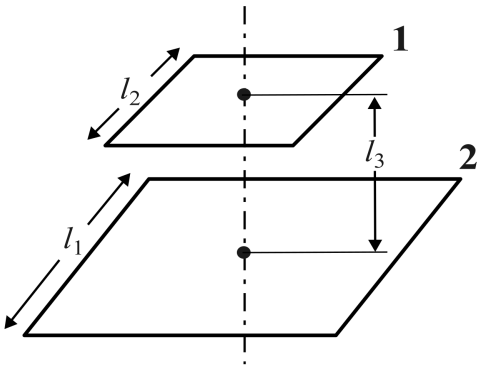


Figure 5: Configuration of the case used to verify the developed Monte Carlo ray tracing code, adapted from *thermalradiation.net*, featuring two coaxial, parallel square plates

case involves two coaxial, parallel square plates with differing edge lengths. For the dimensions considered, namely $l_1 = 100$ cm, $l_2 = 10$ cm, and $l_3 = 100$ cm, the reference view factors were calculated using the formulations provided in [111].

3.2.6.1 Verification of View Factor Calculation

The statistical analyses were conducted for varying numbers of rays set at 20×10^3, 80×10^3, 320×10^3, 2×10^6 and 200×10^6. For each number of rays, a subset of 100 MCRT simulations were run to calculate the mean view factors for both squares, denoted by $\widetilde{\Gamma}_{1-2}$ and $\widetilde{\Gamma}_{2-1}$, and their respective relative standard deviations.

Fig. 6 demonstrates the calculated view factors with vertical bars representing a range of plus or minus three standard deviations, which indicates the interval within which the real value lies with a probability of 97%. It is observed that the calculated view factors are converging towards the reference values as the number of rays increases. Additionally, the relative standard deviation decreases, highlighting an inverse relationship between the number of rays used in the simulations and the variability of the results. This relationship is further illustrated by the linear decrease in the relative standard deviation on the logarithmic plot. These observations are consistent with what one would anticipate from a normal distribution in statistical

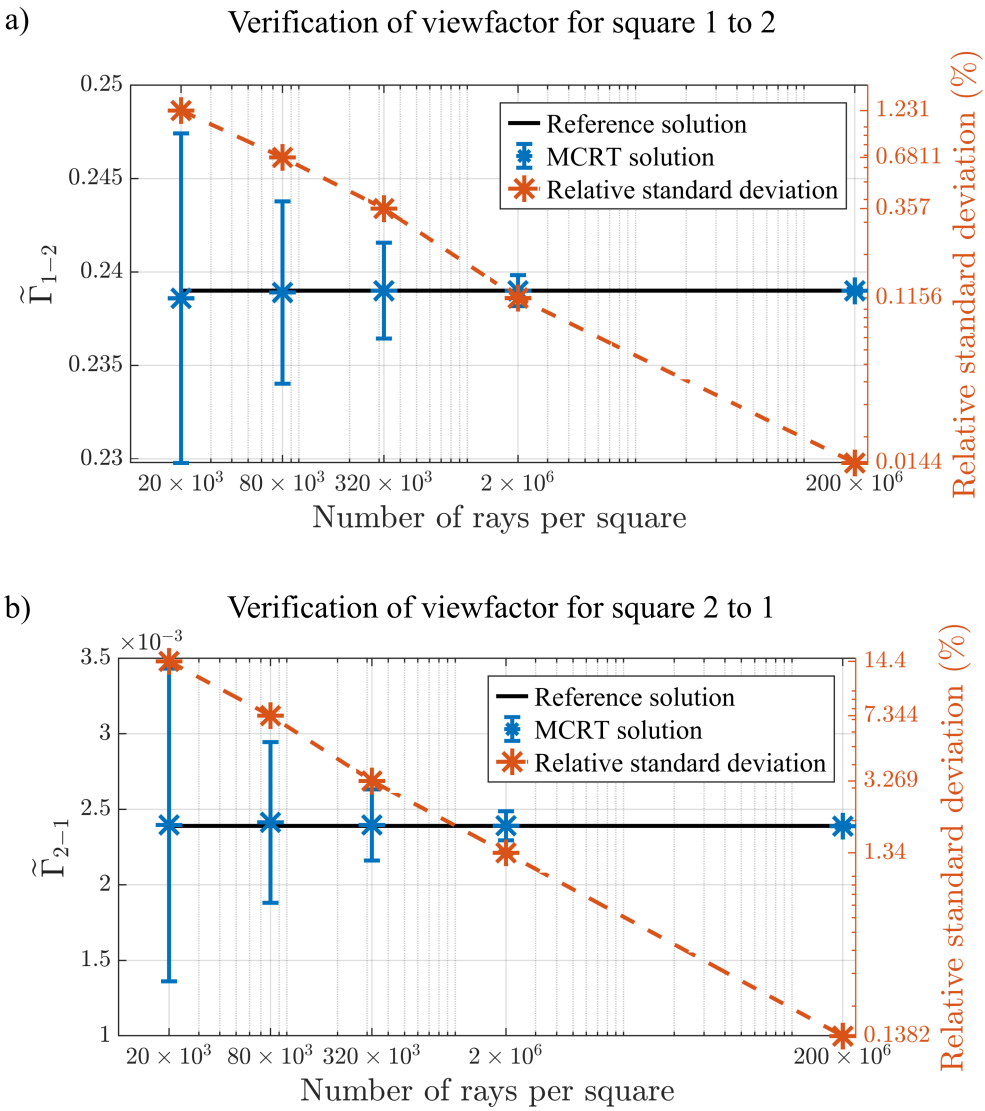


Figure 6: Verification of view factor calculation: Comparison of mean view factors against the reference value and their corresponding relative standard deviations for varying numbers of rays used in Monte Carlo ray tracing simulations.

analysis, thus validating the Monte Carlo ray tracing code used in this study for view factor calculation.

3.2.6.2 Verification of Exchange Factor Calculation

The developed MCRT code for calculating exchange factors was further verified by assigning surface emissivity values of $\epsilon_1 = 0.9$ and $\epsilon_2 = 0.8$ to two square surfaces. A series of MCRT simulations was executed, involving 100 subsets, each with 200×10^6

Table 2: Verification of exchange factor calculation: Calculated mean exchange factors (Γ) with their relative standard deviations RSD_Γ, and the net radiative heat transfer rates (Q_r). The table also compares the calculated net radiative heat transfer rates with reference values $Q_{r,\mathrm{REF}}$, showcasing the relative errors (RE_{Q_r}) to emphasize the accuracy of the calculations.

	Γ	RSD_Γ (%)	Q_r (W)	$Q_{r,\mathrm{REF}}$ (W)	RE_{Q_r} (%)
$1 \to 2$	2.151×10^{-1}	1.33×10^{-2}	1.282×10^{1}	1.282×10^{1}	1.2×10^{-3}
$2 \to 1$	1.190×10^{-3}	1.58×10^{-1}	6.194×10^{3}	6.194×10^{3}	2.7×10^{-4}

rays per square surface. Statistical analysis of these subsets yielded the mean exchange factors Γ_{1-2} and Γ_{2-1}, along with their respective relative standard deviations (RSD_Γ), as shown in Table 2.

The subsequent analysis entailed a comparison between the net rates of thermal radiation heat transfer, calculated using the mean exchange factors with the established reference values. These reference values were determined through the net radiation method, as detailed in [20], incorporating the reference view factors in Section 3.2.6.1. For these calculations, the temperatures were set to $T_1 = 600$ K for square surface 1, $T_2 = 500$ K for square surface 2, and $T_{\mathrm{env}} = 300$ K for the surrounding environment.

Results displayed in Table 2 demonstrate an excellent correspondence between the calculated net radiative heat transfer rates and the reference values, with relative errors under 0.01%. Such precision underscores the accuracy of the developed MCRT code, establishing its efficacy for exchange factor computations in radiative heat transfer analysis.

3.2.7 Remarks on Monte Carlo Ray Tracing for Exchange Factor Calculation

The Monte Carlo ray tracing method stands out in radiative heat transfer analysis for its adaptability to complex physical phenomena. This includes handling participating media, spectral or directional properties, and anisotropic scattering. MCRT is particularly beneficial due to its flexibility and accuracy, making it a suitable choice

for intricate simulations.

In comparison to traditional methods in radiative heat transfer, MCRT is easier to develop and implement. Although historically known for being computationally intensive, advancements in computing technologies have significantly enhanced its efficiency. Particularly noteworthy is the method's inherent suitability for parallel computing environments, especially GPUs, which substantially boost its computational performance.

A central feature of MCRT is its statistical foundation, which inherently links the accuracy of the results to the number of photon bundles used in simulations. This aspect necessitates a balance between computational resources and the desired level of precision, making strategic planning essential for efficient simulations.

A unique advantage of the MCRT method is its scalability with increasing problem complexity. Unlike traditional methods, MCRT does not introduce very high proportional increase in computation with added complexities into the model [110]. This makes it exceptionally effective for problems featuring complex phenomena, such as wavelength- and direction-dependent properties, or intricate geometries with shading or blockage effects. As a result, MCRT has evolved from a benchmarking tool to a preferred method in many complex radiative heat transfer analyses.

The exchange factors determined through the MCRT, combined with the radiative heat flux equations outlined in Eqs. (7) and (8), provide analytical formulations for the surface elements of both the furnace and workpiece. These formulations enable analytical differentiation with respect to the surface temperatures. This capability is particularly beneficial for calculating sensitivity coefficients in inverse solution methodologies, as elaborated in Section 4.2.4.

3.3 Computational Framework Developed for Forward Solution

The forward problem solver was developed using the open-source framework OpenFOAM [112], building upon the existing solver *laplacianFoam* which is designed for solving Laplace's equation and commonly used in heat transfer simulations. In addition, for computing exchange factors, we utilized the NVIDIA OptiX ray tracing engine [113], taking advantage of GPU capabilities for high-performance ray tracing. The following subsections offer a brief overview of these tools, each playing a significant role in ensuring efficient implementation and execution of computations in the forward solution.

3.3.1 OpenFOAM

OpenFOAM (Open-source Field Operation And Manipulation) is a finite volume-based open-source library highly regarded for its extensive solvers and utilities, enabling accurate modeling of fluid dynamics and heat transfer processes. Additionally, MPI integration in OpenFOAM facilitates efficient parallel processing, enhancing computational speed and scalability. OpenFOAM's comprehensive toolkit, encompassing its solvers and utilities, empowers forward solutions of heat transfer processes, making it an invaluable asset within the computer code framework developed for this study.

3.3.2 OptiX Ray Tracing Engine

NVIDIA's OptiX ray tracing engine is a cutting-edge technology renowned for its high-performance ray tracing computations, extending beyond rendering tasks. While it excels in rapid and realistic rendering of complex scenes with intricate lighting and

shadow effects, OptiX is equally adept at scientific computations. Its efficient algorithms and parallel processing capabilities enable real-time or near-real-time simulation of physical phenomena, making it invaluable for scientific research and computational simulations across diverse fields. For the present study, OptiX stands as a powerful tool for the calculation of exchange factors in radiative heat transfer, offering fast ray tracing speed without compromising precision.

CHAPTER IV

NUMERICAL METHODOLOGY FOR INVERSE SOLUTION

This chapter details the computational methodologies employed for solving the inverse problem associated with heat treatment processes. In this context, the chapter elaborates on the gradient-based optimization approach employing the Gauss-Newton algorithm, while also providing a detailed description of sensitivity coefficient calculation. Furthermore, regularization strategies, convergence criteria, and the integration of subdomain optimization are elaborated. Finally, the computational tools utilized in the developed inverse solver are discussed.

4.1 Inverse Solution

The inverse problem seeks to determine the unknown furnace operating parameters u by solving a nonlinear least squares minimization problem as defined in Eq. (11), aimed at minimizing the objective function $\Phi(u)$ outlined in Eq. (12). Employing an iterative optimization approach that utilizes gradient information from the objective function, this section provides the details of the inverse solution procedure.

4.1.1 Gradient-Based optimization

Starting with an initial guess u^0, the optimization process updates the estimation u^k at every iteration k as

$$u^{k+1} = u^k + a^k p^k \tag{22}$$

where p^k determines the direction of the subsequent update within the solution space. The scalar step length a^k dictates the magnitude of the step taken in the chosen direction, ensuring that the new estimate u^{k+1} yields a lower objective function value,

hence improving the estimate over u^k. In this study, the step length a^k is calculated by Bounded Moré-Thuente line search algorithm [114].

Gradient-based optimization algorithms determine the search direction p^k through the partial derivatives of the objective function with respect to the unknown parameters. These algorithms vary in their specific strategies for computing p^k.

4.1.2 Gauss-Newton Algorithm

The Gauss-Newton method works by approximating the Hessian matrix of the residual vector. At each iteration k, the search direction p^k is determined by solving the following linear system.

$$((\boldsymbol{J}^k)^T \boldsymbol{J}^k)p^k = -\nabla\Phi^k \tag{23}$$

In the equation above, commonly referred to as the search direction equation, ∇ represents the gradient operator, defined as $\nabla = \partial/\partial u_n$ for $n = 1, 2, ...N$. The symbol $\boldsymbol{J}$ denotes the Jacobian of the residual vector, a $M \times N$ matrix comprising the derivatives of the residual components with respect to the unknown variables. The Jacobian can be expressed as follows:

$$\boldsymbol{J}(u) = \left[\frac{\partial r_m}{\partial u_n}\right]_{\substack{m=1,2,...,M \\ n=1,2,...,N}} = \begin{bmatrix} \nabla r_1(u)^T \\ \nabla r_2(u)^T \\ \vdots \\ \nabla r_m(u)^T \\ \vdots \\ \nabla r_M(u)^T \end{bmatrix}_{(M\times N)} \tag{24}$$

For nonlinear least square problems, the gradient of the objective function can be expressed as follows [115].

$$\nabla\Phi(u) = \boldsymbol{J}(u)^T r(u) \tag{25}$$

The terms above are expressed as functions of u, however, during the optimization iterations, they are evaluated at the current estimate u^k. The residual vector at the

current estimate, denoted as $r(u^k)$, is computed by solving the forward problem, as elaborated in Section 3.1.

The Gauss-Newton algorithm is known for its strong local convergence, indicating that it rapidly converges a solution u^* when the current estimate u^k is in proximity to u^* [115]. This rapid convergence is attributed to the diminishing magnitude of the residual near u^*, which results in a more accurate Hessian approximation. In such scenarios, the second-order derivative terms in the Hessian are dominated by the first-order derivative terms, namely $\boldsymbol{J}^T\boldsymbol{J}$. A detailed analysis of the convergence of the Gauss-Newton algorithm can be found in [115].

Upon formation of the search direction equation, a linear system solver is utilized to determine p^k. We have employed the Generalized Minimal Residual Algorithm (GMRES) [116] for this purpose. The convergence criteria for solving the linear system is set with a relative tolerance of 10^{-5}.

4.1.3 Sensitivity Coefficients

Gradient-based optimization methods progressively minimize the objective function $\Phi(u)$ by finding search directions p^k based on the local curvature of $\Phi(u)$ at u^k. This curvature is quantified by derivatives of $\Phi(u)$ with respect to the unknown variable u, known as *sensitivity coefficients*, which provide valuable information about the impact of the changes in u on the desired outcomes in the inverse problem. Following the Gauss-Newton algorithm, the required sensitivity coefficients are gradients of the residual components, denoted by $\nabla r_m(u^k)$, representing the first-order derivatives of the residual components $r_m(u^k)$ with respect to the unknown variables u_n^k. Then, the sensitivity coefficients can be expressed as

$$\nabla r_m(u) = \frac{\partial r_m}{\partial u_n} = \frac{\partial T_D(l,d)}{\partial u_n} \tag{26}$$

for a design point d at a time step l, where the residual $r(u)$ is defined in Eq. (13). Note that, the design point temperature T_D depends on the unknown variable u

and its derivative is always evaluated at the current estimation u^k. Recalling that the unknown variable u defined in Eq. (10) is the furnace operating parameters, it encompasses both the spatial and temporal aspects of the operating conditions of the furnace surface elements.

Calculation of sensitivity coefficients is a critical routine in gradient-based optimization algorithms, crucial for achieving efficient convergence and manageable computational demands. Elaborate explanations regarding our methodology for computing sensitivity coefficients are provided in Section 4.2.

The regularization techniques detailed in the next section requires additional steps for sensitivity coefficient calculations. These calculations are typically straightforward, thus, their explicit elaboration is omitted. In our inverse framework, the calculations emerging from the incorporation of regularization were implicitly integrated by the optimization framework utilized.

4.1.4 Regularization Applied to Inverse Problem

Solving the inverse problem often involves adding a regularization term to the objective function. This approach mitigates the problem's ill-posedness to a desired extent and may also enhance the convergence performance of gradient-based optimization methods.

Our implementation adds a regularization term $\zeta\beta(u^k)$ to the original objective function $\Phi(u)$ given in Eq. (12), as its regularized version is

$$\Phi(u) = \frac{1}{2}\sum_{m=1}^{M} r_m(u)^2 + \zeta\beta(u) \tag{27}$$

where $\beta(u^k)$ represents the regularizer function, and the scalar ζ is the regularization weight.

The application of regularization enhances the solution performance in two key aspects:

- Improvement in convergence: Gradient-based algorithms can exhibit poor global convergence and may even diverge, particularly when the initial estimate is far from the solution's local minima. Regularization can modify search directions, steering the iterative process towards local or global minima more effectively, and also helps in preventing divergence, especially in cases with large $r(u^0)$.

- Achievement of desired solution characteristics: Due to the ill-posed nature, inverse problems often have many distinct sub-optimal solutions that can nearly produce the desired design condition. Regularization functions as an additional constraint, guiding the solution towards a subset with desirable characteristics that are well-suited for specific applications. By incorporating these characteristics into the objective function through the regularization term, solutions can be tailored to meet particular needs or desires.

The regularizer function and the regularizer weight must be carefully chosen considering the context of the problem being addressed. Generally, the regularizer weight value is selected to achieve an optimal balance between stability and convergence, in accordance with the specific design considerations. It is important to note that in our implementation, the regularizer weight ζ is kept constant throughout the iterative process. The specific values of ζ used in various cases are detailed in the respective results sections.

Two types of regularizers are employed in this thesis, as elaborated in the following subsections. The specific regularization approaches used for each problem are discussed in the respective results chapters.

4.1.4.1 Proximal Point Regularizer with L2-norm

The L2-norm proximal point regularizer incorporates the differences between successive estimates into the objective function, as given below.

$$\beta(u^k) = \frac{1}{2}\sum_{n=1}^{N}(u_n^k - u_n^{k-1})^2 \tag{28}$$

This form of regularization encourages the new estimate u^{k+1} to stay proximate to u^k, moderated by the regularizer weight ζ. Generally, a higher ζ value implies stronger regularization, leading to smaller steps in the iterative process. While this can enhance stability, it may also slow down convergence and potentially yield sub-optimal solutions. Conversely, a lower ζ value allows for larger steps, accelerating convergence but potentially increasing the risk of divergence or obtaining infeasible solutions.

4.1.4.2 Custom Regularizer with L1-norm

The custom regularizer employs the L1-norm of the unknown variable, incorporating a dictionary matrix $\boldsymbol{D}$ that should be set by a design engineer. This regularization function is expressed as

$$\beta(u^k) = \sum_{\nu=1}\sqrt{w_\nu^2 + e^2} - e \text{ where } w = \boldsymbol{D}u^k \tag{29}$$

where e represents a smoothing scalar introduced to prevent numerical instabilities that might arise from the absolute values in the L1-norm. The index ν refers to the components of w, which can vary in size depending on the number of rows the matrix $\boldsymbol{D}$ contains.

This specific form of regularization allows design engineers flexibility to impose constraints tailored to address particular challenges inherent to the considered inverse problem. Such customization can be crucial for achieving a more refined solution, particularly in scenarios where certain features or aspects of the solution are of interest or importance. For instance, in problems where unknown variables depend on both space and time, this regularizer can be strategically applied to specifically address

the temporal aspects of the unknown variable. This targeted application allows for nuanced adjustment over the obtained solution, minimizing transient fluctuations over time.

4.1.5 Convergence Criteria

In the optimization process, the unknown parameter vector u^k is iteratively updated until a convergence criterion is met. The selection of this criteria is pivotal, as it influences solution accuracy, computational costs, and the characteristics of the solution. Overly strict criteria may lead to redundant iterations with marginal gains in precision, yielding solutions that are not practically feasible. Therefore, it is essential to establish a convergence criteria that judiciously balances the demands of accuracy and computational efficiency, while ensuring the solution's applicability.

In our implementation, the convergence criteria is assessed by measuring the average relative estimated error in design point temperatures. This error at the kth iteration is given as the following.

$$\%E^k_{T_D} = \frac{1}{M}\sum_{m=1}^{M}\left(\frac{\mid T_{D,m}(u^k) - T^*_{D,m} \mid}{T^*_{D,m}} \times 100\right) \tag{30}$$

In the equation above, $T_D(u^k)$ denotes the resulting design point temperature for the current estimate u^k, and T^*_D is the desired design point temperature. The convergence of the iterative process is tracked by the change in this average relative error between successive iterations, defined as below.

$$\Delta\%E^k_{T_D} = \mid \%E^{k-1}_{T_D} - \%E^k_{T_D} \mid < \varepsilon \tag{31}$$

The iterative process is deemed to have converged when the change $\Delta\%E^k_{T_D}$ falls below a predetermined tolerance level ε, indicating that further iterations do not significantly improve the resulting design point temperature. In this work, a tolerance of $\varepsilon = 10^{-3}$ has been selected to balance computational efficiency with the required accuracy, unless specified otherwise.

4.1.6 Inverse Solution Flowchart

The algorithm flowchart, as depicted in Fig. 7, outlines the steps involved in the inverse solution process. The process begins with an initial guess for the unknown parameter vector, establishing the starting point for optimization. In each iteration, labeled by the index k, the residual vector $r(u^k)$ is computed by solving the forward problem with the current estimate u^k, as detailed in Section 3.1. Subsequently, sensitivity coefficients are calculated, which are used to form the Jacobian matrix $J(u^k)$ and the gradient of the objective function $\nabla\Phi(u^k)$, as explained in Section 4.2 Next, the algorithm checks the convergence criteria. If this criteria is not satisfied, it continues by solving the search direction equation to determine p^k. The search direction p^k guides the update to the new estimate u^{k+1}, adjusted by the scalar step length a^k. These steps are iterated until the convergence is achieved.

4.2 Sensitivity Coefficient Calculation

Our approach to calculate the sensitivity coefficients given in Eq. (26) employs the direct differentiation method. It involves deriving the dependent (known) variable, in our case, the design point temperature T_D, through a series of explicit expressions. These expressions originate from the variable itself and involve intermediate variables, ultimately leading through to the independent (unknown) variable u. These explicit expressions are then analytically differentiated using the chain rule of differentiation, to evaluate $\partial T_D/\partial u$ for a given u^k.

Fig. 8 illustrates the variables involved in the inverse problem for both temperature and power-based approaches, encompassing dependent, intermediate, and independent variables. Here, we present the explicit formulations of these variables, starting from the intermediate variable most closely related to u and proceeding backward through the dependencies depicted by the arrows in Fig. 8.

In the direct differentiation approach for calculating sensitivity coefficients, it is

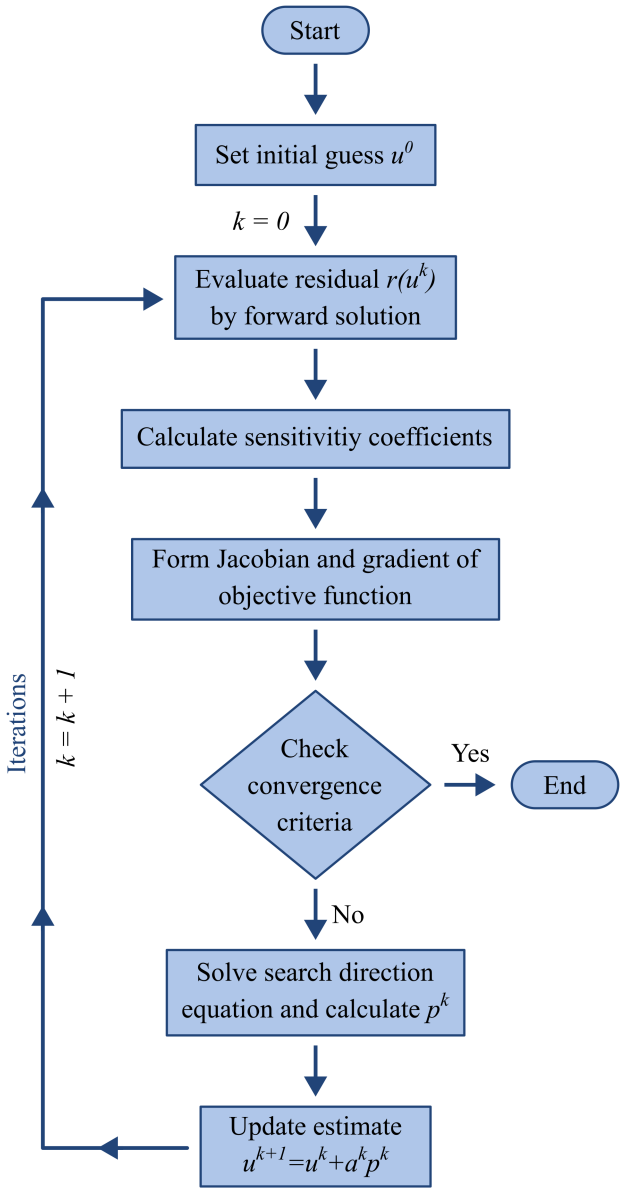


Figure 7: Flowchart depicting the computational steps of the inverse solution algorithm

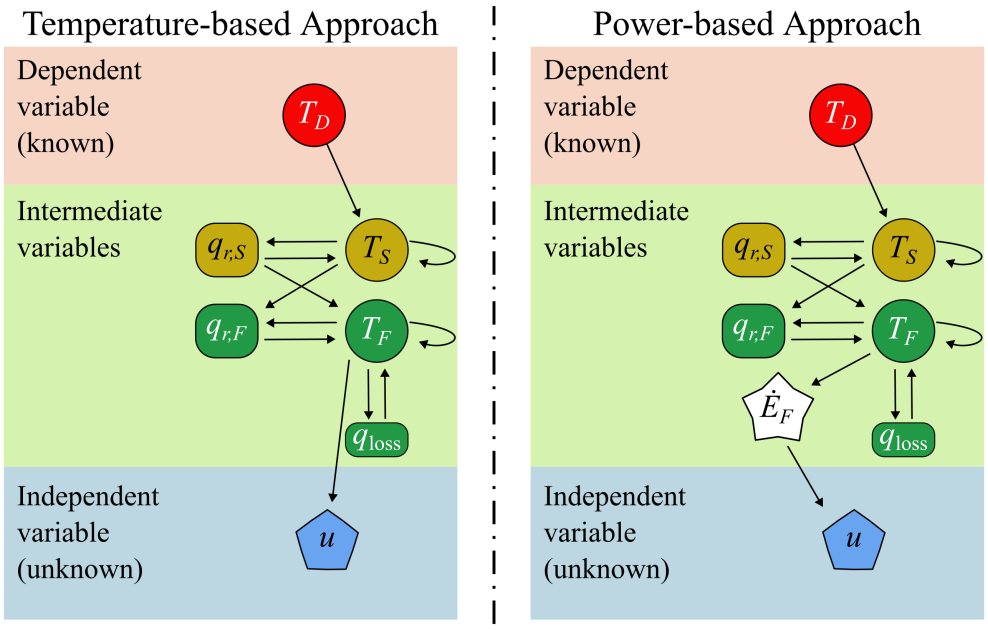


Figure 8: Variables in the inverse problem for both approaches. The direction of dependency among the variables is indicated by arrows. For example; T_D depends on T_S.

necessary to explicitly formulate the workpiece surface temperature T_S and the design point temperature T_D for problems involving conduction within the internal domain of workpieces. However, these formulations are often not explicitly available. Instead, they are implicit and include the temperatures of all cells within the internal workpiece domain. This poses a computational challenge, as calculating the sensitivity coefficients requires solving a system of equations derived from conduction heat transfer, incorporating the temperatures of all internal cells.

To address this challenge, our methodology employs the Floating Random Walk (FRW) method, which allows us to explicitly formulate both the workpiece surface temperature T_S and the design point temperature T_D. This approach bypasses the need to account for the internal temperatures of the workpieces, thereby eliminating the necessity of solving the entire system of equations. Details regarding the FRW method can be found in Chapter 5.

4.2.1 Derivatives of the Furnace Operating Variable Function

The variable most closely related to u is the furnace operating variable function, which governs T_F in the Temperature-based Approach or $\dot{E}_F$ in the Power-based Approach, affecting only the operating furnace surface elements. Its expression, as given in Eq. (10), facilitates straightforward differentiation, yielding the derivative $\partial\Psi/\partial u$. This derivative corresponds to $\partial T_F/\partial u$ for the Temperature-based Approach and $\partial\dot{E}_F/\partial u$ for the Power-based Approach, for the operating furnace surface elements.

4.2.2 Derivatives of the Furnace Surface Element Temperature

The derivation $\partial T_F/\partial u$ for the furnace surface elements other than those operating in the Temperature-based Approach is presented here. (This also encompasses non-operating furnace surface element temperature in the Temperature-based Approach.) Following the explicit time scheme described in Section 3.1.5, the derivative of T_F for a furnace surface element f at time t is formulated as follows.

$$\begin{aligned}\frac{\partial T_F(t,f)}{\partial u} =& \frac{\partial T_F(t-\Delta t,f)}{\partial u} + \\ & \frac{\Delta t}{\rho_f V_f c_{p,f}}\left(\frac{\partial \dot{E}_F(t-\Delta t/2,f)}{\partial u}\right. \\ & \left. - A_f\left(\frac{\partial q_{r,F}(t-\Delta t,f)}{\partial u} + \frac{\partial q_{\text{loss}}(t-\Delta t,f)}{\partial u}\right)\right)\end{aligned} \tag{32}$$

Due to the explicit time scheme, the derivatives at time t depend solely on the terms on the right-hand side evaluated at $t-\Delta t$. These terms can be readily computed beforehand using a sequential calculation procedure, ensuring their availability for calculating $\partial T_F(t,f)/\partial u$.

4.2.3 Derivatives of the Heat Loss at the Furnace Surfaces

The derivative $\partial q_{\text{loss}}/\partial u$ for a furnace surface element f at time t is expressed as the equation below.

$$\frac{\partial q_{\text{loss}}(t,f)}{\partial u} = \bar{U}(f)\frac{\partial T_F(t,f)}{\partial u} \tag{33}$$

4.2.4 Derivatives of the Radiative Heat Fluxes

Following the radiative heat fluxes at the workpiece and furnace surfaces given in Eq. (7) and (8), their derivatives are as the following. For a workpiece surface elements i, the derivative $\partial q_{r,S}/\partial u$ at time t can be expressed as:

$$\frac{\partial q_{r,S}(t,i)}{\partial u} = \epsilon_i \sigma \Bigg(4T_S(t,i)^3 \frac{\partial T_S(t,i)}{\partial u} - \sum_{f=1}^{N_f} \Gamma_{S,i\to f} 4T_F(t,f)^3 \frac{\partial T_F(t,f)}{\partial u} - \sum_{i^*=1}^{N_i} \Gamma_{S,i\to(N_f+i^*)} 4T_S(t,i^*)^3 \frac{\partial T_S(t,i^*)}{\partial u} \Bigg) \tag{34}$$

For a furnace surface element f, the derivative $\partial q_{r,F}/\partial u$ at time t can be expressed as:

$$\frac{\partial q_{r,F}(t,f)}{\partial u} = \epsilon_f \sigma \Bigg(4T_F(t,f)^3 \frac{\partial T_F(t,f)}{\partial u} - \sum_{f^*=1}^{N_f} \Gamma_{F,f\to f^*} 4T_F(t,f^*)^3 \frac{\partial T_F(t,f^*)}{\partial u} - \sum_{i=1}^{N_i} \Gamma_{F,f\to(N_f+i)} 4T_S(t,i)^3 \frac{\partial T_S(t,i)}{\partial u} \Bigg) \tag{35}$$

4.2.5 Derivatives of the Workpiece Surface Temperature

The analytical expression of the workpiece surface temperature is formulated utilizing the Modified Floating Random Walk method as a function of both itself and the radiative heat flux at the workpiece surfaces, as described in Section 5.4 and the expression given in Eq. (49). Analytical differentiation applied to this equation results in

$$\frac{\partial T_S(l,i)}{\partial u} = \sum_{i^*=1}^{N_i} \Bigg(- \frac{\partial q_{r,S}(l-1,i^*)}{\partial u} \frac{r_{\min}}{\lambda} S_S(i,1,i^*) \Bigg) + \sum_{l^*=1}^{l-1} \sum_{i^*=1}^{N_i} \Bigg(\frac{\partial T_S(l^*,i^*)}{\partial u} S_S(i,l-l^*+1,i^*) \Bigg) \tag{36}$$

where the time step index l corresponds to the time $t = l \times \Delta t$ for $l = 1, 2, \ldots, N_l$. The equation above evaluates $\partial q_{r,S}/\partial u$ at time step $l-1$ for $\partial T_S/\partial u$ at time step l, which differs from the original relation in Eq. (49) where $q_{r,S}$ was evaluated at the same time step as T_S. This manipulation corresponds to radiation-conduction

coupling at workpiece boundary in the forward solution described in Section 3.1.2, also avoids solving a linear set of equations when calculating sensitivity coefficients.

4.2.6 Derivatives of the Design Point Temperature

The analytical expression for the design point temperature T_D is formulated using the classical Floating Random Walk method, as described in Section 5.3 and the equation given in Eq. (48). Applying analytical differentiation to this equation yields

$$\frac{\partial T_D(l,d)}{\partial u} = \sum_{l^*=1}^{l} \sum_{i=1}^{N_i} \left(\frac{\partial T_S(l^*,i)}{\partial u} S(d, l-l^*+1, i) \right) \tag{37}$$

where the time step index l corresponds to the time $t = l \times \Delta t$ for $l = 1, 2, \ldots, N_l$. Given that T_D is the dependent variable and no other variable depends on it, $\partial T_D/\partial u$ can be obtained after calculating $\partial T_S/\partial u$ at all time steps.

4.2.7 Final Form of the Sensitivity Coefficients

At the optimization iteration k in the inverse solution, the sensitivity coefficients evaluated at the current estimate u^k is calculated as illustrated in Fig. 9. In Step 1, the derivatives of furnace operating variable function are calculated. Step 2 involves computing specific components of $\partial T_F/\partial u$ based on both the type of furnace surface element and the type of operating variable. Step 3 clarifies that the initial condition dictates the workpiece surface temperatures at time $t = 0$, thus establishing their independence from u. Step 4 employs a sequential computational procedure with respect to time to calculate derivatives of intermediate variables. Each derivative is computed based on previously calculated terms. Finally, Step 5 calculates $\partial T_D/\partial u$ from $\partial T_S/\partial u$ using Eq. (37) for all time steps.

In this section, the derivatives are denoted as $\partial/\partial u$ for simplicity. However, it's important to note that they actually represent the derivatives with respect to each unknown variable u_n. Therefore, they should be interpreted as $\partial/\partial u_n$.

The time step Δt in this section indicates the level of temporal resolution employed

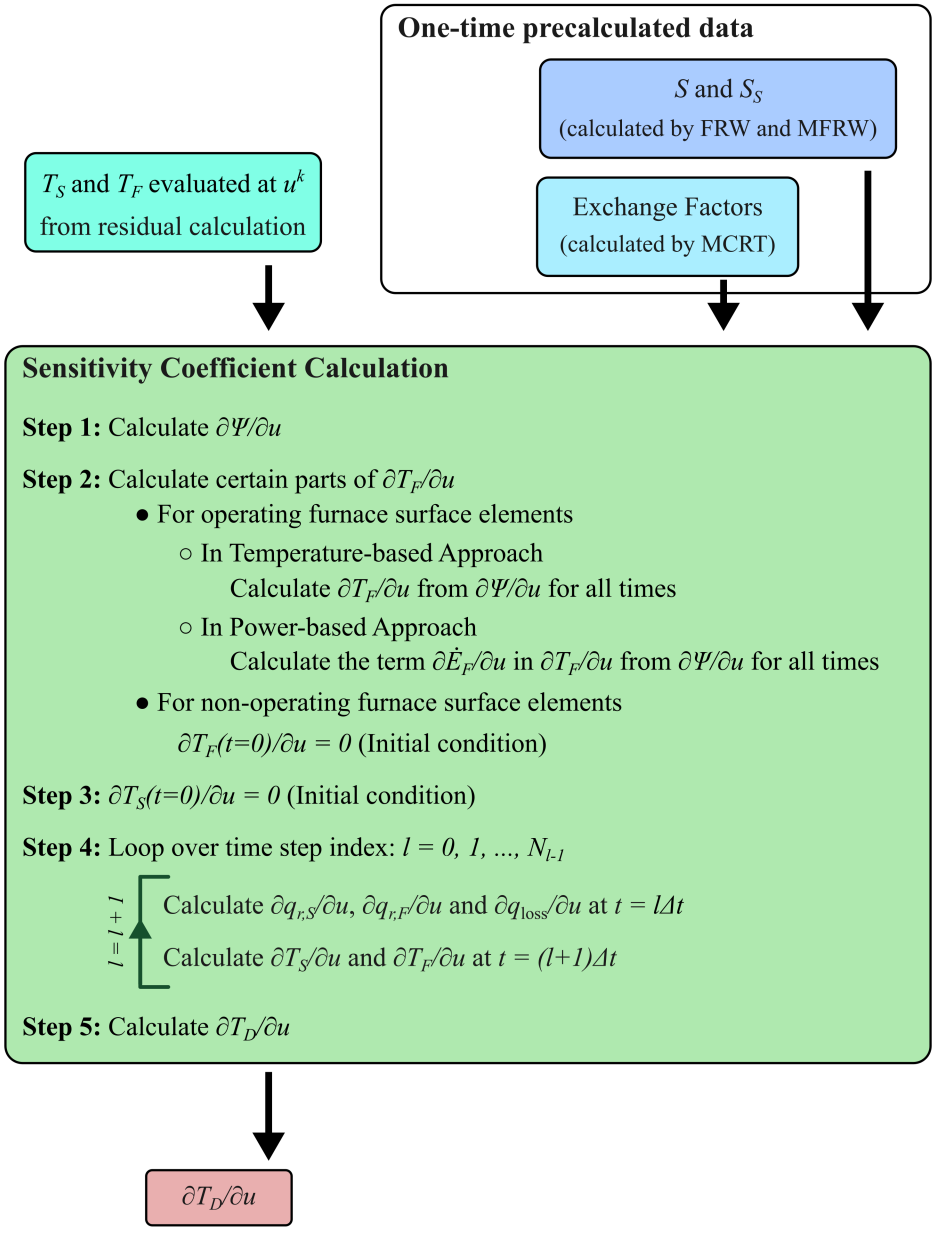


Figure 9: Overview of the sensitivity coefficient calculation procedure

in the calculation of sensitivity coefficients. Our calculation methodology aligns Δt with Δt_{FRW}, which is determined from the FRW simulations explained in Chapter 5. The most accurate sensitivity coefficient calculations are achieved when Δt_{FRW} matches Δt_{FS}. However, to accelerate computations, Δt_{FRW} can be set as a multiple of Δt_{FS}, introducing a form of approximation to the sensitivity coefficients. After calculating the sensitivity coefficients using a time resolution of Δt_{FRW}, extracting the final coefficients at the inverse time resolution of Δt_{INV} can be easily accomplished, ensuring $\Delta t_{\mathrm{FRW}} \leq \Delta t_{\mathrm{INV}}$. The time resolutions utilized for sensitivity coefficient calculation in this thesis are specified in the corresponding results section.

Our approach to calculating sensitivity coefficients involves Monte Carlo-based statistical methods, namely Monte Carlo ray tracing and floating random walk. However, in our implementation, we don't treat the inherent randomness typically associated with these methods as they are executed once, and their resulting data are then utilized. While Monte Carlo ray tracing doesn't introduce errors into the sensitivity coefficients due to consistent use of exchange factors in the forward solution, there exist statistical errors within the particle-boundary interaction arrays S and S_S. These errors can be reduced by employing a large number of particles and are assessed through statistical analysis reported in the relevant result sections.

4.3 Subdomain Optimization with Overlap

In the inverse solution of heat treatment processes using gradient-based optimization methods, we encountered a significant challenge related to computational time demand to calculate sensitivity coefficients when solving the problem with large time domain. Our direct calculation approach for sensitivity coefficients tends to be more computationally intensive for increasing number of time steps in the inverse solution. This is due to increasing summations in the formulas for the design point temperature and the workpiece surface temperature as the time step progresses, as indicated in

Eqs. (48) and (49), respectively.

To address this issue, we employed an approach known as *subdomain optimization*. This method involves dividing the total time domain into smaller, consecutive subdomains, each covering a duration of Δt_{subd}. For each subdomain, an individual inverse solution is computed, and its results are retained. To ensure temporal continuity of the unknown parameters across subdomains, the bound constraints in the minimization problem are set accordingly. The process begins with the initial subdomain and progresses sequentially through to the final one, covering the entire duration of $t_{\max}$. By applying subdomain optimization, we reduce the maximum time considered for inverse solution from $t_{\max}$ to Δt_{subd}. This effectively decreases the computational time cost of our sensitivity coefficient calculation routine.

Subdomain optimization presents a notable challenge: Accurately determining the furnace operating parameter's final time segment within each subdomain can be problematic, due to the delayed response characteristic of conductive heat transfer. The impact of the furnace operating parameter governing the latest time segments in Eq. (10) on the design point temperatures may not fully realized within the duration of a particular subdomain. This issue can lead to a loss of sensitivity information, thereby undesired oscillations in the final solution obtained across the entire time domain.

To mitigate this issue, we extend each subdomain beyond its original time span by a specific duration, denoted by $\Delta t_{\text{overlap}}$. Consequently, while the inverse problem for each subdomain is computed over an extended duration of $\Delta t_{\text{subd}} + \Delta t_{\text{overlap}}$, only the data corresponding to the initial duration of Δt_{subd} are collected. This ensures that the furnace operating parameters determined meet the design condition throughout the extended time span of the system, fully capturing each subdomain, despite inherent delays in conductive heat transfer. The exception to this extension is the final subdomain, which is constrained by the overall maximum time limit of

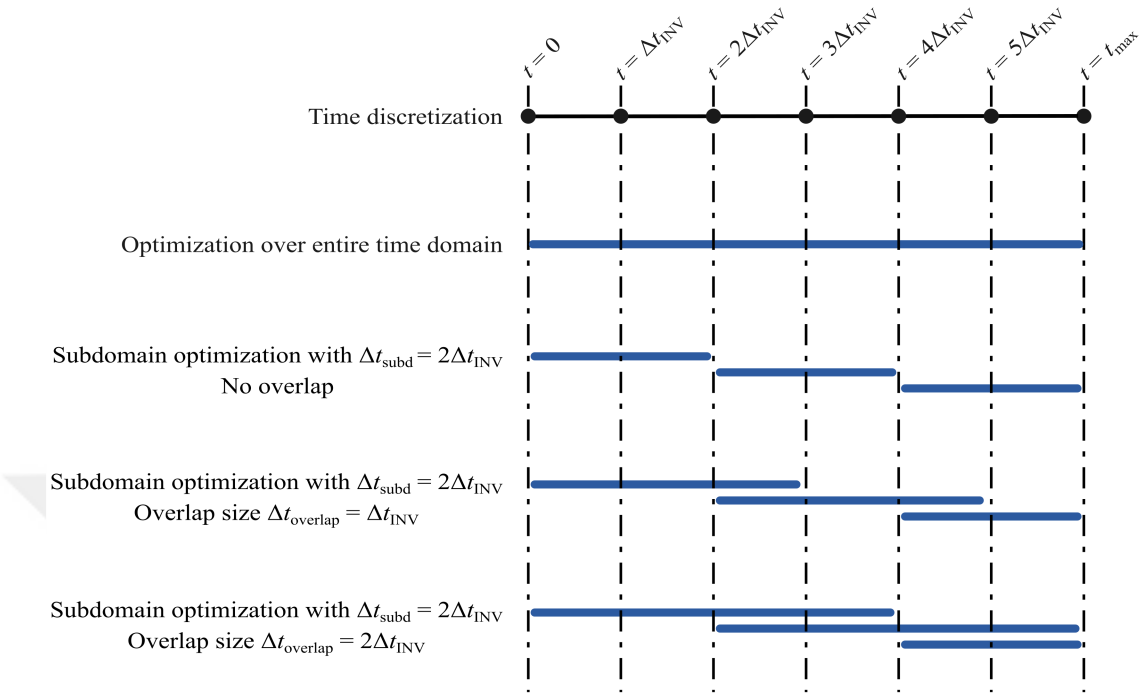


Figure 10: Illustration of optimization over the entire time domain alongside examples of subdomain optimization with varying extents of overlap

the problem. This technique, termed as *overlapping subdomains*, is instrumental in enhancing the accuracy of subdomain optimization by accounting for temporal continuity of the solution between successive subdomains.

To enhance clarity, Fig. 10 illustrates the different approaches to solving an inverse problem discretized into six time steps as $N_{l,\mathrm{INV}} = 6$. The second row depicts a standard solution approach, where the problem is solved across the entire time domain. In contrast, the rows below provide examples of subdomain optimization with $\Delta t_{\mathrm{subd}} = 2\Delta t_{\mathrm{INV}}$, with varying sizes of overlap.

While our exploration does not extend to the accuracy impacts of subdomain optimization, reference [103] suggests an accuracy enhancement in inverse heat conduction problems when using the random walk method.

4.4 Computational Framework Developed for Inverse Solution

The main frame of the inverse solver was developed using the PetSc/TAO library [117], which provided a robust foundation for our nonlinear least square optimization framework. Calculation of the sensitivity coefficients were executed on the GPU using CUDA C++ programming [118]. The following subsections offer a brief overview of these tools.

4.4.1 PetSc/TAO

PetSc, or the Portable, Extensible Toolkit for Scientific Computation, stands as a comprehensive suite for scientific computation, offering a broad array of linear and nonlinear solvers alongside versatile data structures. Complementing PetSc, the Toolkit for Advanced Optimization (TAO) specializes in optimization algorithms that leverage PetSc's robust structures and solvers. At the core of our computational framework for solving inverse problems is PetSc/TAO. This platform handles the optimization process, while integrating essential routines like forward solution evaluation and sensitivity coefficient calculations. Although PetSc/TAO is renowned for its scalability in large-scale problems, in our research, we did not utilize its parallel computing capabilities, as it was not necessary for the scope of our work. The utilization of PetSc/TAO has been pivotal in our research, primarily owing to its robust linear and nonlinear least square solvers. It provides significant control over the solvers and facilitate incorporation of the bound constraints, enhancing the efficacy of our work.

4.4.2 GPU Computing with CUDA C++

The CUDA C++ programming language allows for the direct leveraging of GPU capabilities for scientific computing. Utilizing CUDA C++, we significantly enhanced the performance of sensitivity coefficient calculations by directly controlling GPU resources, enabling rapid computation of a large number of summations and drastically

reducing the computational time of the inverse solution process compared to CPU computing. However, developing fast GPU code presents its own challenges, particularly in terms of memory management and thread organization, which necessitate careful consideration and expertise from the code developer.

4.5 Computational Hardware Specifications

All numerical analyses presented in this thesis were conducted using a personal desktop computer equipped with an Intel Core i5-12400 CPU, 32 GB of RAM, and an NVIDIA RTX 3060 GPU with 12 GB of VRAM. The NVIDIA RTX 3060 GPU significantly accelerated the parallel processing tasks, particularly those executed via CUDA C++ and OptiX ray tracing engine. The memory capacity of 32 GB RAM and 12 GB VRAM was sufficient for the developed methodology when solving the problems discussed in the results chapters.

CHAPTER V

FLOATING RANDOM WALK METHOD

In our approach to sensitivity coefficient calculation, we employ direct differentiation, which necessitates the explicit formulation of all variables involved in the problem. Given that our thermal model includes heat conduction within the internal domain of the workpieces, it is essential to explicitly formulate the temperatures at the workpiece surfaces and at the design points inside the workpieces. To achieve this, we utilized the Floating Random Walk (FRW) method, which allows for the explicit formulation of these temperatures. These formulations can then be differentiated analytically for use in sensitivity coefficient calculations.

The chapter begins by detailing the fundamental principles and mathematical formulations of the FRW method. It then verifies the method through the examination of two distinct heat conduction problems. The FRW method's application in the inverse solution is centered on formulating temperatures at design points and workpiece surface elements, facilitated by the FRW and modified FRW (MFRW) methods, respectively, as elaborated in Sections 5.3 and 5.4. Lastly, the chapter concludes with insightful remarks regarding the method's effectiveness and its potential applications.

5.1 Classical Floating Random Walk Method

The Floating Random Walk method, a Monte Carlo-based statistical approach, has found extensive application in various fields, particularly in solving heat conduction problems. Its primary advantage in thermal analysis lies in its ability to determine temperatures at specific points within a domain without necessitating the computation of the entire temperature field. This feature distinctively positions the FRW method above traditional discretization-based numerical methods, particularly in its

capability to directly assess the impact of boundary conditions on local temperature variations.

This section delves into the classical Floating Random Walk method in computational heat transfer analysis, detailing the mathematical formulations and procedural steps for particle movement, boundary interactions and terminations.

5.1.1 Fundamentals of Particle's Random Walk

Consider a homogeneous solid sphere with radius r_i, centered at the point (x_0, y_0, z_0) in three-dimensional space. The sphere is characterized by constant material properties with a thermal diffusivity denoted by α. Initially, the sphere's temperature is uniformly set at T_0. As a boundary condition, a prescribed temperature $T(r_i, \theta, \phi, t)$ is applied, where θ and ϕ represent the zenith and azimuthal angles, respectively. Following [95, 96], the temperature at the center point at time t_0 is expressed as

$$T(x_0, y_0, z_0, t_0) = \int_{F=0}^{1} \int_{G=0}^{1} \int_{\tau=0}^{t_0} T(r_i, \theta, \phi, t_0 - \tau) dF(\phi) dG(\theta) dH^{(3)}\left(\frac{\alpha\tau}{{r_i}^2}\right) \tag{38}$$

where F and G denote the angular cumulative distributions corresponding to ϕ and θ, respectively. They are defined as follows:

$$\begin{aligned} F(\phi) &= \frac{\phi}{2\pi} \\ G(\theta) &= \frac{1}{2}(1 - \cos\theta) \end{aligned} \tag{39}$$

The function $H^{(3)}$ represents the time cumulative distribution and is formulated as below.

$$H^{(3)}\left(\frac{\alpha\tau}{{r_i}^2}\right) = 1 + 2\sum_{h=1}^{\infty}(-1)^h \exp\left(-h^2\pi^2\left(\frac{\alpha\tau}{{r_i}^2}\right)\right) \tag{40}$$

Monte Carlo-based floating random walk method fundamentally computes the temperature of the center point at time t_0 by statistically evaluating the integrals in Eq. (38). In this process, a large number of particles are released from the center point at time t_0. Each particle takes a step with the length of r_i in a direction defined by angles ϕ_p and θ_p, which are determined according to the distributions F

and G. The time elapsed during this step, denoted by τ_p, is calculated using Eq. (40). Upon completing their step, the particles reach the boundary of the sphere at a time $t_p = t_0 - \tau_p$, implying a backward traversal in time. A particle that reaches the boundary is absorbed, due to the prescribed temperature boundary condition, and it records the boundary temperature at its arrival time, denoted by $T_p(r_i, \theta_p, \phi_p, t_p)$. If a particle reaches the boundary at a time $t_p \leq 0$, it indicates absorption under the initial condition. Assuming all particles reach the boundary within the time domain, the Monte Carlo procedure computes the center point temperature as the arithmetic mean of the recorded temperatures as

$$T(x_0, y_0, z_0, t_0) = \frac{1}{N_p} \sum_{p=1}^{N_p} T_p(r_i, \theta_p, \phi_p, t_p) \tag{41}$$

where N_p is the number of particles released from the center point.

5.1.2 Application in Complex-Shaped Domains

The procedure above is also applicable to problems involving complex-shaped geometries. Consider a three-dimensional complex shaped domain, as shown in Fig. 11. The objective is to determine the temperature at point (x_0, y_0, z_0) at time t_0. In complex-shaped scenarios, particles execute consecutive steps until their path terminates upon absorption.

Focusing on a single particle released from (x_0, y_0, z_0), we track its random walk until absorption. The subscript i denotes the particle step index. At each step, the particle's first task is to determine the shortest distance, r_i, to the boundary from its current position; this distance also serves as the step length.

5.1.3 Updating Particles' Position and Time

The step direction, characterized by angles (θ_i, ϕ_i), and the elapsed time, τ_i, is determined through statistical sampling. The details of how those are statistically sampled is provided in Section 5.1.4. As the particle progresses, both its position and time are

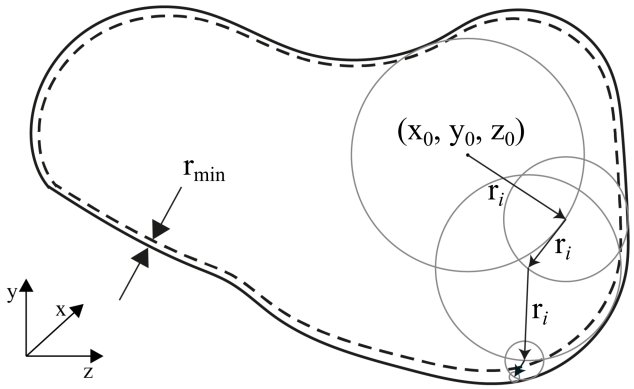


Figure 11: Illustration of a random walk within a complex-shaped domain, showing consecutive steps taken from the initial point (x_0, y_0, z_0) with variable step lengths r_i terminating at the boundary. $r_{\min}$ denotes the boundary strip thickness.

updated. The time is adjusted by $t_{i+1} = t_i - \tau_i$. The new position after each step is calculated using the following equations.

$$\begin{aligned} x_{i+1} &= x_i + r_i \sin\theta_i \cos\phi_i \\ y_{i+1} &= y_i + r_i \sin\theta_i \sin\phi_i \\ z_{i+1} &= z_i + r_i \cos\theta_i \end{aligned} \tag{42}$$

5.1.4 Sampling from Cumulative Distribution Functions

Sampling of the zenith and azimuthal angles from their respective cumulative distribution functions is straightforward: A uniformly distributed random number is substituted into the inverse of the functions in Eq. (39) to determine the values of θ_i and ϕ_i. The elapsed time for each step, τ_i, can be determined either by employing a curve fit based on Eq. (40) or by referencing precalculated data stored within the computer's memory, as described in [119]. For our implementation, we generated a table with 10^5 intervals between 0 and 1, along with the corresponding values for $\alpha\tau/{r_i}^2$. Noted that, even with identical step lengths r_i, the corresponding τ_i values will vary due to their derivation from a cumulative distribution, leading to a *floating* time. Plots of the cumulative distribution functions can be found in [95].

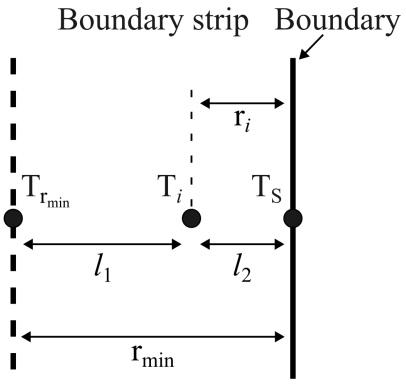


Figure 12: The boundary strip when a particle arrives within. The temperature at particle's position is denoted by T_i.

5.1.5 Implementation in Boundary Strip

The boundary strip is the region immediately adjacent to the domain's boundary and is characterized by a defined thickness, $r_{\min}$, as depicted in Fig. 11. The temperature at the particle's position within the boundary strip is denoted by T_i, as demonstrated in Fig. 12, Upon the particle's arrival within the boundary strip, its next step is governed as follows. The boundary strip temperature $T_{r_{\min}}$, and the boundary temperature T_S, are each expanded in second-order Taylor series around T_i:

$$\begin{aligned} T_{r_{\min}} &= T_i - \frac{\partial T_i}{\partial s} l_1 + \frac{\partial^2 T_i}{\partial s^2} \frac{(-l_1)^2}{2} \\ T_S &= T_i + \frac{\partial T_i}{\partial s} l_2 + \frac{\partial^2 T_i}{\partial s^2} \frac{(l_2)^2}{2} \end{aligned} \tag{43}$$

In the equation above, s represents the outward normal direction of the boundary. After dividing the first equation by l_1 and the second by l_2, and subsequently summing the resultant equations, the following expression is obtained.

$$\frac{\partial^2 T_i}{\partial s^2} = T_{r_{\min}} \left(\frac{2}{r_{\min} l_1} \right) + T_S \left(\frac{2}{r_{\min} l_2} \right) - T_i \left(\frac{2}{l_1 l_2} \right) \tag{44}$$

Note that the distances are $l_1 = r_{\min} - r_i$ and $l_2 = r_i$. Then, substituting the one-dimensional transient heat equation, expressed as $\partial^2 T_i / d\partial s^2 = (1/\alpha)(\partial T_i / \partial t)$, into the above equation, and employing an explicit time discretization scheme with a time

step size τ_i yields:

$$T_i^{t_i} = T_{r_{\min}}^{t_i-\tau_i}\left(\frac{2\alpha\tau_i}{r_{\min}l_1}\right) + T_S^{t_i-\tau_i}\left(\frac{2\alpha\tau_i}{r_{\min}l_2}\right) + T_i^{t_i-\tau_i}\left(1 - \frac{2\alpha\tau_i}{l_1 l_2}\right) \tag{45}$$

By setting $\tau_i = (l_1 l_2)/(2\alpha)$, we obtain the temperature at the particle's position within the boundary strip as:

$$T_i^{t_i} = T_{r_{\min}}^{t_i-\tau_i}\left(\frac{r_i}{r_{\min}}\right) + T_S^{t_i-\tau_i}\left(1 - \frac{r_i}{r_{\min}}\right) \tag{46}$$

The equation above expresses the temperature at the particle's current position within the boundary strip at the current time t_i. The terms in the parentheses are the probabilities of the particle's next step along the edge of the boundary strip or directly to the boundary, respectively. A uniformly distributed random number determines the particle's next step, with a straightforward position update. The time increment, τ_i, as previously determined, remains constant and is not influenced by the random number. Note that τ_i could assume different values, provided that the resulting probabilities remain non-negative. Altering τ_i would modify the probabilities, potentially introducing a nonzero probability of the particle remaining stationary at its current position.

5.1.6 Implementation at Boundary

When a particle arrives at a boundary, it is absorbed or reflected, determined by the type of boundary condition defined. If a prescribed temperature (Dirichlet boundary condition) is set at the boundary, the particle is absorbed, thereby terminating its walk. Then, the boundary temperature T_S at the particle's arrival time, is recorded. If a prescribed heat flux, denoted as q, is defined at the boundary (Neumann boundary condition), the particle is reflected to the edge of the boundary strip, as described by the following equation.

$$T_S^{t_i} = T_{r_{\min}}^{t_i-\tau_i} - q^{t_i-\tau_i}\left(\frac{r_{\min}}{\lambda}\right) \tag{47}$$

The derivation of the equation above follows a similar approach to that in Section 5.1.5, with the additional step of substituting the heat flux expression $q = -\lambda(\partial T/\partial s)$. Upon reflection, the particle records a value of $-q^{t_i-\tau_i}(r_{\min}/\lambda)$ and then continues its random walk within the domain from its updated position. The time update corresponding to this reflection is $\tau_i = r_{\min}^2/2\alpha$. Discussion of other types of boundary conditions, while not covered in this study, can be found in [96, 119].

5.1.7 Particle Termination

A particle is terminated only under one of the following two conditions:

- The particle is absorbed at a boundary, terminating its walk. The boundary temperature at the particle's arrival time is then recorded.
- The particle's total elapsed time exceeds the time domain ($(t_0 - \sum \tau_i) \leq 0$). In this case, the walk is terminated, and the initial temperature is recorded. This represents absorption at time $t \leq 0$, a time at which the temperature is already known.

5.1.8 Overview of the Floating Random Walk Procedure

The floating random walk procedure (FRW simulation) for a single particle is outlined as follows:

1. The particle is released from the specified point and time of interest $(x_0, y_0, z_0, t_{\max})$.
2. It travels the domain step-by-step, following a path determined by cumulative distribution functions.
3. Upon reaching the boundary strip, the particle either moves to the boundary or to the edge of the boundary strip, as dictated by Eq. (46).

4. At the boundary, the particle's interactions are recorded, depending on the boundary condition defined.

5. If the particle is reflected or moved to the boundary strip edge, it continues its random walk, following the procedure in 2.

6. Particles that exceed the total time domain are terminated, with their final interactions noted.

To simulate the temperatures at points of interest, a large number of particles undergo this procedure. Their random walks are traced until termination, with all boundary interactions recorded. The arithmetic mean of these recordings provides the temperatures at the points of interest, similar to Eq. (41). For analytical formulation, rather than direct temperature calculation, the data from the particle's boundary interactions are stored in arrays. This data is then utilized in formulating the temperature expression, a topic further discussed in Section 5.3.

5.2 Verification of Floating Random Walk Solution for Conduction

We present the verification of FRW solution through two test problems that serve to benchmark the method's accuracy against known analytical solutions. Importantly, these problems are forward problems, not inverse problems. We consider two distinct scenarios: a semi-infinite three-dimensional steady-state heat conduction problem and a one-dimensional transient heat conduction case. These verifications not only demonstrate the method's reliability under both temperature and heat flux boundary conditions but also include an analysis of various particle sizes to observe the related standard deviations. Additionally, we assess the computational performance of the method on different hardware platforms.

Table 3: Verification of the floating random walk solution for semi-infinite three-dimensional steady-state heat conduction problem: Comparison of analytical solution ($T_{\text{analytical}}$) with floating random walk solution (T_{FRW}). Standard deviation (SD) is also provided.

Design point index	Position (m)	$T_{\text{analytical}}$ (K)	T_{FRW} (K)	SD (K)
1	(0.5, 0.5, 0.5)	21.31	21.30	0.0374
2	(0.5, 0.5, 0.25)	50.06	50.07	0.0501
3	(0.5, 0.5, 0.125)	72.97	72.97	0.0561
4	(0.5, 0.5, 0.0625)	86.19	86.18	0.0372

5.2.1 Semi-infinite Three-dimensional Steady-state Heat Conduction

A semi-infinite, three-dimensional rectangular solid is considered with the spatial domain defined by 0 m $\leq x \leq$ 1 m, 0 m $\leq y \leq$ 1 m and 0 m $\leq z \leq \infty$. At the surface $z = 0$, a constant temperature of $T(z = 0) = 100$ K is prescribed. The surface at $y = 0$ is insulated, while all other surfaces are maintained at 0 K. The analytical solution for this problem is provided in [120]. In this problem, the temperatures of four design points located within the solid domain are calculated, with their coordinates detailed in Table 3. The boundary strip thickness for FRW simulations is set to $r_{\min} = 10^{-4}$ m.

The analytical and FRW solutions are compared in Table 3, where $N_p = 5 \times 10^7$ particles are used in FRW simulations for each design point. The standard deviations in the table are calculated using 50 independent runs, each containing 10^6 particles. The mean values of these runs are used to calculate T_{FRW}. The FRW solutions are found to closely align with the analytical solutions.

Figure 13 shows the temperature of design point 1 and the corresponding standard deviation for different particle sizes used in FRW simulations. The standard deviations are calculated using 50 independent runs with varying particle sizes, as indicated on the x-axis. As expected, an increase in particle (sample) size leads to a decrease in the standard deviation of the solution, demonstrating a linear decrease in standard deviation on the logarithmic plot.

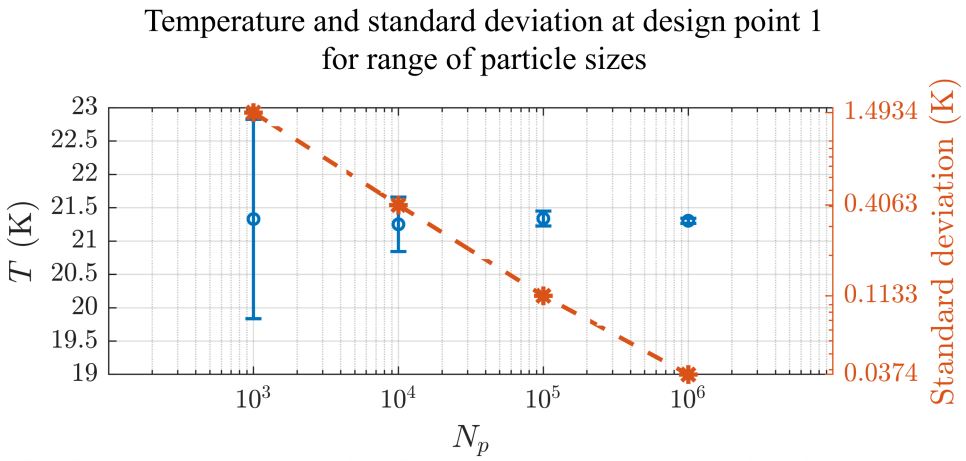


Figure 13: Temperature estimates with associated standard deviations at design point 1 obtained from the FRW solution, depicted for a range of particle sizes (N_p). Each circle represents the mean temperature estimate, and the error bars indicate the standard deviation, demonstrating the impact of particle count on solution precision.

Table 4: Computational time comparison between CPU and GPU implementations for floating random walk simulations in semi-infinite three-dimensional steady-state heat conduction problem

N_p	CPU (s)	GPU (s)	Speed-up Ratio
10^2	0.2545	0.4879	0.52
10^3	3.6149	0.7904	4.57
10^4	35.8081	1.2908	27.74

Table 4 compares the elapsed time during FRW simulations for single-thread CPU computations in C++ and GPU computing using CUDA/C++. For a smaller number of particles (fewer than 10^3), the CPU version of the solver was found to be faster. However, for larger numbers of particles, the GPU-parallelized version significantly outperformed the serial CPU version, achieving speed-up levels of about 27 times with 10^4 particles.

5.2.2 One-dimensional Transient Heat Conduction

One-dimensional transient heat conduction within a solid, characterized by a thermal diffusivity $\alpha = 5.45 \times 10^{-7}$ m^2/s, is examined within the domain of -0.01 m $\leq x \leq 0.01$ m. A constant incoming heat flux is applied at both boundaries, inducing

temperature gradients of 5×10^4 K/m. The time domain 0 s $\leq x \leq$ 10 s is discretized with a time step of $\Delta t = 0.1$ s, and the initial temperature condition is set to $T_0 = 300$ K. The analytical solution for this problem is provided in [121]. Three sensors are placed within the domain: one on the boundary at $x = -0.01$ m, and the others at $x = -0.005$ m and $x = -0.0025$ m. FRW simulations utilize $N_p = 10^6$ particles with a boundary strip thickness of $r_{\min} = 10^{-5}$ m.

Figure 13 presents a comparison between the FRW solutions (T_{FRW}) and the analytical solutions ($T_{\text{analytical}}$) for the design points. The FRW results are in excellent agreement with the analytical results. The right y-axis in the plots shows the relative error percentages between the FRW and analytical solutions, which are maintained below 0.02%.

5.3 Formulation of Design Point Temperature by Classical FRW method

To formulate the temperature at the design points within the workpieces in heat treatment processes, we adopt a prescribed temperature boundary condition at the workpiece boundaries. This approach enables the expression of T_D as a function of the workpiece surface temperature T_S, as $T_D = T_D(T_S)$. Additionally, it is necessary to formulate T_D at each time step of the inverse solution. Importantly, for each design point, conducting a single FRW simulation from the latest time $t_{\max}$ is sufficient. This provides the necessary information to accurately formulate temperatures at times $t \leq t_{\max}$ [96, 119].

The design point temperatures are formulated as follows: Suppose the time domain is divided into $N_{l,\text{FRW}}$ equal time steps, each of size Δt_{FRW}, where the time step index l corresponds to the time $t = l\Delta t_{\text{FRW}}$. During the FRW simulations, data regarding particle absorptions are stored in an array, denoted as S, organized as a three-dimensional array of size $N_d \times N_{l,\text{FRW}} \times N_i$. Each element $S(d, l, i)$ records the number of absorptions at workpiece surface element i within the time interval

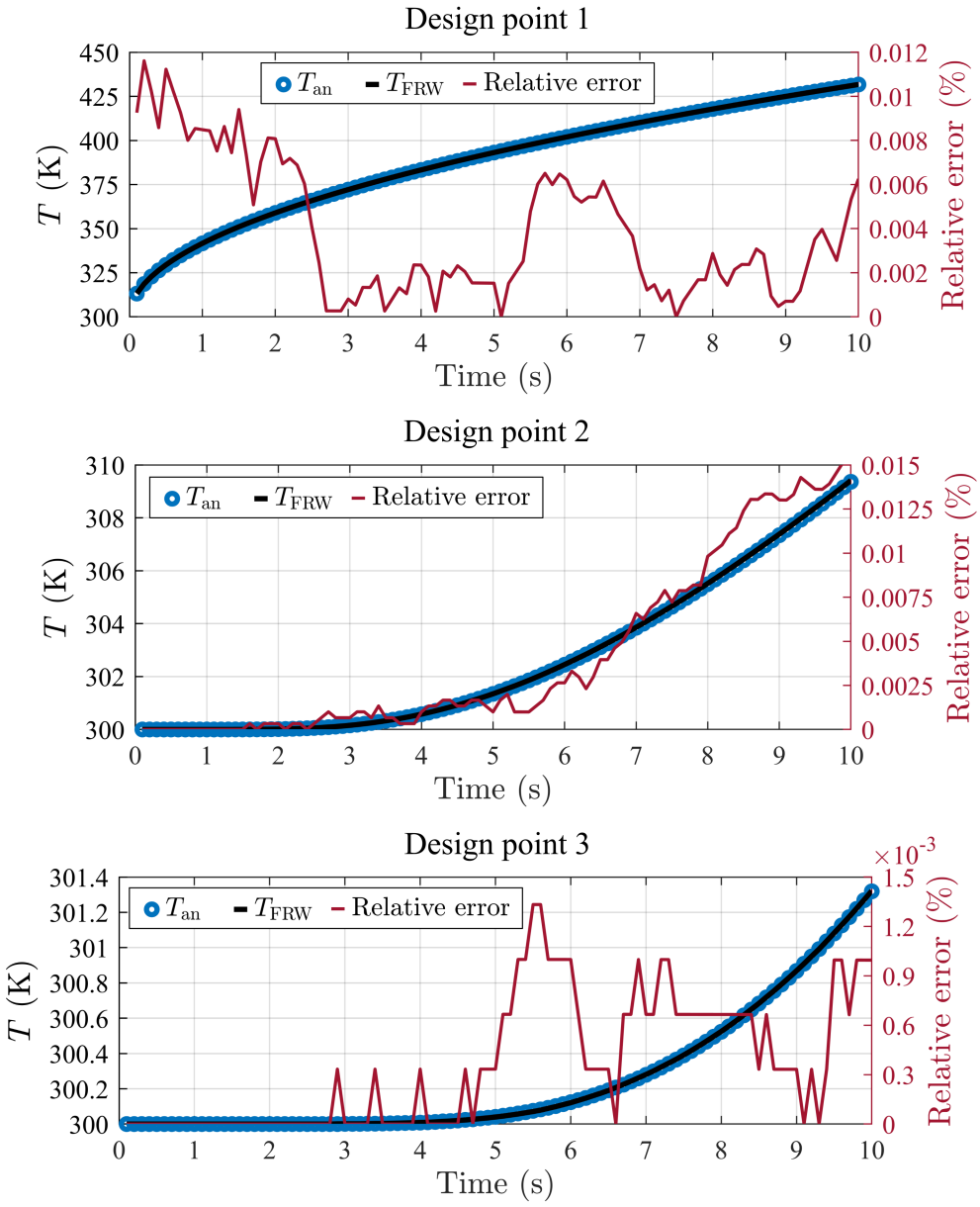


Figure 14: Comparison of design point temperatures from FRW simulations T_{FRW} and analytical solutions T_{an} for one-dimensional transient heat conduction problem. Relative error percentages are demonstrated on the right y-axis.

$(N_{l,\mathrm{FRW}} - l)\Delta t_{\mathrm{FRW}} \leq t < (N_{l,\mathrm{FRW}} - l + 1)\Delta t_{\mathrm{FRW}}$ for particles released from design point d. These elements are normalized by dividing by the total number of particles N_p released from each design point. Assuming a uniform initial temperature field T_0, the temperature at design point d at time step l is determined using the following equation.

$$T_D(l,d) = \sum_{l^*=1}^{l} \sum_{i=1}^{N_i} \Big(T_S(l^*,i) S(d, l-l^*+1, i) \Big) + C(l,d) T_0 \tag{48}$$

In this equation, $C(l,d)$ represents the number of particles that are still traveling within the domain at the end of time step l for particles originating from design point d. In addition to this, the final row of C also accounts for the particles that have exceeded the overall time domain. Note that, in this particular section, N_i stands for the number of surface elements at the boundary of a single workpiece, differentiating it from the usage of N_i for multiple workpieces in other parts of the thesis.

The formulation of T_D in Eq. (48) establishes an explicit relationship linear to the boundary condition T_S. This equation can be analytically differentiated with respect to the unknown variable u using the chain rule and is utilized for calculating the sensitivity coefficient in the inverse solution, as detailed in Section 4.2.6.

5.4 Formulation of Workpiece Surface Temperature by Modified FRW method

In our study, it was necessary to derive an explicit relationship between the workpiece surface temperature and the radiative heat flux applied to its boundary. Recall that the radiation-conduction coupling at the workpiece boundary uses an explicit time scheme, allowing radiative heat flux values to be evaluated for the current time step. By doing so, the radiative heat flux is treated as a generic heat flux boundary condition for the calculations related to sensitivity coefficients.

In our analysis, we encountered significant computational challenges related to

the use of classical Floating Random Walk methods, particularly due to the extensive number of reflections at boundaries, which increased computational costs. This is because the heat flux boundary condition at workpiece surfaces acts as reflective boundaries. To address this issue, we adopted a modified version of the FRW method, inspired by the shrinking boundary method [97]. This modification was essential for efficiently handling boundary condition management and improving the computational efficiency of our simulations.

Various variants of the random walk method have been developed for heat transfer problems, with some notable examples collected in [119]. One such variant is the shrinking boundary method. Initially similar to the classical random walk approach, in this method, once a temperature at a nodal point is calculated, that point transforms into an absorbing barrier. This modification allows subsequent particles to be absorbed more quickly, thus reducing computational costs.

In this study, we draw inspiration from the shrinking boundary method to develop a modified variant of the FRW method. Consider a classical FRW simulation where the boundary conditions are defined by prescribed net radiative heat fluxes q_r. To derive an explicit expression for the workpiece surface temperature, particles are released from the central point of each workpiece surface element. Assuming the temperatures of the workpiece surface elements at times $t \leq (t_{\max} - \Delta t_{\mathrm{FRW}})$ are known, the FRW procedure can be modified accordingly. During the first-time interval $(t_{\max} - \Delta t_{\mathrm{FRW}}) < t < t_{\max}$, particles are reflected due to the prescribed heat flux boundary condition, similar to the classical FRW. After this first-time step, the boundaries are treated as absorbing, given the assumed knowledge of boundary temperatures at subsequent times. Therefore, particles arriving at the boundaries for $t < (t_{\max} - \Delta t_{\mathrm{FRW}})$ are absorbed and terminated. In this case, each element $S_S(i, l, i^*)$ records the number of boundary interactions at workpiece surface element i^* within the time interval $(N_{l,\mathrm{FRW}} - l)\Delta t_{\mathrm{FRW}} \leq t < (N_{l,\mathrm{FRW}} - l + 1)\Delta t_{\mathrm{FRW}}$ for particles released from

surface element i, divided by the particle size. The term *boundary interaction* refers to reflections at the first-time step ($l = 1$) and absorptions at all subsequent time steps ($l > 1$).

With an assumed uniform initial temperature T_0, the temperature of a workpiece surface element i at a time step l can be formulated as follows:

$$\begin{aligned} T_S(l,i) = &\sum_{i^*=1}^{N_i} \left(\frac{-q_r(l,i^*) r_{\min}}{\lambda} S_S(i,1,i^*) \right) \\ &+ \sum_{l^*=1}^{l-1} \sum_{i^*=1}^{N_i} \left(T_S(l^*,i^*) S_S(i,l-l^*+1,i^*) \right) + C_S(l,i) T_0 \end{aligned} \tag{49}$$

In the equation above, $C_S(l,i)$ serves a similar function to $C(l,d)$ in Eq.(48), storing records of particles originating from the workpiece surface element i. The formulation of T_S in Eq. (49) establishes a linear relationship with q_r and T_S itself. This equation can be analytically differentiated with respect to the unknown variable u using the chain rule and is utilized for calculating the sensitivity coefficient in the inverse solution, as detailed in Section 4.2.5.

The Modified Floating Random Walk method strategically transforms reflecting boundaries into absorbing ones at a specific time, significantly reducing computational costs associated with the particles released from workpiece surface elements. This transformation is a key feature of the MFRW approach, as it significantly shortens the particle's lifetime by terminating those reaching the boundaries. This prevents a large number of reflections, which is a computationally expensive routine.

5.5 Remarks on Floating Random Walk Method

The Floating Random Walk method stands out in the field of computational heat transfer for its distinctive approach to temperature determination. Unlike traditional methods, often involving calculations over the entire spacial domain, the FRW method focuses on calculating temperatures at discrete points without including entire solid domain in calculations and a volume mesh. By storing particle records in an array,

the method enables the explicit analytical formulation of design point temperatures. This approach not only streamlines the calculation process but also facilitates the analytical differentiation with respect to prescribed boundary conditions, a critical step in calculation of the sensitivity coefficients in the inverse solution.

Another advantage of the FRW method is the independence of its particles. This characteristic makes the method inherently suitable for parallel computation implementations, allowing simulations to take advantage of modern multi-threaded and distributed computing environments. Such an attribute is pivotal in reducing computational time and improving the efficiency of large-scale simulations.

Several modifications can be made concerning particle behavior within the boundary strip or at the boundary, including variations in time schemes and the selection of τ_i values. We evaluated the impact of using an implicit time scheme and alternative τ_i selections on accuracy. Our findings indicate that these modifications do not yield substantial improvements, affirming the robustness of the methods outlined in this document for the range of problems investigated.

It is important to note that the resolution of time discretization when storing particle records imposes a limit on the accuracy of the formulations. In scenarios where higher precision is required, small time step sizes should be used. In each case presented in this thesis, we conducted a set of analyses that includes the evaluation of time step size in the FRW method, ensuring sufficient accuracy in the calculation of sensitivity coefficients. This comprehensive approach has verified that the chosen time step sizes in the FRW simulations are adequately sized to yield reliable and accurate results for the purposes of our study.

Complex geometries pose a challenge for implementation of the FRW method, as the computational algorithm demands an efficient routine to find the closest domain boundary (where r_i is determined), a function that is invoked numerous times for a single particle. In this study, we restricted our focus to simple quadrilateral workpiece

geometries, where the determination of the closest boundary point is computationally straightforward. Future research could extend the method to more complex geometries, where an efficient boundary-finding algorithm would be essential for maintaining computational feasibility.

The implementation of the FRW and MFRW simulations were executed on the GPU using CUDA C++ programming (Section 4.4.2), ensuring optimal use of the available computational resources. The direct control over GPU resources meant that we could perform random walk simulations with millions of particles calculations rapidly, significantly reducing the computational time and enhancing the overall performance.

CHAPTER VI

DETERMINATION OF STEADY HEATER TEMPERATURES FOR TRANSIENT HEATING OF TWO GLASS PANES

The aim of this chapter is to utilize the developed inverse solution methodology for estimating steady heater temperatures in a radiant furnace, focusing on the transient heating of two glass panes. The problem is characterized by a radiant furnace with completely reflective chamber surfaces, ensuring no heat loss from the chamber, and the heater temperatures are treated as unknown variables to be determined.

The investigations aim to verify the sensitivity coefficient calculations and analyze the impact of design point configurations, such as layout, depth, and plane, on the convergence behavior and determined heater temperatures. By reconstructing an assumed heater temperature profile, we verify the inverse solution methodology. Moreover, we determine the necessary heater temperatures for achieving spatially uniform heating. Additionally, we assess the computational costs associated with the inverse solution and examine the stability of the methodology in the presence of noisy input data. A comparative analysis between steady and transient heater temperature solutions highlights the benefits of transient modeling for furnace operating condition. Furthermore, we investigate the influence of initial guesses and the regularizer weight to ensure practical applicability of the solutions obtained.

6.1 Problem Definition: Heating of Two Glass Panes

The problem under consideration involves the transient heating of two identical glass panes within a radiant furnace, as depicted in Fig. 15(a). The furnace's heating

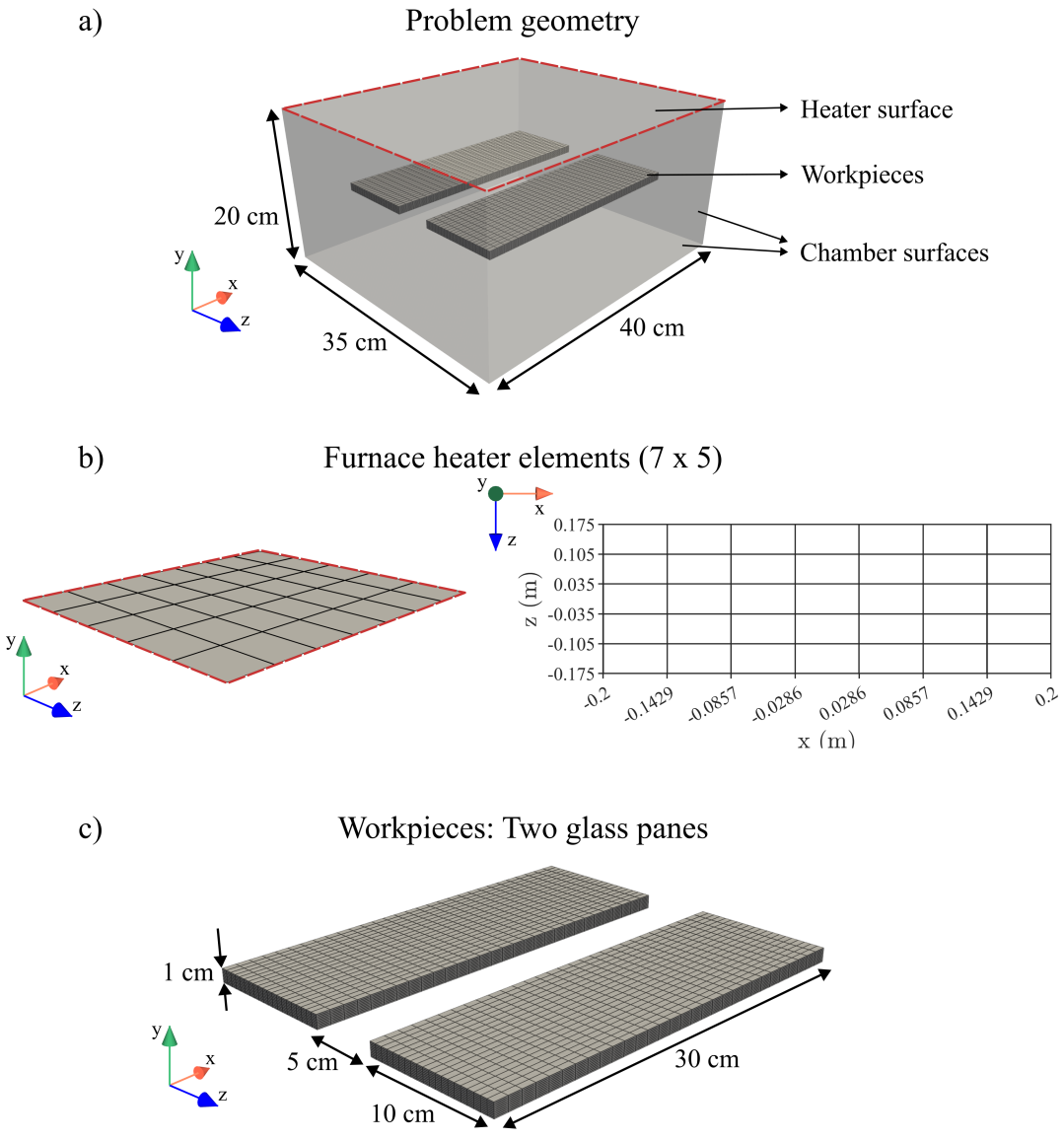


Figure 15: The problem of transient heating of two workpieces (glass panes) inside a radiant furnace. (a) Geometry of the problem. (b) Heater surface elements located at the furnace upper wall. (c) Workpiece geometry.

mechanism includes 35 uniformly distributed graphite heater elements along the upper wall, as shown in Fig. 15(b). Fig. 15(c) shows the two glass panes, positioned centrally within the radiant furnace. The side and bottom walls of the furnace are modeled as chambers with completely reflective surfaces. Consequently, the chamber temperatures do not contribute to the heat treatment of the workpieces.

The initial temperature of the workpieces is uniform and 300 K. The transient heating process is considered up to the maximum time of $t_{\max} = 50$ s.

In this problem, *Temperature-based Approach* is considered with the furnace operating parameter governs the heater temperatures T_H. Throughout most of this chapter, the heater temperatures are assumed as time-independent unless specified otherwise. Consequently, the number of unknowns corresponds to the number of heater elements, set as $N = 35$ in this inverse problem.

Several design points are placed inside the workpieces where the desired heating histories are imposed at. The number of design points and their positioning within the workpieces could have an important influence on the characteristics of the inverse problem. In order to address that, the following three sets of design point configurations about the positioning of the design points are considered:

1. **Transverse cut plane with varying layouts at a fixed depth:** A set of five layout configurations are generated as shown in Fig. 16(a). In this set, the design points are all positioned transversely on $x - z$ plane and located at the depth of 0.5 mm measured from the upper surface of the workpiece. A case with a design points in x-direction and b design points in z-direction is named as $a \times b$. This leads to a total number of design points of $N_d = 2 \times a \times b$ (as two workpieces exist).

2. **Transverse cut planes at varying depths with a fixed layout:** A set of three configurations are chosen to address the impact of design points depth. In this regard, the design points are positioned at a depth of 0.5 mm, 2.5 mm, and

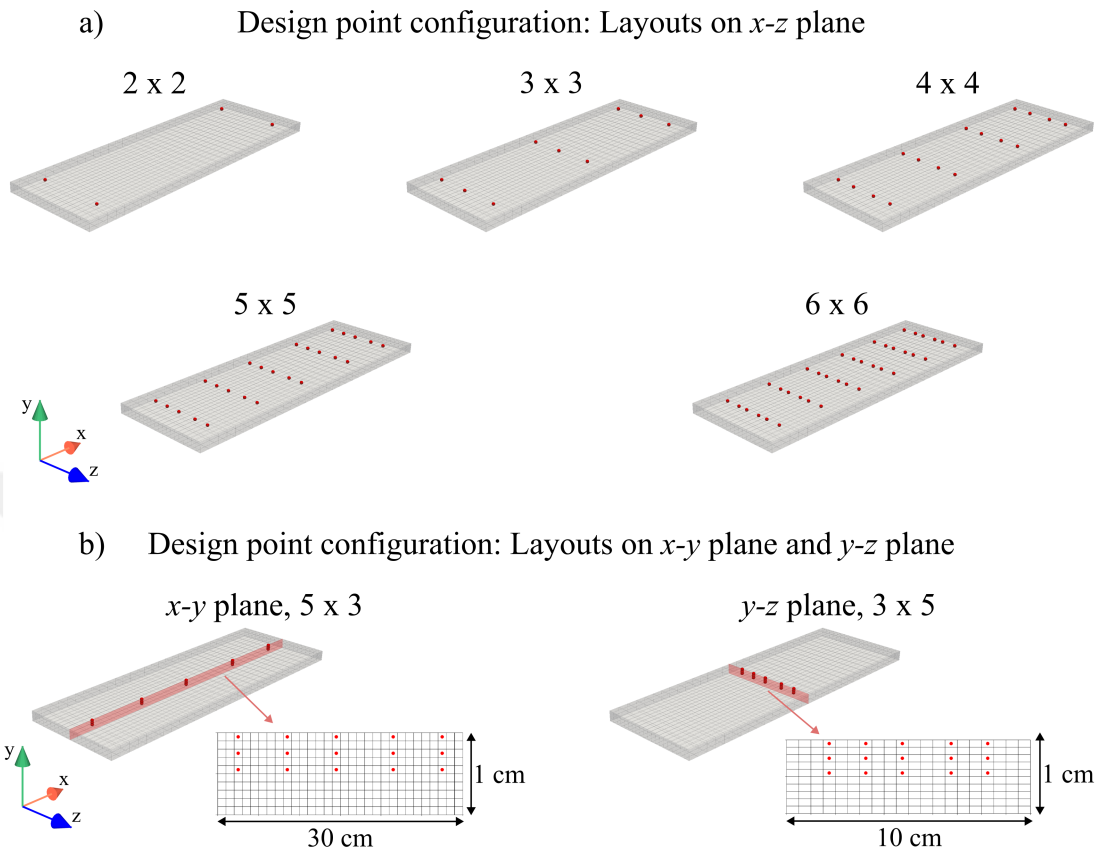


Figure 16: Design point configurations in each workpiece where the design points are marked as red dots. The design points are overlapped with the finite volume cell centers. Grid lines represent finite volume cell edges. (a) Configurations with the design point layouts on $x-z$ plane with depth of 0.5 mm. (b) Configurations with the design point planes $x-y$ and $y-z$.

4.5 mm away from the upper surface of the workpiece. In these configurations, the design points are distributed on $x-z$ plane using a layout of 5×5.

3. **Different cut planes:** A set of three configurations are chosen to address the impact of different planes on the distribution of design points. The first configuration uses a 5x5 layout on the $x-z$ plane, as shown in Fig. 16(a). The remaining two configurations distribute the design points on the $x-y$ and $y-z$ planes, with the latter two illustrated in Fig. 16(b).

6.2 Numerical Settings and Parameters

The unknown steady furnace heater temperatures are determined using the Gauss-Newton algorithm, incorporating the proximal-point regularizer with L2-norm. The regularization weights are carefully chosen to balance stability and convergence, where its impact is studied in Section 6.4.3.4. In accordance with the specific design conditions, the chosen regularization weights are given in their corresponding sections. Since the heater temperature is steady, there is no need for a subdomain optimization approach in this problem. The constraints for the heater temperatures are set with lower and upper bounds of 300 K and 2000 K, respectively.

The exchange factors were calculated using a total of 1.1×10^9 rays released from the workpiece surfaces, which translates to a minimum of 2,500 rays per square millimeter on the workpiece surfaces. In the FRW and MFRW simulations, the number of particles is set to $N_p = 10^9$ and $N_p = 10^6$, respectively, with the boundary strip thickness of $r_{\min} = 10^{-4}$ m. The time domain in the FRW and MFRW simulations is discretized by the time step size of $\Delta t_{\text{FRW}} = 0.5$ s.

6.3 Sensitivity Coefficients

Since the unknown variable is the steady heater temperatures T_H within Temperature-based Approach, the sensitivity coefficients for this problem can be expressed as

$$\nabla r_m(u) = \frac{\partial r_m}{\partial u_n} = \frac{\partial T_D(l,d)}{\partial T_H(n)} \tag{50}$$

where $T_H(n)$ represents the temperature of the nth furnace heater. Due to the modeling of chamber surfaces in this problem, derivatives related to q_{loss} and T_C (as part of $T_F = [T_C, T_H]$) are disregarded.

6.4 Results

The inverse solution seeks to determine the heater temperatures for thirty-five (5 $\times$ 7) independently controlled heaters positioned at the furnace's top wall, aiming

to achieve desired design point temperatures within the workpieces. These desired temperatures are specified at 10-second intervals, setting the time step size for the inverse problem at $\Delta t_{INV} = 10$ s. This configuration results in a total of $N_{l,\mathrm{INV}} = t_{\max}/\Delta t_{INV} = 5$ time steps. Given the configuration of at least eight design points, the system always features more knowns ($M = N_{l,\mathrm{INV}} \times N_d$) than unknowns ($N$ heater temperatures to be determined), $M > N$. Initially, the heater temperatures (the initial guess u^0) are set to a uniform 850 K which are then corrected in the optimization iterations.

The mesh size of the workpieces is chosen as $30 \times 10 \times 20$ (seen in Fig. 15(c)) as a result of the mesh independence study, ensuring that the forward problem's resolution is sufficiently detailed without being computationally excessive.

Solution of the problem is addressed through two test cases, as illustrated in Fig. 17(a):

1. The objective of **Test Case 1** is to reconstruct an assumed heater temperature profile depicted in Fig. 17(b). The inverse solution utilizes desired design point temperature histories as its input, which are calculated from forward solution that apply the assumed heater temperatures. The inverse solution then determines the necessary heater temperatures that would result in the desired design point temperatures. This approach guarantees existence of at least one global minimum within the solution space, yet the presence of multiple local minima is likely, especially when the number of design points is limited. Moreover, it is not guaranteed for a design point configuration that the global minimum is unique.

2. In **Test Case 2**, we impose a specific heating history as a design condition to be ensured across all design points uniformly. The uniform heating profiles, corresponding to different design point depths, are illustrated in Fig. 17(c). These profiles are derived by averaging the design point temperatures obtained

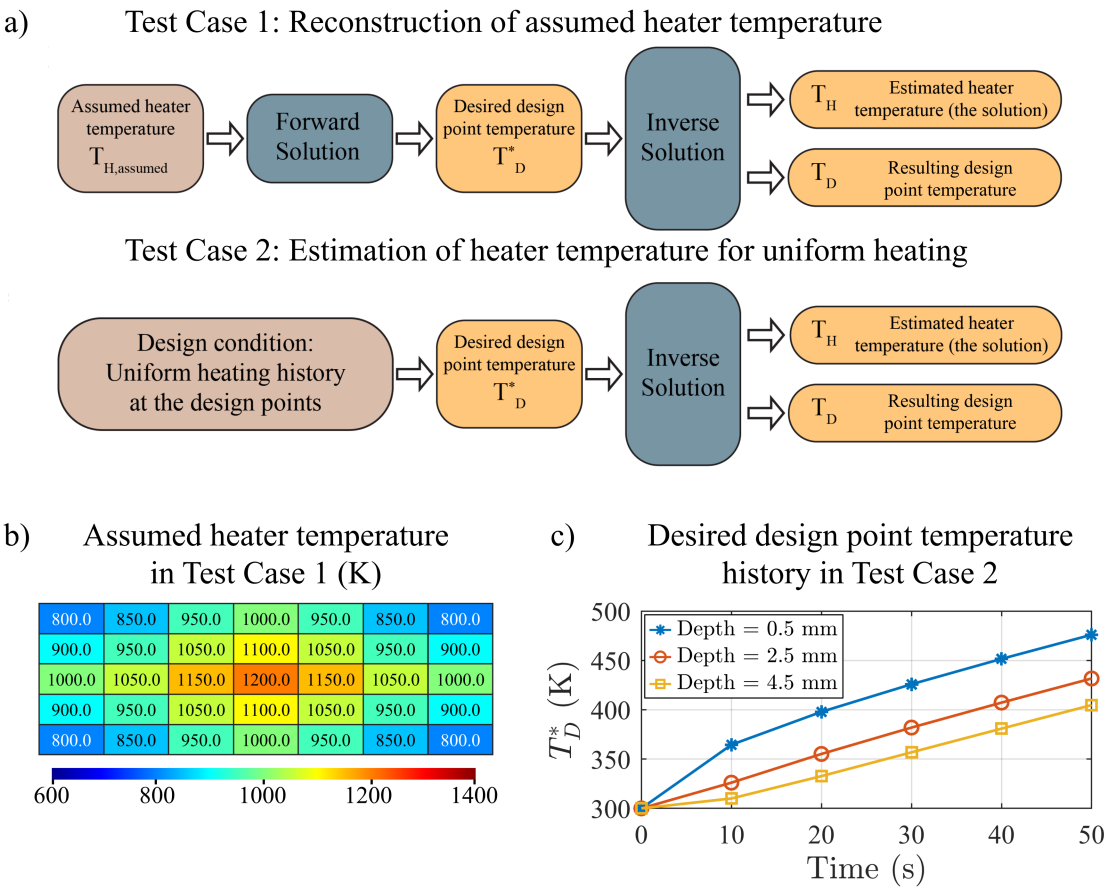


Figure 17: Overview of the two test cases. (a) Flow charts of the two test cases. (b) Assumed heater temperature imposed in Test Case 1. (c) Desired uniform heating history imposed as design condition in Test Case 2 for the specified design point depths.

from forward solutions that use the assumed heater temperature and a 5×5 design point layout with varying depths. The inverse solution then determines the necessary heater temperatures to achieve this uniform heating profile at the design points within the workpieces uniformly. In this scenario, the existence of a global minimum is not assured.

6.4.1 Numerical Analyses

In this section, we have conducted the following key analyses: (i) determining a reasonable time step size for the forward solution; (ii) conducting statistical analyses

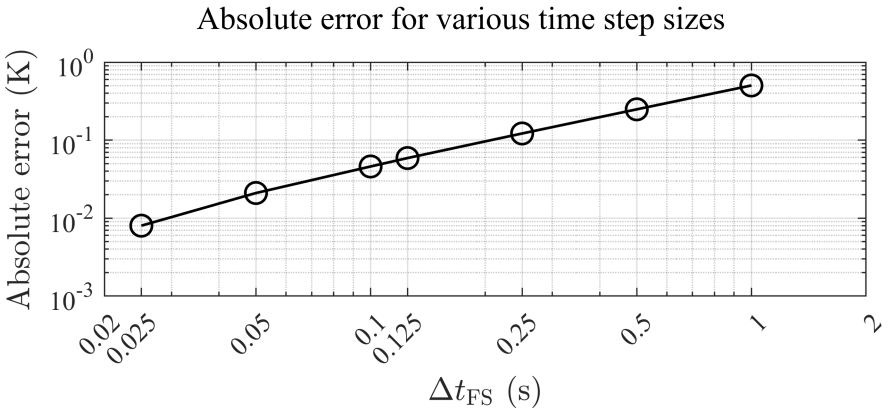


Figure 18: Time step size analysis: Temperature differences at a specific design point at $t = 10$ s for various time step sizes.

to establish a sufficient number of rays for MCRT and particles for FRW simulations; (iii) carrying out a verification analysis for the sensitivity coefficients derived from our methodology. In these analyses, a 5×5 design point configuration was set on the $x - z$ plane at a depth of 0.5 mm, and the assumed heater temperatures depicted in Fig. 17(b) were applied.

6.4.1.1 Time Step Size Analysis

The determination of the time step size in forward solutions is crucial, and was conducted using various values of $\Delta t_{FS} = 1$ s, 0.5 s, 0.25 s, 0.125 s, 0.1 s, 0.05 s, 0.025 s, and 0.01 s. We monitored the design point temperatures at $t = 10$ s, 20 s, 30 s, 40 s, and 50 s. Assuming the smallest time step size, $\Delta t_{FS} = 0.01$ s, yields the most accurate results, we calculated the design point temperature differences between this time step size and the others. Fig. 18 illustrates the temperature differences observed at a specific design point at $t = 10$ seconds, which shows the most significant temperature error.

The findings suggest a clear deduction where smaller time step sizes result in lower errors in design point temperatures. This relationship is depicted in the logarithmic plot, which shows a linear correlation between the magnitude of the time step size and

the corresponding temperature error. Based on our observations, we have selected a time step size of $\Delta t_{\mathrm{FS}} = 0.125$ s for the forward solution, which results in a maximum temperature error at the design points of 0.118 K -a relative error of 0.031%- compared to the finest time step size of 0.01 s.

We now turn our attention to the time step sizes employed in the inverse problem and FRW simulations. The time step size for the inverse problem, Δt_{INV}, is determined by the time resolution of the input data, which includes the desired design point temperatures. For FRW simulations, the time step size Δt_{FRW} should be appropriately chosen within the bounds of Δt_{FS} and Δt_{INV}. The most accurate sensitivity coefficients are achieved when Δt_{FRW} is equivalent to the forward solution time step size Δt_{FS}. In this chapter, the selected time step size of $\Delta t_{FRW} = 0.5$ s ensures a balance between accuracy and computational cost demands.

6.4.1.2 Statistical Analyses

The statistical analyses were conducted to evaluate the reliability of the stochastic methods employed. Using subsets of rays and random walk particles, we have thoroughly examined the variability in design point temperatures and sensitivity coefficients, respectively, to ensure the robustness of our computational approach, as below:

- **Monte Carlo ray tracing:** Statistical analysis has been performed using 100 subsets of the 1.1×10^9 rays. For each subset, a forward problem was solved with the calculated exchange factors to examine the statistical effects on the design point temperatures. At the design point and time of the highest standard deviation was observed, the mean value of the design point temperature was found to be 498.4 K, where the real value should lie between ± 0.38 K ($\pm 0.08\%$) of this value with a probability of 99.7%.

- **Floating Random Walk method:** Statistical analysis with 50 subset have

resulted in a maximum relative standard deviation of 0.4% in the calculated sensitivity coefficients $\partial T_D/\partial T_H$. Furthermore, a relative standard deviation of 0.25% was observed in the calculated sensitivity coefficient corresponding to the maximum standard deviation value.

6.4.1.3 Sensitivity Coefficient Verification

The present methodology for the calculation of sensitivity coefficients is verified by the following analysis. As a reference solution, the sensitivity coefficients are also calculated by finite difference approximation using first order accurate formulation, as shown below.

$$\frac{\partial T_D}{\partial T_H} \approx \frac{T_D(T_H + \Delta T_H) - T_D(T_H)}{\Delta T_H} \tag{51}$$

However, the sensitivity coefficients calculated in this manner are prone to two main sources of errors; (i) the numerical errors in the forward solutions and the (ii) truncation error in the finite difference calculation. Having a very small ΔT_H would bring the truncation error in the finite difference calculation to near zero. On the other hand, a very small ΔT_H would amplify the effect of numerical errors present in the forward problem solutions which would yield to a large overall error in the sensitivity coefficients.

The selected design points and heater elements in this analysis are demonstrated on the geometry in Fig. 19 to provide a clear understanding about the relative values of the sensitivity coefficients. Fig. 20 presents a comprehensive analysis of sensitivity coefficients.

Initially, we computed the sensitivity coefficients with different ΔT_H values, as shown in Fig. 20(a), to identify the most suitable ΔT_H for this problem. The smallest and largest values of ΔT_H exhibit sensitivity coefficients that differ significantly from the majority of ΔT_H values. We observe that the sensitivity coefficients calculated using the present methodology are consistent with those derived from various ΔT_H

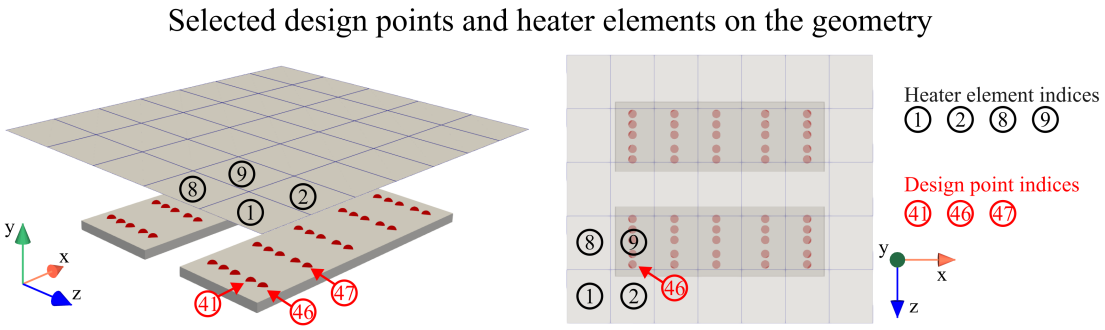


Figure 19: Selected design points and heater elements for sensitivity verification analysis

values, particularly at 10 K, which was chosen as a reference. Additionally, the design points in closest proximity to heater element 1, specifically design points 46 and 41, exhibit the highest sensitivity values, consistent with the anticipated geometrical influences of the problem.

Fig. 20(b) demonstrates the comparison between the reference solution and the present methodology, focusing on the sensitivity coefficients at design point 46 at $t = 50$ s with respect to the temperatures of entire heater elements. The present methodology exhibits a close agreement with the reference values. Furthermore, the influence of the problem's geometrical characteristics is recognizable in the values of the sensitivity coefficients. The highest coefficients are noted for heater elements 9, 2, and 8, which are in proximity to design point 46.

Finally, Fig. 20(c) plots the time evolution of the sensitivity coefficient for design point 46 with respect to the temperature of heater element 9, revealing an increasing impact of heater temperature on design point temperatures as time progresses.

6.4.2 Test Case 1: Reconstruction of Known Solution

Test Case 1 focuses on reconstruction of the assumed heater temperature in Fig. 17(b), based on the precalculated desired design point temperatures from a forward solution. This section will present and discuss the determined heater temperatures and the corresponding average relative errors across iterations defined in Eq. (30).

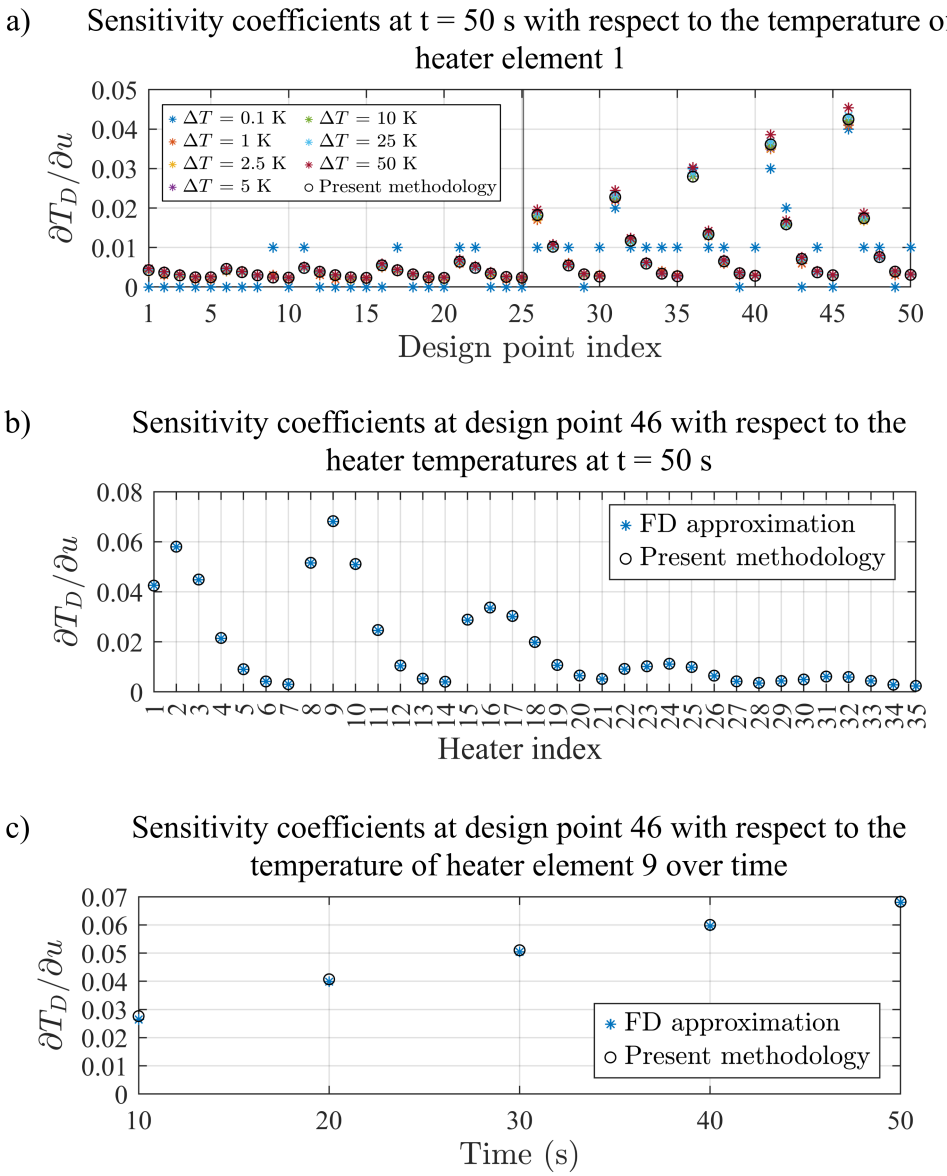


Figure 20: Sensitivity verification analysis. (a) Sensitivity coefficients evaluated for all design points temperatures at $t = 50$ s with respect to the temperature of heater element 1. (b) Sensitivity coefficients evaluated for the temperature of design point 46 at $t = 50$ s with respect to heater temperatures, where unknown index represents heater index. (c) Sensitivity coefficients evaluated for the temperature of design point 46 with respect to the temperature of heater element 9 over time.

Test Case 1 takes into account the influence of several parameters, including the layout of design points, their depth, their plane, and the presence of noise in the temperature data. The regularization weight is set as $\zeta = 10^{-5}$ in this test case, unless otherwise reported.

6.4.2.1 Impact of Design Point Layout

The impact of the design point layout is studied through five configurations: 2 × 2, 3 × 3, 4 × 4, 5 × 5, 6 × 6, as the layouts are illustrated in Fig. 16(a). The findings show that solutions for all layouts converge within seven iterations or fewer, as evidenced by the estimated error histories in Fig. 21(a). Notably, as the number of design points increases, the final estimated error diminishes.

Fig. 21(b) illustrates the heater temperatures determined by the inverse solution for five distinct design point layouts. The results demonstrate that with a higher number of design points distributed within the workpieces, the similarity to the assumed heater temperature profile improves. For example, the 2 × 2 layout's solution exhibits a notable deviation from the assumed profile. Conversely, the layout with 6 × 6 design points closely predicts both the individual heater temperatures and their distribution pattern, yielding the lowest estimated error in the convergence plot.

This trend is expected because configurations with more design points provide more precise sensitivity data towards all heater temperatures. Conversely, configurations with fewer design points may yield a solution that lies in proximity to a local minimum within the solution space, as observed with the 2 × 2 layout. These findings underscore that the layout of design points significantly influences the characteristics of the solution space, with fewer design points leading to varying local minima.

6.4.2.2 Impact of Design Point Depth

We assess how the positioning of design points at different depths influences the convergence behavior and determined heater temperatures. The convergence rates

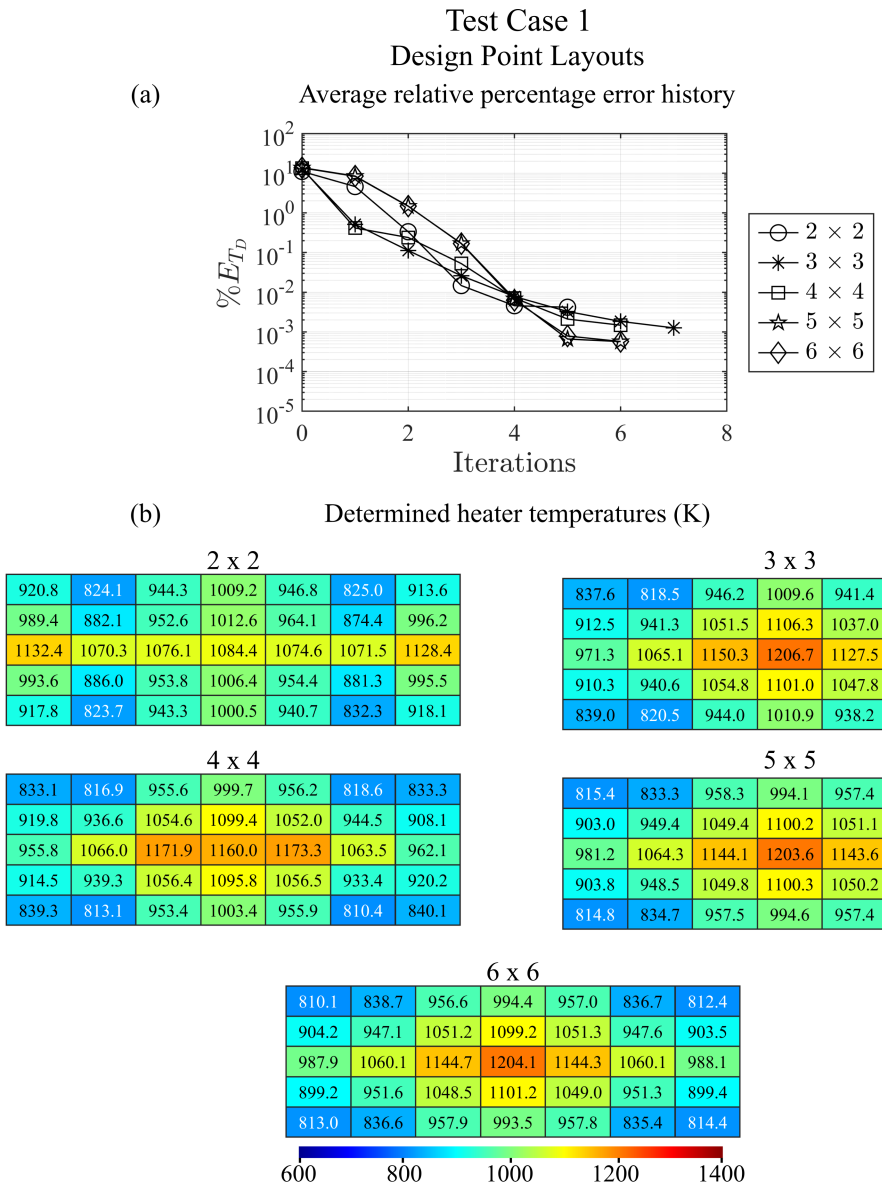


Figure 21: Impact of the design point layout on (a) average relative percentage error history and (b) determined heater temperature in Test Case 1

for the varied depths —0.5 mm, 2.5 mm, and 4.5 mm— show a consistent pattern, as observed in Fig. 22(a_1). The determined heater temperatures in Fig. 22(b_1) exhibit patterns that closely resemble the assumed profile. These findings imply that the depth of design points has a negligible impact on both the methodology's process and the solutions obtained.

6.4.2.3 Impact of Design Point Plane

On the right side of Fig. 22, the impact of design point distribution across the three planes is analyzed. We observe from Fig. 22(a_2) that there are variations in the error histories among the planes, however, this does not clearly indicate a definitive pattern of convergence superiority for any particular plane. On the other hand, the determined heater temperatures in Fig. 22(b_2) show that the $x - z$ plane's distribution most accurately reconstructs the assumed heater temperatures. The findings also show that for design point configurations on the x-y and y-z planes, the heater temperatures that are geometrically close to the design points are predominantly adjusted. This implies that the orientation of design point planes affects the resulting heater temperature patterns, highlighting the geometric impact of design point placement on the determined heater temperatures.

6.4.2.4 Impact of Noise in Desired Design Point Temperature Data

The stability of our methodology is studied by evaluating the influence of noise in the desired design point temperature data, with the noisy data obtained by the following equation.

$$T^*_{D,\text{noisy}} = T^*_D + \mu\Theta \tag{52}$$

In this equation, Θ is normally distributed random variable with a 99.7% probability of falling within the range of -3 K to +3 K. We examined noise factors μ of $0.0, 0.25, 0.5, 1.0$. In these simulations, a 5×5 design point layout is utilized and the

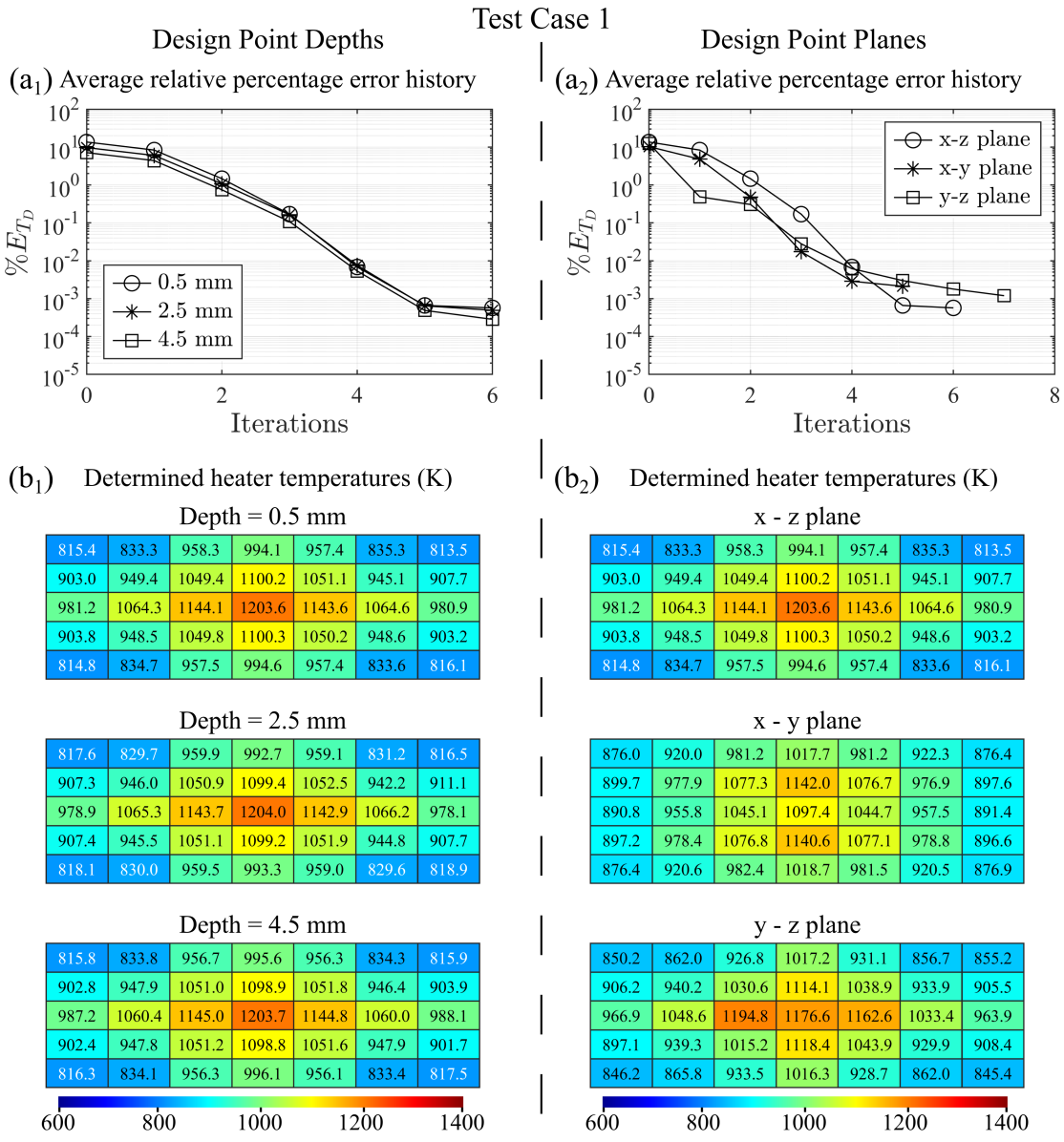


Figure 22: Impact of depth and plane of design points on average relative percentage error history (a_1 and a_2), and determined heater temperature (b_1 and b_2) in Test Case 1

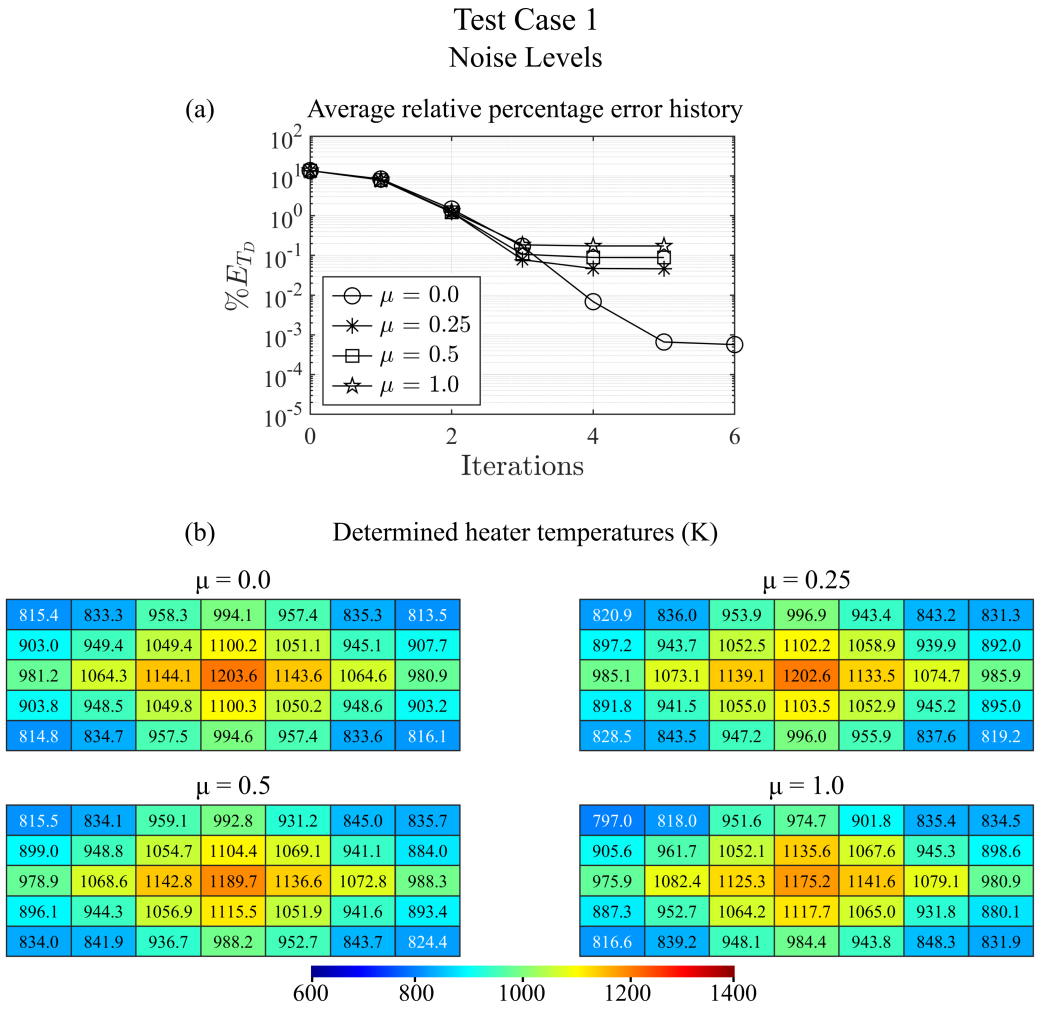


Figure 23: Impact of the noise in design point temperature data on (a) average relative percentage error history and (b) determined heater temperature in Test Case 1

regularizer weight is set to $\zeta = 10^{-3}$. Fig. 23(a) illustrates an increase in average percentage errors with rising noise levels.

Specifically, the final average relative percentage errors were found as 0.00074%, 0.045%, 0.091% and 0.19% for the considered noise factors, respectively. The maximum deviations between the desired and resulting design point temperatures due to the determined heater temperatures were 0.01 K, 0.75 K, 1.53 K, and 3.10 K for each respective noise factor. Despite the escalating errors due to noisy data, Fig. 23(b) confirms that the resulting heater temperature patterns align well with the assumed

heater temperature pattern. Furthermore, the regularizer weight is particularly important in the presence of noisy input data; while lower regularizer weights can reduce final error levels, they often produce heater temperatures with substantial practical issues due to significant temperature nonuniformities. Overall, these observations indicate that the proposed solution methodology demonstrates stability when subjected to noisy input data.

6.4.3 Test Case 2: Determination of Heater Temperature for Uniform Heating

Test Case 2 focuses on achieving a desired heating profile uniformly across all design points, defined by the heating curves depicted in Fig. 17(c). The objective here is to determine the necessary heater temperatures that most effectively fulfill the desired uniform heating. For these solutions, the regularization parameter is set to $\zeta = 10^{-3}$.

6.4.3.1 Impact of Design Point Layout

The results presented in Fig. 24(a) indicate that the design point layout has a slight influence on convergence rates, and the final average errors are notably low, under 0.2%. These errors correspond to temperature variations of 1.33 K and 1.23 K between the desired and resulting design point temperatures for the 2×2 and 6×6 layouts, respectively. The heater temperatures observed for different design point layouts in Fig. 24(b) demonstrate a checkerboard-like pattern, regardless of the layout. While the layouts vary, this pattern persists, with heater temperatures differing across the configurations. Notably, the checkerboard-like pattern suggests that nonuniform heater temperatures are required to achieve the goal of uniform heating at the design points.

In our analysis, the determination of heater temperatures was influenced by several inverse solver parameters, including the regularizer weight and the tolerance value for convergence criteria. It was observed that utilizing lower regularizer weights and

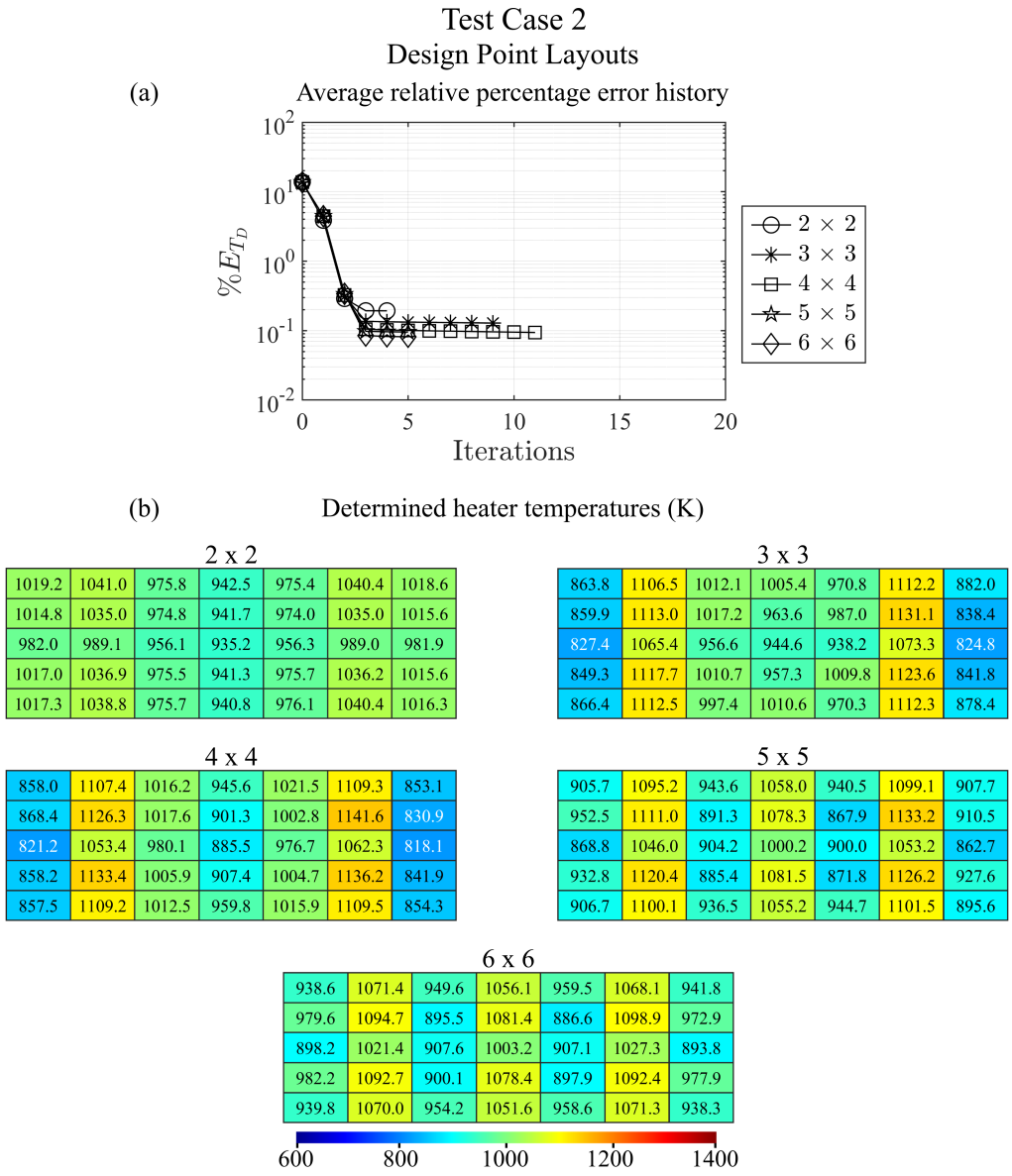


Figure 24: Impact of design point layout on (a) average relative percentage error history and (b) determined heater temperature in Test Case 2

tighter tolerance values could lead to solutions with lower final error levels. However, this approach resulted in highly nonuniform heater temperatures, with variations spanning up to 600 K. Such extreme temperature disparities are likely impractical for real-world applications. Therefore, we strategically selected solver parameters that strike a balance between minimizing final error levels and maintaining a reasonable level of heater temperature uniformity. For instance, in the 2×2 layout configuration, we set the regularizer weight at $\zeta = 5 \times 10^{-3}$, a decision guided by this balance-seeking approach. This balance-seeking strategy could also be managed by choosing a larger stopping condition for convergence criteria. Consequently, when aiming for uniform heating at design points, it is crucial to remain mindful of the practical applicability of the solutions obtained while setting the solution parameters.

6.4.3.2 Impact of Design Point Depth

The desired uniform heating profiles corresponding to various design point depths in Test Case 2 are illustrated in Fig. 17(c). An analysis of these design point depths, as presented in Fig. 25(a), reveals that the convergence behavior is relatively consistent across various depths.

Examining the heater temperature distributions in Fig. 25(b) reveals that varying depths have resulted in subtle differences in the heater temperature patterns. Indeed, achieving uniform heating at varying depths naturally alters the inverse problem significantly, leading to expected variations in the determined heater temperature patterns. As the design point depth increases, the sensitivity information of design point temperatures with respect to heater temperatures blends due to geometrical impact, leading to more uniform heater temperatures. These findings reinforce the idea that design points depth is not a major influencing factor on both the convergence behavior, but can alter the determined heater temperature pattern in Test Case 2.

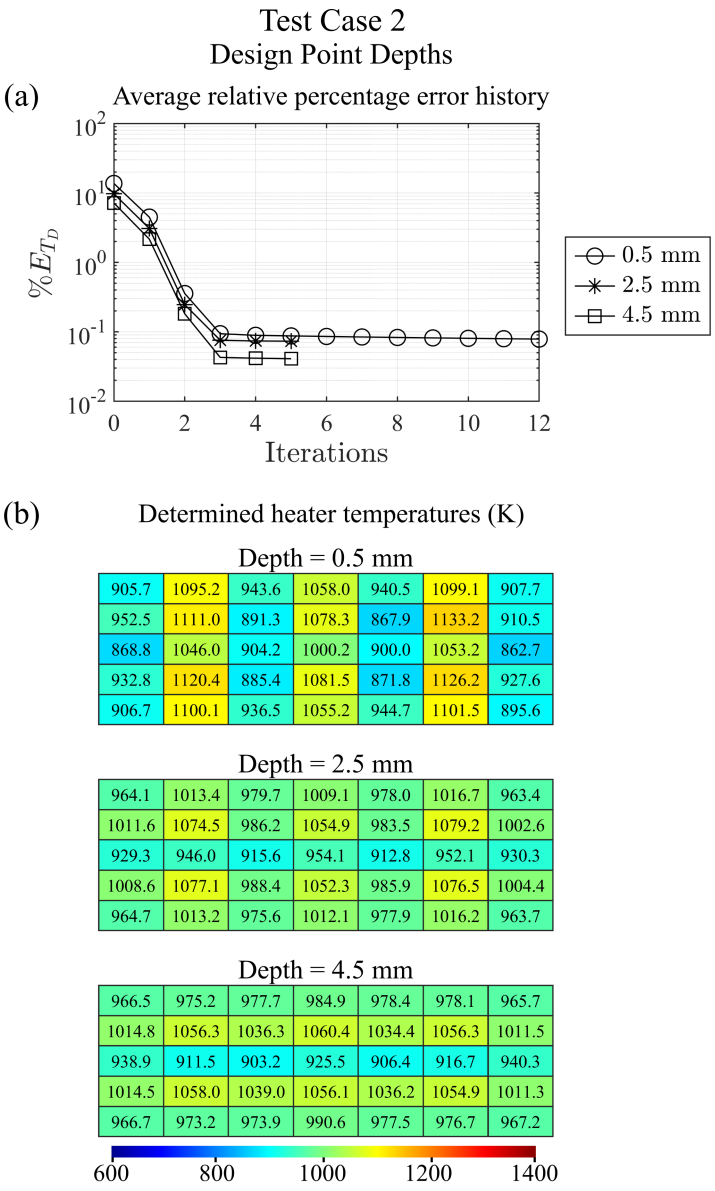


Figure 25: Impact of design point depth on (a) average relative percentage error history and (b) determined heater temperature in Test Case 2

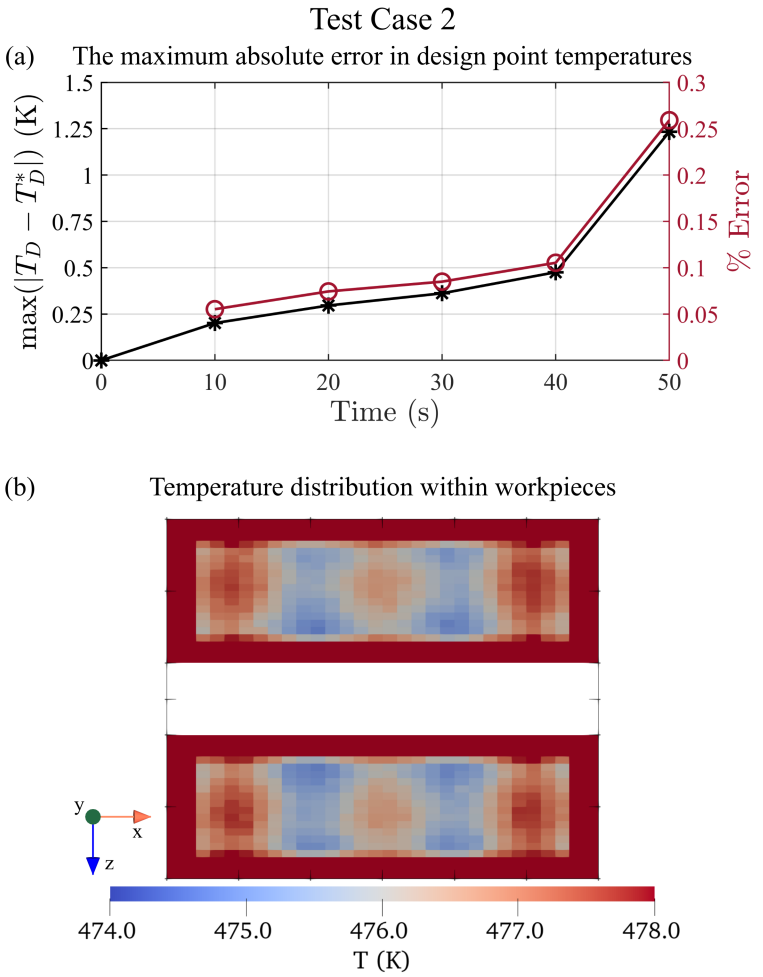


Figure 26: Heating uniformity at the design points and within workpieces: (a) Maximum absolute and relative error in design point temperatures over time. (b) Temperature distribution across the two workpieces at the 50-second mark, shown at the cross-section y = 4.5 mm where design points are situated. The color code reflects a ±2 K range around the desired design point temperature.

6.4.3.3 Heating Uniformity

To investigated the heating uniformity at the design points over time and within whole workpieces domain, we focused on the design point layout 6 × 6 on the $x - z$ plane with a depth of 0.5 mm. Fig. 26(a) shows the maximum absolute errors across all design points over time, demonstrating that the uniform heating condition is achieved within a ±1.23 K tolerance. The peak discrepancy is observed at time 50 s, corresponding to a relative error of 0.26%.

Fig. 26(b) provides an insight into the temperature distribution within the workpieces, where the color code has been calibrated to highlight minor temperature nonuniformities of ±2 K. This visualization emphasizes a central region where the temperature variance is minimal, consistently maintaining a range within ±2 K. However, greater temperature deviations are detected at the edges and corners, as expected, owing to geometric effects during heating of low thermal diffusive material. Overall, the results indicate that the central zones of the workpieces meet the uniform heating condition effectively.

To assess the potential improvement in heating uniformity at the design points, we evaluated several configurations with varying numbers of furnace heater elements. Building upon the original setup shown in Fig. 15(b), this investigation included expanded layouts with 9 × 7 and 11 × 9 heater element configurations. Despite these variations, our numerical experiments did not demonstrate any significant enhancement in heating uniformity. This outcome likely indicates that, given steady operating parameters of the furnace heaters, achieving transient uniform heating in the workpieces reaches a threshold beyond which further uniformity is unattainable. Essentially, this implies that the existence of a global minimum solution to the nonlinear least squares problem is highly improbable in these conditions.

6.4.3.4 Regularizer Weight Analysis

To investigate the impact of the regularizer weight ζ on the performance of the inverse solution, numerical experiments were carried out in Test Case 2 using a range of ζ values: 10^0, 10^{-1}, 10^{-2}, 10^{-3}, $5{\times}10^{-4}$, 10^{-4}, 10^{-5}, and 0. Recalling that, the proximal-point regularizer with L2-norm employed here encourages successive estimates during the inverse iteration to remain close, proportionate to the specified weight. In this analysis, the design point configuration was established with a 5 × 5 layout on the $x-z$ plane at a depth of 0.5 mm. The resulting heater temperatures and the average

relative estimated errors based on the design point temperatures across iterations are shown in Fig. 27.

Our findings are summarized as follows:

- *High values (e.g.,* 10^0*,* 10^{-1}*)*: These strong regularization weights slow the error decline, suggesting that excessive regularization can inhibit convergence and reduce result accuracy.

- *Decreasing the value of* ζ: Lowering ζ enhances the convergence rate and decreases the final error levels. Moreover, a smaller ζ tends to reduce computational time due to reduced number of iteration, improving algorithm efficiency.

- *Low values*: Lower ζ values lead to reduced estimated error levels, achieving smaller discrepancies between the resulting design point temperatures and the desired values. However, reducing the ζ value below 10^{-4} leads to highly nonuniform heater temperature patterns, leading to impractical solutions for engineering applications. $\zeta = 0$ resulted in both higher errors and nonuniform heater temperatures.

The optimal value of ζ depends on the specific problem at hand as well as on various design decisions and constraints. In developing a robust framework for inverse problems, striking a balance between stability, accuracy and practicality is critical in the regularization settings. Our choice of moderate ζ values, for 10^{-5} Test Case 1 and for 10^{-3} Test Case 2, demonstrates our commitment to achieving stable and practical solutions across various scenarios. The choice of a lower ζ value for Test Case 1 is informed by the fact that it has an exact solution in the form of the assumed heater temperature, making the problem inherently less challenging and thus manageable with a reduced level of regularization.

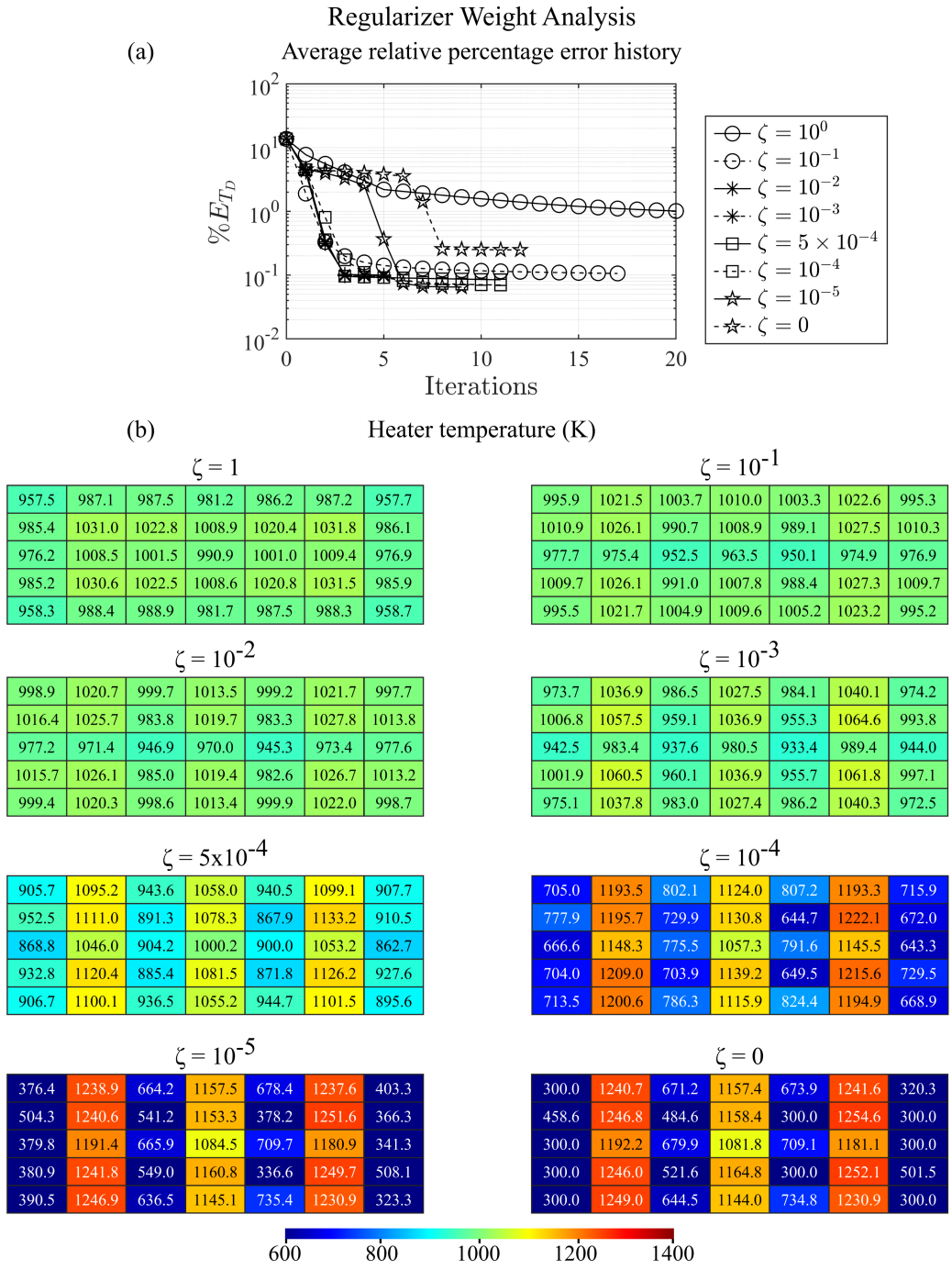


Figure 27: Regularizer weight analysis: Impact of various regularizer weights on (a) average relative percentage error history and (b) determined heater temperature in Test Case 2.

6.4.3.5 Initial Guess Analysis

In exploring the influence of initial guesses on the inverse solution, our study in Test Case 2 involved a series of numerical experiments with five distinct initial guesses, at 700 K, 800 K, 850 K, 900 K and 1000 K. For this analysis, a 3 $\times$ 3 layout was configured on the $x - z$ plane with a depth of 0.5 mm for the design points. As depicted in Fig. 28(a), these different initial guesses led to varying initial average relative error values.

Despite these initial differences, we observed that the final error levels across all scenarios converged to a consistent level, indicating the robustness of the solution methodology. Analyzing Fig. 28(b), it's evident that the variation in initial guesses did not substantially alter the resulting heater temperature profiles. This observation implies that while the initial guess may not directly affect the final temperature values, it influences the trajectory taken within the solution space during the optimization iterations. Despite different starting points, the algorithm consistently converges to similar temperature patterns, although not identical in exact values.

This analysis was also conducted using both 2 $\times$ 2 and 5 $\times$ 5 design point layouts in addition to the original 3 $\times$ 3 configuration. In the case of the 2 $\times$ 2 layout, there was a noticeable difference in the determined heater temperatures when compared to the original configuration. However, when the analysis was performed with the 5 $\times$ 5 layout, there was no notable distinction in the heater temperatures. These findings underscores the importance of design point configuration in the inverse problem. The positioning and quantity of design points play a crucial role in how initial guesses shape the eventual heater temperature patterns, suggesting that an increased number of design points and their strategic placement can alleviate the variability introduced by different initial guesses. Additionally, we conducted tests with a reduced convergence tolerance value of $\varepsilon = 10^{-5}$ (originally, it is $\varepsilon = 10^{-3}$) with the 5 $\times$ 5 layout. These tests revealed a consistent behavior akin to what was observed with

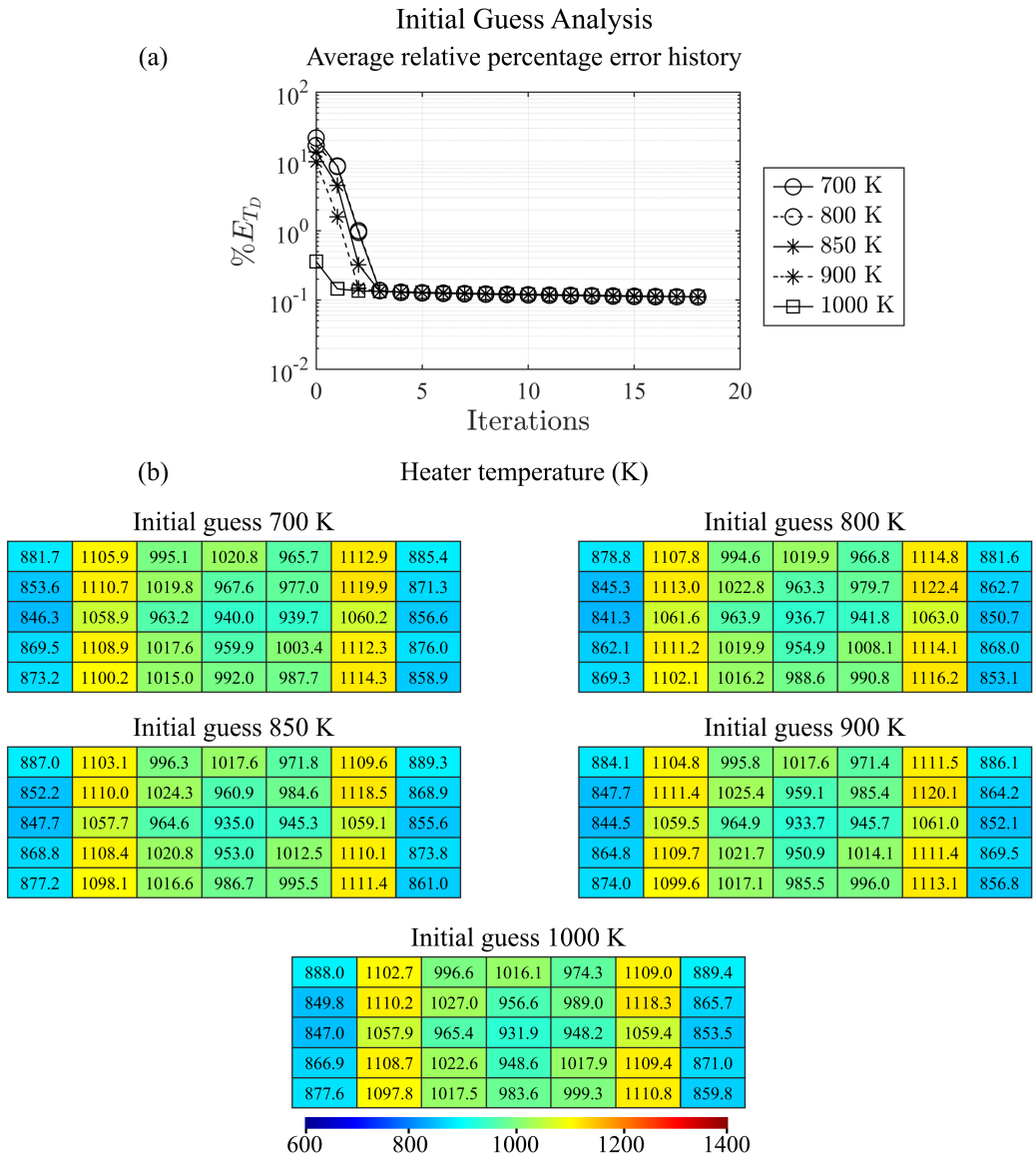


Figure 28: Initial guess analysis: Impact of various initial guesses on (a) average relative percentage error history and (b) determined heater temperature in Test Case 2.

the original tolerance value.

6.4.4 Comparison Between Steady and Transient Heater Temperature Solutions

In our investigation, we conducted a comparative analysis between steady and transient heater temperature solutions to ascertain their impact on heating uniformity. For the transient heater temperature model, we considered a time segments of 25 seconds with linear transitions between these time steps, as described in Eq. (10). Our findings presented in Fig. 29 indicate that employing transient heater temperature modeling significantly improves the resulting uniformity at the design points.

As illustrated in Fig. 29(a), the final value of the average estimated error was noticeably lower for the transient heater temperature solution than for the steady one. Fig. 29(b) further reveals that the maximum absolute error in design point temperatures was also reduced with the application of transient heater temperature modeling. Specifically, we observed a decrease in the maximum absolute error from 1.23 K in the steady model to 0.43 K in the transient model, with the relative error remaining below 0.1%. This marked reduction in errors highlights the enhanced heating uniformity achieved through temporal management of heater temperatures. In addition, Fig. 29(c) presents the temperature patterns at selected times, illustrating the shifts in heater temperatures that contribute to achieving the desired uniform heating at the design points. These patterns reflect the algorithm's response to the temporal aspects of the desired heating process.

This comparison reveals that the transient modeling of heater temperatures allows for a finer optimization, facilitating a more responsive system that can adapt to the transient demands of the heating process.

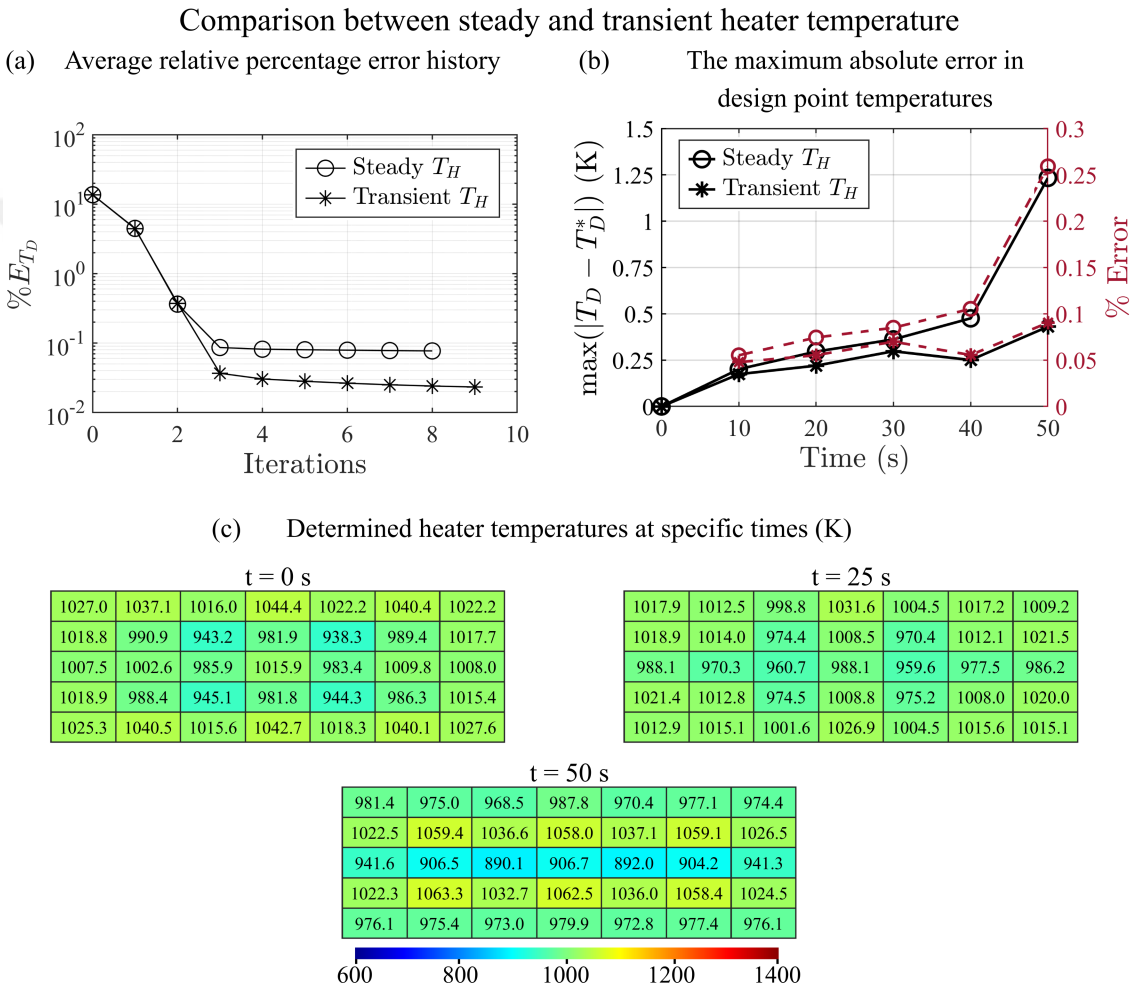


Figure 29: Comparative analysis of steady vs. transient heater temperature solutions. (a) Average relative percentage error histories. (b) Maximum absolute error in design point temperatures over time. (c) Heater temperatures at specific times in the transient model.

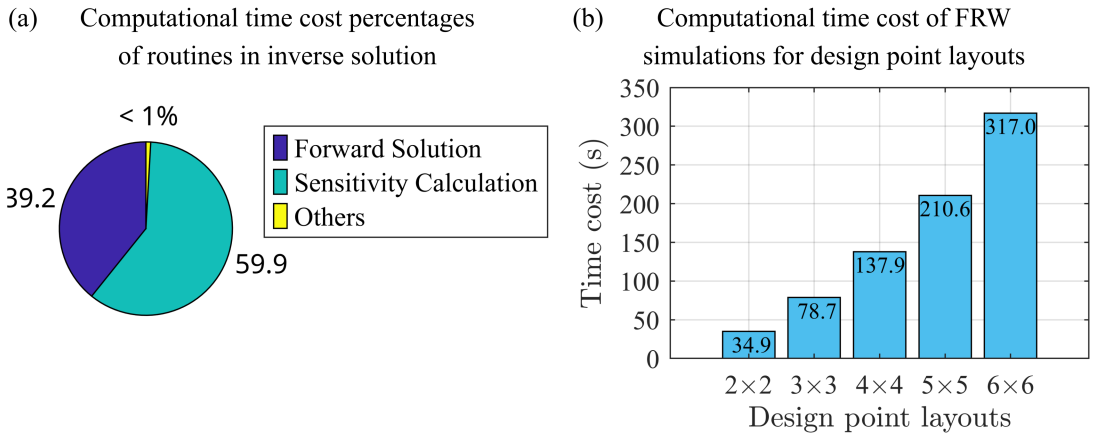


Figure 30: Computational time cost of (a) routines in inverse solution, (b) FRW simulations for design point layouts

6.4.5 Computational Time Costs

The inverse solutions in Test Case 1 demonstrated a total computation time cost varied between 2 to 3 minutes across different scenarios. Notably, 59.9% of this time was allocated to calculating sensitivity coefficients, while 39.2% was utilized for forward solutions during optimization iterations, as shown in Fig. 30(a). The "Others" category in the figure represents the time spent on other routines involved in the optimization process, such as solving the search direction equation. This time cost pattern was similarly observed in the solutions for Test Case 2.

The FRW simulations, executed prior to the inverse solution, exhibit varied computational times based on different design point layouts, as shown in Fig. 30(b). The computational time exhibits a linear relationship with the number of design points. As these computations are executed individually for each design point, an increase in their quantity leads to a proportional rise in computational time. For instance, the computational time rises from 34.9 s to 317.0 s (a 9.1x factor), when the design point count ascends from 4 to 36 (a 9x factor).

When analyzing the computational time of FRW simulations for design point depths with a 5×5 layout, it increases from 210.6 seconds to 257.8 and 258.7 seconds

as the depth of the design points shifts from the 0.5 mm to 2.5 mm and 4.5 mm, respectively. This suggests that deeper design points require more computation time, but there's a threshold beyond which the impact on time is minimal. FRW simulations associated with design points on both $x-y$ and $x-z$ planes required a similar computation time of 145.1 seconds. The computational time for MFRW simulations, which encompassed 2200 surface elements per workpiece, was 78.4 seconds.

The exchange factor calculation required only 4.7 seconds of GPU time, despite using a large number of rays, totaling 1.1 billion.

In the context of computational time costs for forward solutions and sensitivity coefficient calculations, various parameters significantly influence the overall time required for these processes.

- **Forward solutions:** The time cost for forward solutions is predominantly affected by the time step size, the mesh size of the finite volume discretization for the workpiece, and the size of the furnace surface elements. Additionally, the number of rays used in Monte Carlo ray tracing impacts the computation time but only up to a certain threshold, beyond which all surfaces are taken into account (no sparse exchange factors). On the other hand, the design point configuration does not significantly impact the time cost of forward solutions, as these solutions address the entire temperature field, independent of the specific design point setup.

- **Sensitivity coefficient calculations:** The computation time for sensitivity coefficient calculations is influenced by various factors, including the number of unknown variables in the inverse problem, the time step sizes in FRW and MFRW simulations, the size of the finite volume mesh for the workpiece, and the size of furnace surface elements. Additionally, the particle size in FRW and MFRW simulations significantly affects the computational time cost, as more particles involve more workpiece surface elements in the computations,

up to a threshold that encompasses all surfaces. This increase in particle count consequently reduces the sparsity of the particle-boundary interaction arrays produced from these simulations. The ray count in MCRT also plays a role, similar to its impact on forward solutions. Notably, the design point configuration does not considerably affect the time demand for sensitivity coefficient calculations. This is primarily because the most computationally intensive part of this process is the calculation of derivatives at workpiece surface elements, rather than the derivatives related to design point temperatures. However, this holds true as long as the number of design points does not approach the scale of the number of workpiece surface elements, which could otherwise alter the computational time demands.

6.5 Concluding Remarks

In this chapter, we have delved into the inverse solution methodology for determining steady heater temperatures in a radiant furnace, focusing on the transient heating of two glass panes. Through a series of numerical analyses and test cases, we have explored the impact of various design point configurations and other parameters on the convergence behavior and determined heater temperatures.

The key outcomes from this chapter can be summarized as follows:

- **Verification of Methodology:** The developed inverse solution methodology and the proposed sensitivity coefficient calculation approach were verified through reconstructing an assumed heater temperature profile, demonstrating the reliability and accuracy of our approach.

- **Impact of Design Point Configuration:** Placing design points along the $x - z$ plane with a sufficiently large number of design points is essential for optimizing the entire heater temperature profile. An increased number of design points enhances the accuracy of the inverse solution by providing more precise

sensitivity information.

- **Effect of Design Point Depth and Plane:** The depth of the design points has a minimal impact on the convergence behavior but can alter the heater temperature patterns. Design points distributed on the $x - y$ and $y - z$ planes lead to the adjustment of heater temperatures that are geometrically close to the design points, highlighting the geometric impact of design point placement.

- **Stability in the Presence of Noisy Data:** Our methodology demonstrated robustness and stability even when subjected to noisy input data. The use of regularizer weights is crucial in managing the impact of noise and ensuring practical solutions.

- **Achieving Uniform Heating:** Adjusting heater temperatures effectively achieves uniform heating for the heat treatment of workpieces. This outcome is particularly significant for ensuring consistent temperature distribution across the workpieces, crucial for industrial applications requiring precise thermal management.

- **Transient vs. Steady Heater Temperature Solutions:** Transient modeling of heater temperatures significantly enhances the uniformity of heating at design points by allowing finer optimization for transient demands. This approach results in lower errors and improved heating uniformity compared to steady-state heater temperature solutions.

- **Influence of Initial Guesses and Regularizer Weights:** While different initial guesses may lead to varying initial errors, the final heater temperature profiles converge to similar patterns, demonstrating the robustness of the solution methodology. Adjusting regularizer weights is essential for balancing error levels and practical applicability of the solutions.

Overall, the findings from this chapter provide a comprehensive understanding of the factors influencing the inverse solution process for heater temperature optimization in thermal processes. These insights offer valuable guidance for design engineers aiming to achieve effective heat treatment management and optimization in industrial applications.

CHAPTER VII

COMPARISON OF FURNACE OPERATION APPROACHES AND HEATING STRATEGIES FOR HEAT TREATMENT OF SIX GLASS PANES

This chapter aims to compare the approaches of modeling furnace operating conditions, specifically the Temperature-based and Power-based Approaches, to evaluate their effectiveness in achieving uniform treatment at design points, practical applicability of the determined furnace operating. Additionally, the investigation covers three design conditions, each outlining unique heating strategies for the heating and soaking phases, focusing on temperature uniformity and the energy demands of the treatments.

We focused on a 10-minute heating process of six glass panes within a radiant furnace. Three design conditions were explored: linear heating with a sharp transition to soaking (Case 1), heating with a smooth transition to soaking (Case 2), and prolonged heating with a smooth transition to soaking (Case 3). By solving the inverse problem using both Temperature-based and Power-based Approaches, we aimed to determine the furnace operating parameters that would achieve the desired uniform heating profiles while evaluating the practical and energy implications of each approach.

7.1 Problem Definition: Heating and Soaking of Six Glass Panes

A 10-minute long heating process of six glass panes in a heat treatment radiant furnace is investigated, with the problem geometry demonstrated in Fig. 31(a). In this configuration, the furnace's top wall serves as the heater, composed of graphite, while the remaining walls, made of stainless steel, function as chamber surfaces. These chamber surfaces are segmented into square elements, each with an edge length of 2.5 cm, as shown in Fig. 31(b). The heater surface is divided into 64 discrete surface elements, arranged in an 8×8 layout as illustrated in Fig. 31(c). Although the furnace's elements, including both chamber and heater surfaces, are modeled as having no physical thickness, a thickness of 5 mm is assigned in the thermal calculations to account for lumped conduction analysis.

All workpieces are uniformly sized, being 17.5 cm along the x-axis, 1 cm along the y-axis, and 10 cm along the z-axis. The workpieces are symmetrically placed at the center of the furnace, aligned evenly with respect to both the x-axis and the z-axis, as demonstrated in Fig. 31(d). Based on a mesh independence analysis, each workpiece is discretized using a $20 \times 10 \times 20$ finite volume mesh, the cell edges of which are visible in Fig. 31(d).

A total of 150 design points are defined within these workpieces, aligned with the centers of the finite volume cells and marked as red dots in Fig. 31(e). The design points are uniformly distributed across all workpieces and positioned on a plane 0.5 mm below workpieces' upper boundary.

At the beginning of the heating process, the initial temperatures are set at 750 K for the heater and chamber, and 500 K for the workpieces. The environment temperature is assumed to be constant and set as $T_{\text{env}} = 300$ K.

In this problem, all aspects of the thermal modeling detailed in Section 2.3 are incorporated. A value of 1.0 $\text{W/m}^2\text{K}$ has been assigned to the overall heat transfer

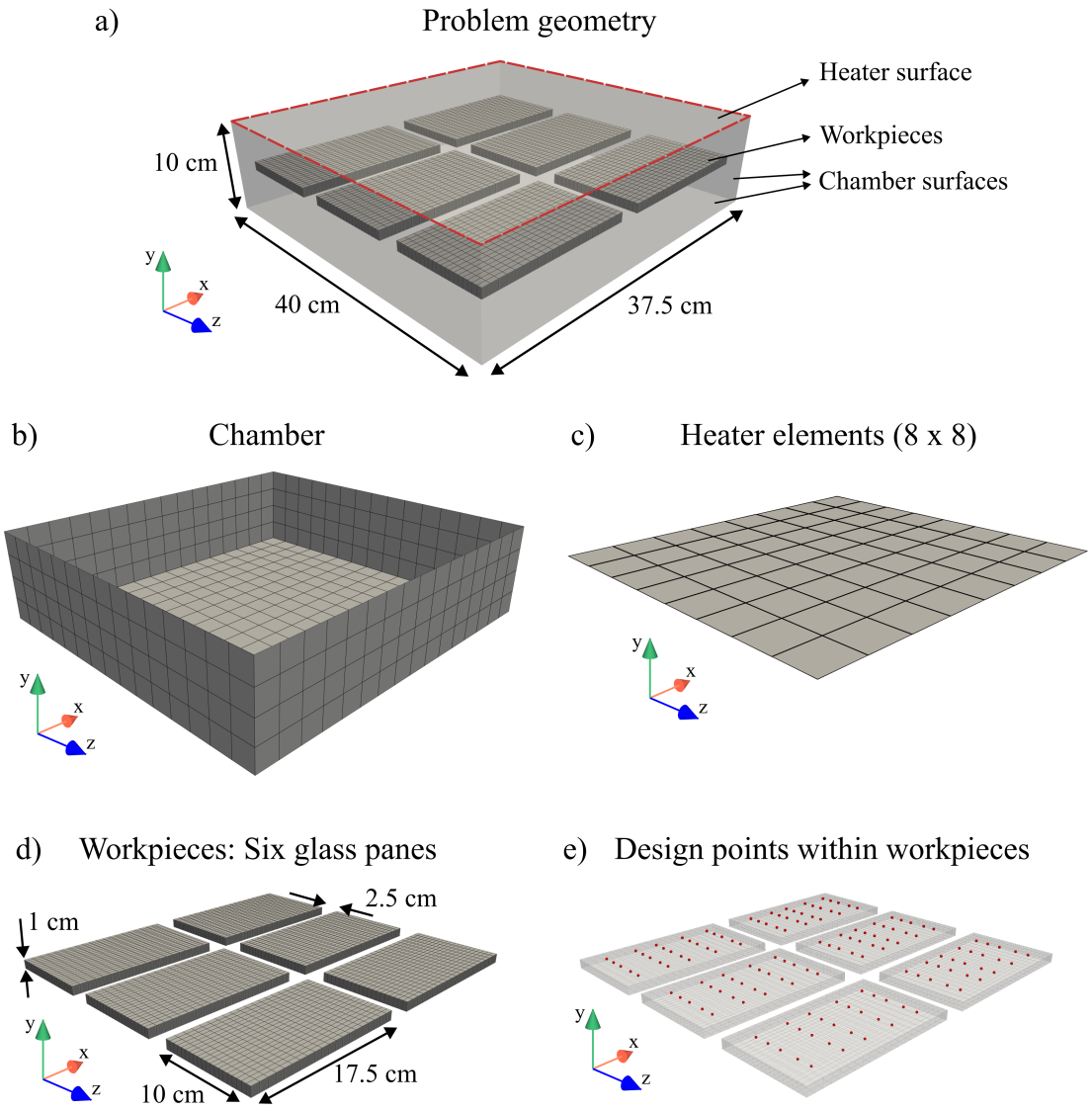


Figure 31: The problem of transient heating of six workpieces (glass panes) inside a radiant furnace. (a) Geometry of the problem. (b) Chamber surfaces divided into square elements. (c) Heater surface elements located at the furnace upper wall. (d) Geometry of the workpieces. (e) Design points within the workpieces, represented by red dots.

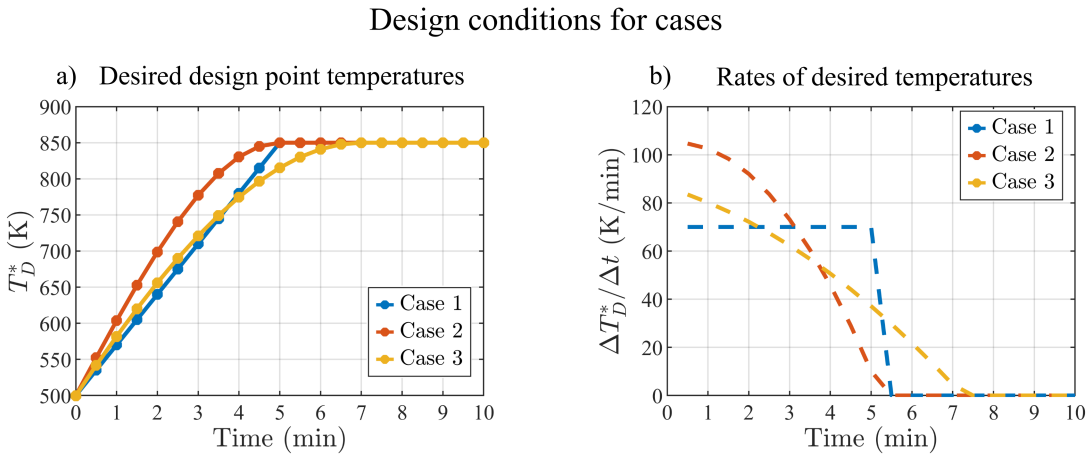


Figure 32: Design conditions: (a) Desired uniform heating profiles used as design conditions across three distinct cases. (b) Heating rates of the desired heating profiles.

coefficient $\bar{U}$, used to characterize the insulation of the furnace chamber from the environment, without regard to its physical equivalence.

7.1.1 Design Conditions for Three Cases

We have investigated three distinct design conditions, each corresponding to different heating curves at the design points from 500 K to 850 K. These are categorized as follows: Case 1 involves linear heating with a sharp transition to soaking, Case 2 focuses on heating with a smooth transition to soaking, and Case 3 features prolonged heating with a smooth transition to soaking. The specific temperature profiles for each of these cases are demonstrated in Fig. 32(a). Fig. 32(b) illustrates the rates at which the desired temperatures change for each case over a 10-minute period. It highlights constant rates with a sharp transition for Case 1, and smoothly decreasing rates for Case 2 and 3 with distinct slopes.

For each inverse solution of the cases, corresponding heating profile is applied to every single design point illustrated in Fig. 31(e), ensuring an overall uniform heating. The desired design point temperatures T_D^* of these design conditions are imposed at each time in interval of $\Delta t_{INV} = 30$ s, defining time time step size in the inverse solution.

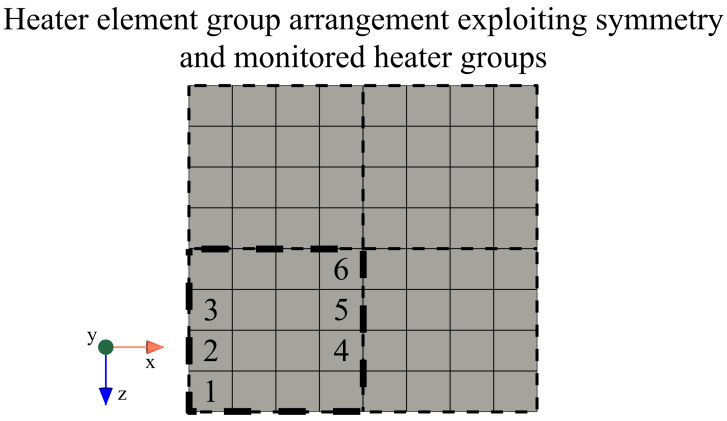


Figure 33: Arrangement of heater element groups exploiting geometric symmetry. The six indexed heater element groups are designated as monitoring groups where temperatures and powers are plotted.

7.1.2 Design Variable and Heater Arrangement

The inverse problems are solved for furnace operating parameters through two distinct operating variable separately, as detailed in Section 2.6.2, each leading to different types of unknowns. The first approach, the Temperature-based Approach, focuses on the determination of time-varying heater temperatures T_H, while the second, the Power-based Approach, aims at establishing the time-varying heater powers $\dot{E}_H$.

For the aim of achieving uniformity in design point temperatures, we employ a strategic approach that utilizes the geometric symmetry of the problem. The heater elements, arranged in an 8×8 grid on the upper wall as shown in Fig. 31(c), are further divided into four 4×4 quarters, as illustrated in Fig. 33, with each quarter governed by the same set of operating parameters. By grouping the 64 heater elements into $4 \times 4 = 16$ groups, this symmetrical arrangement reduces the number of unknown parameters, thereby improving the computational efficiency of the inverse solution. By capitalizing on this geometric symmetry, we ensure a more manageable approach to solving the inverse problem.

For detailed monitoring, six specific heater groups are selected as monitoring groups, as indexed in Fig. 33. These element groups are used to observe and plot the

temperatures and power levels throughout the transient treatment process, providing a clear demonstration of the obtained heater operating conditions.

7.2 Numerical Settings and Parameters

For the inverse solutions, initial guess is set at 750 K for the Temperature-based Approach and 0 W for the Power-based Approach. In the Temperature-based Approach, to maintain consistency with the initial conditions of the problem, a bound of 750 K is imposed on the heater temperature at $t = 0$ s. In the Power-based Approach, a lower bound of 0 W is employed to prevent energy draw from the heaters, which is often impractical for heat treatment applications.

For both FRW and MFRW simulations, we employed $N_p = 10^6$ particles with a boundary strip thickness of $r_{\min} = 10^{-4}$ m, and used a time step size of $\Delta t_{\text{FRW}} = 2.5$ s to balance computational efficiency and accuracy. The exchange factors were calculated using the backward Monte Carlo ray tracing, with a total of 5.8×10^8 rays employed.

In our implementation, the 10-minute time domain of the heat treatment process is divided into one-minute subdomains. Within these subdomains, the furnace operating parameter function is represented as piecewise linear functions, as detailed in Eq. 10, with each time segment designed for a 30-second interval. To enhance the accuracy of our results, we extended these subdomains by an additional minute. Consequently, while the inverse problem for each subdomain is computed over a maximum duration of two minutes, only the data belonging to the first minute are collected. To ensure continuity in the solution over time within overlapping subdomain optimization, adjustments are made to the initial guess and bound constraints in the inverse solutions. This involves utilizing the solution from the overlapping region as the initial guess for the subsequent subdomain solution. Furthermore, the solution from the latest time segment of the non-overlapping region serves as both lower and

upper bound constraint for the next subdomain solution.

To enhance the smoothness of the heater temperature or power profiles over time, a regularization strategy was devised to minimize fluctuations between consecutive values over time. For instance, within the first time segment for a heater group index $\bar{h}$, the furnace operating parameter is described by a linear function $u_{\bar{h},1} + (u_{\bar{h},2} - u_{\bar{h},1})t/t_1$, as outlined in Eq. 10. This translates to $w_{\bar{h},1} = [1\ -1][u_{\bar{h},1}\ u_{\bar{h},2}]^T = u_{\bar{h},1} - u_{\bar{h},2}$, which is incorporated into the objective function through the regularizer β. Accordingly, the dictionary matrix $\boldsymbol{D}$ of the regularizer in Eq.(29) is formed for all operating surfaces. This implementation manipulates the progression of temperature or power levels from one time segment to the next, leading to a smoother furnace operation. For the Temperature-based approach, a regularization weight of $\zeta = 10^{-3}$ was used across all cases. In the Power-based approach, the most accurate and smoothest solutions were achieved using regularization weights of $\zeta = 10^{-1}$ for Case 1 and 2, and $\zeta = 10^{-2}$ for Case 3. The smoothing scalar was in regularization term set to $e = 10^{-6}$.

7.3 Numerical Analyses

In this section, we present several analyses: first, we identified an reasonable time step size for forward solutions; second, we conducted statistical analyses to determine an adequate number of rays for MCRT and particles for FRW simulations; and third, we carried out a verification analysis for the sensitivity coefficients derived from our methodology.

7.3.1 Time Step Size Analysis

Time step size analysis was performed using values of Δt_{FS} = 2 s, 1 s, 0.5 s, 0.25 s, 0.125 s, and 0.1 s. For each value, the design point temperatures were evaluated by a forward solution. We assumed that the smallest time step size, Δt_{FS} = 0.1 s, would yield the most accurate results and compared the temperature differences with

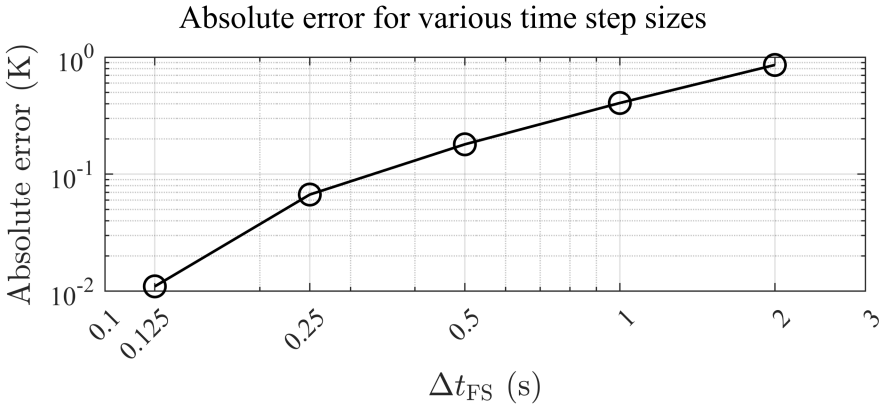


Figure 34: Time step size analysis: Error in design point temperatures for various time step sizes.

larger time steps. Fig. 34 shows these differences at the design points and at the time when the maximum error is observed, revealing that smaller time step sizes reduce temperature errors. This trend is confirmed by a logarithmic plot that illustrates a linear correlation between time step size and temperature error. Consequently, we chose $\Delta t_{FS} = 0.5$ s for forward solutions, which provides an acceptable maximum temperature error of 0.2 K at the design points, corresponding to a relative error of 0.02%, when compared to the finest time step size of 0.1 s.

7.3.2 Statistical Analyses

Using subsets of rays and random walk particles, we have thoroughly examined the variability in design point temperatures and sensitivity coefficients to ensure the robustness of our computational approach, as discussed the following statistical analyses below:

- Monte Carlo ray tracing: Statistical analysis has been performed using 100 subsets of the 5.8×10^8 rays. For each subset, a forward problem was solved with the calculated exchange factors to examine the statistical effects on the design point temperatures. At the design point and time of the highest standard deviation was observed, the mean value of the design point temperature was

found to be 689.8 K, where the real value should lie between ±0.5 K (±0.08%) of this value with a probability of 99.7%.

- Floating Random Walk method: Statistical analysis with 50 subset have resulted in a maximum relative standard deviation of 0.22% in the calculated sensitivity coefficients $\partial T_D/\partial u$.

7.3.3 Sensitivity Coefficient Verification

The accuracy of the sensitivity coefficients calculated by our present methodology was verified against coefficients obtained through first-order finite difference approximation, , as described in Section 6.4.1.3. This verification was conducted for the Temperature-based approach, employing furnace operating parameter functions with 2-minute time segments. For the finite difference approximation, a temperature step size of 50 K was utilized, which is subject to potential numerical errors from the forward solution responses and the inherent truncation error of the approximation method itself.

The data depicted in Fig. 35(a) represents the derivatives of the temperatures at each design point at $t = 30$ s, with respect to the unknown variable that dictates the temperature of the selected heater elements demonstrated in Fig. 35(b) (with blue shading) during the time interval $0 \leq t \leq 60$ seconds. The sensitivities of T_D related to workpieces 3 and 4 are higher than those for other workpieces, as the workpiece ordering is demonstrated in Fig. 35(b). This observation aligns with the problem's geometry, given that the design points within these workpieces are positioned closer to the selected heater elements.

The findings show that, the sensitivity coefficients derived from our present methodology show a strong correspondence with those determined by finite difference approximation. It is important to note that while the exact values do not match perfectly, the alignment between the two sets of coefficients is evident, affirming the

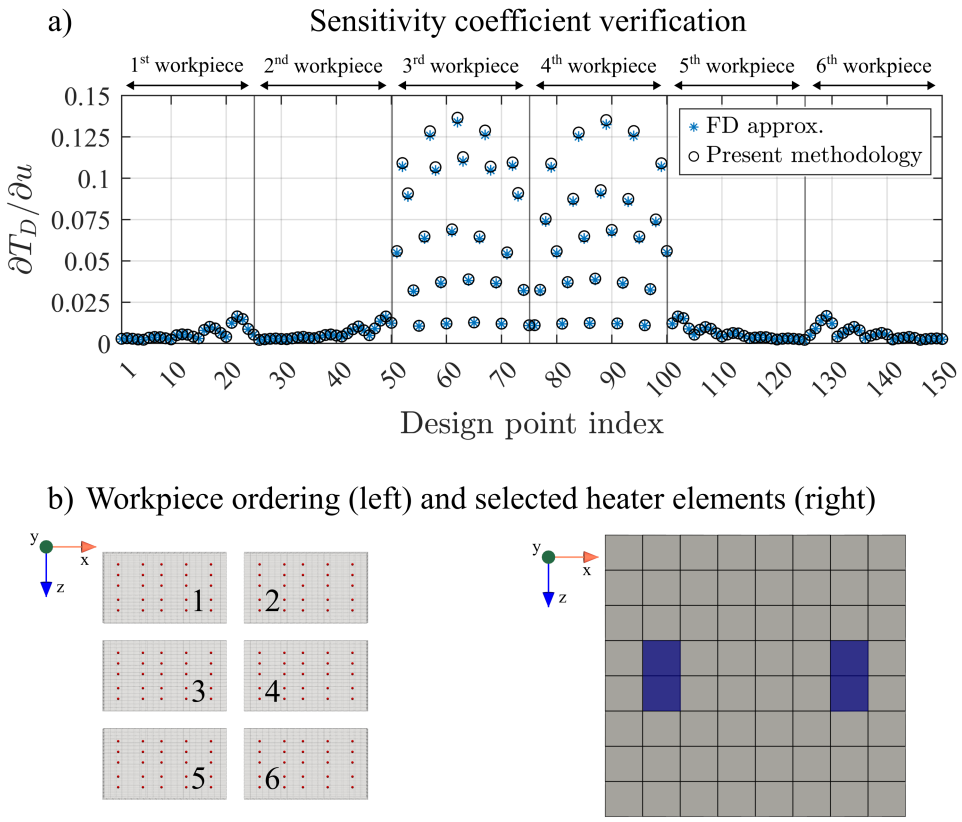


Figure 35: Sensitivity verification analysis. (a) Sensitivity coefficients calculated by present methodology and finite difference approximation. (b) Workpiece ordering and selected heater elements used in sensitivity coefficient verification.

reliability of our approach.

7.4 Results

The results from solving the inverse problem for different heat treatment scenarios are presented, comparing the effectiveness of Temperature-based and Power-based approaches in achieving uniform heating at design points. The analyses focus on the obtained operation conditions, resulting design point temperature distributions, and energy efficiencies of the systems under various design conditions. Detailed findings, including computational time costs and behaviors during transitions, are discussed in the subsequent subsections.

7.4.1 Case 1: Linear Heating with Sharp Transition to Soaking

The inverse problem is solved for the first design condition including linear heating phase with a sharp transition to soaking phase of a heat treatment process and the obtained results for both Temperature and Power-based Approaches are presented in Fig. 36. The results indicate that both the Temperature-based and Power-based approaches successfully maintained a uniformity in the design point temperatures within a 5 K deviation as depicted in Fig. 36(a_1) and (a_2), while the temperature nonuniformity increases around the transition from heating to soaking. This demonstrates the efficacy of both methods in achieving the desired uniform heating.

The furnace operating conditions determined by the inverse solutions are illustrated in Fig. 36(b_1) for the Temperature-based Approach and in Fig. 36(c_2) for the Power-based Approach. A notable difference emerges in the practicality of these approaches for this design condition when applied to real-world scenarios. The Temperature-based solution indicates the need for heat withdrawal from the heaters, as suggested by the resulting negative heater powers seen in Fig. 36(c_1). Such a requirement is not feasible in actual furnace operations, thereby limiting the applicability of this approach because extracting heat from heater surfaces is often

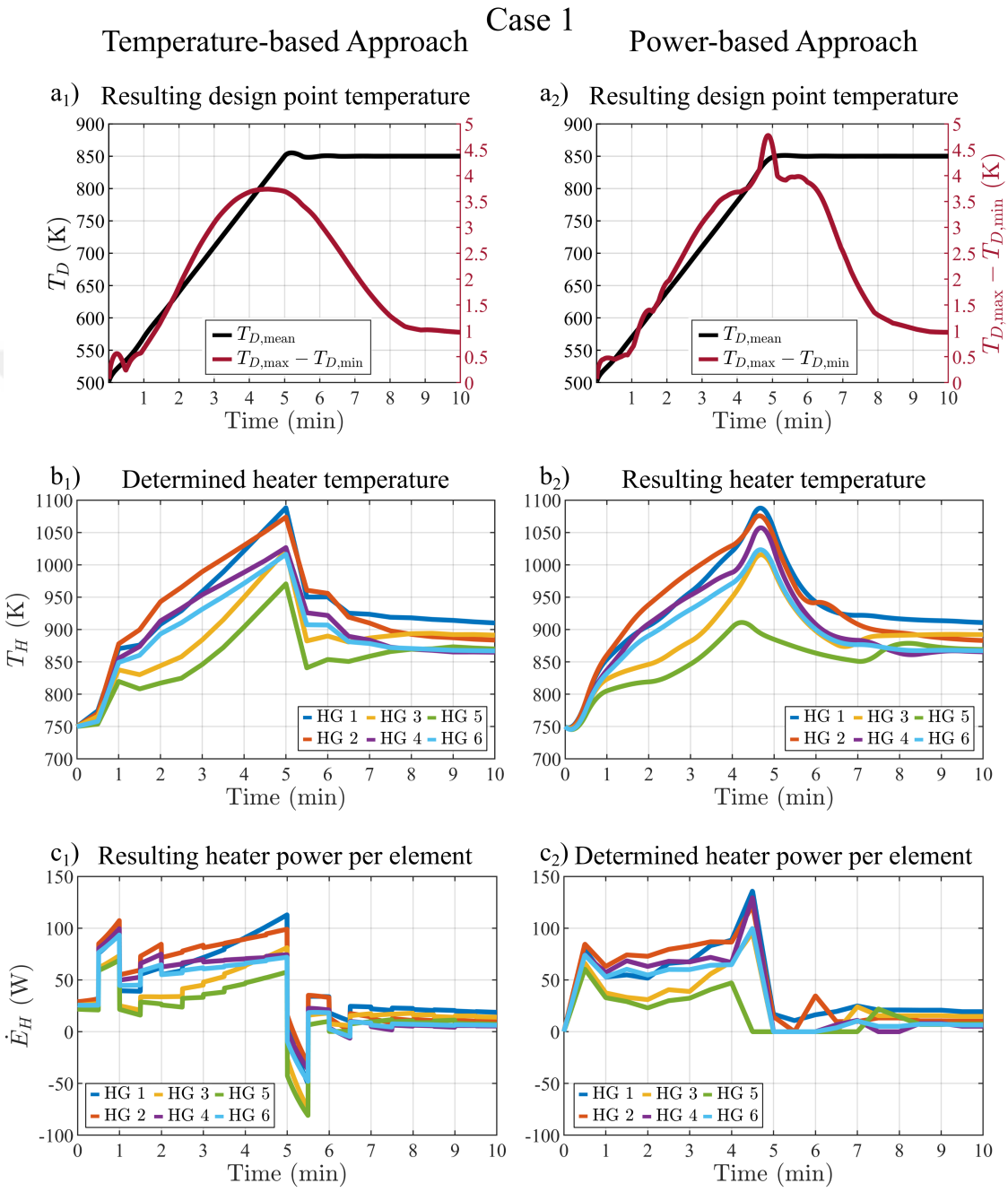


Figure 36: Inverse solution results for the design condition in Case 1. (a_1) and (a_2): Resulting design point temperature and resulting temperature uniformity. (b_1) and (b_2): Temperatures of the selected heater groups over time. (c_1) and (c_2): Powers of the selected heater groups per heater element over time. The selected heater group indices are demonstrated in Fig. 33. 'HG' denotes heater group index.

impractical.

In contrast, the Power-based solution, which sets a lower bound constraint of 0 in the inverse solution, avoids the scenario of heat withdrawal from heater elements. This constraint, which can be observed in Fig. 36(c_2), ensures that the solution remains practical and applicable, aligning better with real-world furnace operations. Implementing such constraints in the Temperature-based Approach, however, is not as straightforward.

The occurrence of resulting negative power values in the Temperature-based Approach is dependent on the specific problem being solved. In certain problems and under specific design conditions, these negative power values might not manifest. Our findings suggest that attention should be paid to this aspect in the Temperature-based Approach when practicality is concerned.

Despite this advantage, the Power-based Approach exhibits fluctuating nonuniformities in the resulting design point temperatures during the sharp transition. This indicates that, within this model problem design and the imposed zero lower bound, further improvement in the uniformity of the design point temperatures may not be possible due to the limitations inherent in the current configuration.

Furthermore, the heater powers resulting from the Temperature-based approach display a discontinuous pattern, reflecting the challenges associated with maintaining a linear heater temperature profile over time. This discontinuity could pose difficulties in actual furnace control. Nevertheless, if one were to consider implementing the Temperature-based solution, smoothing the resulting heater power profile over time could be investigated to evaluate the potential benefits and to assess whether this approach could be refined for practical use.

In addition to our primary analyses, we conducted further investigations to evaluate the impact of the time step size of inverse solution Δt_{INV} and the temporal resolution of the furnace operating parameters. This involved examining scenarios

with the values of $\Delta t_{\mathrm{INV}} = 15$ and 10 seconds, which improved the time resolution of the desired design point temperature data. Additionally, the furnace operating parameters were refined using narrower time segments of 20, 15, and 10 seconds, as defined in Eq. 10. However, our findings from these analyses indicate that these adjustments did not enhance the temperature uniformity at the design points. This outcome suggests that the level of uniformity achieved may be a threshold for the current heater configuration in our model geometry.

7.4.2 Case 2: Heating with Smooth Transition to Soaking

In the investigation of Case 2, which implements a smoothed transition from heating to soaking, both the Temperature-based and Power-based approaches ensured uniform treatment at the design points with deviations held below 4 K, as evidenced in Fig. 37(a_1) and (a_2). Furthermore, the Power-based approach shows no fluctuations during the transition phase, indicative of a more stable thermal treatment compared to Case 1.

The implementation of a smoothed transition in the desired design point temperatures has markedly influenced the heat management within the furnace. In the Temperature-based solution, the determined heater temperatures displayed in Fig. 37(b_1) led to a decrease in heat extraction from the heaters, as indicated by the resulting heater powers shown in Fig. 37(c_1). Moreover, the smoother transition has resulted in smoother heater powers in the Power-based solution as shown in Fig. 37(c_2) and has minimized the discontinuities in the resulting heater powers in the Temperature-based solution as depicted in Fig. 37(c_1).

The determined heater temperature profiles in the Temperature-based solution and the resulting heater temperatures in the Power-based solution, as shown in Fig. 37(b_1) and (b_2) respectively, exhibit a similar and smooth pattern. This similarity suggests that despite methodological differences, both approaches can produce similar

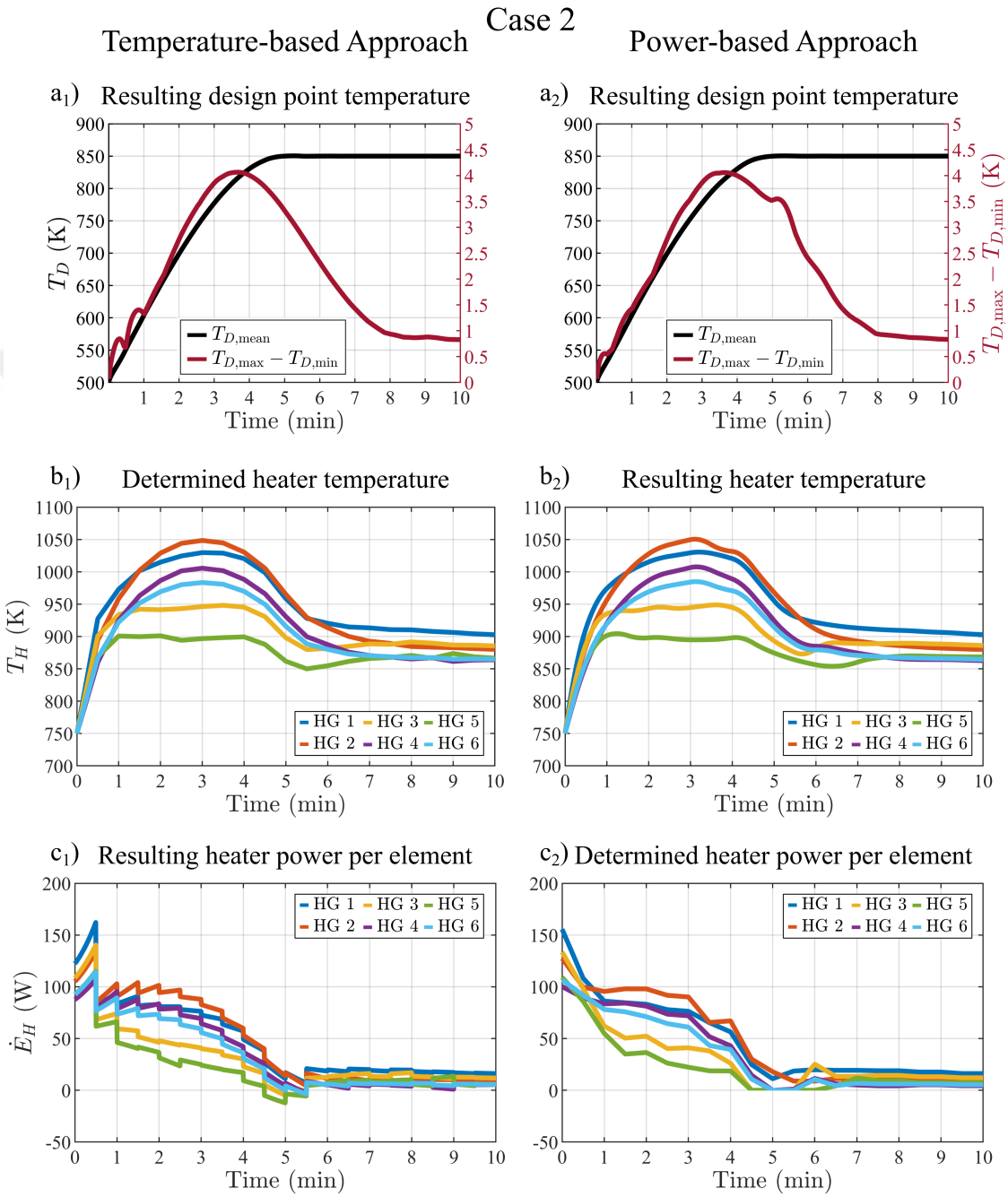


Figure 37: Inverse solution results for the design condition in Case 2. (a_1) and (a_2): Resulting design point temperature and resulting temperature uniformity. (b_1) and (b_2): Temperatures of the selected heater groups over time. (c_1) and (c_2): Powers of the selected heater groups per heater element over time. The selected heater group indices are demonstrated in Fig. 33. 'HG' denotes heater group index.

thermal behaviors within the furnace for the desired design point temperatures in Case 2.

7.4.3 Case 3: Prolonged Heating with Smooth Transition to Soaking

The analysis in Case 3 demonstrated in Fig. 38 reveals that despite the extended heating period, the uniformity of the resulting design point temperatures maintained by both the Temperature-based and Power-based approaches is consistent with that achieved in Cases 1 and 2. As indicated in Fig. 38(b_1), the Temperature-based approach ensures the desired treatment with negligible energy drawn from the heaters, highlighting its suitability for practical industrial processes. The extended duration of the heating phase results in lower maximum power requirements for both approaches, indicating a decrease in peak power demands when compared to the previous cases. The similarity in heater temperature profiles for both approaches is evident in Fig. 38(b_1) and (b_2), with a notable decrease in peak heater temperatures compared to the previous cases.

7.4.4 Determined Heater Temperature Distributions

The temperature distribution across the furnace heater elements in the Temperature-based approach are captured at specific times for all three cases and illustrated in Fig. 39. The finding exhibits nonuniform heater temperature distribution that are essential for achieving uniform treatment at the design points.

During the heating phase, the heater element temperatures display a checker-board-like pattern, indicative of the heat transfer interactions required to maintain treatment uniformity. In Case 1, the peak temperatures are found at the corners, while in Cases 2 and 3, the peak temperatures shift to an adjacent element. Despite this shift, the overall pattern remains similar across the cases, pointing to an inherent consistency in the thermal behavior of the system.

As the process transitions from heating to soaking, the temperature alignment

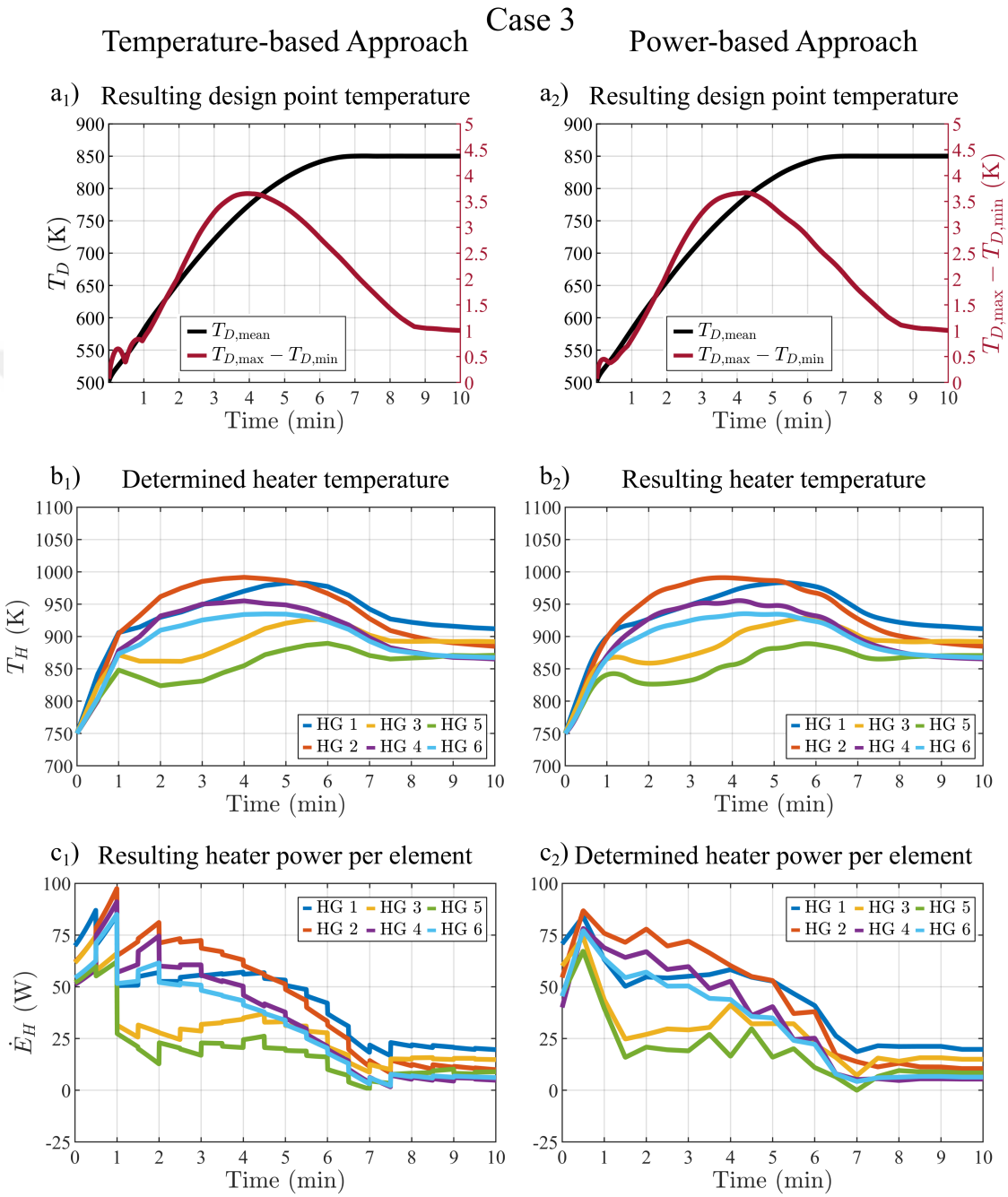


Figure 38: Inverse solution results for the design condition in Case 3. (a_1) and (a_2): Resulting design point temperature and resulting temperature uniformity. (b_1) and (b_2): Temperatures of the selected heater groups over time. (c_1) and (c_2): Powers of the selected heater groups per heater element over time. The selected heater group indices are demonstrated in Fig. 33. 'HG' denotes heater group index.

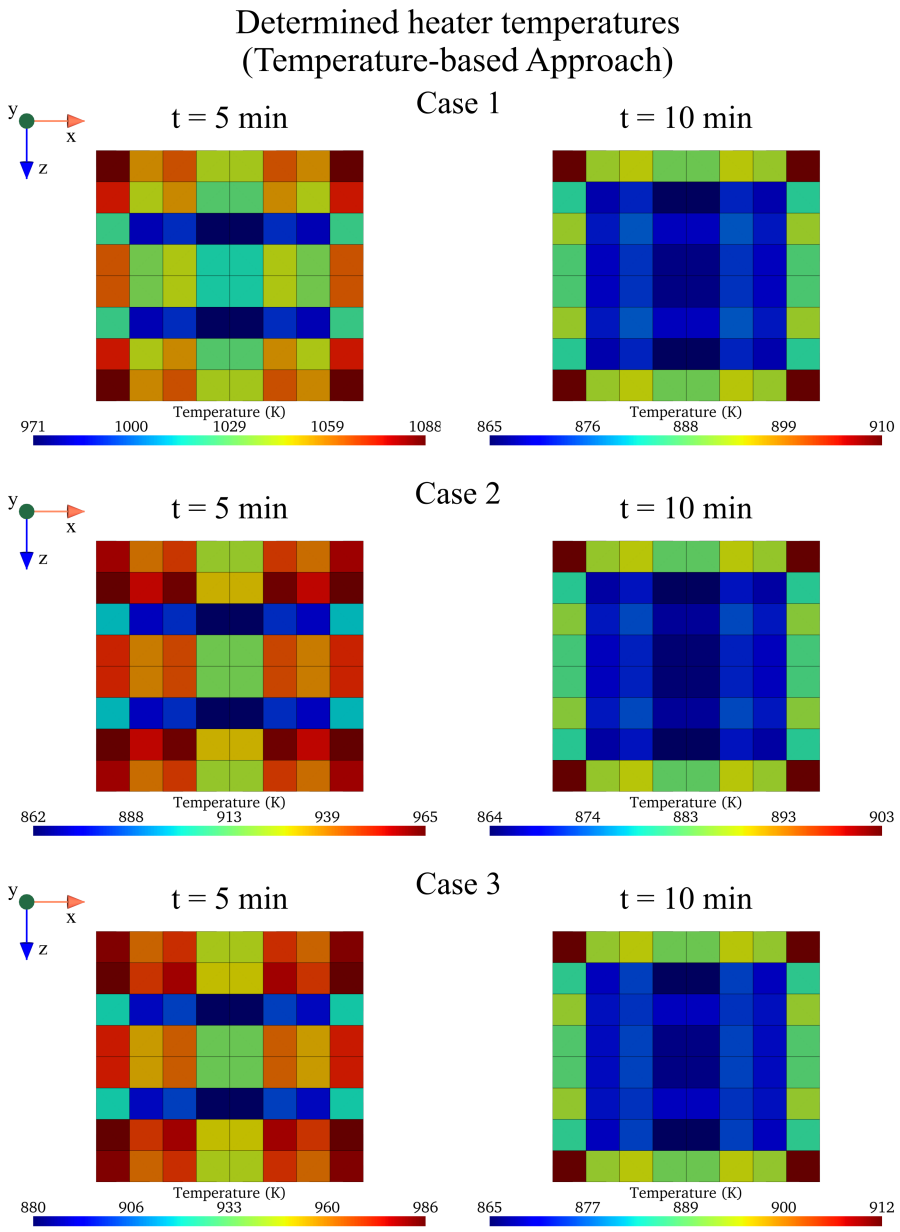


Figure 39: Heater temperature distributions determined from the Temperature-based approach for three cases

among the heater elements undergoes a realignment, observable in all cases. This change reflects the heater elements' adaptive response to the evolving requirements of the heat treatment process, emphasizing the need for careful temperature management to achieve uniformity within the workpieces.

At the end of the 10-minute treatment, the temperature patterns across the cases converge, showing near-identical distributions with only minor variations in temperature readings. This convergence indicates that the furnace system is likely to stabilize into a consistent thermal state as the treatment progresses to soaking phase, regardless of the initial heating conditions. It is worth noting that very similar heater temperature patterns to those reported here are also observed in the Power-based approach.

7.4.5 Determined Total Heater Powers

The Power-based Approach's inverse determination of heater powers provides a comparative analysis across three cases, as shown in Fig. 40. This analysis offers insights into the thermal energy requirements of the heat treatment furnace model. The patterns observed in the determined total heater powers for the three cases highlight the impact of the transition strategies between the heating and soaking phases. Case 1 exhibits a sharp transition marked by a peak in total heater power, reaching approximately 6 kW towards the end of the heating phase, and is followed by a rapid decline. This behavior is in contrast to the other cases, which do not exhibit such sudden changes, thanks to their smoother temporal transition.

In Case 2 and 3, the peak power demands occur at the onset of the heat treatment process, correlating with the increased initial heating rate caused from the smoothed transition dictated by the design conditions. This initial heating rates can be noticed in Fig. 32(b) and leads to a higher initial power draw. Case 2, in particular, displays the most considerable energy requirement, with the furnace power reaching around

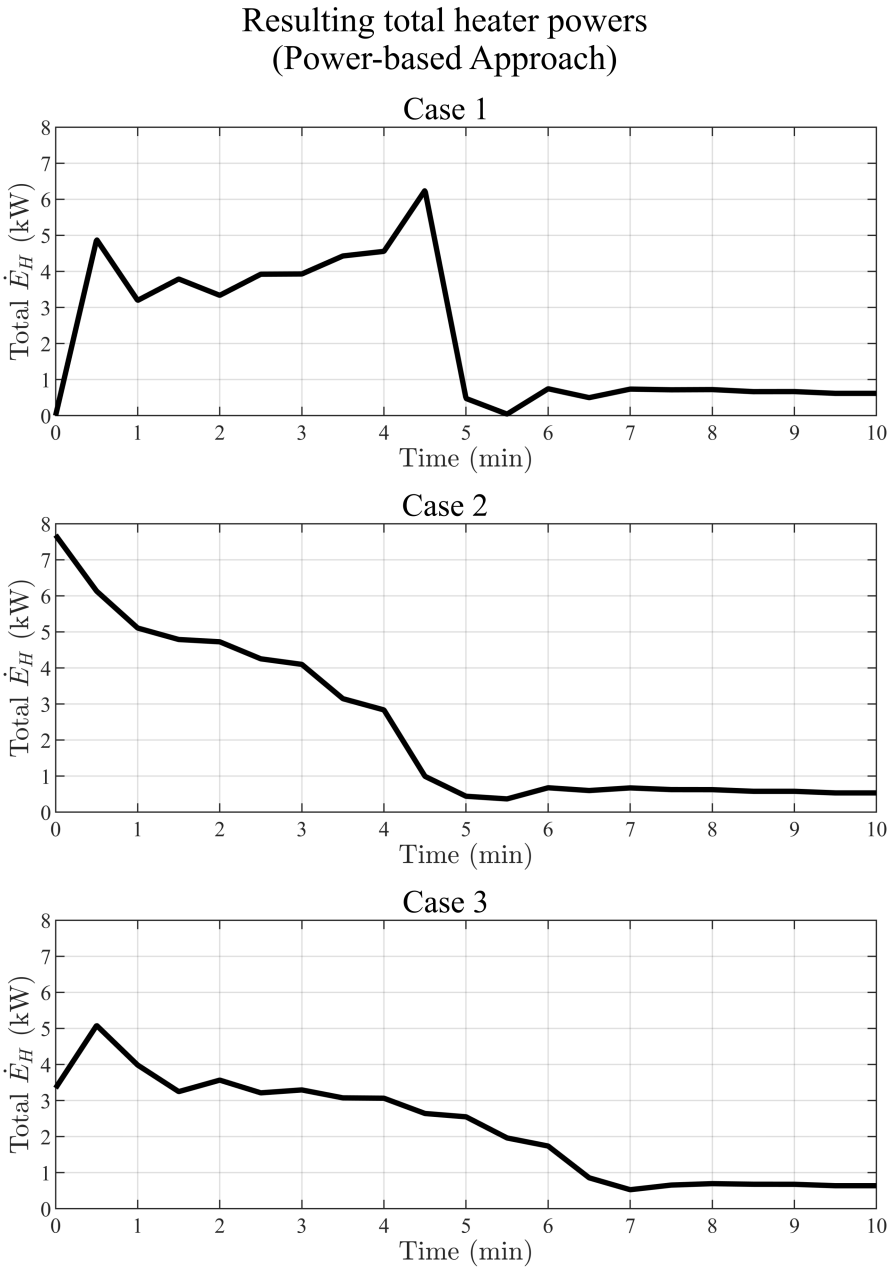


Figure 40: Total heater powers determined by the Power-based approach for three cases

8 kW. This spike in demand aligns with the case's design condition, which includes the highest heating rate without an extended heating phase. It highlights the impact of design conditions on the furnace's energy consumption, emphasizing the need for careful planning in the thermal design condition to accommodate such high initial power demands.

Table 5 presents a comparison of energy requirements for three different cases of thermal treatment in the radiant furnace. Case 2 exhibited the highest peak power demand at 7.7 kW, while Case 1 and Case 3 showed a 19.5% lower and 33.8% lower demand, respectively. The total energy requirement for Case 1 is 0.371 kWh, with Case 2 requiring 3.15% more energy and Case 3 requiring 0.80% less. This variation is attributed to the net thermal energy transferred to the furnace elements (including heater and chamber surfaces); for Case 1, it is 0.1101 kWh, with Case 2 experiencing an increase of about 9.5% and Case 3 a decrease of approximately 2.5%. These differences arise from the desired heating curves defined as the design condition. The average design point temperatures at the end of the treatment are similar across all cases.

Table 5: Energy requirements for three distinct heating strategies

	Peak power demand (kW)	Total energy requirement (kWh)	Net thermal energy transfered to workpieces (kWh)	Net thermal energy transfered to furnace elements (kWh)	Average T_D at the end of the treatment (K)
Case 1	6.2	0.371	0.2373	0.1101	841.0
Case 2	7.7	0.382	0.2380	0.1205	842.1
Case 3	5.1	0.368	0.2371	0.1073	840.8

Inverse solutions not only provide optimized furnace operating conditions for specific desired heating curves but also offer valuable insights when solving multiple inverse problems. This process aids in selecting the most appropriate heating curves

for optimal thermal management tailored to a target application. Such a comprehensive approach enhances the practical application of inverse solutions, enabling design engineers to make informed decisions in their design processes.

7.4.6 Computational Time Costs

The computation time for inverse solutions ranged from 18 to 32 minutes, depending on the scenario. For example, in Case 1 using the Temperature-based approach, the inverse solution required 32 minutes, with 77.7% of that time spent on calculating sensitivity coefficients and 21.6% on forward solutions during optimization iterations. This distribution of time costs was consistent across various scenarios.

Calculating the exchange factors took 0.5 seconds for furnace surface elements and 3.7 seconds for workpiece surface elements, using GPU-accelerated computing.

7.5 Concluding Remarks

This chapter presents a comparative analysis of the Temperature-based and Power-based Approaches in modeling furnace operating conditions for the heat treatment of six glass panes. By examining three different heating strategies—linear heating with a sharp transition to soaking, heating with a smooth transition to soaking, and prolonged heating with a smooth transition to soaking—the study evaluates the effectiveness of these approaches in achieving uniform heating and their practical applicability. The results highlight the advantages and limitations of each approach, offering valuable insights for optimizing heat treatment processes.

The analyses reveal that both approaches can achieve uniform heating at the design points, with the Power-based Approach proving more practical for real-world applications due to its avoidance of impractical negative power values. Additionally, the choice of heating strategy significantly impacts energy requirements and peak power demands, emphasizing the importance of selecting appropriate design conditions. These findings provide design engineers with critical information to optimize

furnace operations, ensuring efficient and effective thermal treatments.

The main findings of this chapter can be summarized as follows:

- **Uniform Heat Treatment Achievement:** Both the Temperature-based and Power-based Approaches maintained design point temperature uniformity within acceptable deviations (below 5 K for most cases).

- **Practical Applicability:** The Power-based Approach avoids negative power values, making it more practical for real-world applications compared to the Temperature-based Approach, which sometimes requires impractical heat withdrawal from heaters.

- **Impact of Heating Strategies:** Different heating strategies significantly affect energy consumption and peak power demands. Case 2, with the highest peak power demand, required 3.15% more energy than Case 1, highlighting the influence of the desired heating curves.

- **Heater Temperature and Power Profiles:** Smoother transitions in heating profiles (as in Case 2 and 3) result in smoother heater power distributions and lower peak temperatures, which can enhance energy efficiency and reduce control difficulties.

- **Optimization Insights:** The study demonstrates that solving multiple inverse problems provides insights into selecting optimal heating curves for specific applications, aiding design engineers in making informed decisions to optimize heat treatment processes.

The findings highlight the crucial role of choosing suitable heater operating variables and design conditions to optimize heat treatment processes. The insights gained not only demonstrates the utilization of both Temperature-based and Power-based

approaches but also provide guidance for practical applications, thereby improving the design and effectiveness of heat treatment furnaces.

CHAPTER VIII

EVALUATING FURNACE DESIGN CONFIGURATION FOR DESIRED HEATING OF STAINLESS-STEEL CUBIC WORKPIECE

In this chapter, we aim to determine the necessary heater powers to achieve uniform treatment of a stainless-steel cubic workpiece within a radiant furnace. By employing the developed inverse solution methodology, we analyze the contributions of individual heater groups, emphasizing their importance in maintaining temperature uniformity, especially during the transitions between heating and soaking phases. The resulting heater temperatures, design point temperatures, workpiece surface temperatures, and radiative heat fluxes on the workpiece surface are thoroughly investigated.

Additionally, this chapter assesses the energy requirements of the determined furnace operating conditions, including the energy lost to the environment and the energy transferred to both the workpiece and furnace components. We examine the impact of several key factors such as the overall heat transfer coefficient governing heat loss from the furnace chamber to the environment, chamber reflectivity, heater layout with fewer heater elements, and heater material. These analyses provide comprehensive insights into how these variables influence the determined heater powers, treatment uniformity, and overall energy considerations.

8.1 Problem Definition: Heating Phase of a Cubic Workpiece in a Radiant Furnace

Transient heat treatment of a single workpiece inside a radiant furnace is considered. The problem geometry, depicted in Fig. 41(a), consists of a chamber (Fig. 41(b)), heater elements (Fig. 41(c)), and a workpiece located at the furnace's center (Fig. 41(d)). Each side wall of the furnace chamber is divided into 16×16 surface elements, with the chamber material considered as Inconel 610. On each face, an arrangement of 36 square-shaped graphite heater elements with a 3 cm edge length is established, resulting in a total number of 216 heaters. The workpiece is composed of stainless steel (AISI 410) and is discretized using a $20 \times 20 \times 20$ finite volume mesh. Design points are positioned at the center of the finite volume cells closest to the workpiece surfaces, with a proximity of 6.7 mm to the surface, as depicted by the red dots in Fig. 41(e). In accordance with the density of the finite volume mesh, there are a total of $N_d = 2168$ design points.

A six-hour-long heating phase is considered for the transient heat treatment of the workpiece. The initial condition is defined by constant temperatures of 600 K for both the furnace and the workpiece.

8.1.1 Thermal Model

In this problem, all aspects of thermal modeling detailed in Section 2.3 are incorporated, offering an improved representation of a real treatment process within a vacuum batch furnace.

We have modeled the heat loss from furnace chamber to its environment as demonstrated in Fig. 42, utilizing the overall heat transfer coefficient $\bar{U}$. This model assumes an insulation layer composed of ceramic fiber with a thermal conductivity of 0.15 W/mK, and the heat transfer from the exterior shell surface by means of convection, characterized by a convection heat transfer coefficient of $h_{\text{conv}} = 5$ W/m^{2}K,

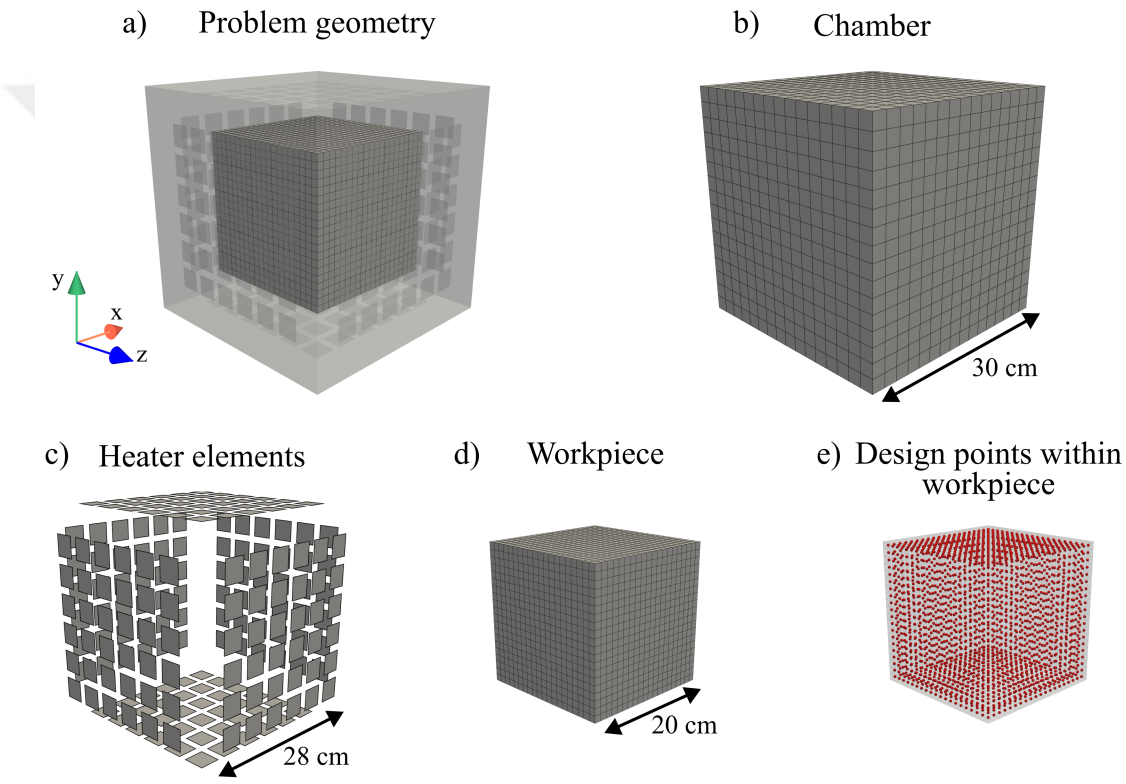


Figure 41: Geometry of the heat treatment problem, including (a) the overall setup, comprising (b) the chamber, (c) heater elements, and (d) a single workpiece. Additionally, (e) illustrates the design points within the workpiece.

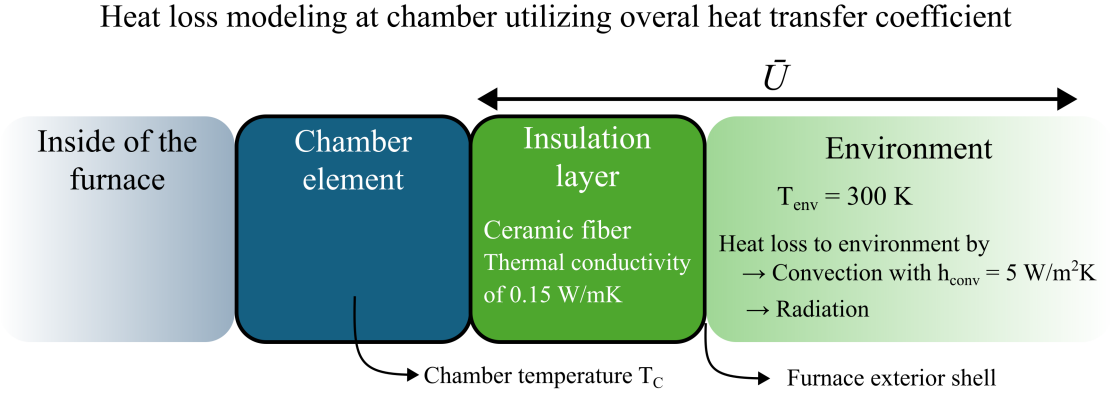


Figure 42: Demonstration of thermal modeling for heat loss from chamber surface elements. Overall heat transfer coefficient represents the effect of insulation layer and heat transferred to environment from the exterior shell surface.

along with black-body radiation. Thus, $\bar{U}$ represents the effect of insulation layer and heat transferred to environment from the shell surface.

To assign realistic values to the coefficient $\bar{U}$, we conducted separate steady-state one-dimensional heat transfer analyses within the insulation domain. Assuming a constant chamber temperature of $T_C = 900$ K and an insulation layer thickness of 10 cm, we obtained $\bar{U}$ value of 1.33 W/m^{2}K, with exterior shell temperatures reaching 95 °C. While this modeling is kept relatively simple, it lays the groundwork for more sophisticated models to be incorporated for further studies. The impact of $\bar{U}$ on the findings of the inverse solution is explored for insulation thicknesses of 5 cm, 10 cm, and 15 cm in Section 8.4.2.

8.1.2 Design Condition

The design condition is defined by the temperature profile illustrated in Fig. 43, considering the heating of the workpiece from 600 K to 1100 K, with an intermediate soaking period starting at $t = 2$ hours. This heating profile is applied to to every single design point illustrated in Fig. 41(e), ensuring an overall uniform heating at a close proximity to the workpiece surfaces. The desired heating profile assumes that the workpiece can be safely heated at a rate below 3 K/min without incurring any

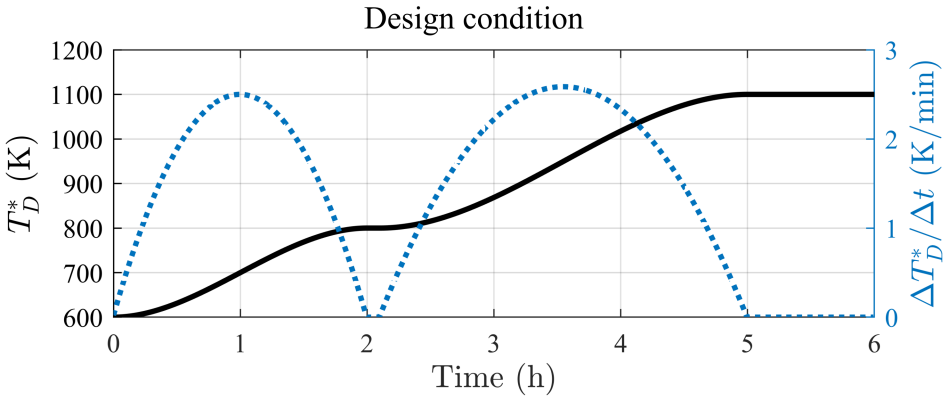


Figure 43: Design Condition: Desired design point temperatures T_D^* to be uniformly maintained across all design points. The right y-axis shows the equivalent heating rate.

damage or cracks. The desired design point temperatures T_D^* of this design condition are imposed at each time in interval of $\Delta t_{INV} = 30$ s, defining time time step size in the inverse solution.

8.1.3 Design Variable and Heater Element Grouping

The aim of the inverse problem in this chapter is to determine the time-varying heater powers necessary for achieving the desired heat treatment, ensuring that the temperatures at the design points within the workpiece correspond to the desired temperature profiles. This entails employing a Power-based Approach on the operating surfaces, specifically the heater elements.

Seeking temperature uniformity at the design points enclosing the entire workpiece surface enables utilization of a strategic approach that leverages the geometric symmetry of the problem. As demonstrated in Fig. 44, the heater elements are arranged into six distinct groups, indexed as 1 through 6. Each group is governed by identical furnace operating parameters. The grouping is managed by utilizing a quarter of each face of the cubic heater configuration, ensuring that each quarter is symmetrical and consistent. This deliberate grouping significantly reduces the number of unknown parameters that need to be determined and thus enhances the computational efficiency

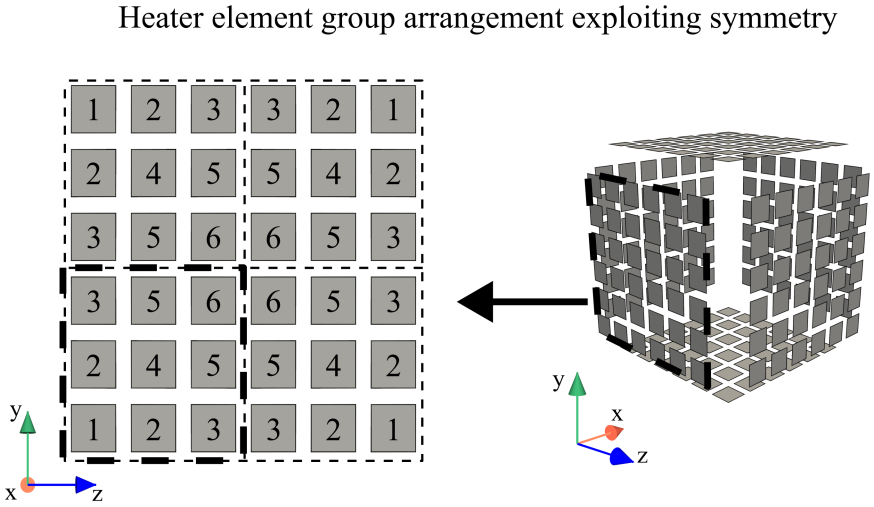


Figure 44: Arrangement of heater element groups exploiting geometric symmetry, where the numbers represent the six distinct heater group indices. The 6×6 layout on the left is replicated on each face of the cubic heater configuration to the right.

of the inverse solution.

8.2 Numerical Settings and Parameters

To ensure a smoother transition in heater powers over time due to practicality concerns of the determined solution, we have devised the following custom regularizer with L1-norm. Consider the furnace operating variable function for a specific heater element group indexed as $\bar{h}$ during the initial time segment in Eq. (10). Corresponding power of the heater group $\bar{h}$ is then expressed as $u_{\bar{h},1} + (u_{\bar{h},2} - u_{\bar{h},1})t/t_1$. Fluctuations between consecutive power values can minimized by incorporating $w_{\bar{h},1} = [1 \ -1][u_{\bar{h},1} \ u_{\bar{h},2}]^T = u_{\bar{h},1} - u_{\bar{h},2}$ into the objective function through the regularizer β. Accordingly, the dictionary matrix $\boldsymbol{D}$ of the regularizer in Eq.(29) is formed for all heater groups. This implementation manipulates the progression of power levels from one time segment to the next, leading to a smoother furnace operation. For this problem, the most accurate and smoothest solutions were achieved using regularization weight of $\zeta = 1$. The smoothing scalar was set to $e = 10^{-6}$.

In our implementation, the six-hour long time domain is divided into small subdomains with a size of $\Delta t_{\text{subd}} = 3$ minutes. Each time segment in the furnace operating variable function in Eq. (10) is defined for 1 minute long time period. To improve accuracy, the subdomains are extended by $\Delta t_{\text{overlap}} = 1$ minute. Thus, each inverse problem is solved over a maximum time of 4 minutes, but the results beyond 3 minutes were ignored. Starting from the first subdomain, the total number of 120 subdomains are solved sequentially.

The initial guess for optimization iterations is set as $u^0 = 0$ MW/m^3. To avoid impractical heat removal from the heaters, a lower bound constraint of 0 W is imposed. To ensure continuity in the solution over time within overlapping subdomain optimization, adjustments are made to the initial guess and bound constraints in the inverse solutions, as described in Chapter 7.

The exchange factors were computed utilizing a total of 1×10^9 rays, corresponding to a minimum of 500 rays per square millimeter on the workpiece surfaces, 250 on the chamber surfaces, and 500 on the heater surfaces. In the FRW and MFRW simulations, the number of particles is set to $N_p = 10^5$ with a boundary strip thickness of $r_{\min} = 10^{-4}$ m. The time domain in both FRW and MFRW simulations is discretized using a time step size of $\Delta t_{\text{FRW}} = 15$ s. For forward solutions, a time step size of $\Delta t_{\text{FS}} = 5$ s is employed.

8.3 Numerical Analyses

An analysis of the finite volume mesh independence was conducted for the workpiece, with the mesh size being varied uniformly across each coordinate: 10, 20, 30, 40, and 50. Based on the findings, the mesh size of $20 \times 20 \times 20$ was chosen as it resulted in a maximum error of less than 0.5 K across the entire domain when compared to the mesh size of $50 \times 50 \times 50$.

A thorough analysis of time step size was carried out, and a time step size of

$\Delta t_{FS} = 5$ s was chosen for the forward solution. This was found to result in a maximum design point temperature error of 0.1 K - a relative error of 0.02% - compared to the time step size of 0.25 s.

Statistical analysis was performed for the Monte Carlo ray tracing method using 50 subsets of the 1×10^9 rays. For each subset, a forward problem was solved with the calculated exchange factors to examine the statistical effects on the design point temperatures. At the design point and time of the highest standard deviation, the mean value of the design point temperature was found to be 770.1 K, where the real value is expected to lie within ± 0.03 K ($\pm 0.004\%$) of this value with a probability of 99.7%.

Statistical analysis for floating random walk simulations with 50 subset resulted in a maximum relative standard deviation of 0.45% in the calculated sensitivity coefficients.

Verification analysis for the sensitivity coefficient calculated in this problem by the present methodology has been conducted, comparing with the finite difference approximation, as described in Section 6.4.1.3. This verification considers the initial 10 minutes of the temporal analysis. The number of time segments for the operating variable function Ψ was set as $N_\eta = 5$. With the inclusion of six heater groups, the total number of operating parameters being analyzed amounts to $N = 6 \times (N_\eta + 1) = 36$. After conducting an analysis to determine a suitable step size, the step size in the finite difference approximation for heater power was set as 3 MW/m^3. Figure 45(a) illustrates the sensitivity coefficients related to the temperature at the first design point, located at the outermost corner of the workpiece, calculated at 10 minutes with respect to the 36 operating parameters. Fig. 45(b) plots the time evolution of the sensitivity coefficient related to the temperature at the first design point with respect to the operating parameter defining the power of the first heater group at $t = 0$ s. The present methodology demonstrates close agreement with the finite difference

approximation, despite slight discrepancies in exact values, which is expected in such analyses.

8.4 Results

In this section, we present the results of the transient heat treatment optimization for a cubic workpiece in a radiant furnace. The analysis focuses on determining the necessary heater powers to achieve uniform heating, examining the impact of overall heat transfer coefficient, chamber reflectivity, heater layout, and heater material on the heat treatment process.

8.4.1 Determining Necessary Heater Powers for Uniform Heating

The necessary powers for the heater elements that ensure the design condition given in Fig. 43 are determined by the inverse solution and presented in Fig. 46(a). This plot illustrates the determined powers for a single heater element in each heater group demonstrated in Fig. 44, with each group denoted by 'HG'. The results indicate that the workpiece is primarily heated by the heaters in group 6, located at the center of the furnace face. While it's evident that the heaters near the furnace's edges contribute less to the overall heating process, they play a crucial role during the transitions between the heating and soaking phases to maintain temperature uniformity at the design points. The findings show that these transitions can be effectively managed by reducing the power to the center heaters and increasing the power to the edge heaters with precise adjustment.

The total power required to be supplied to the furnace heaters is presented in Fig. 46(b) over time. According to the inverse solution, a furnace with a maximum power of 2.5 kW is sufficient for this optimized heating treatment process. The total energy supplied to the heaters is found to be 8.68 kWh with 33.6% (2.92 kWh) of it being lost to the environment from the furnace chamber. The stored energy change was found to be 3.99 kWh for the workpiece and 1.77 kWh for the furnace surface

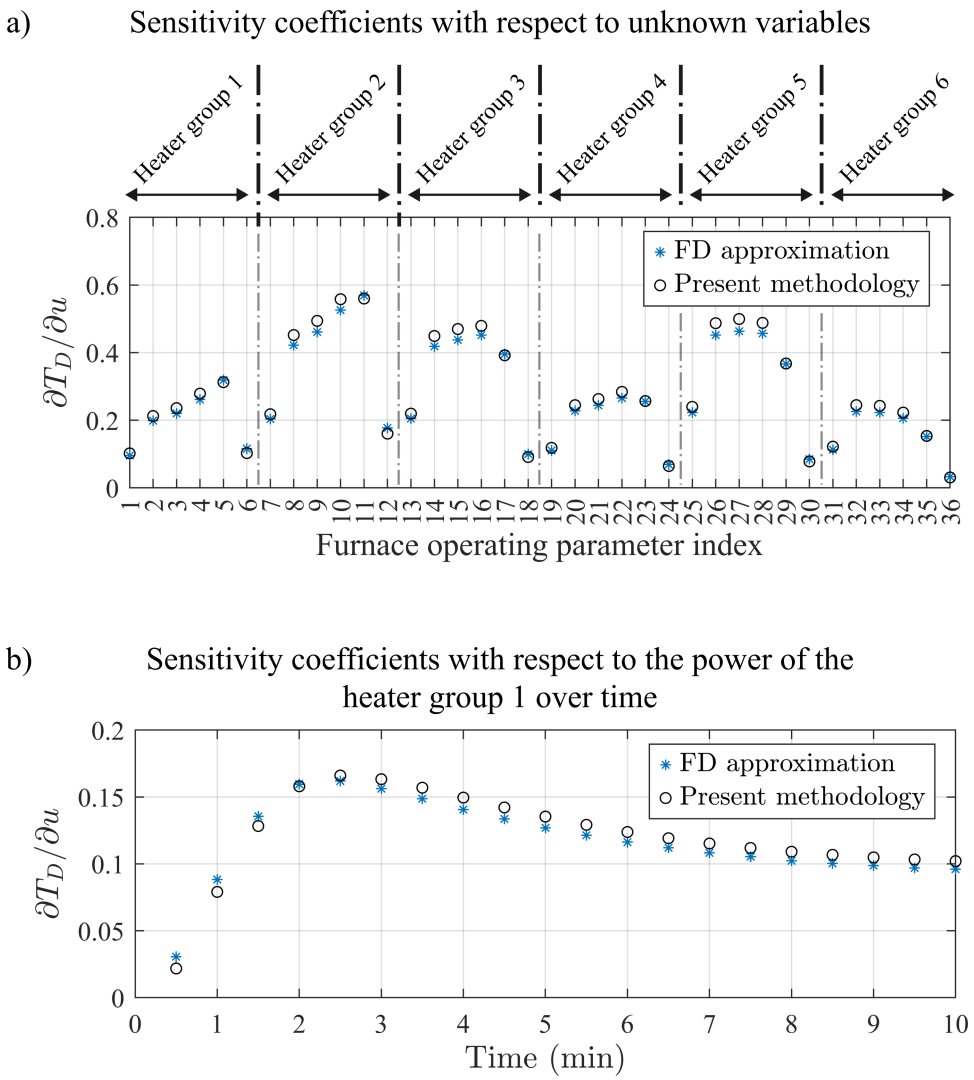


Figure 45: Sensitivity coefficient verification analysis. (a) Sensitivity coefficients related to the temperature at the first design point at $t = 10$ minutes. (b) Time evolution of sensitivity coefficient related to the temperature at the first design point with respect to power of the first heater group.

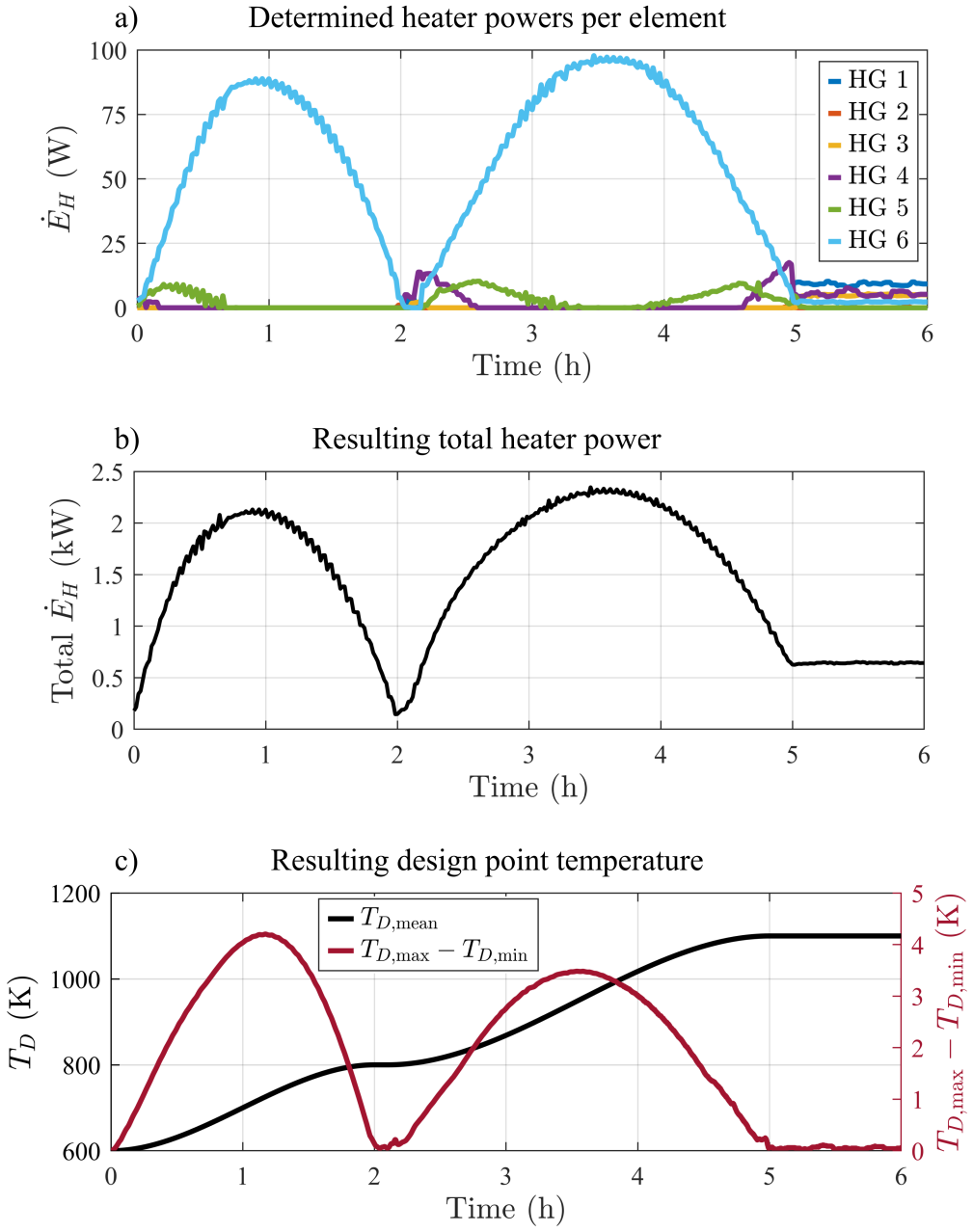


Figure 46: Findings of the inverse solution for uniform heating: (a) Determined powers for six heater groups per element. 'HG' denotes heater group index. (b) Total heater power needed for the treatment. (c) Resulting design point temperatures.

elements including chamber and heaters. This indicates that 46.0% of the supplied energy was transferred to the workpiece for the desired heat treatment.

Fig. 46(c) illustrates the average temperatures of the design points resulting from the determined heater powers. The graph also depicts the maximum temperature deviations in the mean temperatures over time on the right y-axis, indicating the uniformity of temperature distribution across the design points. The results indicate that the design point temperatures effectively followed the desired heating profile depicted in Fig. 43, with a maximum temperature deviation of less than 4.5 K, signifying successful temperature uniformity. During the soaking periods, which initiated around 2 hours and 5 hours into the process, exceptional temperature uniformity of less than 0.2 K was achieved at the design points.

The temperatures of six heater element groups resulting from the determined powers are presented in Fig. 47(a), exhibiting a pattern consistent with that observed in the determined heater powers. Additionally, the heater temperatures at certain time points are illustrated on the geometry in Fig. 47(b). These findings highlight a noteworthy phenomenon: achieving uniform treatment across the workpiece necessitates highly nonuniform heater temperatures, with variances reaching up to 364 K during the initial stages of heating. However, as the process progresses into soaking phases, the variance in heater temperatures diminishes significantly. Importantly, the dynamic adjustment of heater temperature patterns by the determined powers plays a crucial role in promoting uniform treatment, particularly during transitions between heating and soaking stages.

Furthermore, Fig. 48 presents the resulting workpiece surface temperatures at 1-hour intervals throughout the six-hour heating process. Notably, during the heating, including the intermediate soaking phase, the highest temperatures were observed in the central region and at the corners. As the process transitions to the soaking phase, temperature uniformity is enhanced, resulting in a changed workpiece surface

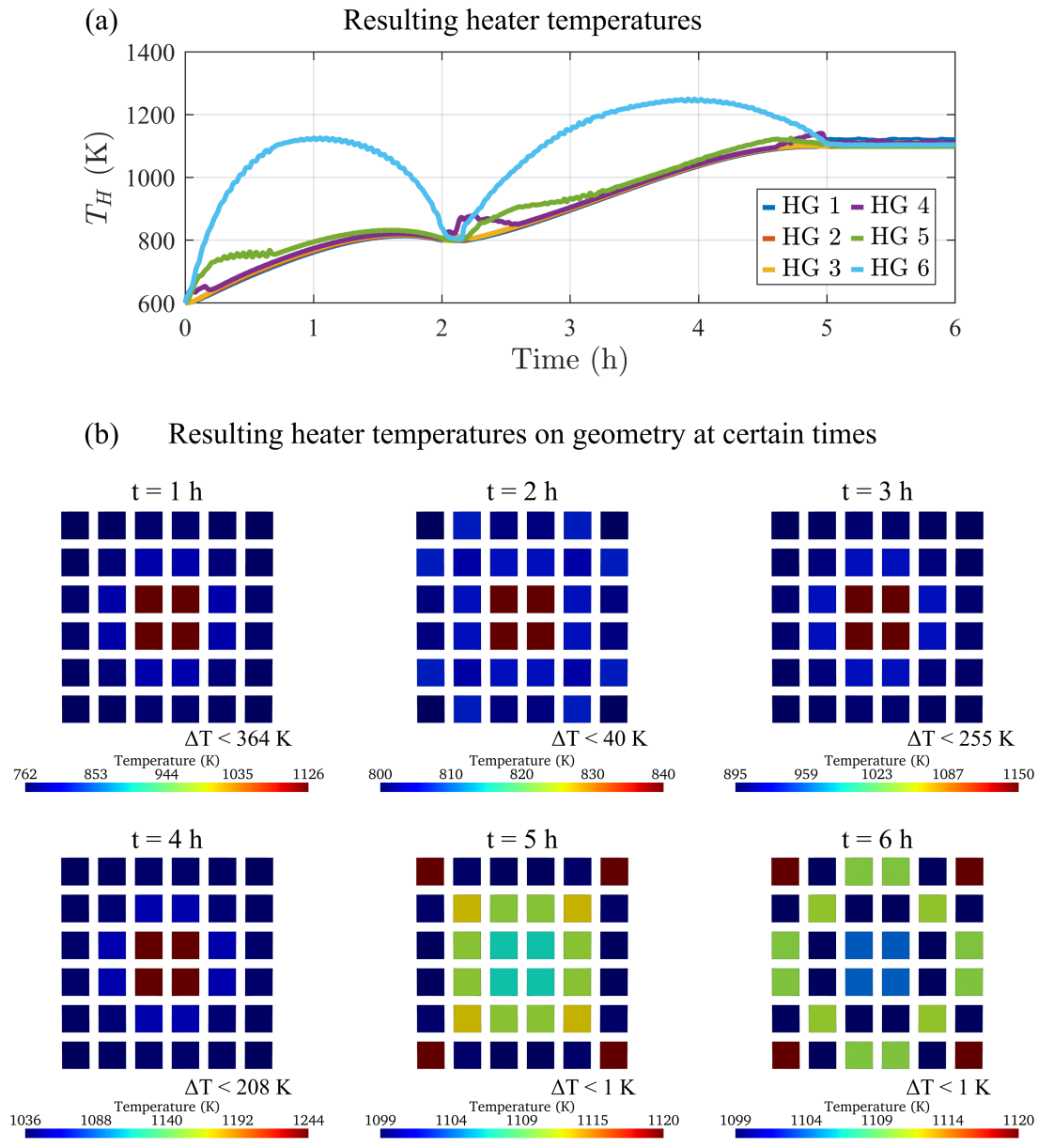


Figure 47: Resulting heater temperatures for uniform heating: (a) A line plot representing the temperatures of six heater groups over time. 'HG' denotes heater group index. (b) Visualization of temperatures at specific time points on the geometric layout. The color code illustrates the local temperatures at these times. ΔT denotes the maximum temperature differences between heater elements.

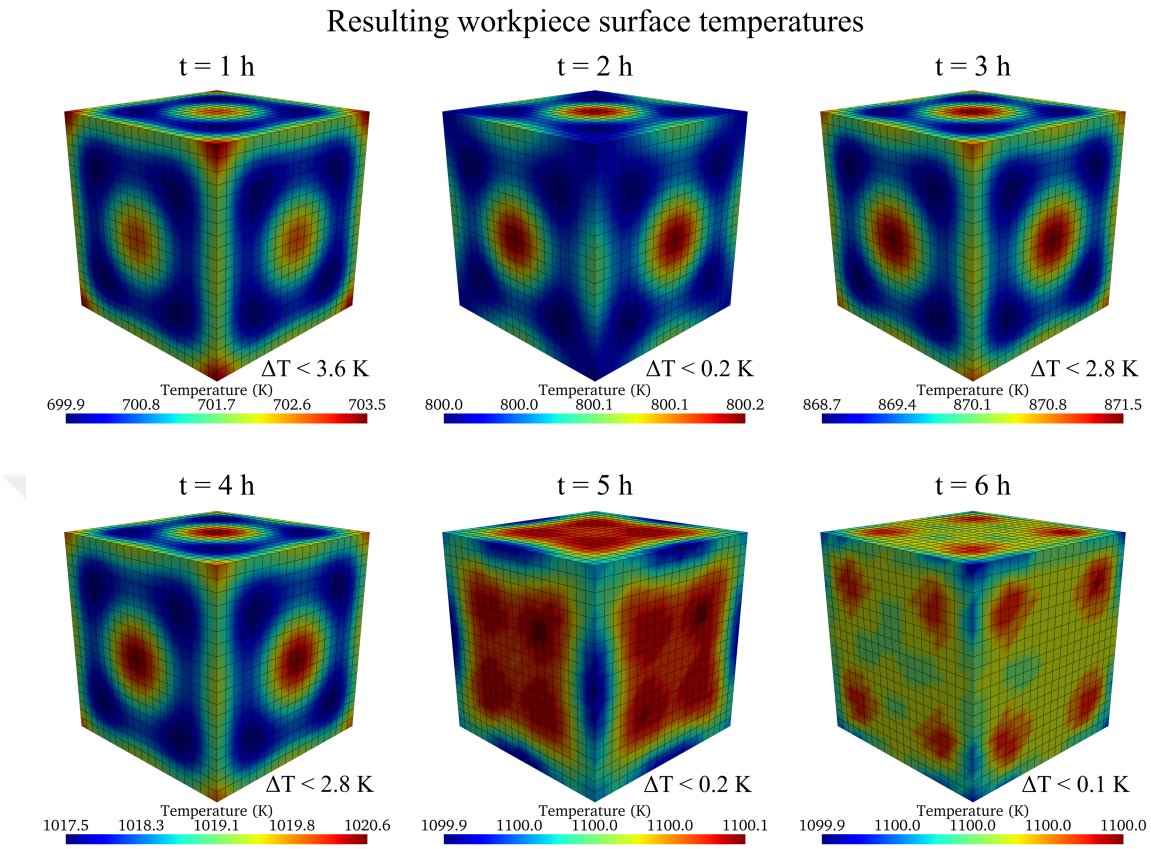


Figure 48: Resulting workpiece surface temperatures at specific times. ΔT denotes the maximum temperature difference at specified times.

temperature pattern.

In addition to the surface temperatures, the resulting temperature field inside the workpiece is depicted in Fig. 49. This figure shows the internal temperature distribution, highlighting the temperature variations (ΔT) within one-eighth of the workpiece volume at each time point. As expected, significant temperature gradients exist during the heating phases. Across the entire workpiece volume, temperature differences remained below 15.2 K. By the end of the six-hour period, during the soaking phase, the temperature uniformity improved significantly, with temperature gradients substantially reduced.

Fig. 50 demonstrates the incoming radiative heat flux on the workpiece surface

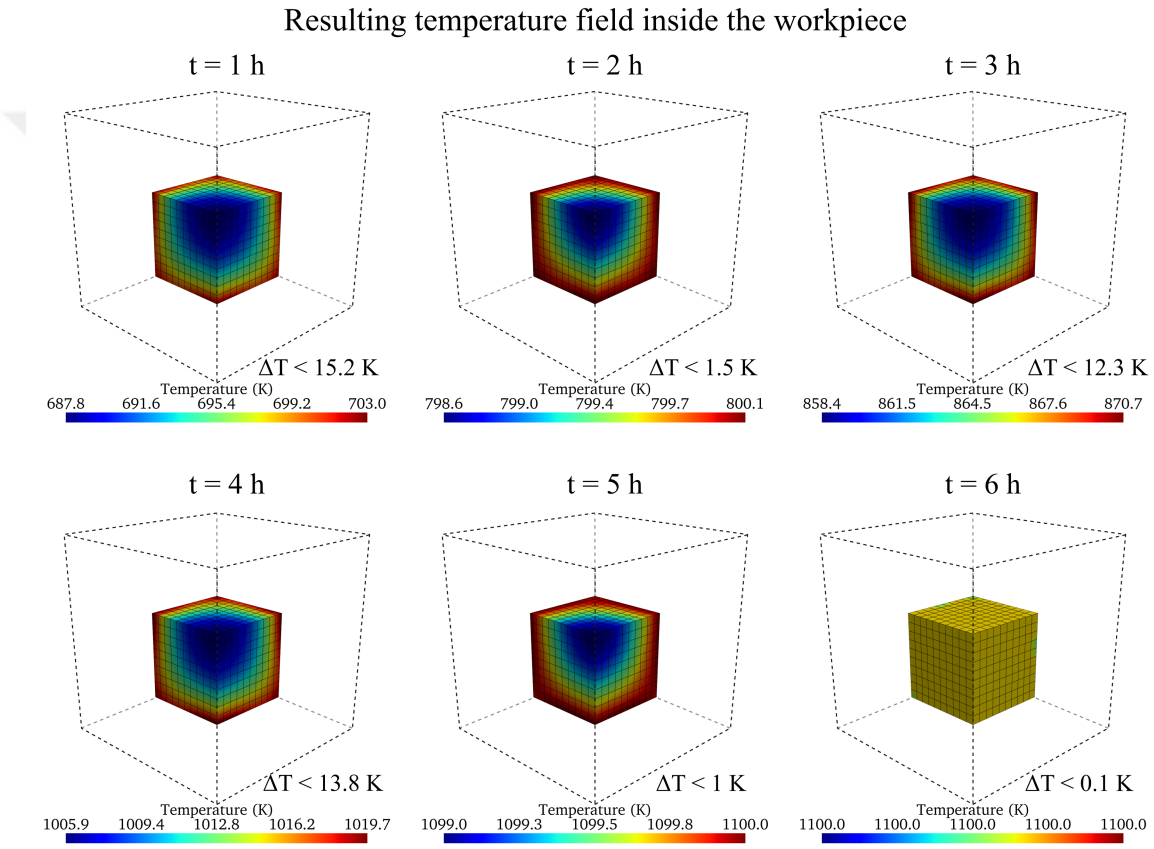


Figure 49: Resulting temperature field inside the workpiece (representing one-eighth of the entire workpiece) at specific times. ΔT denotes the maximum temperature difference at specified times.

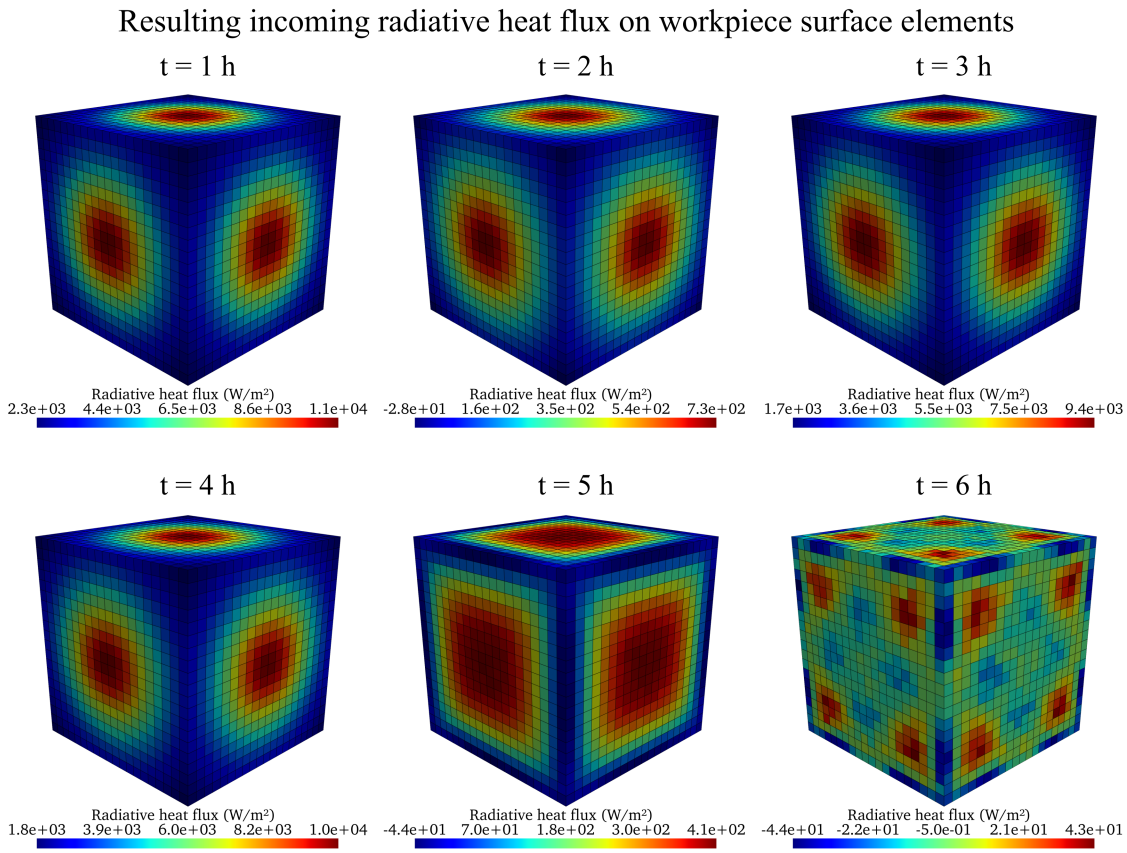


Figure 50: Resulting incoming radiative heat flux on workpiece surface elements at specific times

elements. With the determined heater powers from the inverse solution, it is observed that the heat is primarily provided from the central region of the workpiece. The magnitudes of radiative heat flux in the soaking phases show reduced values, aligning with the requirement for temperature uniformity. By the end of the process, a checkerboard-like pattern is observed in the radiative heat flux distribution, which is a result of the adjusted power levels of the heater elements to ensure temperature uniformity.

8.4.2 Impact of Overall Heat Transfer Coefficient $\bar{U}$

The impact of the overall heat transfer coefficient $\bar{U}$, governing the heat loss from the furnace chamber to the environment as detailed in Section 2.3.4, has been investigated for values of 0.92, 1.33, and 2.45, with the value of 1.33 corresponding to the reference

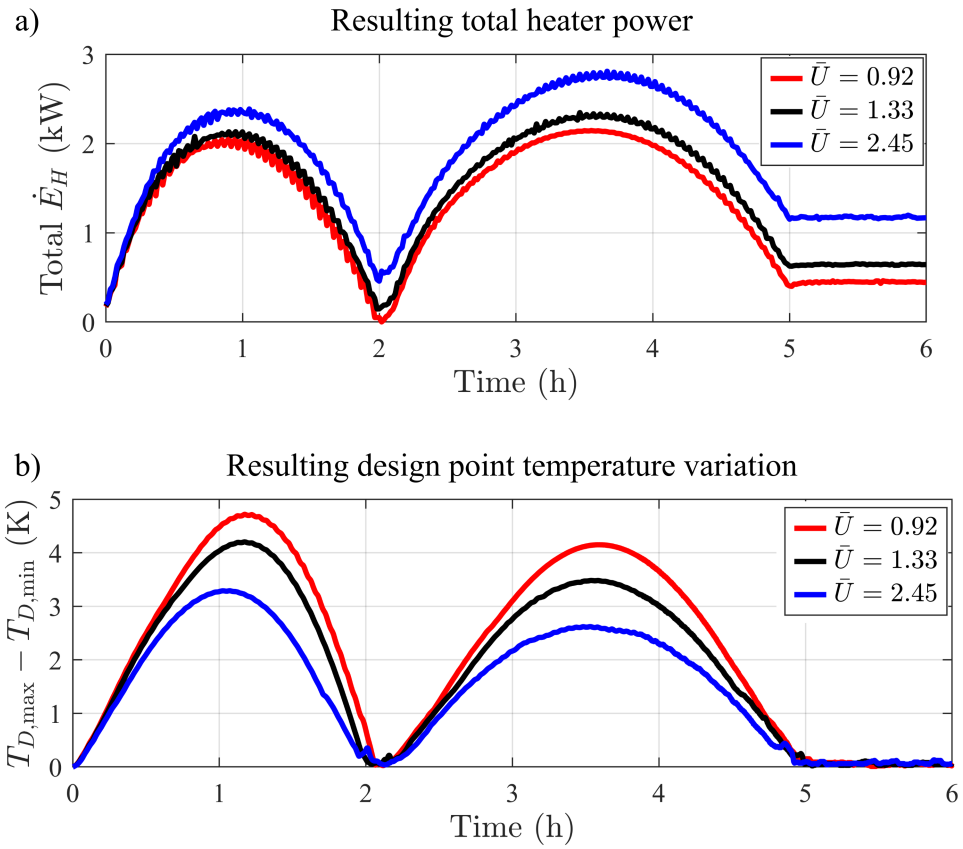


Figure 51: Impact of the overall heat transfer coefficient on (a) total heater powers and (b) temperature uniformity at the design points

case. Those $\bar{U}$ values were obtained as described in Section 8.1.1.

The temporal powers at each heater group determined for the considered $\bar{U}$ values exhibited similar patterns to the reference case. In Fig. 51(a), the resulting total heater powers over time are depicted. The comparison shows that higher $\bar{U}$ values requires increased total heater power during the treatment. This is anticipated, as higher energy loss to the environment naturally necessitates greater power requirements for the treatment.

Importantly, the design point temperatures resulting from the determined heater power using inverse solutions, as depicted in Fig. 51(b), suggest that increasing $\bar{U}$ yields a noticeable enhancement in the uniformity of design point temperatures. This

suggests that higher heat loss to the environment enables achieving better temperature uniformity at the design points, facilitated by the determination of necessary heater powers through the inverse solution.

Table 6 summarizes the resulting energy consumption, energy loss to the environment, and estimated furnace exterior shell temperatures while comparing various insulation levels with corresponding $\bar{U}$ values. Given that the inverse solution achieved uniform treatment to a reasonable extent in each case, such comparative analyses offer valuable guidance to design engineers in their decision-making processes.

Table 6: Impact of the overall heat transfer coefficient on energy considerations with estimated equivalent insulation thicknesses

	Insulation thickness (cm)	$\bar{U}$ (W/m^2K)	Energy consumption (kWh)	Energy loss to environment (kWh)	Exterior shell temperature (°C)
High insulation	15	0.92	7.81	2.04	76
Reference case	10	1.33	8.67	2.92	95
Low insulation	5	2.45	10.98	5.25	137

The findings of this investigation suggest that heat loss to the environment serves as a balancing factor for achieving more uniform treatment, enabling the heaters to respond more effectively to enhance temperature uniformity. Despite reducing energy consumption, improved furnace insulation with lower $\bar{U}$ comes at the cost of compromised temperature uniformity. This highlights an inverse proportion between heat loss to the environment and the uniformity of workpiece temperature.

8.4.3 Impact of Chamber Reflectivity

The impact of chamber surface reflectivity on the heat treatment process is investigate, noting that reflections within our model are diffuse. We addressed this by

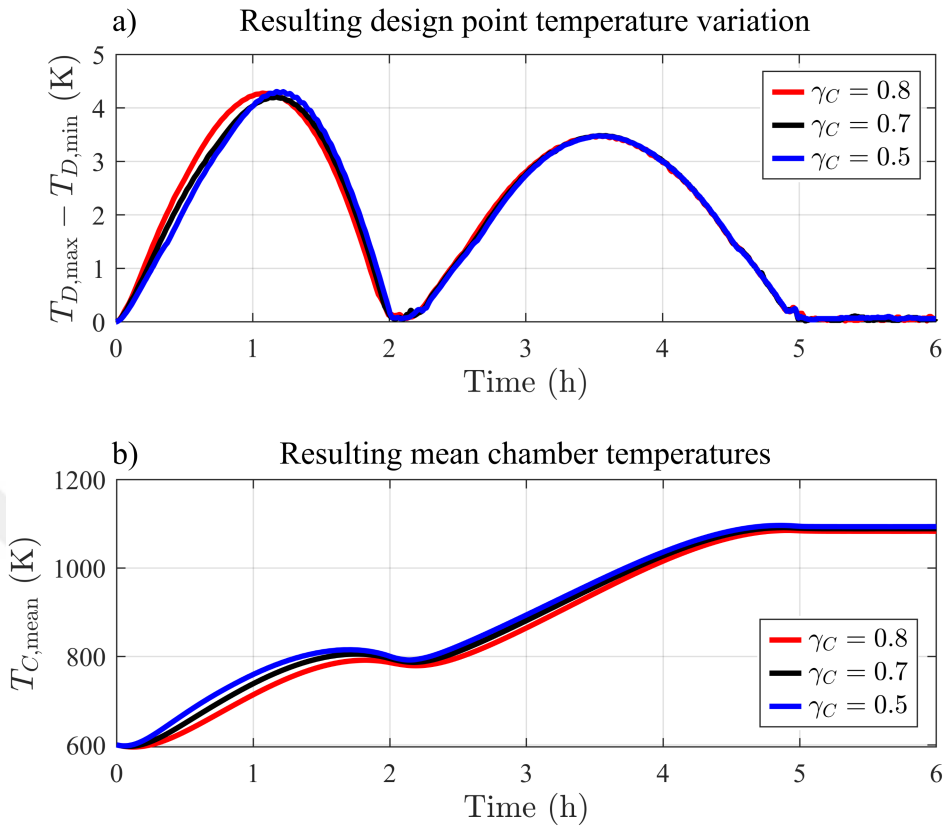


Figure 52: Impact of the chamber surface reflectivity on (a) temperature uniformity at the design points and (b) resulting mean chamber temperatures

solving set of inverse problems with chamber reflectivity values of 0.8, 0.7, and 0.5, with 0.7 being the value corresponding to the reference case. Our findings showed that varying chamber reflectivities did not substantially alter the determined heater powers, suggesting minimal influence on the required heater powers for achieving uniform treatment. Similarly, there were no significant differences observed across the resulting design point temperature uniformities, as evidenced in Fig. 52(a).

However, notable disparities were noted in mean chamber temperatures for different chamber reflectivities. Fig. 52(b) illustrates that surfaces with higher reflectivity consistently resulted in lower mean chamber temperatures throughout the treatment process.

Moreover, the resulting energy consumption and energy loss to environment, as

provided in Table 7, revealed that surfaces with low reflectivity resulted in higher chamber temperatures, subsequently increasing heat loss from the chamber to the environment and leading to higher energy consumption. Specifically, high reflective chamber surfaces showed a 1.7% decrease in energy consumption and a 4% reduction in energy loss to the environment compared to the case with low reflectivity.

Table 7: Impact of the chamber surface reflectivity on energy considerations

	Chamber reflectivity	Energy consumption (kWh)	Energy loss to environment (kWh)
High reflectivity	0.8	8.59	2.85
Reference case	0.7	8.67	2.92
Low reflectivity	0.5	8.74	2.97

These findings suggest that energy efficiency can be enhanced by employing high reflective chamber surfaces without compromising design point temperature uniformity. This highlights the potential for optimizing energy usage in heat treatment processes through strategic selection of chamber reflectivity.

8.4.4 Impact of Heater Layout

The investigation extended to explore the impact of heater layout on the heat treatment process, comparing two layouts: 4×4 and 6×6, with the latter serving as the reference case. The 4×4 layout with its heater element group arrangement is presented in Fig. 53, while maintaining the total heater area consistent for both layouts. Specifically, with edge lengths of 3 cm and 4.5 cm for the 6×6 and 4×4 layouts, respectively, each furnace face retained a total heater area of 324 cm^2.

Upon solving the inverse problem for the 4×4 layout, the resulting heater powers per element for the heater groups, shown in Fig. 54(a), exhibited a pattern similar to the reference case. Heating is predominantly governed by the center heater elements, with lesser contribution from the others compared to the 6×6 layout.

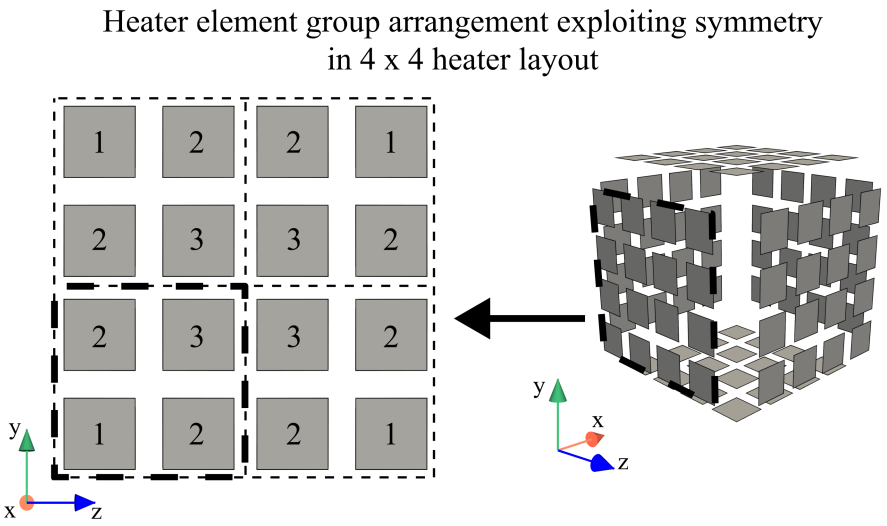


Figure 53: Arrangement of heater element groups in 4×4 layout exploiting geometric symmetry, where the numbers represent the three distinct heater groups. The 4×4 layout on the left is replicated on each face of the cubic heater configuration to the right.

Comparison of the resulting design point temperature variances between the 6×6 and 4×4 heater layouts, as illustrated in Fig. 54(b), revealed that the 6×6 layout achieved better temperature uniformity in treating the workpiece. This suggests that employing more heater elements enhances heater power adjustment ability, leading to improved uniform treatment.

Additionally, the resulting heater temperatures for the 4×4 heater layout are observed more uniform compared to 6×6. Specifically, the maximum temperature variations among the heaters decreased from 365 K to 221 K within the first hour. Considering energy consumption, employing the 4×4 heater layout resulted in 0.01 kWh (0.1%) increase in consumed energy compared to the 6×6 layout.

Overall, our findings highlight the significant influence of heater layout on the furnace's capability to ensure uniform temperatures for the heat treatment of the workpiece.

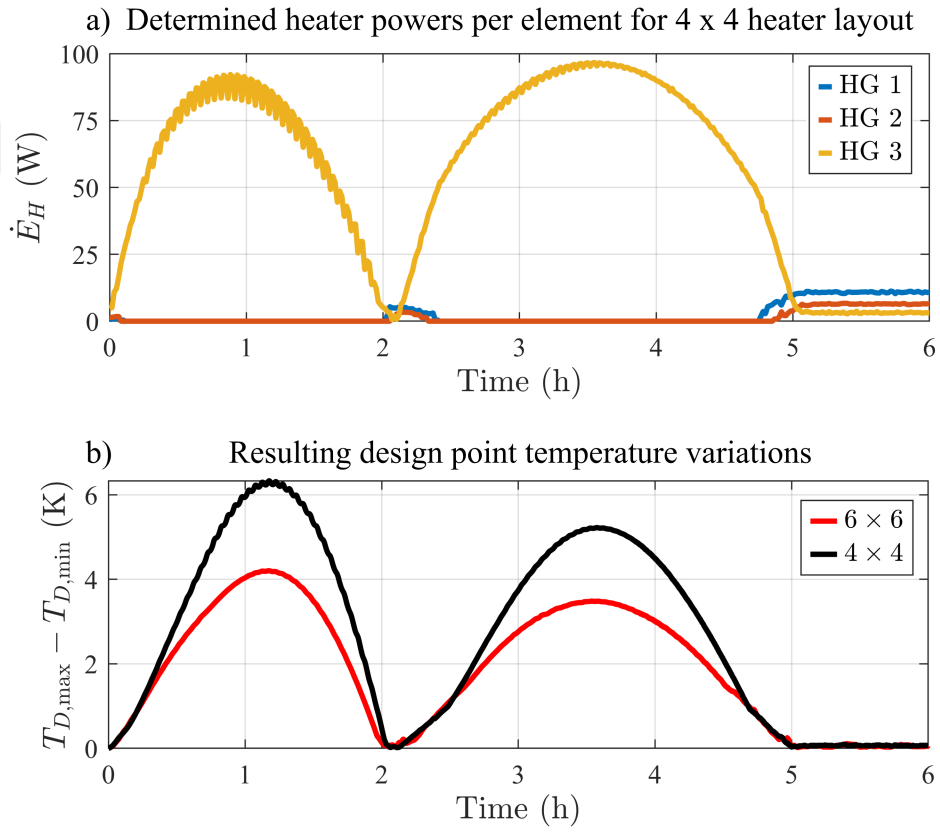


Figure 54: (a) The determined powers of heater groups per element in 4×4 heater layout. 'HG' denotes heater group index. (b) Impact of the heater layout on temperature uniformity at the design points

8.4.5 Impact of Heater Material

The following investigation focuses on how different heater materials affect the heat treatment process, with graphite being used as the reference case and tungsten as the alternative material.

The inverse solution using tungsten heaters yielded heater powers with a pattern and magnitudes closely resembling those obtained with graphite heaters When comparing the resulting design point temperature uniformities with tungsten heaters, as illustrated in Fig. 55(a), we observed only a minor difference, which is often insignificant for practical applications. Comparing the total heater powers over time, Fig. 55(b) illustrates that initially, tungsten heaters required slightly more power to achieve the desired uniformity. However, as the treatment progressed, this difference became negligible.

The temperatures of the six heater element groups, depicted in Fig. 55(c), showed significantly higher temperatures for tungsten heaters while maintaining a similar pattern to graphite heaters. Our findings revealed that utilizing tungsten heater also influenced the energy requirements of the treatment process, leading to an increase in the net furnace stored thermal energy from 1.77 kWh to 1.91 kWh (7.9%). Consequently, the total energy consumption rose by 1.6% compared to the reference case with graphite heaters.

These findings are consistent with tungsten's higher thermal inertia and surface reflectivity relative to graphite, indicating that materials with higher reflectivity necessitate elevated temperatures to deliver the required radiative heat flux to the workpiece. In essence, although tungsten heaters had a negligible impact on treatment uniformity, the increased energy consumption underscores the importance of carefully selecting appropriate heater materials for particular applications and prioritizing energy efficiency.

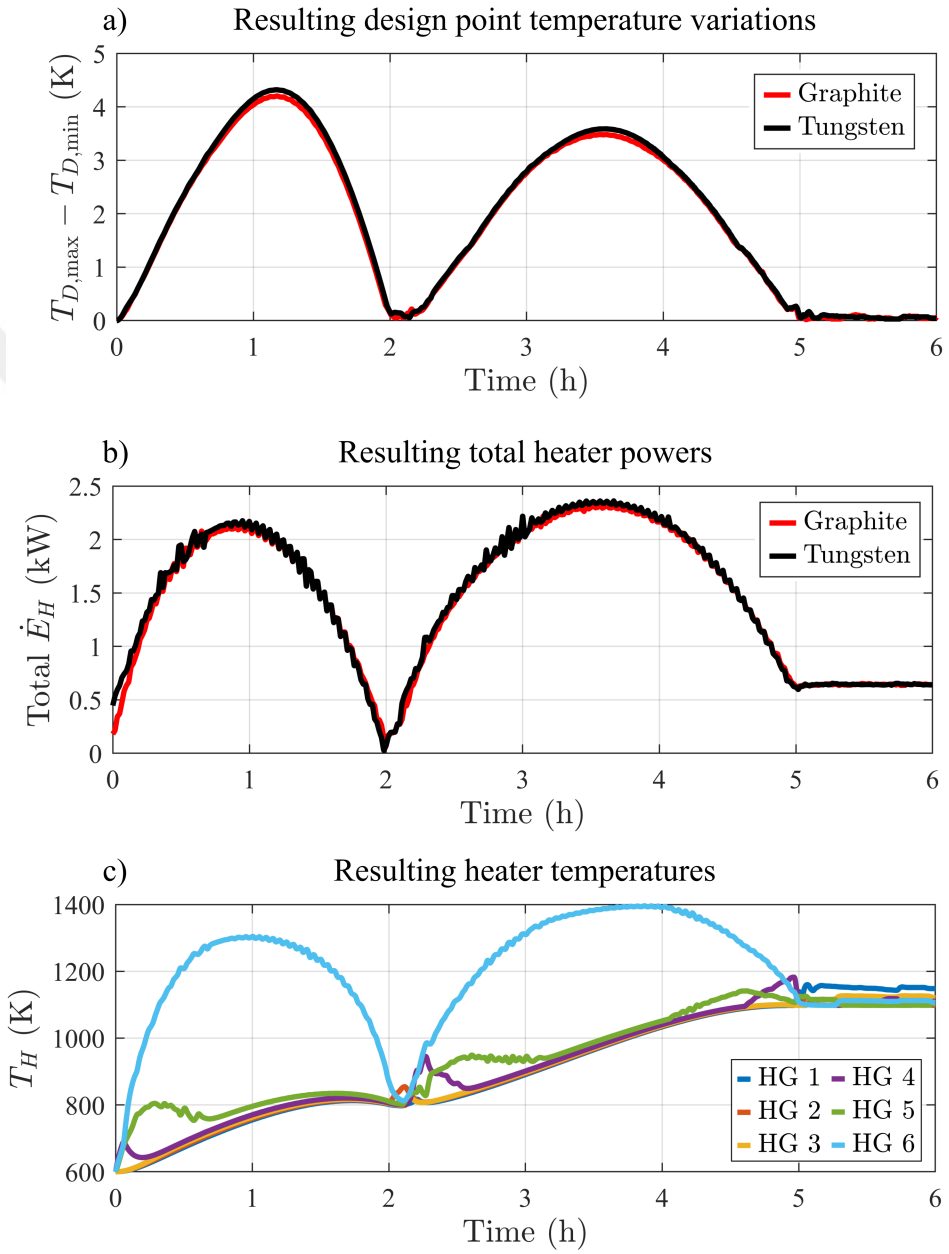


Figure 55: Comparison of the impact of heater material on (a) resulting design point temperature variations, (b) total heater powers, and (c) heater temperatures. 'HG' denotes heater group index.

8.5 Computational Time Costs

The time required for computing inverse solutions varied between 32 and 88 minutes, depending on the specific scenario. For the reference case, the total computation time was 49 minutes. Within this duration, approximately 55% of the time was allocated to solving the forward problem, while 42% was spent on calculating the sensitivity coefficients.

8.6 Concluding Remarks

This chapter investigates the impact of furnace configuration and material on the performance of radiant furnaces during the transient heat treatment of a cubic workpiece. The study considers various parameters, including the overall heat transfer coefficient, chamber reflectivity, heater layout, and heater material, to optimize the heating process and achieve uniform temperature distribution. The analysis is conducted using the developed inverse solution methodology to determine the necessary heater powers, evaluate the resulting treatment uniformity and energy consumption.

The outcomes of this chapter reveal significant insights into optimizing furnace operation for efficient and uniform heat treatment. By solving the inverse problem, the study provides a detailed understanding of how different configurations and materials affect the heating process, leading to practical recommendations for real-world applications.

Below, we summarize the key findings and their implications:

- **Achieved Temperature Uniformity:** The inverse solutions successfully determined the required transient heater powers to achieve uniform treatment of the workpiece. The resulting design point temperatures followed the desired heating profile with a maximum deviation of less than 4.5 K, and during the soaking periods, temperature uniformity was achieved within 0.2 K.

- **Relative Contributions of Heater Groups:** The central heater groups (Group 6) primarily drove the heating process, while edge heaters played a crucial role during transitions to maintain uniformity. Temporal adjustment of heater powers, such as reducing center heater power and increasing edge heater power, effectively managed transitions between heating and soaking phases, ensuring consistent temperature uniformity across the workpiece.

- **Workpiece Thermal Characteristics:** The highest workpiece surface temperatures were observed at the center and corners during heating, while temperature uniformity improved during the soaking phase, reducing temperature gradients significantly. The incoming radiative heat flux primarily concentrated at the central regions of the workpiece, with a checkerboard-like pattern emerging towards the end of the process. These insights into surface temperatures and heat fluxes are vital for optimizing heat distribution and achieving uniform treatment in heat-sensitive materials.

- **Overall Heat Transfer Coefficient:** The heat loss from chamber surface to environment is modeled utilizing an overall heat transfer coefficient $\bar{U}$. Higher $\bar{U}$ values required increased total heater power, while achieving more uniform treatment process, highlighting inverse relation between heat loss to environment and treatment uniformity.

- **Chamber Reflectivity:** High reflective chamber surfaces showed a 1.7% decrease in energy consumption and a 4% reduction in energy loss compared to low reflectivity. Using high reflectivity materials in furnace design can enhance energy efficiency, leading to cost savings and reduced environmental impact.

- **Heater Layout:** The 6×6 heater layout achieved better temperature uniformity than the 4×4 layout. An increased number of heaters improves the furnace's ability to ensure uniform treatment processes.

- **Heater Material:** Tungsten heaters required slightly more initial power but had a negligible impact on treatment uniformity, with a 1.6% increase in energy consumption compared to graphite heaters. Selecting appropriate heater materials affects energy consumption and furnace performance, guiding material choices to enhance efficiency and effectiveness in industrial applications.

The findings of these investigations provide valuable guidance for optimizing furnace design and operation in industrial settings. By understanding the effects of different configurations and materials, engineers can make informed decisions to enhance energy efficiency and achieve uniform heat treatment, which is crucial for the quality and performance of treated materials. The outcomes of this chapter contribute to improving the thermal management of radiant furnaces, leading to better resource utilization and reduced operational costs.

CHAPTER IX

EVALUATING FURNACE OPERATION PRACTICES FOR ACHIEVING DESIRED COOLING OF STAINLESS-STEEL CUBIC WORKPIECE

This chapter focuses on determining the necessary furnace operating conditions for the cooling phase of a transient heat treatment process for a stainless-steel cubic workpiece within a radiant furnace. The goal is to reduce the temperature uniformly across all design points within the workpiece, ensuring minimal variation in temperatures. The furnace must be operated in such a way that both heater and chamber powers are adjusted to achieve this uniform cooling.

To address this problem, two distinct approaches for determining furnace operating conditions were investigated: Operating Group Set 1, which uses predefined constant cooling, and Operating Group Set 2, which simultaneously adjusts heater and chamber powers through an inverse solution approach. These approaches are systematically examined, comparing their effectiveness in achieving uniform cooling, analyzing energy requirements, and understanding the dynamic behavior of heater and chamber elements. The investigations provide comprehensive insights into the operational dynamics during the cooling phase, highlighting the trade-offs and optimization strategies for enhancing treatment uniformity.

9.1 Problem Definition: Cooling Phase of a Cubic Workpiece in a Radiant Furnace

The cooling phase of the transient heat treatment of a cubic workpiece within a radiant furnace is examined. The geometric setup, materials, and spatial discretization are identical to those specified during the heating phase, as described in Chapter 8. Similarly, the thermal model, including the heat loss from the furnace chamber to the environment, remains unchanged from the one utilized during the heating phase, as detailed in Section 8.1.1.

Initial conditions for the cooling phase are set according to the system's final thermal state, including both the furnace and workpiece, at the conclusion of the heating phase. These conditions were established through the inverse solution of the reference case, detailed in Section 8.4.1 of the preceding chapter, which identified the temperatures of both the furnace and workpiece to be around 1100 K.

While the cooling phase is considered for up to a maximum duration of one hour, the objective is to ensure uniform cooling across all design points within the workpiece. To achieve this, we utilize an inverse solution approach to determine the furnace's operating parameters, facilitating a adjusted and even cooling process.

9.2 Design Variable and Furnace Operating Surface Grouping

We continue to employ the Power-based Approach, extensively used in previous chapters to determine the necessary power settings for furnace operating surface elements. Previously, our focus was exclusively on the heating phases, where the design variables—either heater temperatures or heater powers—were defined at the heater elements.

As we transition our focus to the cooling phase, the configuration of radiant furnaces encourages an exploration of varied furnace operating approaches. Typically,

distinct surfaces within these systems facilitate heating and cooling because using heater elements for cooling is impractical due to the challenges associated with efficient heat removal. To explore strategies such as balancing predefined cooling with heater operation or simultaneously managing heaters and cooling elements in a single inverse solution, we have implemented two distinct Operating Group Sets.

9.2.1 Operating Group Set 1

Operating Group Set 1 includes only the heater groups, which are represented in Fig. 56(a), remaining the same as in Chapter 8. In this group set, cooling is primarily provided by an additional cooling source, denoted $\bar{U}_{\text{cooling}}$, applied similarly to how the overall heat transfer coefficient addresses heat loss from chamber surface elements. This primary cooling source $\bar{U}_{\text{cooling}}$ is predefined. In this setup, the heater powers—determined through an inverse solution—act as a counterbalance a predefined cooling source, allowing precise adjustment for the desired uniform cooling treatment.

9.2.2 Operating Group Set 2

Operating Group Set 2 comprises both the heater groups and chamber groups. The chamber surfaces, as depicted in Fig. 56(b), are grouped into four concentric chamber groups for each furnace face. This configuration allows for deliberate management over the furnace's cooling conditions. The inverse solution for Operating Group Set 2 involves solving for the necessary powers for both the heater element groups and the chamber surface groups.

Summarized in Fig. 56(c), these two group sets are intended to explore the outcomes of various furnace operation strategies, with their operating parameters determined through separate inverse solutions. The impact of these strategies on resulting cooling performance, energy requirements, and the trade-offs between the findings of these two operating group sets are evaluated.

It is worth reminding that the furnace operating surface elements within a single

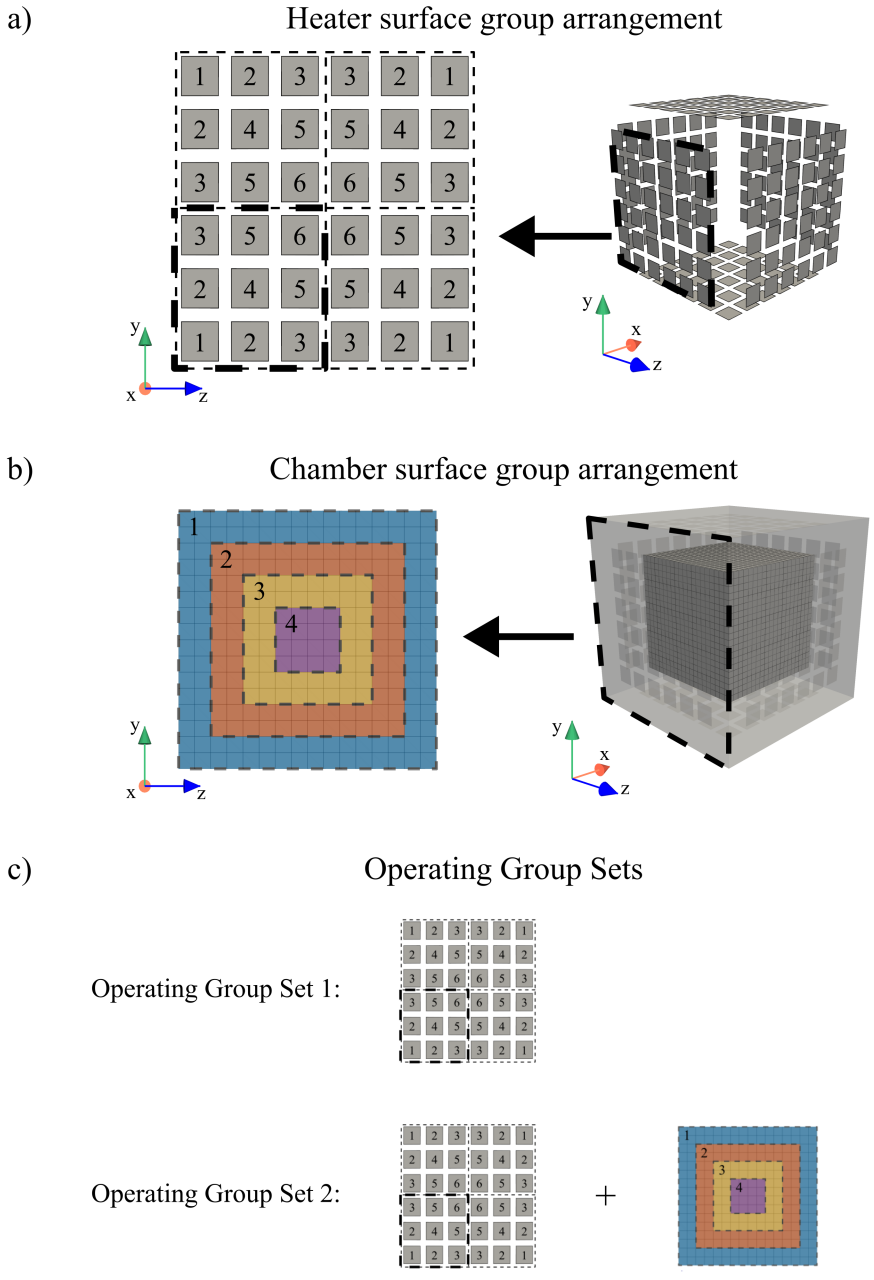


Figure 56: (a) Arrangement of heater element groups with the indices for six heater element groups. (b) Arrangement of chamber surface groups with the indices for four chamber surface groups. The arrangements on the left are replicated on each face of the cubic heater configuration to the right. (c) The operating surfaces employed in two distinct Operating Group Sets.

group are operated by the same set of operating parameters (unknown variables). This grouping of furnace surface elements is made possible by the pursuit of uniform treatment and the utilization of geometric symmetry, which also reduces the number of unknowns in the inverse problem.

9.3 Numerical Settings and Parameters

This chapter employs a setting similar to that discussed in previous chapters but is adapted to meet the specific requirements of the cooling phase.

The one-hour-long time domain is now divided into a total of 20 subdomains. Each subdomain spans 3 minutes, with overlaps extending by 1 minute to ensure accuracy across transitions. Each inverse problem is solved within a maximum time frame of 4 minutes, disregarding results beyond the 3-minute mark.

For Operating Group Set 1, which employs only heater groups, we continue using the regularization approach from Section 8.2, adjusting the regularization weight to $\zeta = 100$ to facilitate smoother transitions in heater powers over time.

For Operating Group Set 2, which includes both heater and chamber groups, we expand the regularization approach. The term $w_{\bar{h},1} = [1\ -1][u_{\bar{h},1}\ u_{\bar{h},2}]^T = u_{\bar{h},1} - u_{\bar{h},2}$ for heater groups is retained as used in previous chapters. For chamber groups, we introduce a similar term $w_{\bar{c},1} = [10\ -10][u_{\bar{c},1}\ u_{\bar{c},2}]^T = 10u_{\bar{c},1} - 10u_{\bar{c},2}$. Additionally, to minimize the magnitude of the power levels, a term $w_{\bar{f},1} = u_{\bar{f},1}$ is included for both groups. This regularization setup is scaled with a regularization weight of $\zeta = 10$.

9.4 Results

This chapter presents the results from optimizing the cooling phase of the heat treatment process, focusing on achieving uniform cooling across all design points. We explore two distinct cases each employs unique furnace operation approach.

Initially, we explore a forward solution with a predefined cooling source to establish a baseline for the cooling dynamics of both the workpiece and the furnace.

In Case 1, we consider a design condition derived from the resulting design point temperatures obtained from that forward solution. An inverse solution is then employed, utilizing both Operating Group Set 1 and Operating Group Set 2. This case provides critical insights into the trade-offs between the operating group sets.

In Case 2, we focus exclusively on Operating Group Set 2, guided by a user-defined cooling curve. This approach tests the adaptability of the inverse solution procedure to achieve specific cooling profiles and ensures a uniform treatment that matches the desired cooling trajectory.

9.4.1 Forward Solution with Predefined Cooling Source

This section examines the thermal behavior under a predefined cooling source, established by the term $\bar{U}_{\text{cooling}}$. This additional overall heat transfer coefficient governing the predefined cooling at chamber surfaces is set at 0, 0, 25, and 50 W/m^{2}K for chamber surface groups 1, 2, 3, and 4, respectively, as the chamber surface groups are illustrated in Fig. 56(c). In this forward solution scenario, the heater elements are turned off.

The forward solution for this setup yielded the design point temperatures as illustrated in Fig. 57(a). Starting from the final temperatures discussed in the previous chapter, the mean design point temperature decreased from approximately 1100 K to 935 K, at an average rate of -2.75 K/min. The temperature variance across the design points remained under 15 K, with a peak variance observed around the 25-minute mark.

The predefined cooling source, $\bar{U}_{\text{cooling}}$, resulted in the chamber powers as depicted in Fig. 57(b). Initially, the cooling power for chamber group 4 was 15 W per single surface element, which gradually decreased to below 5 W by the end of the cooling phase.

Considering the entire system, the total chamber power required for cooling started

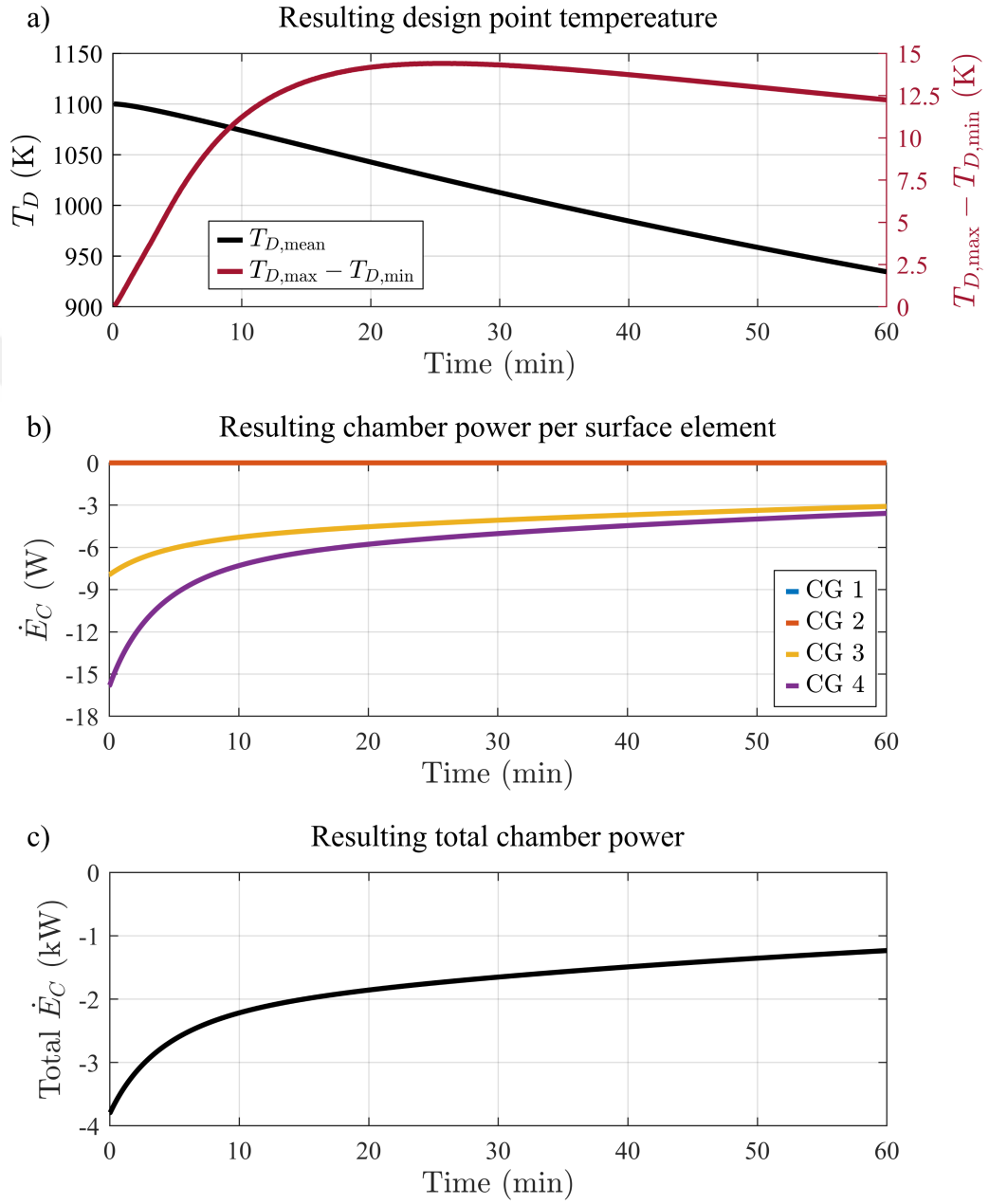


Figure 57: Results of the forward solution with the predefined cooling $\bar{U}_{\text{cooling}}$ at chamber surfaces: (a) Resulting design point temperatures. (b) Resulting chamber power per surface element for each chamber group, where 'CG' denotes the chamber group index. (c) Total chamber power required for the cooling treatment.

at approximately 4 kW, as shown in Fig. 57(c), and decreased to below 2 kW towards the end of the treatment.

Fig. 58 illustrates the cooling dynamics of the chamber surfaces. Fig. 58 (a) shows the time-dependent profiles of the maximum, mean, and minimum chamber temperatures, denoted by $T_{C,\max}$, $T_{C,\text{mean}}$, and $T_{C,\min}$, respectively. Fig. 58 (b) displays the spatial distribution of temperatures across the chamber surfaces at $t = 60$ minutes. The resulting chamber temperature pattern corresponds closely with the predefined cooling source $\bar{U}_{\text{cooling}}$ values, which are specifically cooling the chamber groups 3 and 4. This visual representation highlights significant cooling in specific regions, with cooler areas shown in blue contrasting sharply against warmer red areas. The disparity in temperature, which exceeds 400 K across the chamber surfaces, indicates substantial spatial temperature gradients. These sharp transitions in temperature suggest that an enhancement in the thermal modeling of furnace surfaces would be beneficial. A more refined model could potentially provide a more realistic depiction of heat transfer between adjacent surface elements, thus aiding in an enhanced analysis of the cooling phase.

Fig. 59(a) presents the heater element temperatures over a 60-minute cooling period, with each line representing a distinct heater group. Throughout the cooling phase, the temperatures of the heater elements exhibit a gradual decrease. Fig. 59(b) displays the spatial distribution of heater temperatures across the geometry at $t = 60$ minutes, revealing cooler temperatures in the central region, which demonstrates the influence of chamber cooling. Despite this localized cooling, the overall temperature distribution among the heater groups remains relatively uniform, with the greatest deviations being around 30 K.

The temperature distribution on the surface and within the internal domain of the workpiece after a 60-minute cooling phase is illustrated in Fig. 60. The surface temperature distribution shown in left side presents the highest temperatures at the

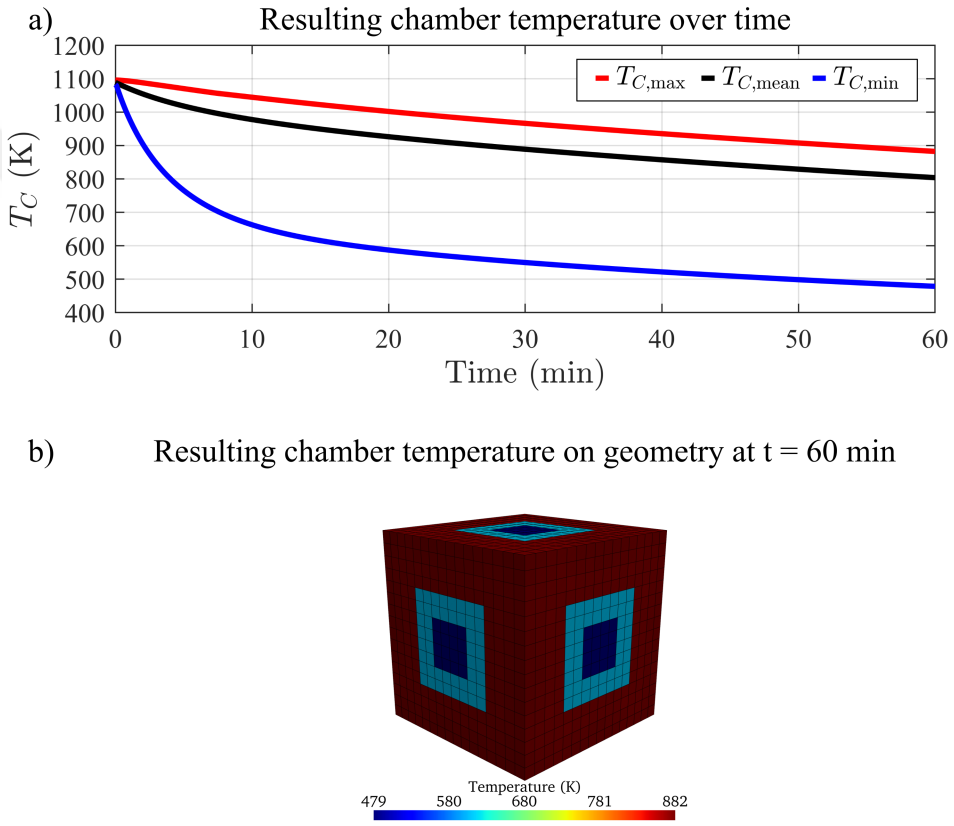


Figure 58: Resulting chamber temperatures: (a) Time-dependent profiles of the maximum, mean, and minimum chamber temperatures, demonstrating changes over a 60-minute period. (b) Spatial distribution of temperatures across the chamber surfaces at $t = 60$ minutes.

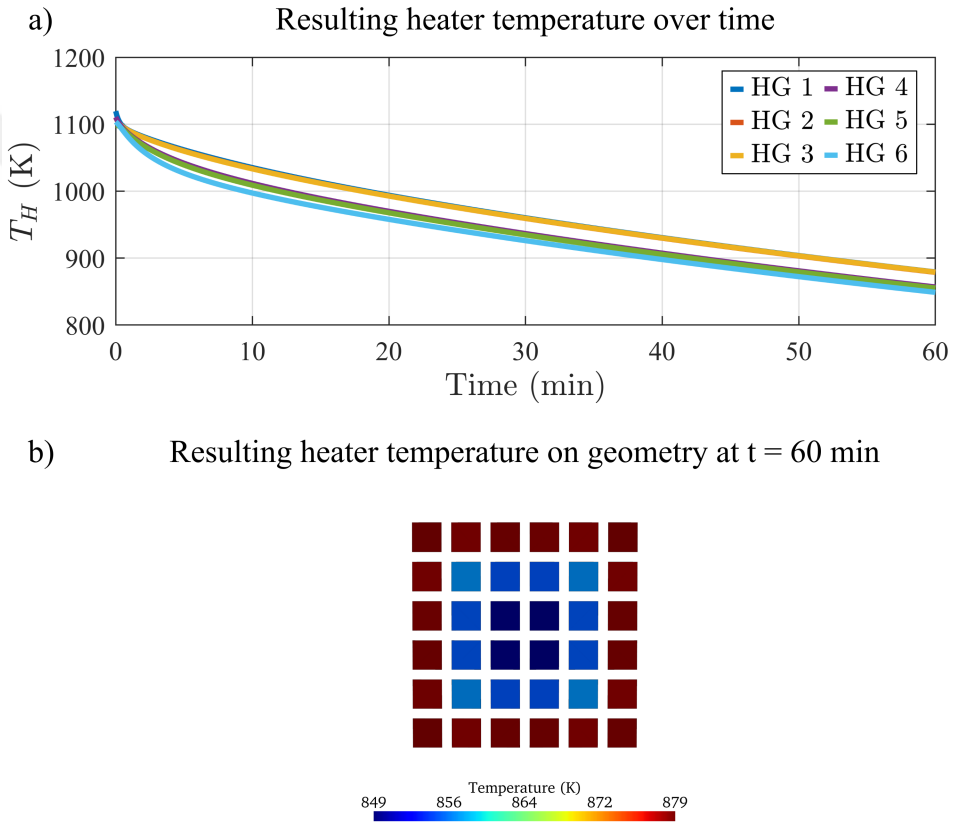


Figure 59: Resulting heater temperatures: (a) Heater element temperatures over a 60-minute, where each line corresponds to a different heater group, denoted as 'HG'. (b) Spatial distribution of temperatures across the heater elements at $t = 60$ minutes.

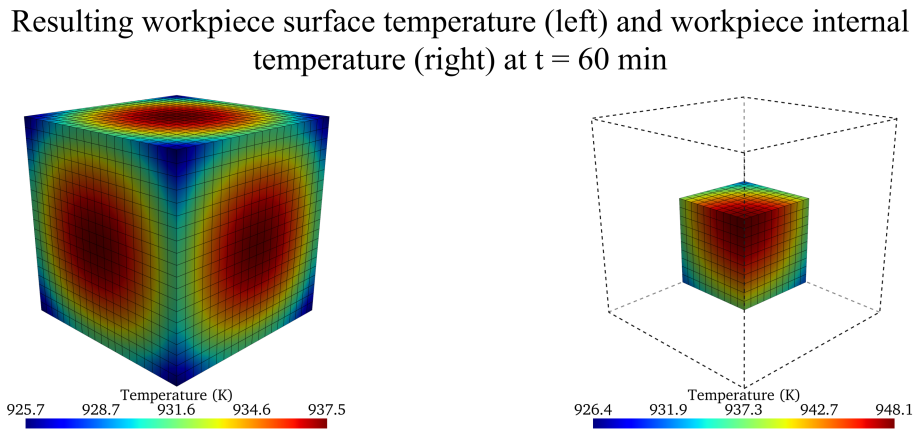


Figure 60: Temperature distributions of the workpiece on the surface showing a high-temperature center with cooler edges and corners (left), and within the internal domain (right, representing one-eighth of the entire workpiece), illustrating the slower cooling rates of the core compared to the surface.

center, gradually decreasing towards the edges and corners despite cooling primarily initiated from the central region of the chamber. Fig. 60(b) reveals the internal temperature distribution of one-eighth of the entire workpiece. This depiction exhibits a similar gradient pattern as the surface but with temperatures consistently higher than those at the surface, emphasizing the thermal inertia within the core of the workpiece.

These observations affirm that conductive effects within the cubic workpiece are pivotal in shaping the thermal dynamics during the cooling phase. Notably, while the cooling source impacts the central region of the chamber surface directly, the most pronounced cooling on the workpiece manifests at the edges and corners, highlighting the combined interplay of radiation and conduction heat transfer mechanisms.

9.4.2 Case 1: Comparison of Operating Group Sets

In Case 1, a comparative analysis was performed on the inverse solutions to ensure uniform cooling, utilizing the two distinct operating group sets outlined in Section 9.2.

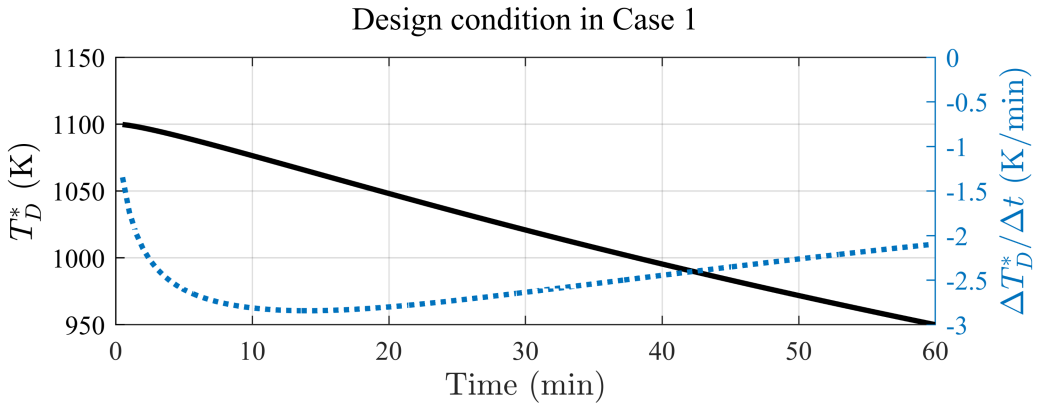


Figure 61: Design condition in Case 1: Desired cooling curve at design points.

9.4.2.1 Design Condition

Operating Group Set 1 incorporates a predefined, constant cooling source, implemented by $\bar{U}_{\text{cooling}}$. Consequently, it is essential to establish a design condition that is physically feasible given this constraint. Therefore, the design condition is derived from the average temperatures at the design points obtained in the forward solution in Section 9.4.1. Additionally, as we maintain the same values for $\bar{U}_{\text{cooling}}$ throughout the inverse solution with Operating Group Set 1, it is necessary to adjust the desired design point temperatures. Specifically, temperatures are increased to provide a room for the energy input required for the heater powers that will be determined through the inverse solution.

In Case 1, the desired design point temperature T_D^* is strategically set as follows: Initially, we calculated the average of the design point temperatures derived from the forward solution in Section 9.4.1. This average temperature is then linearly adjusted to start at approximately 1100 K and decrease to a target of 950 K by the end of the cooling phase, with a cooling rate not exceeding 3 K/min. The final form of the desired design point temperature is depicted in Fig. 61.

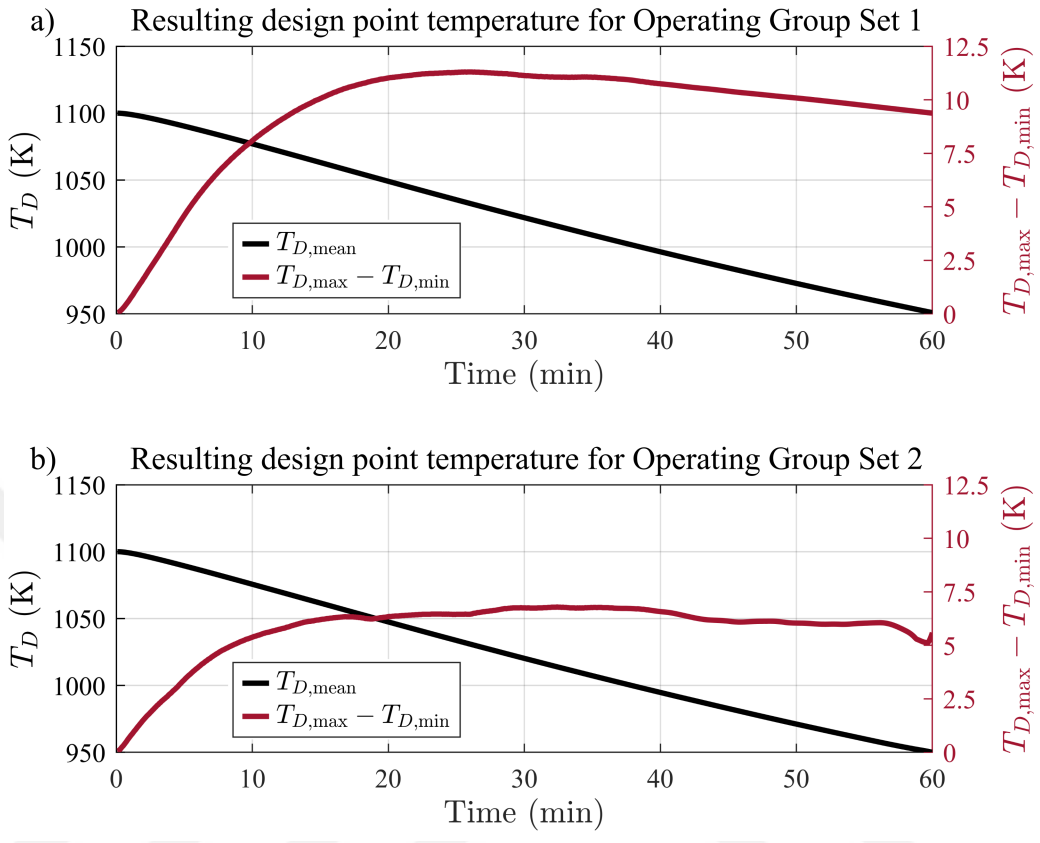


Figure 62: Resulting design point temperatures (a) for Operating Group Set 1 and (b) for Operating Group Set 2

9.4.2.2 Resulting Design Point Temperatures and Temperature Uniformity

The resulting design point temperatures obtained by the inverse solutions are illustrated in Fig. 62. Fig. 62(a) shows the results for Operating Group Set 1, which achieves a temperature uniformity within a variation of less than 12.5 K throughout the cooling process. In contrast, Fig. 62(b) depicting Operating Group Set 2, demonstrates superior temperature uniformity, with variations not exceeding 7.5 K.

Additionally, the temperature uniformity within the workpiece domain exhibits a similar pattern over time to that observed at the design points, with temperature variations peaking at 25 K for Operating Group Set 1 and 20 K for Operating Group Set 2.

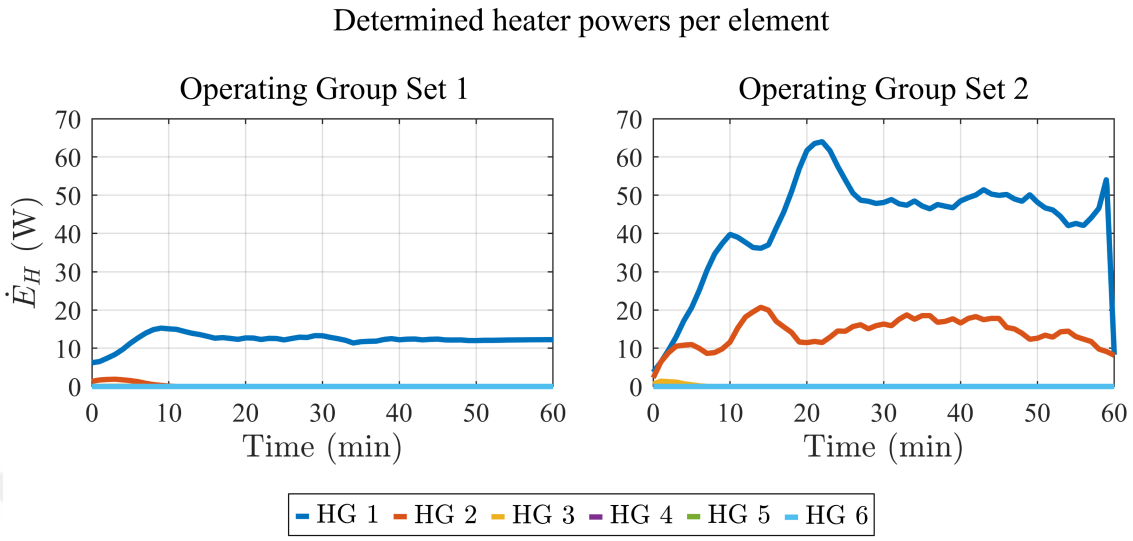


Figure 63: Determined heater powers per element (left) for Operating Group Set 1 and (right) for Operating Group Set 2, where each line corresponds to the heater group denoted by 'HG'

These results indicate that employing both heater and chamber elements in Operating Group Set 2 provides enhanced control over the furnace's operational conditions, ensuring more consistent temperature uniformity across the workpiece. This enhanced control could be particularly beneficial for processes requiring strict temperature uniformities, suggesting that adjustments in operational strategy could be key to optimizing heat treatment outcomes.

9.4.2.3 Determined Heater and Chamber Powers

The heater power levels per element for each group, as determined by the inverse solutions, are depicted in Fig. 63. In Operating Group Set 1, the configuration ensures a relatively steady and low energy input throughout the cooling phase. In contrast, for Operating Group Set 2, heater groups 1 and 2 play significant roles, contributing substantially higher levels of power.

Fig. 64 illustrates the chamber powers per surface element for Operating Group Sets 1 and 2. Note that the chamber power for Operating Group Sets 1 is resulted from

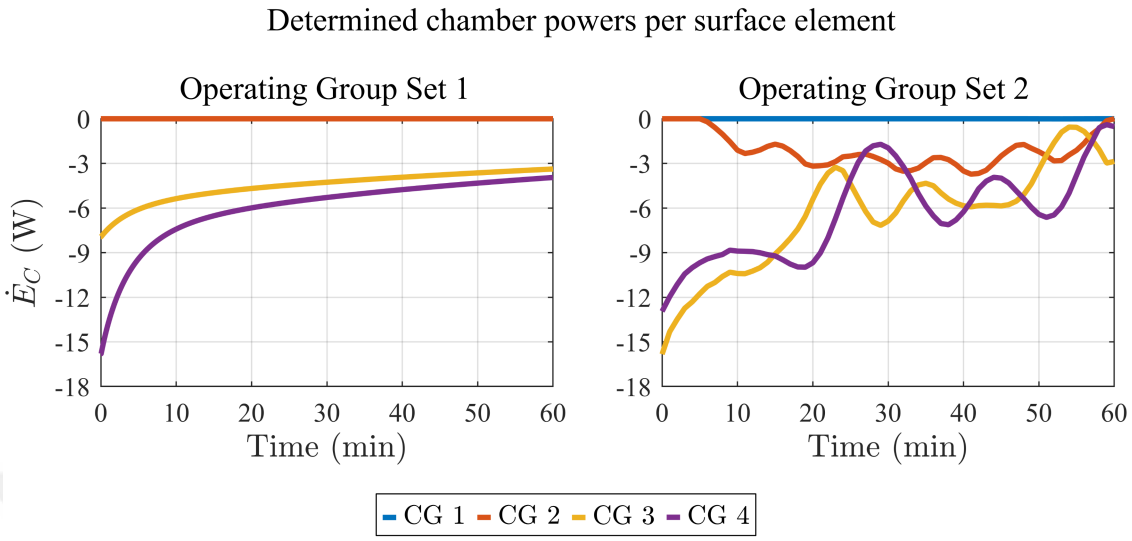


Figure 64: Chamber powers per surface element (left) resulting from predefined cooling for Operating Group Set 1 and (right) determined by inverse solution for Operating Group Set 2. Each line corresponds to the chamber group denoted by 'CG'.

the predefined constant cooling provided by $\bar{U}_{\text{cooling}}$, while the chamber powers for Operating Group Sets 2 is determined by the inverse solutions. In Operating Group Set 1, the chamber power curves exhibit relatively stable and consistent behavior, which is indicative of the influence of the constant $\bar{U}_{\text{cooling}}$. Conversely, Operating Group Set 2 shows fluctuating power levels across different chamber groups, with chamber group 2 particularly active in the cooling process. These fluctuations demonstrate a more dynamic approach determining required heat extraction form the chamber surfaces to ensure uniform cooling across the design points.

Fig. 65 presents the total heater and chamber power over time for both operating group sets. The heater power, indicated in red, demonstrates a positive power due to heat being supplied to the system, while the chamber power, shown in blue, represents a negative power, indicative of heat extraction from the chamber surfaces. In Operating Group Set 1, the heater powers are relatively restrained due to the predefined cooling settings implemented by $\bar{U}_{\text{cooling}}$. As a result, the energy balance limits the possible magnitudes of heater power, ensuring they remain moderate, while the

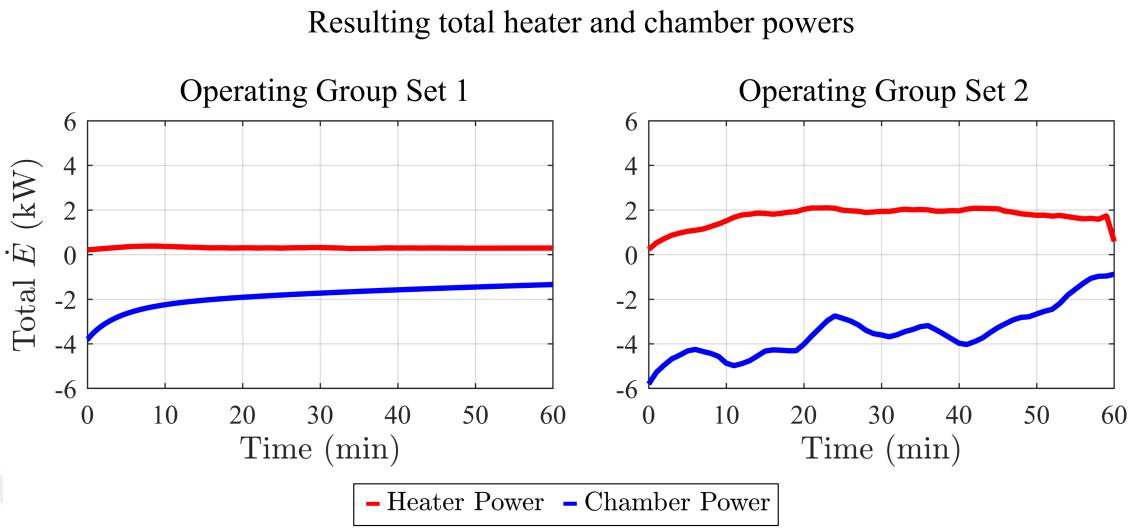


Figure 65: Resulting total heater and chamber powers over time for Operating Group Set 1 and 2

chamber powers directly reflect the predefined constant cooling settings. Conversely, Operating Group Set 2, as determined by the inverse solutions, exhibits significantly higher total powers for both heaters and chambers.

The analysis revealed significant differences between the two operating group sets in terms of determined powers for uniform cooling and resulting energy requirements. Operating Group Set 1, characterized by predefined constant cooling, exhibited stable and consistent power curves with lower overall energy input, totaling 0.31 kWh for heaters and 1.87 kWh for chamber cooling. In contrast, the determined heater and chamber powers in Operating Group Set 2 showed fluctuating power levels with higher energy demands, amounting to 1.73 kWh for heaters and 3.48 kWh for chamber cooling.

Although Operating Group Set 2 enables more precise adjustments to enhance cooling uniformity across the design points, it demands significantly higher energy for both heater elements and heat extraction from chamber surfaces. These outcomes highlight the trade-offs between stable, energy-efficient settings and more adaptable, energy-intensive strategies in optimizing furnace operation for uniform cooling.

9.4.2.4 Resulting Heater and Chamber Temperatures

The resulting temperature profiles for both heater and chamber surfaces elements across the two operating group sets are demonstrated in Figs. 66 and 67.

Fig. 66(a) shows the temperature profile over time for each heater group. It is evident that Operating Group Set 2 experiences significantly higher and more variable heater temperatures, particularly in heater groups 1 and 2. Conversely, the corresponding chamber temperatures in Operating Group Set 2, as seen in Fig. 67(a), are notably lower, with temperatures dipping to as low as 300 K. This contrast in heater and chamber temperatures highlights that the determined powers from the inverse solution balances heating and cooling effects to obtain uniform cooling treatment for the workpiece.

The spatial distribution of temperatures for both heater and chamber elements at a specific time point is illustrated in Figs. 66(b) and 67(b). In Operating Group Set 1, the majority of the cooling is consistently provided by chamber group 4, driven by the preset parameters of $\bar{U}_{\text{cooling}}$. This leads to a stable but less flexible cooling pattern across the workpiece.

In contrast, Operating Group Set 2 displays a more dynamic cooling interaction, where the primary cooling sources shift between chamber groups 3 and 4 over time. This variability is indicated by the fluctuating profiles of minimum chamber temperatures ($T_{C,\text{min}}$) and cooling power ($\dot{E}_C$). Notably, at $t = 10$ minutes, as shown in Fig. 67(b), chamber group 3 exhibits lower temperatures compared to chamber group 4. This shifting dynamic in Set 2 suggests a more responsive and adaptable cooling strategy that can adjust to different thermal needs within the workpiece, unlike the more static approach observed in Set 1.

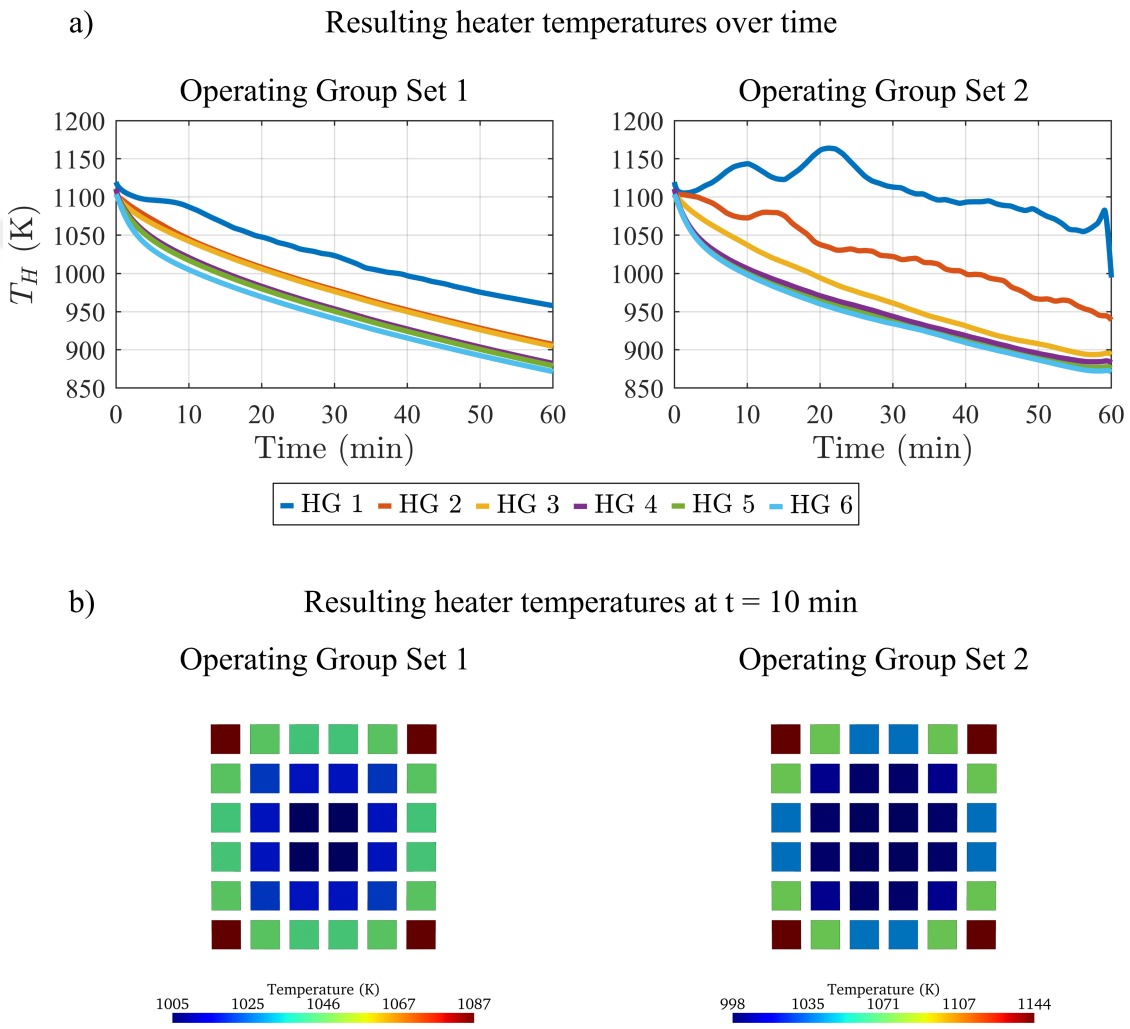


Figure 66: Resulting heater temperatures for Operating Group Set 1 and 2 in Case 1: (a) Resulting heater temperatures, where each line corresponds to the heater group denoted by 'HG'. (b) Spatial distribution of temperatures across the heater elements at t = 10 minutes.

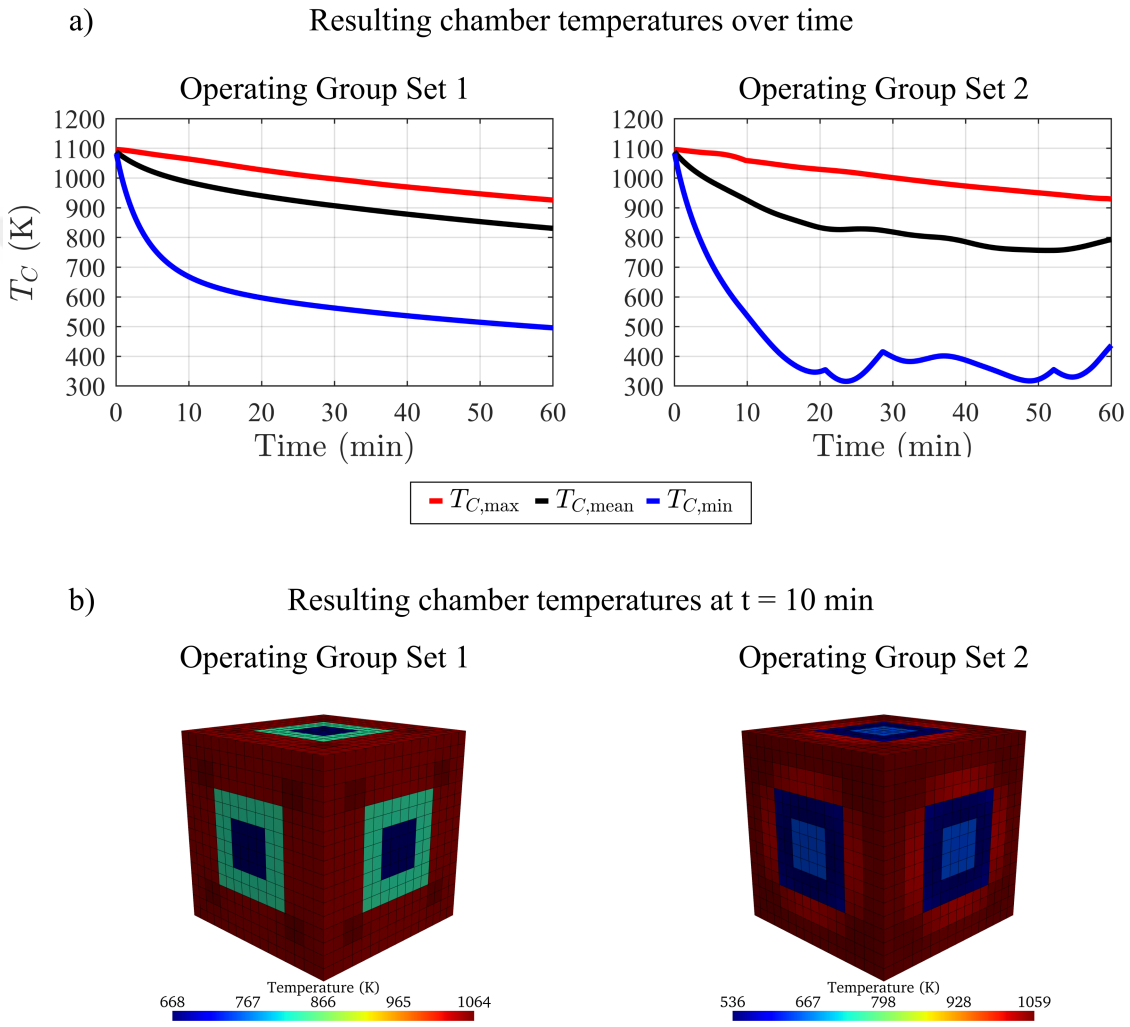


Figure 67: Resulting chamber temperatures for Operating Group Set 1 and 2 in Case 1: (a) Resulting chamber temperatures, where each line corresponds to the chamber group denoted by 'CG'. (b) Spatial distribution of temperatures across the chamber surfaces at t = 10 minutes.

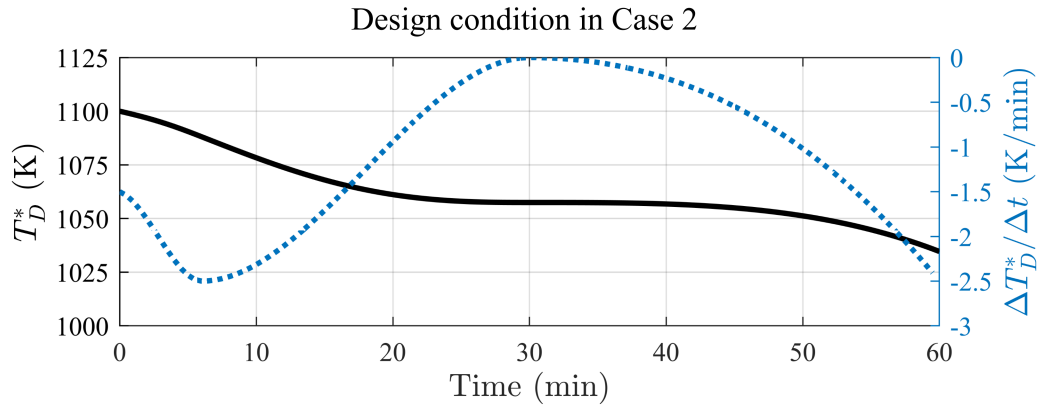


Figure 68: Design condition in Case 2: Desired cooling curve at design points.

9.4.3 Case 2: Ensuring a Custom Cooling Curve Uniformly

In Case 2, we utilize Operating Group Set 2, which includes both heater and chamber groups as operating surfaces, with the goal of achieving a user-defined cooling curve at the design points uniformly.

9.4.3.1 Design Condition

The inverse solution in this case targets the cooling curve demonstrated in Fig. 68. This cooling profile is designed to incorporate an intermediate soaking period starting around the 25-minute mark, with a cooling rate that does not exceed 2.5 K/min. The flexibility of Operating Group Set 2 enables the definition of any desired cooling profile, as the powers for both heaters and chambers are adjusted by the inverse solution.

9.4.3.2 Resulting Design Point Temperature and Determined Heater and Chamber Powers

The design point temperatures resulting from the inverse solution are depicted in Fig. 69(a), showing that temperature uniformity is maintained below 6 K throughout the one-hour treatment. Notably, prior to the intermediate soaking period, temperature variations are kept below 5 K. During the intermediate soaking period, uniformity improves further, with variations reducing to less than 1 K. Following this, as the

cooling rate increases, the variation in design point temperatures also rises.

Additionally, the temperature field within the workpiece domain exhibits a pattern of uniformity similar to that observed at the design points, with temperature variations peaking at 15 K and diminishing to around 1 K during the intermediate soaking phase.

The heater and chamber power levels, as shown in Fig. 69(b) and Fig. 69(c), indicate that the essential cooling effect is predominantly provided by chamber groups 3 and 4, situated in the central region of the chamber faces. Moreover, heater groups 1 and 2, positioned at the edges and corners, play a significant role in facilitating uniform treatment. During the intermediate soaking period, cooling by the chamber groups is completely suspended, while heaters in the central region are activated to maintain the necessary temperatures.

These observations demonstrate that the inverse solution dynamically adjusts the power settings for heaters and chambers to conform to a specified cooling curve that includes an intermediate soaking period, thereby ensuring a uniform cooling treatment.

9.4.3.3 Resulting Total Heater and Chamber Powers

Fig. 70 demonstrates the resulting total power requirements for both heater and chamber elements over time. It is observed that the chamber power required for cooling peaks at about -5 kW, reflecting the heat extraction necessary to maintain the target cooling curve. Conversely, the heater power, which is kept below 2 kW, provides the necessary heat input to balance the cooling process. Furthermore, at the conclusion of the intermediate soaking period, the total heater power required to maintain steady and uniform temperatures is found to be 0.36 kW.

It was observed that the total energy supplied for heating amounted to 0.96 kWh. In contrast, the energy required for cooling was 1.50 kWh. Additionally, the energy

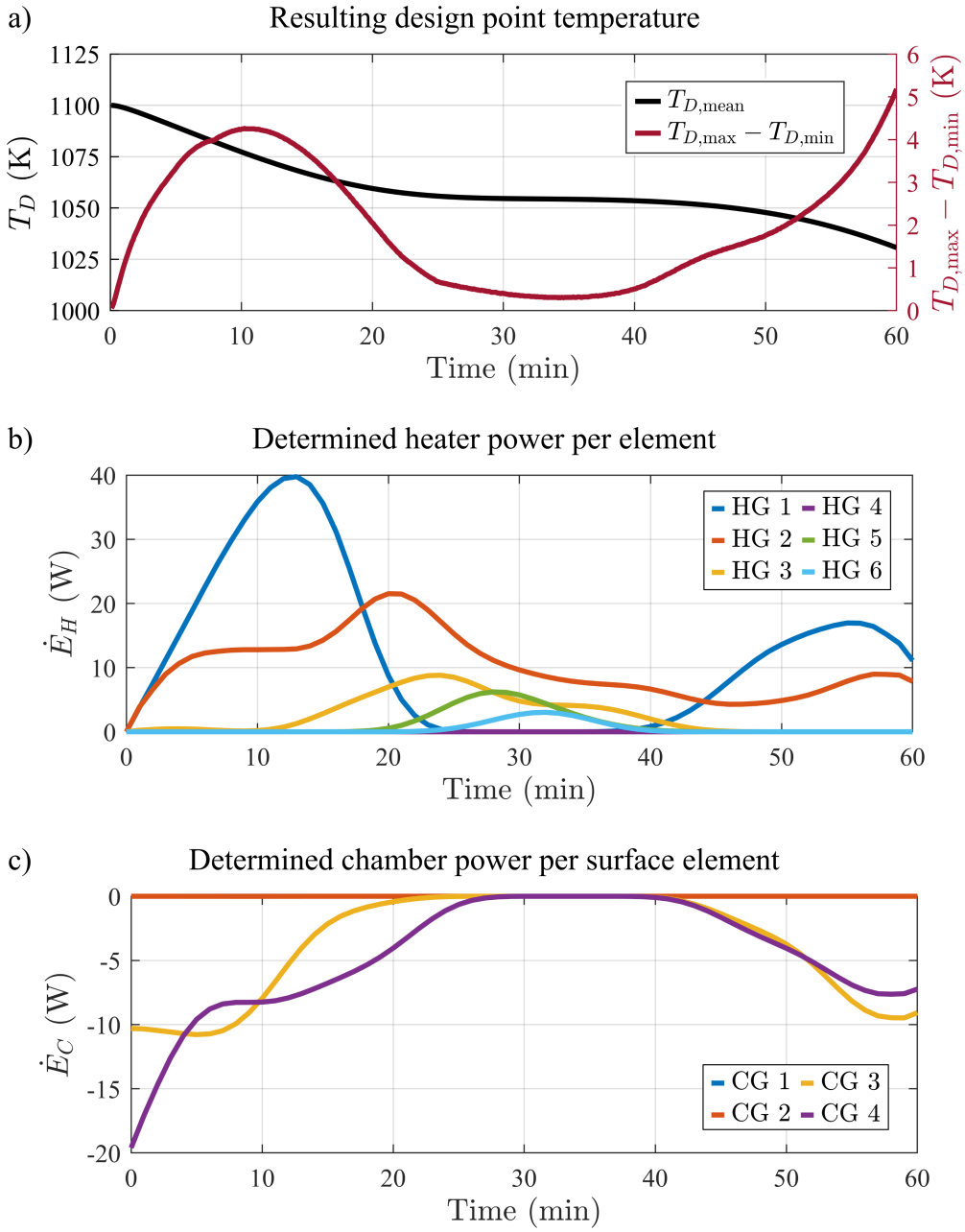


Figure 69: Results of the inverse solution in Case 2: (a) Resulting design point temperatures. (b) Determined heater powers per element for each heater group, where 'HG' denotes the heater group index. (b) Determined chamber power per surface element for each chamber group, where 'CG' denotes the chamber group index.

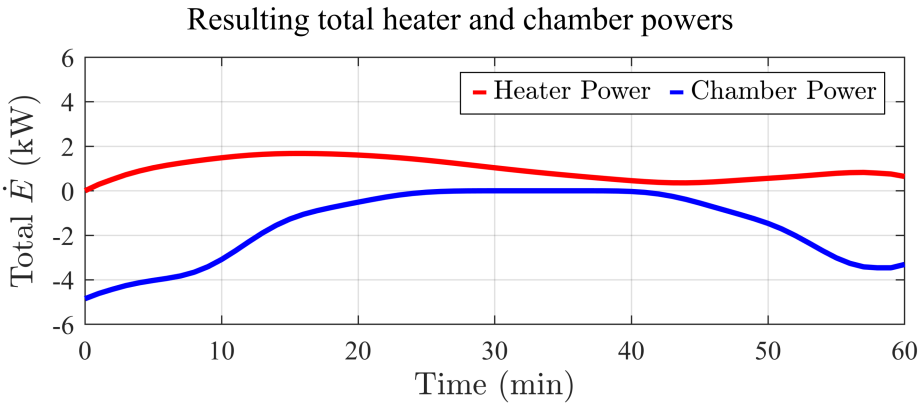


Figure 70: Resulting total heater and chamber powers over time for Case 2 with Operating Group Set 2

associated with heat loss from the chamber surfaces to the environment was calculated to be 0.58 kWh. During the cooling treatment, the change in stored thermal energy within the workpiece itself was also observed to be 0.59 kWh.

These findings indicate that a specific uniform cooling rate can be maintained with the determined distribution of heating and cooling powers by the inverse solution, reflecting the complex interplay between heat addition and extraction. This demonstrates the significance of utilizing Operating Group Set 2 in modeling furnace operating conditions to ensure user-defined desired cooling profile across design points.

9.4.3.4 Resulting Heater and Chamber Temperatures

The resulting temperatures for both heater and chamber elements from the inverse solution are depicted in Figs. 71 and 72.

Fig. 71(a) shows the temperature profile over time for each heater group, which correlate with the determined heater power levels. Fig. 71(b) provides snapshots of the heater temperatures at specific times, revealing significant temperature disparities among the groups, with differences reaching up to 140 K initially.

Fig. 72(a) captures the declining chamber temperatures essential for achieving the

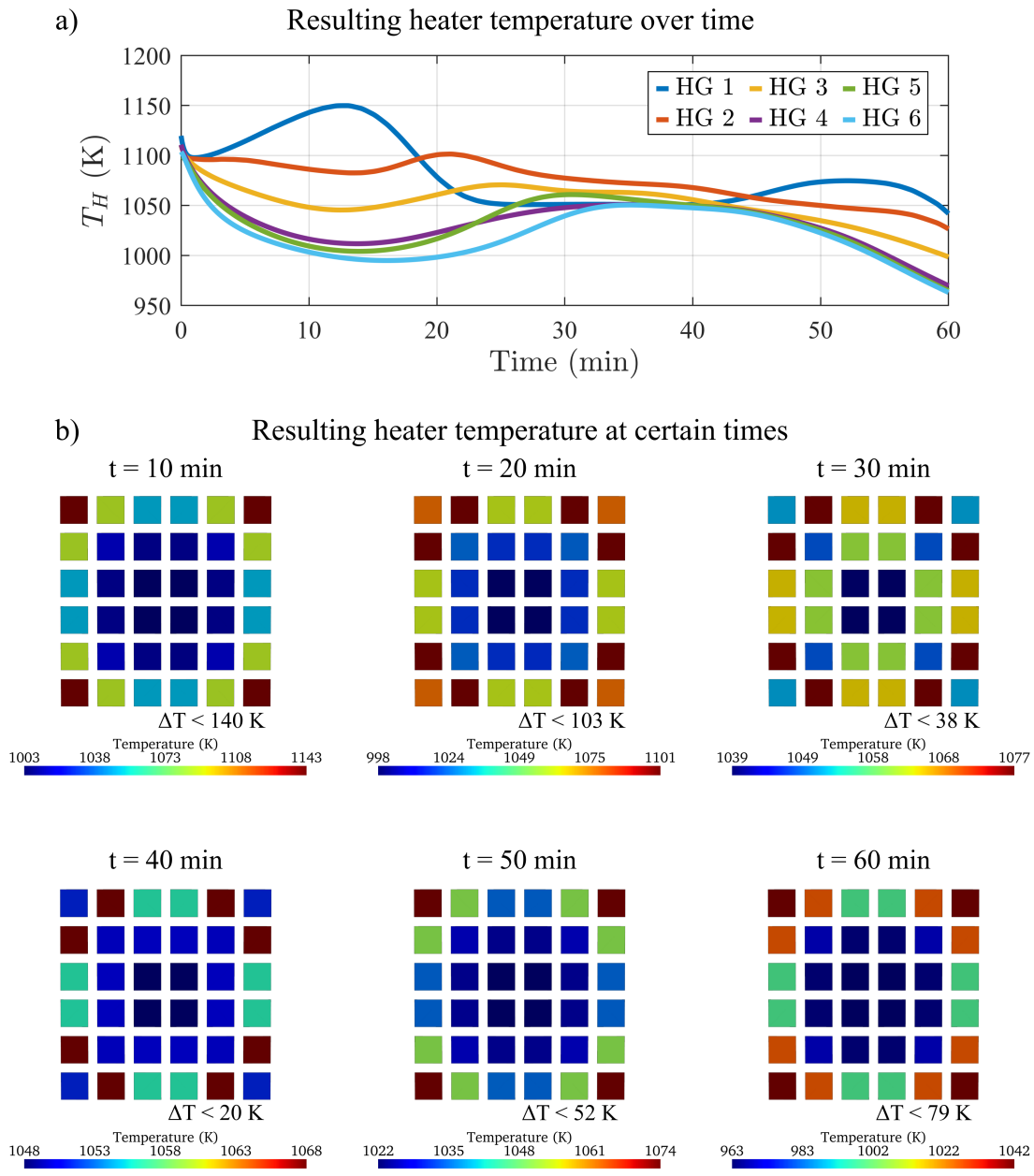


Figure 71: Resulting heater temperatures in Case 2: (a) Time-dependent profiles of the heater temperatures, where each line corresponds to a different heater group, denoted as 'HG'. (b) Spatial distribution of temperatures across the heater elements at certain times.

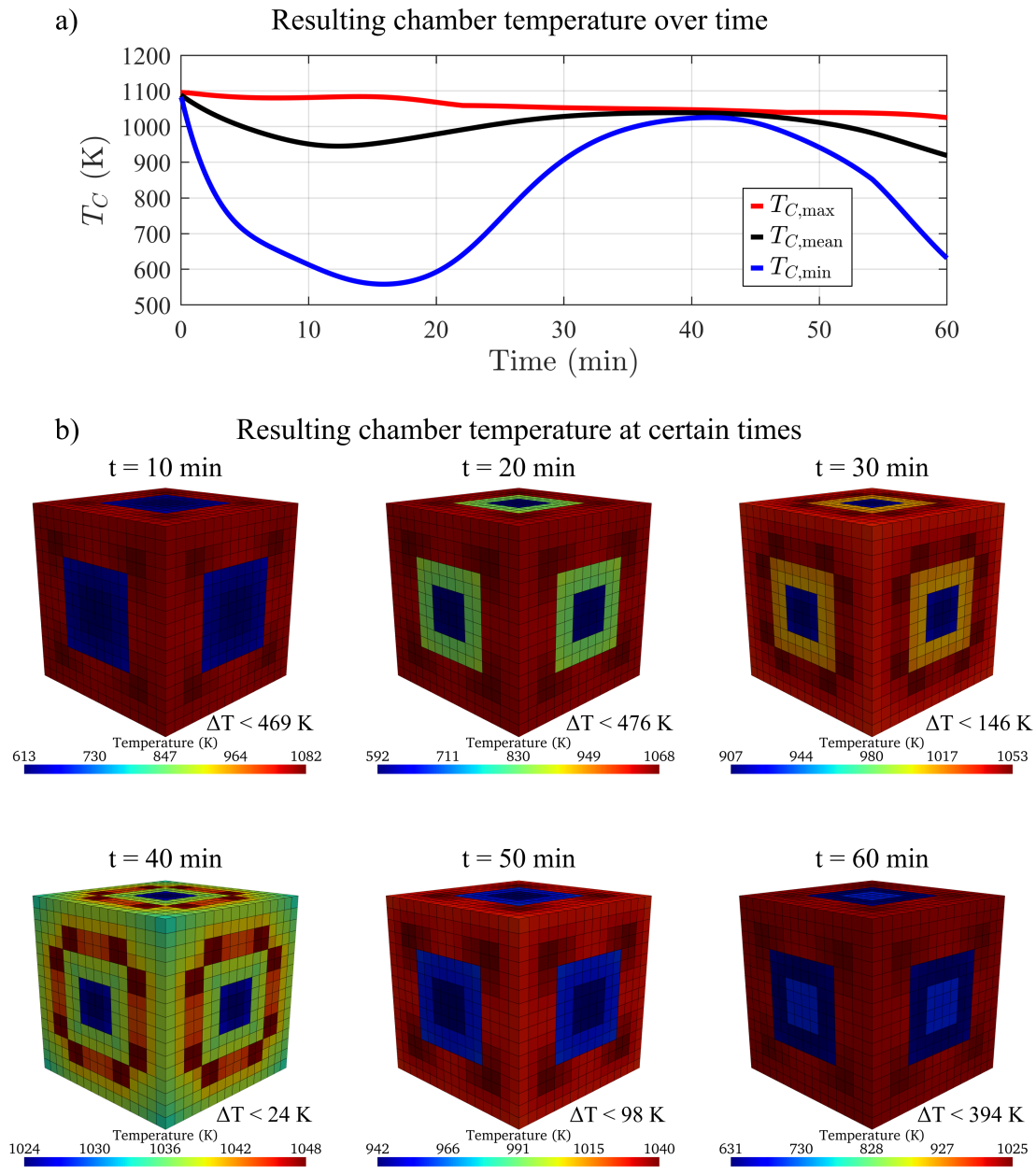


Figure 72: Resulting chamber temperatures in Case 2: (a) Time-dependent profiles of the chamber temperatures, where each line corresponds to a different chamber group, denoted as 'CG'. (b) Spatial distribution of temperatures across the chamber surfaces at certain times.

necessary cooling effect, particularly in the central regions of the chamber surfaces, as shown in Fig. 72(b). Notably, the chamber temperatures display considerable nonuniformity, especially in the first 20 minutes, with sharp transitions evident, similar to those seen in the forward solution discussed in Section 9.4.1.

These findings illustrate that maintaining uniform cooling across the workpiece necessitates adaptively managed, highly nonuniform temperatures across heater and chamber elements to meet specific thermal treatment effectively.

9.5 Computational Time Costs

The computational time required for solving inverse problems varied between 17 and 79 minutes, depending on the scenario.

For Case 1 with Operating Group Set 1, the solution process was completed in 17 minutes. During this time, approximately 53% was spent on solving the forward problem, while 45% was dedicated to calculating the sensitivity coefficients. In contrast, for Case 1 with Operating Group Set 2, the solution took 79 minutes. Here, about 27% of the time was allocated to the forward problem, and 71% was used for sensitivity coefficient calculations. This indicates that as the number of unknowns increases in Operating Group Set 2, due to determining both heater and chamber powers within a single inverse solution, the computational cost for sensitivity coefficient calculations also increases.

9.6 Concluding Remarks

The aim of this chapter was to investigate the cooling phase of a transient heat treatment process for a cubic workpiece within a radiant furnace, focusing on achieving uniform cooling across all design points. The analysis involved two distinct approaches for determining furnace operating conditions: Operating Group Set 1, which uses predefined constant cooling, and Operating Group Set 2, which simultaneously adjusts heater and chamber powers. Comparison allowed for a comprehensive evaluation of

the trade-offs between different operational strategies.

Through detailed inverse solutions, we assessed the impact of these operating strategies on temperature uniformity, energy requirements, and the dynamic behavior of heater and chamber elements. By comparing the resulting power levels and temperature distributions, we were able to determine the effectiveness of each approach in maintaining a uniform cooling profile and the associated energy costs.

The significant outcomes of the investigations conducted in this chapter are summarized as follows:

- **Achieved Temperature Uniformity:** The inverse solutions effectively determined the required furnace operating conditions to achieve uniform cooling of the workpiece. In Operating Group Set 2, the design point temperatures showed a variation of less than 7.5 K, ensuring a high level of temperature uniformity throughout the cooling phase.

- **Energy Requirements:** Operating Group Set 1, with predefined constant cooling, exhibited lower overall energy input. In contrast, Operating Group Set 2 required higher energy, highlighting the trade-offs between cooling uniformity management and energy requirement.

- **Heater and Chamber Power Dynamics:** In Operating Group Set 2, both heater and chamber powers are determined by the inverse solution, showing fluctuating levels, with higher energy demands, allowing for precise adjustments to maintain uniform cooling. This approach is beneficial for processes that require strict thermal management for greater temperature uniformity.

- **Resulting Heater and Chamber Temperatures:** The results indicated significant temperature disparities among heater and chamber elements for Operating Group Set 2. This nonuniformity is essential for achieving enhanced

temperature uniformity, while it might be impractical for certain treatment in real-world applications.

- **Trade-Offs Between Strategies:** Operating Group Set 1 provided stable and consistent power curves with lower energy input, while Operating Group Set 2 enabled more precise adjustments for enhanced cooling uniformity but required significantly higher energy. These findings highlight the importance of choosing the appropriate strategy based on specific process requirements and energy considerations.

- **Ensuring Any Desired Cooling Rate:** Case 2 focused on utilizing Operating Group Set 2 to achieve any desired cooling curve at the design points uniformly. This case demonstrated the flexibility of Operating Group Set 2, which is not directly achievable with Operating Group Set 1 due to its predefined cooling source.

The findings of this chapter underscore the critical importance of selecting appropriate furnace operating strategies to achieve uniform cooling of workpieces. The demonstrated ability of Operating Group Set 2, which allows both heater and chamber powers as variables, ensures precise temperature control and highlights its potential for applications requiring stringent thermal uniformity. In contrast, setting a predefined cooling source and adjusting only the heater elements presents a viable solution for real-world applications.

Ultimately, these insights provide valuable guidance for optimizing furnace operations, balancing energy efficiency, and enhancing the quality of heat-treated materials. The inverse solutions serve as powerful tools for evaluating potential design strategies, guiding us toward solutions that meet technical objectives while considering practical implementation concerns.

CHAPTER X

CONCLUSIONS

10.1 Outcomes of The Study

This study focuses on optimizing heat treatment processes, which are critical for manufacturing industries in terms of energy efficiency and product quality. Utilizing inverse solution methodology, this research aims to optimize the heat treatment processes for achieving the desired treatment of workpieces through heating, soaking, and cooling stages. A novel methodology has been developed to determine furnace operating conditions that ensure the desired heat treatment of workpieces.

Inverse problems are challenging due to their ill-conditioned nature arising from a lack of sufficient information. This often leads to multiple solutions that nearly satisfy the desired outcomes but may have issues due to practicality concerns. The challenge is even higher for inverse radiant boundary design problems because of the nonlinearity of heat transfer mechanisms.

Previous studies conducted before this research have typically focused on uniform treatment over the workpiece surface, often disregarding internal conduction within the workpiece domain. However, such an approach suffers from modeling errors when thermal gradients inside the workpieces are crucial, which is often the case in real industrial problems.

To address these, this study developed a gradient-based optimization approach combined with a direct differentiation method for calculating sensitivity coefficients. The developed model and methodology stand out due to their novel sensitivity coefficient calculation approach and the explicit formulation of temperature profiles using

floating random walk methods. The methodology also carefully utilized a regularization term in the objective function to promote desired furnace operating characteristics, leading to practically suitable solutions.

Our model involves the heat treatment process of workpieces, considering conduction within the internal domain of the workpiece, radiative heat transfer within the radiant enclosure, heat loss from the chamber, and the thermal model of the furnace. The entire system for the inverse problem solution is considered as a nonlinear least squares minimization problem.

The main conclusions are listed below:

- An inverse solution methodology has been developed to optimize heat treatment processes applied to radiant furnaces. The methodology accounts for internal conduction within workpieces, offering a more accurate model for the applications where internal thermal gradients within workpieces are significant.

- The inverse solutions for a six-hour heat treatment of a cubic workpiece were completed in under 1.5 hours on a personal desktop computer using multi-threaded CPU and GPU-accelerated computations for sensitivity coefficient calculations.

- The methodology is applied to the transient heating of two glass panes, where optimal heater temperatures are determined ensuring uniform heating of workpieces. Analyses with different design point configurations demonstrated its impact on convergence behavior and the obtained solution. The robustness of the methodology was demonstrated even with noisy data, highlighting the importance of regularizer weights in managing the impact of noise and ensuring practical solutions.

- Among the temperature-based and power-based furnace operating approaches for heat treating six glass panes, the Power-based Approach was found to

be more practical. Analysis of different desired heating curves revealed that smoother transitions between heating and soaking phases enhance temperature uniformity and lead to lower energy consumption and peak power demands.

- For the uniform heating of a stainless-steel cubic workpiece, the study evaluated various factors including overall heat transfer coefficient, chamber reflectivity, heater layout, and heater material. High reflective chamber surfaces and increased number of heater elements improved temperature uniformity and energy efficiency. Additionally, heat loss from the furnace chamber to the environment was observed to act as a balancing cooling source, improving the uniformity of workpiece treatment.

- An inverse problem considering the cooling phase of a heat treatment process is formulated, where both heating and cooling surfaces are actively operated. Specifically, determining both heating and cooling powers simultaneously through a single inverse solution leads to improved temperature uniformity, while increasing power demands. On the other hand, when heater powers were adjusted in presence of a constant cooling source at furnace chamber, energy demand decreased, but temperature uniformity suffered. This illustrates the trade-offs between temperature uniformity and energy efficiency in furnace operation approaches.

This study has significant implications for the operation and design of heat treatment furnaces. By incorporating internal heat transfer within workpieces, it offers a more accurate modeling of heat treatment processes, leading to more reliable and precise heat treatment outcomes. This improved understanding facilitates more effective optimization of furnace operating parameters, leading to enhanced energy efficiency and better achievement of the desired treatment outcomes. The findings are particularly valuable for industries such as automotive and aerospace, where precise heat

treatment is crucial for producing high-quality components. Furnace designers and operators can benefit from detailed insights into the effects of different configurations and materials on heating and cooling processes, enabling more informed decisions that enhance energy efficiency and reduce operational costs. Adopting the recommended practices can lead to more efficient furnace operations and consistent high-quality outcomes.

10.2 Contributions to Literature

Key contributions to the literature are as follows:

- **Incorporation of Workpiece Internal Conduction:** The study includes the conduction heat transfer within the internal domain of workpieces, an aspect typically not considered in inverse radiant boundary design problems.
- **Design Condition Definition:** The design conditions are defined based on internal design points within workpieces rather than just on the workpiece surfaces. This approach enhances the practical application of inverse solutions, leading to more representative and precise heat treatment management for internal locations of workpieces.
- **Explicit Temperature Formulation:** Explicit formulations for workpiece surface temperature and internal design point temperatures are derived using floating random walk methods. These formulations are used in direct differentiation to calculate sensitivity coefficients in gradient-based algorithms, offering sufficiently accurate and computationally feasible calculation procedure.
- **Comprehensive Investigations:** The study provides extensive investigations through conducted set of inverse solutions, covering aspects including design point configuration, furnace operating variables, heating strategies, furnace design configurations, and furnace operating practices.

- **Combined Use of Heating and Cooling Surfaces for Uniform Treatment:** The study demonstrates that enhancing treatment uniformity is achievable through the precise adjustment of both heating and cooling sources simultaneously. Despite the higher energy demands, this approach offers furnace operating conditions suitable for heat treatment applications requiring high precision.

- **Valuable Insights and Design Trade-offs:** Through detailed analyses, the study offers valuable insights into optimized furnace operating conditions and the resulting treatment effectiveness. It ensures desired treatment characteristics while highlighting the trade-offs between design aspects and the resulting energy costs.

10.3 Recommendations for Future Work

Future research can build upon the findings of this study in several ways. One significant direction is to assess the scalability of the developed methodologies when applied to large-scale industrial applications with higher fidelity.

Integrating multiphysics modeling approaches to account for transmissivity in radiative transfer, temperature-dependent and directionally dependent material properties, and fluid flow for convective effects will provide a more comprehensive understanding of process dynamics for specific problems.

To refine furnace modeling, future studies should emphasize enhanced thermal modeling for both furnace components and enclosures. Specifically, a more detailed consideration of conduction within furnace components is recommended, with a focus on energy transfer between neighboring cells or surface elements. Additionally, incorporating a detailed thermal model that effectively considers insulation layers could further refine the modeling process. These improvements will likely lead to more accurate simulations and optimizations of furnace operation.

Future research could benefit from deriving explicit formulations for workpiece surface temperatures and temperatures at design points within the workpieces using finite-volume based random walk methods, in the context of sensitivity coefficient calculations. These methods, which incorporate the finite-volume mesh of the workpieces, will provide a more suitable approach for workpiece materials with transmissivity in radiative transfer and internal heat generation. Exploring this approach further could provide improvements in modeling of sensitivity coefficient calculation for specific problems.

Engaging in collaborative research with industry partners to apply these methodologies in practical settings is crucial. Such collaborations can offer valuable insights into practical challenges and opportunities for refining the solutions. Conducting experimental studies to validate the numerical results obtained from these methodologies will further ensure their practical applicability and accuracy in real-world scenarios.

By addressing these areas, future research can continue to advance the field of heat treatment optimization, leading to improved industrial processes, enhanced product quality, and greater energy efficiency.

10.4 Final Thoughts

In conclusion, this dissertation has addressed critical challenges in optimizing heat treatment processes through innovative methodologies and comprehensive analyses. The journey of this research has been both challenging and rewarding, providing valuable insights into optimizing heat treatment processes. The contributions made by this work lay a strong foundation for future research and development in the field.

REFERENCES

[1] O. Baik, M. Marcotte, and F. Castaigne, "Cake baking in tunnel type multi-zone industrial ovens part i. characterization of baking conditions," *Food Research International*, vol. 33, no. 7, pp. 587–598, 2000.

[2] H. Erturk, O. Ezekoye, and J. Howell, "Inverse transient boundary condition estimation problem in a radiating enclosure," in *Proc. 2001 ASME National Heat Transfer Congress*, 2001.

[3] H. Ertürk, O. A. Ezekoye, and J. R. Howell, "Comparison of three regularized solution techniques in a three-dimensional inverse radiation problem," *Journal of Quantitative Spectroscopy and Radiative Transfer*, vol. 73, no. 2, pp. 307–316, 2002. Third International Symposium on Radiative Transfer.

[4] X. Haohua, X. Tao, T. Jian, F. Lulu, X. Tianshuang, and Y. Tatsuo, "Research on the temperature uniformity of vacuum furnace and size optimization of working zone," in *2015 8th International Conference on Intelligent Computation Technology and Automation (ICICTA)*, pp. 789–792, 2015.

[5] H. Zhang and S. Deng, "Evaluating heat flux profiles in aluminum reheating furnace with regenerative burner," *Energies*, vol. 10, no. 4, 2017.

[6] J. Liu, J. Li, Z. Wang, Y. Tian, and H. Wang, "Optimization of heating process for bearing rings in a vacuum furnace based on numerical analysis," *ISIJ International*, vol. 61, no. 1, pp. 302–308, 2021.

[7] R. Yadav, S. Tripathi, S. Asati, and M. K. Das, "A combined neural network and simulated annealing based inverse technique to optimize the heat source control parameters in heat treatment furnaces," *Inverse Problems in Science and Engineering*, vol. 28, no. 9, pp. 1265–1286, 2020.

[8] X. Hao, J. Gu, N. Chen, W. Zhang, and X. Zuo, "3-d numerical analysis on heating process of loads within vacuum heat treatment furnace," *Applied Thermal Engineering*, vol. 28, no. 14, pp. 1925–1931, 2008.

[9] A. Mochida, K. Kudo, Y. Mizutani, M. Hattori, and Y. Nakamura, "Transient heat transfer analysis in vacuum furnaces heated by radiant tube burners," *Energy Conversion and Management*, vol. 38, no. 10, pp. 1169–1176, 1997. International Symposium on Advance Energy Conversion Systems and Related Technologies.

[10] R. Yadav, C. Balaji, and S. Venkateshan, "Inverse estimation of number and location of discrete heaters in radiant furnaces using artificial neural networks and genetic algorithm," *Journal of Quantitative Spectroscopy and Radiative Transfer*, vol. 226, pp. 127–137, 2019.

[11] H. Amiri, S. H. Mansouri, A. Safavinejad, and P. J. Coelho, "The optimal number and location of discrete radiant heaters in enclosures with the participating media using the micro genetic algorithm," *Numerical Heat Transfer, Part A: Applications*, vol. 60, no. 5, pp. 461–483, 2011.

[12] L. D. Lemos, R. Brittes, and F. H. França, "Application of inverse analysis to determine the geometric configuration of filament heaters for uniform heating," *International Journal of Thermal Sciences*, vol. 105, pp. 1–12, 2016.

[13] S. Sun, "Geometric optimization of radiative enclosures using sequential quadratic programming algorithm," *ES Energy & Environment*, vol. 6, pp. 57–68, 2019.

[14] K. J. Daun, J. R. Howell, and D. P. Morton, "Optimization of transient heater settings to provide spatially uniform heating in manufacturing processes involving radiant heating," *Numerical Heat Transfer, Part A: Applications*, vol. 46, no. 7, pp. 651–667, 2004.

[15] A. G. Fedorov, K. H. Lee, and R. Viskanta, "Inverse optimal design of the radiant heating in materials processing and manufacturing," *Journal of Materials Engineering and Performance*, vol. 7, pp. 719–726, 1998.

[16] H. Erturk, M. Gamba, O. Ezekoye, and J. Howell, "Design of a rapid thermal processing chamber using an inverse formulation," in *8th AIAA/ASME Joint Thermophysics and Heat Transfer Conference*, 2002.

[17] K. Daun, F. França, M. Larsen, G. Leduc, and J. R. Howell, "Comparison of methods for inverse design of radiant enclosures," *Journal of Heat Transfer*, vol. 128, no. 3, pp. 269–282, 2005.

[18] J. Ben-Hamida and M. Rink, "Use of new types of large and middle size vacuum batch furnaces for heat treatment of moulds and dies," *International Heat Treatment and Surface Engineering*, vol. 3, no. 1-2, pp. 5–8, 2009.

[19] Z.-Z. Li, Y.-D. Shen, K.-S. Heo, J.-W. Lee, S.-Y. Seol, Y.-H. Byun, and C.-J. Lee, "Feasible optimal design of high temperature vacuum furnace using experiences and thermal analysis database," *Journal of Thermal Science and Technology*, vol. 2, no. 1, 2007.

[20] J. R. Howell, M. P. Mengüç, K. Daun, and R. Siegel, *Thermal Radiation Heat Transfer*. CRC press, 7th edition ed., 2020.

[21] C. Wang, Y. Heng, J. Luo, and X. Wang, "A fast bayesian parallel solution framework for large-scale parameter estimation of 3d inverse heat transfer problems," *International Communications in Heat and Mass Transfer*, vol. 155, p. 107409, 2024.

[22] D. Allard and H. Najafi, "A systematic study of two machine learning-based approaches for solving non-linear inverse heat conduction problems in one-dimensional domains," *International Communications in Heat and Mass Transfer*, vol. 155, p. 107494, 2024.

[23] H. Farzan, T. Loulou, and S. M. H. Sarvari, "A new approach to speed up the conjugate gradient method by applying the complex variable differentiation method," *Inverse Problems in Science and Engineering*, vol. 27, no. 12, pp. 1703–1717, 2019.

[24] R. Brittes and F. H. França, "A hybrid inverse method for the thermal design of radiative heating systems," *International Journal of Heat and Mass Transfer*, vol. 57, no. 1, pp. 48–57, 2013.

[25] A. Pourshaghaghy, K. Pooladvand, F. Kowsary, and K. Karimi-Zand, "An inverse radiation boundary design problem for an enclosure filled with an emitting, absorbing, and scattering media," *International Communications in Heat and Mass Transfer*, vol. 33, no. 3, pp. 381–390, 2006.

[26] S. A. Rukolaine, "Shape optimization of radiant enclosures with specular-diffuse surfaces by means of a random search and gradient minimization," *Journal of Quantitative Spectroscopy and Radiative Transfer*, vol. 151, pp. 174–191, 2015.

[27] B. Mosavati, M. Mosavati, and F. Kowsary, "Solution of radiative inverse boundary design problem in a combined radiating-free convecting furnace," *International Communications in Heat and Mass Transfer*, vol. 45, pp. 130–136, 2013.

[28] R. P. Chopade, S. C. Mishra, P. Mahanta, and S. Maruyama, "Estimation of power of heaters in a radiant furnace for uniform thermal conditions on 3-d irregular shaped objects," *International Journal of Heat and Mass Transfer*, vol. 55, no. 15, pp. 4340–4351, 2012.

[29] R. P. Chopade, S. C. Mishra, P. Mahanta, S. Maruyama, and A. Komiya, "Uniform thermal conditions on 3-d object: Optimal power estimation of panel heaters in a 3-d radiant enclosure," *International Journal of Thermal Sciences*, vol. 51, pp. 63–76, 2012.

[30] M. Dehghani, S. H. Sarvari, and H. Ajam, "Inverse estimation of boundary conditions on radiant enclosures by temperature measurement on a solid object," *International Communications in Heat and Mass Transfer*, vol. 38, no. 10, pp. 1455–1462, 2011.

[31] R. Hoffmann, A. Seewald, P. Schneider, and F. França, "Inverse design of thermal systems with spectrally dependent emissivities," *International Journal of Heat and Mass Transfer*, vol. 53, no. 5, pp. 931–939, 2010.

[32] N. Bayat, S. Mehraban, and S. Sarvari, "Inverse boundary design of a radiant furnace with diffuse-spectral design surface," *International Communications in Heat and Mass Transfer*, vol. 37, no. 1, pp. 103–110, 2010.

[33] S. Rukolaine, "Regularization of inverse boundary design radiative heat transfer problems," *Journal of Quantitative Spectroscopy and Radiative Transfer*, vol. 104, no. 1, pp. 171–195, 2007.

[34] F. Kowsary, K. Pooladvand, and A. Pourshaghaghy, "Regularized variable metric method versus the conjugate gradient method in solution of radiative boundary design problem," *Journal of Quantitative Spectroscopy and Radiative Transfer*, vol. 108, no. 2, pp. 277–294, 2007.

[35] S. Sarvari, "Inverse determination of heat source distribution in conductive–radiative media with irregular geometry," *Journal of Quantitative Spectroscopy and Radiative Transfer*, vol. 93, no. 1, pp. 383–395, 2005. Fourth International Symposium on Radiative Transfer.

[36] A. Hossein, R. Navid, A. S. Alireza, and M. Mashayekhi, "Two ımproved teaching–learning-based optimization algorithms for the solution of ınverse boundary design problems," *Soft Computing*, vol. 27, no. 17, pp. 12133–12154, 2023.

[37] N. Radfar, H. Amiri, and A. Arabsolghar, "Application of metaheuristic algorithms for solving inverse radiative boundary design problems with discrete power levels," *International Journal of Thermal Sciences*, vol. 137, pp. 539–551, 2019.

[38] S. Sun, "Simultaneous reconstruction of thermal boundary condition and physical properties of participating medium," *International Journal of Thermal Sciences*, vol. 163, p. 106853, 2021.

[39] P. Sepahvand, G. Abdizadeh, and S. Noori, "Inverse design of an irregular-shaped radiant furnace using neural network and a modified hybrid optimization algorithm," *Thermal Science and Engineering Progress*, vol. 20, p. 100730, 2020.

[40] P. Zhang, C. Sun, and X.-L. Xia, "Particle filter algorithms for on-line prediction of transient heat flux of participating medium," *International Communications in Heat and Mass Transfer*, vol. 145, p. 106859, 2023.

[41] M. Mosavati, F. Kowsary, and B. Mosavati, "A novel, noniterative inverse boundary design regularized solution technique using the backward monte carlo method," *Journal of Heat Transfer*, vol. 135, no. 4, p. 042701, 2013.

[42] F. H. R. França and J. R. Howell, "Transient inverse design of radiative enclosures for thermal processing of materials," *Inverse Problems in Science and Engineering*, vol. 14, no. 4, pp. 423–436, 2006.

[43] L. Darvishvand, F. Kowsary, and P. H. Jafari, "Optimization of 3-d radiant enclosures with the objective of uniform thermal conditions on 3-d design bodies," *Heat Transfer Engineering*, vol. 37, no. 1, pp. 1–12, 2016.

[44] L. Darvishvand, B. Kamkari, and F. Kowsary, "Optimal design approach for heating irregular-shaped objects in three-dimensional radiant furnaces using a hybrid genetic algorithm–artificial neural network method," *Engineering Optimization*, vol. 50, no. 3, pp. 452–470, 2018.

[45] B. Moghadassian and F. Kowsary, "Inverse boundary design problem of natural convection–radiation in a square enclosure," *International Journal of Thermal Sciences*, vol. 75, pp. 116–126, 2014.

[46] França, F. H. R., O. A. Ezekoye, and J. R. Howell, "Inverse boundary design combining radiation and convection heat transfer," *Journal of Heat Transfer*, vol. 123, no. 5, pp. 884–891, 2001.

[47] S. M. H. Sarvari and S. H. Mansouri, "Inverse design for radiative heat source in two-dimensional participating media," *Numerical Heat Transfer, Part B: Fundamentals*, vol. 46, no. 3, pp. 283–300, 2004.

[48] R. P. Chopade, S. C. Mishra, P. Mahanta, and S. Maruyama, "On configuration of load in radiant furnace for uniform thermal conditions," *Heat Transfer Engineering*, vol. 35, no. 1, pp. 94–109, 2014.

[49] J. Beck, B. Blackwell, and A. Haji-Sheikh, "Comparison of some inverse heat conduction methods using experimental data," *International Journal of Heat and Mass Transfer*, vol. 39, no. 17, pp. 3649–3657, 1996.

[50] K. Daun and J. Howell, "Inverse design methods for radiative transfer systems," *Journal of Quantitative Spectroscopy and Radiative Transfer*, vol. 93, no. 1, pp. 43–60, 2005.

[51] J. R. Howell, O. A. Ezekoye, and J. C. Morales, "Inverse design model for radiative heat transfer," *Journal of Heat Transfer*, vol. 122, pp. 492–502, 04 2000.

[52] A. J. Marston, K. J. Daun, and M. R. Collins, "Geometric optimization of radiant enclosures containing specularly-reflecting surfaces through quasi-monte carlo simulation," *Numerical Heat Transfer, Part A: Applications*, vol. 59, no. 2, pp. 81–97, 2011.

[53] K. J. Daun, J. R. Howell, and D. P. Morton, "Design of radiant enclosures using inverse and non-linear programming techniques," *Inverse Problems in Engineering*, vol. 11, no. 6, pp. 541–560, 2003.

[54] K. J. Daun, D. P. Morton, and J. R. Howell, "Geometric optimization of radiant enclosures containing specular surfaces," *Journal of Heat Transfer*, vol. 125, no. 5, pp. 845–851, 2003.

[55] K. J. Daun, J. R. Howell, and D. P. Morton, "Geometric optimization of radiative enclosures through nonlinear programming," *Numerical Heat Transfer, Part B: Fundamentals*, vol. 43, no. 3, pp. 203–219, 2003.

[56] Y. Jarny, M. Ozisik, and J. Bardon, "A general optimization method using adjoint equation for solving multidimensional inverse heat conduction," *International Journal of Heat and Mass Transfer*, vol. 34, no. 11, pp. 2911–2919, 1991.

[57] H. Ertürk, O. A. Ezekoye, and J. R. Howell, "Inverse solution of radiative heat transfer in two-dimensional irregularly shaped enclosures," in *Proceedings of the ASME International Mechanical Engineering Congress and Exposition*, vol. Heat Transfer: Volume 1, pp. 109–117, 2000.

[58] H. Ertürk, O. A. Ezekoye, and J. R. Howell, "The use of inverse formulation in design and control of transient radiant systems," in *Proceedings of the Twelfth International Heat Transfer Conference*, 2002.

[59] H. Ertürk, O. A. Ezekoye, and J. R. Howell, "The application of an inverse formulation in the design of boundary conditions for transient radiating enclosures," *Journal of Heat Transfer*, vol. 124, no. 6, pp. 1095–1102, 2002.

[60] H. Ertürk, O. A. Ezekoye, and J. R. Howell, "Boundary condition design to heat a moving object at uniform transient temperature using inverse formulation," *Journal of Manufacturing Science and Engineering*, vol. 126, no. 3, pp. 619–626, 2004.

[61] S. Hosseini Sarvari, S. Mansouri, and J. Howell, "Inverse design of three-dimensional enclosures with transparent and absorbing-emitting medial using an optimization technique," *International Communications in Heat and Mass Transfer*, vol. 30, no. 2, pp. 149–162, 2003.

[62] S. M. H. Sarvari, J. R. Howell, and S. H. Mansouri, "Inverse boundary design conduction-radiation problem in irregular two-dimensional domains," *Numerical Heat Transfer, Part B: Fundamentals*, vol. 44, no. 3, pp. 209–224, 2003.

[63] S. Payan, S. M. H. Sarvari, and A. Behzadmehr, "Inverse boundary design radiation problem within combustion enclosures with absorbing-emitting non-gray media," *Numerical Heat Transfer, Part A: Applications*, vol. 65, no. 11, pp. 1114–1137, 2014.

[64] S. Payan, A. Farahmand, and S. Hosseini Sarvari, "Inverse boundary design radiation problem with radiative equilibrium in combustion enclosures with pso algorithm," *International Communications in Heat and Mass Transfer*, vol. 68, pp. 150–157, 2015.

[65] H. Amiri and S. H. Mansouri, "Inverse boundary design problems in enclosures with non-gray media," *Heat Transfer Engineering*, vol. 38, no. 2, pp. 227–243, 2017.

[66] Y. Zeng, H. Wang, S. Zhang, Y. Cai, and E. Li, "A novel adaptive approximate bayesian computation method for inverse heat conduction problem," *International Journal of Heat and Mass Transfer*, vol. 134, pp. 185–197, 2019.

[67] H. Amiri and K. Lari, "Nongray inverse boundary design problems in enclosures at radiative equilibrium," *Heat Transfer—Asian Research*, vol. 48, no. 6, pp. 2497–2525, 2019.

[68] S. Wen, H. Qi, Z.-T. Niu, L.-Y. Wei, and Y.-T. Ren, "Efficient and robust prediction of internal temperature distribution and boundary heat flux in participating media by using the kalman smoothing technique," *International Journal of Heat and Mass Transfer*, vol. 147, p. 118851, 2020.

[69] L.-Y. Wei, H. Qi, G.-J. Li, and W.-J. Zhang, "Improved teaching-learning-based optimization for estimation of temperature-dependent radiative properties of semitransparent media," *International Journal of Thermal Sciences*, vol. 161, p. 106694, 2021.

[70] M. Deiveegan, C. Balaji, and S. P. Venkateshan, "Comparison of various methods for simultaneous retrieval of surface emissivities and gas properties in gray participating media," *Journal of Heat Transfer*, vol. 128, no. 8, pp. 829–837, 2006.

[71] R. Das, S. C. Mishra, and R. Uppaluri, "Retrieval of thermal properties in a transient conduction–radiation problem with variable thermal conductivity," *International Journal of Heat and Mass Transfer*, vol. 52, no. 11, pp. 2749–2758, 2009.

[72] R. P. Chopade, E. Agnihotri, A. K. Singh, A. Kumar, R. Uppaluri, S. C. Mishra, and P. Mahanta, "Application of a particle swarm algorithm for parameter retrieval in a transient conduction-radiation problem," *Numerical Heat Transfer, Part A: Applications*, vol. 59, no. 9, pp. 672–692, 2011.

[73] J. Su and G. F. Hewitt, "Inverse heat conduction problem of estimating time-varying heat transfer coefficient," *Numerical Heat Transfer, Part A: Applications*, vol. 45, no. 8, pp. 777–789, 2004.

[74] R. Das, S. C. Mishra, and R. Uppaluri, "Multiparameter estimation in a transient conduction-radiation problem using the lattice boltzmann method and the finite-volume method coupled with the genetic algorithms," *Numerical Heat Transfer, Part A: Applications*, vol. 53, no. 12, pp. 1321–1338, 2008.

[75] N. Daouas, A. Fguiri, and M.-S. Radhouani, "Solution of a coupled inverse heat conduction–radiation problem for the study of radiation effects on the transient hot wire measurements," *Experimental Thermal and Fluid Science*, vol. 32, no. 8, pp. 1766–1778, 2008.

[76] M. Cui, L. Zhou, J. Mei, and B. Zhang, "Estimation of slab surface radiative emissivities by solving an inverse coupled conduction, convection, and radiation problem," *Numerical Heat Transfer, Part A: Applications*, vol. 72, no. 10, pp. 765–779, 2017.

[77] J. Hadamard, *Lectures on Cauchy's Problem in Linear Differential Equations*. New Haven, CT: Yale University Press, 1923.

[78] G. J. Stolz, "Numerical solutions to an inverse problem of heat conduction for simple shapes," *Journal of Heat Transfer*, vol. 82, no. 1, pp. 20–25, 1960.

[79] E. M. Sparrow, A. Haji-Sheikh, and T. S. Lundgren, "The inverse problem in transient heat conduction," *Journal of Applied Mechanics*, vol. 31, pp. 369–375, 09 1964.

[80] C.-H. Ho and M. Özişik, "Inverse radiation problems in inhomogeneous media," *Journal of Quantitative Spectroscopy and Radiative Transfer*, vol. 40, no. 5, pp. 553–560, 1988.

[81] H. Y. Li and M. N. Ozisik, "Inverse radiation problem for simultaneous estimation of temperature profile and surface reflectivity," *Journal of Thermophysics and Heat Transfer*, vol. 7, no. 1, pp. 88–93, 1993.

[82] M. P. Menguc and S. Manickavasagam, "Inverse radiation problem in axisymmetric cylindrical scattering media," *Journal of Thermophysics and Heat Transfer*, vol. 7, no. 3, pp. 479–486, 1993.

[83] M. R. Jones, "Inverse analysis of radiative heat transfer systems," *Journal of Heat Transfer*, vol. 121, pp. 481–484, 05 1999.

[84] K. J. Daun, J. R. Howell, and D. P. Morton, "Inverse design methods for high-temperature systems," *Arabian Journal for Science and Engineering*, vol. 27, no. 2, pp. 3–48, 2002.

[85] P. C. Hansen, "Numerical tools for analysis and solution of fredholm integral equations of the first kind," *Inverse problems*, vol. 8, no. 6, p. 849, 1992.

[86] F. H. França, J. R. Howell, O. A. Ezekoye, and J. Carlos Morales, "Inverse design of thermal systems with dominant radiative transfer," in *Advances in Heat Transfer* (J. P. Hartnett, T. F. Irvine, Y. I. Cho, and G. A. Greene, eds.), vol. 36, pp. 1–110, Elsevier, 2003.

[87] H. Ertürk, K. Daun, F. H. R. França, S. Hajimirza, and J. R. Howell, "Inverse methods in thermal radiation analysis and experiment," *ASME Journal of Heat and Mass Transfer*, vol. 145, no. 5, p. 050801, 2023.

[88] M. Andayesh, D. A. Flórez-Orrego, R. Germanier, M. Gatti, and F. Maréchal, "Improved waste heat management and energy integration in an aluminum annealing continuous furnace using a machine learning approach," *Entropy*, vol. 25, no. 11, p. 1486, 2023.

[89] E. Zambaldi, R. R. Magalhães, B. H. Barbosa, S. P. da Silva, and D. D. Ferreira, "Lowcost automated control for steel heat treatments," *Applied Thermal Engineering*, vol. 114, pp. 163–169, 2017.

[90] N. Yoshitani and A. Hasegawa, "Model-based control of strip temperature for the heating furnace in continuous annealing," *IEEE Transactions on Control Systems Technology*, vol. 6, no. 2, pp. 146–156, 1998.

[91] K. Balakrishnan and T. Edgar, "Model-based control in rapid thermal processing," *Thin Solid Films*, vol. 365, no. 2, pp. 322–333, 2000.

[92] J. R. Howel, K. Daun, H. Ertürk, M. Gamba, and M. H. Sarvari, "The use of inverse methods for the design and control of radiant sources," *JSME International Journal Series B Fluids and Thermal Engineering*, vol. 46, no. 4, pp. 470–478, 2003.

[93] D. Ajorloo, M. Nazari, M. Nazari, N. Sepehry, and A. Mohammadzadeh, "Mathematical modeling and designing an optimized fuzzy temperature controller for a vacuum box electric furnace: Numerical and experimental study," *Transactions of the Institute of Measurement and Control*, vol. 45, no. 7, pp. 1193–1212, 2023.

[94] J. Todd, "Experiments in the solution of differential equations by monte carlo methods," *Journal of the Washington Academy of Sciences*, vol. 44, no. 12, pp. 377–381, 1954.

[95] A. Haji-Sheikh and E. M. Sparrow, "The floating random walk and its application to monte carlo solutions of heat equations," *SIAM Journal on Applied Mathematics*, vol. 14, no. 2, pp. 370–389, 1966.

[96] A. Haji-Sheikh and E. M. Sparrow, "The solution of heat conduction problems by probability methods," *Journal of Heat Transfer*, vol. 89, no. 2, pp. 121–130, 1967.

[97] G. E. Zinsmeister and J. A. Sawyerr, "A method for improving the efficiency of monte carlo calculation of heat conduction problems," *Journal of Heat Transfer*, vol. 96, no. 2, pp. 246–248, 1974.

[98] F. Kowsary and M. Arabi, "Monte carlo solution of anisotropic heat conduction," *International Communications in Heat and Mass Transfer*, vol. 26, no. 8, pp. 1163–1173, 1999.

[99] Z.-S. Deng and J. Liu, "Monte carlo method to solve multidimensional bioheat transfer problem," *Numerical Heat Transfer, Part B: Fundamentals*, vol. 42, no. 6, pp. 543–567, 2002.

[100] R. Bahadori, H. Gutierrez, S. Manikonda, and R. Meinke, "Two-dimensional transient heat conduction in multi-layered composite media with temperature

dependent thermal diffusivity using floating random walk monte-carlo method," *International Journal of Heat and Mass Transfer*, vol. 115, pp. 570–580, 2017.

[101] R. Bahadori, H. Gutierrez, S. Manikonda, and R. Meinke, "A mesh-free monte-carlo method for simulation of three-dimensional transient heat conduction in a composite layered material with temperature dependent thermal properties," *International Journal of Heat and Mass Transfer*, vol. 119, pp. 533–541, 2018.

[102] S. Chantasiriwan, "Determination of sensitivity coefficients in linear heat conduction problems by random-walk method," *Numerical Heat Transfer, Part B: Fundamentals*, vol. 34, no. 1, pp. 103–120, 1998.

[103] A. Haji-Sheikh and F. P. Buckingham, "Multidimensional inverse heat conduction using the monte carlo method," *Journal of Heat Transfer*, vol. 115, no. 1, pp. 26–33, 1993.

[104] F. P. Buckingham and A. Haji-Sheikh, "Cooling of high-temperature cylindrical surfaces using a water–air spray," *Journal of Heat Transfer*, vol. 117, no. 4, pp. 1018–1027, 1995.

[105] M. Honner and J. Sroub, "Modeling of thermal spraying heat transfer processes by exodus stochastic method," *Journal of Thermal Spray Technology*, vol. 18, no. 1, pp. 1014–1021, 2009.

[106] S. Milewski, "Application of the monte carlo method with meshless random walk procedure to selected scalar elliptic problems," *Archives of Mechanics*, vol. 71, pp. 337–3375, 2019.

[107] S. Milewski, "Semi-analytical monte carlo optimisation method applied to the inverse poisson problem," in *Computational Science – ICCS 2021*, pp. 243–256, Springer International Publishing, 2021.

[108] M. F. Modest, "Backward monte carlo simulations in radiative heat transfer," *Journal of Heat Transfer*, vol. 125, pp. 57–62, 01 2003.

[109] M. F. Modest, *Chapter 8 - The Monte Carlo Method for Surface Exchange*, pp. 247–266. Boston: Academic Press, third edition ed., 2013.

[110] H. Ertürk and J. R. Howell, *Monte Carlo Methods for Radiative Transfer*, pp. 1–43. Cham: Springer International Publishing, 2017.

[111] M. P. Mengüç, "http://www.thermalradiation.net," 2022. Accessed: 2024-01-24.

[112] H. Jasak, A. Jemcov, Z. Tukovic, *et al.*, "Openfoam: A c++ library for complex physics simulations," in *International workshop on coupled methods in numerical dynamics*, vol. 1000, pp. 1–20, 2007.

[113] S. G. Parker, J. Bigler, A. Dietrich, H. Friedrich, J. Hoberock, D. Luebke, D. McAllister, M. McGuire, K. Morley, A. Robison, and M. Stich, "Optix: a general purpose ray tracing engine," *ACM Trans. Graph.*, vol. 29, no. 4, 2010.

[114] J. J. Moré and D. J. Thuente, "Line search algorithms with guaranteed sufficient decrease," *ACM Trans. Math. Softw.*, vol. 20, no. 3, pp. 286–307, 1994.

[115] J. Nocedal and S. J. Wright, *Least-Squares Problems*, pp. 245–269. New York, NY: Springer New York, 2006.

[116] Y. Saad and M. H. Schultz, "Gmres: A generalized minimal residual algorithm for solving nonsymmetric linear systems," *SIAM Journal on Scientific and Statistical Computing*, vol. 7, no. 3, pp. 856–869, 1986.

[117] S. Balay, W. D. Gropp, L. C. McInnes, and B. F. Smith, "Efficient management of parallelism in object oriented numerical software libraries," in *Modern Software Tools in Scientific Computing* (E. Arge, A. M. Bruaset, and H. P. Langtangen, eds.), pp. 163–202, Birkhäuser Press, 1997.

[118] J. Nickolls, I. Buck, M. Garland, and K. Skadron, "Scalable parallel programming with cuda: Is cuda the parallel programming model that application developers have been waiting for?," *Queue*, vol. 6, p. 40–53, mar 2008.

[119] A. Haji-Sheikh and J. R. Howell, *Monte Carlo Methods*, ch. 8, pp. 249–295. John Wiley & Sons, Ltd, 2000.

[120] D. W. Hahn and M. N. Özisik, *Separation of Variables in the Rectangular Coordinate System*, ch. 3, pp. 75–127. John Wiley & Sons, Ltd, 2012.

[121] V. S. Arpaci, *Conduction heat transfer*. Addison-Wesley, 1966.

VITA

Ersin Yıldız attained a Bachelor of Science degree in Mechanical Engineering from Yıldız Technical University in 2015. Following this, he pursued his Master of Science degree in Mechanical Engineering, which he completed at Boğaziçi University. In 2018, he started his PhD program in Mechanical Engineering at Özyeğin University. His research interests encompass computational heat transfer, radiation heat transfer, solution of inverse problems, and gradient-based optimization algorithms.

Publications:

1. E. Yıldız, A. M. Başol, and M. P. Mengüç, "Segregated modeling of continuous heat treatment furnaces," Journal of Quantitative Spectroscopy and Radiative Transfer, vol. 249, p. 106993, 2020.

2. E. Yildiz, A. M. Basol, and M. P. Menguc, "A Monte Carlo random walk-based methodology for calculation of sensitivity coefficients in inverse radiant boundary design problem," in Proceedings of the 10th International Symposium on Radiative Transfer, RAD-23, pp. 75–82, Begel House Inc., 2023.

3. E. Yıldız, A. M. Başol, "A random walk based methodology to calculate the sensitivity coefficients in inverse radiant boundary design problems," International Journal of Heat and Mass Transfer, vol. 231, p. 125823, 2024.

Conference Presentations

1. The 34th Şişecam International Glass Conference, "Numerical Study of a Continuous Annealing Furnace: Towards Simulation Based Digital Twin of the Annealing Furnace", Istanbul, Türkiye, November 21-22, 2019.

2. The 7th Başarım National Conference on High Performance Computing, “GPU-accelerated Floating Random Walk Based Transient Heat Conduction Solver”, Istanbul, Türkiye, May 11-13, 2022.

3. The 10th International Symposium on Radiative Transfer (RAD-23), “A Monte Carlo Random Walk-Based Methodology for Calculation of Sensitivity Coefficients in Inverse Radiant Boundary Design Problem”, Thessaloniki, Greece, June 12-16, 2023.

4. The 14th International Conference on Computational Heat and Mass Transfer (ICCHMT 14), “Inverse Radiant Boundary Design for Ensuring Desired Heat Treatment in Vacuum Batch Furnaces”, Düsseldorf, Germany, September 4-8, 2023.

5. The 14th European Conference on Industrial Furnaces and Boilers (INFUB 14), “An Inverse Solution Methodology for the Optimization of Heater Powers in a Vacuum Batch Furnace”, Algarve, Portugal, April 2-5, 2024.